

CARDIFF UNIVERSITY
SCHOOL OF CHEMISTRY



**Superparamagnetic Iron Oxide Nanoparticles:
foundations for novel bioconjugate species and
multimodal contrast agents**

**A thesis submitted for the degree of Doctor of
Philosophy by:**

Geraint Rhys Dafydd Roberts

April 2018

DECLARATION

This work has not been submitted in substance for any other degree or award at this or any other university or place of learning, nor is being submitted concurrently in candidature for any degree or other award.

Signed.....(candidate) Date.....

STATEMENT 1

This thesis is being submitted in partial fulfilment of the requirements for the PhD.

Signed.....(candidate) Date.....

STATEMENT 2

This thesis is the result of my own independent work/investigation, except where otherwise stated, and the thesis has not been edited by a third party beyond what is permitted by Cardiff University's Policy on the Use of Third Party Editors by Research Degree Students. Other sources are acknowledged by explicit references. The views expressed are my own.

Signed.....(candidate) Date.....

STATEMENT 3

I hereby give consent for my thesis, if accepted, to be available online in the University's Open Access repository and for inter-library loan, and for the title and summary to be made available to outside organisations.

Signed.....(candidate) Date.....

STATEMENT 4

I hereby give consent for my thesis, if accepted, to be available online in the University's Open Access repository and for inter-library loan **after expiry of a bar on access previously approved by the Academic Standards & Quality Committee.**

Signed.....(candidate) Date.....

Abstract

Doctor of Philosophy

**Superparamagnetic Iron Oxide Nanoparticles: foundations for novel bioconjugate species
and multimodal contrast agents**

By Geraint Rhys Dafydd Roberts

The properties of superparamagnetic iron oxide nanoparticles (SPION) have led to them being a major area of research within the ‘nano-revolution’. A number of SPION species have been used in disease imaging, including multimodal contrast agents active in positron emission tomography (PET) and magnetic resonance imaging (MRI), as well as bioconjugate species where biomolecules have been immobilised on the nanoparticle’s surface. The western world faces an epidemic of conditions for which monoclonal antibodies (mAbs) have become seen as a ‘magic bullet’. However, the expense of mAb therapy, possible side effects and the desire to maximise treatment success require improvements in patient stratification and selection.

Chapter 1 introduces the field of biomedical imaging and immunotherapy and describes how research into immunoPET and PET/MRI imaging overlap in the following chapters. Chapter 2 describes the development of reliable, reproducible methods of synthesising SPION and introducing a number of biocompatible coatings with useful functionalities. These techniques underlie the chemistry to be discussed in Chapter 3- the immobilisation of biomolecules on the surface of SPION. Typical linker chemistry is discussed, with the relative merits of different approaches expanded upon. The effect of initial reaction stoichiometry on enzymatic activity is explored as a model for later experiment design. Chapter 4 incorporates several of the aspects examined in earlier chapters to describe the synthesis of radiolabelled SPION bioconjugated to the clinically approved antibody trastuzumab to give a novel immunoPET contrast agent. Fluorescence activated cell sorting (FACS) analysis and fluorescence microscopy confirm the *in vitro* validation of these agents. *In vivo* experiments show how these agents require further development before reaching a human clinical context.

Chapter 5 relates the effort to synthesise novel coordination systems based on the hypoxia-selective imaging agent ⁶⁴Cu-ATSM. The co-ordination chemistry of these systems with several metals is described.

Acknowledgements

Firstly I would like to express my many thanks to my supervisors, especially Dr. Ian Fallis and Dr. Angelo Amoroso, for giving me the opportunity to work towards a doctoral qualification and their much needed guidance over the years. I'd also like to thank Paul Davies, John Wilkins, James Schouten and the team at Gallient Biomedical Ltd., as well as the Welsh Assembly Government's Life Sciences Research Network, for helping fund this project and providing many stimulating discussions.

My endless appreciation to the Facilities and Workshops team, Dr. Rob Jenkins, Gary Coleman, Jamie Cross, Robin Hicks, Simon Waller, Steve Morris and Alun Davies, and to Rob Ashton, Louise Pritchard, Heather Butler-Madden and Andy Ough, for the use of the teaching laboratory resources when needed.

Thank you to the following: Dr. Joel Loveridge for specialist NMR techniques; Dr. Steve Paisey for guidance in working with radiation and PET imaging; Dr. Alison Paul for DLS analysis; Chris Morgan for XRD guidance; Prof. Chris Von Ruhland for TEM studies; Dr. Matt Smalley and Dr. Howard Kendrick for FACS and fluorescence microscopy, and Prof. Simon Pope, for some necessary pep talks through the years.

It's been my pleasure to be part of the Inorganic Section: Emily, Stokes, Lara, Mark, Brendan, Mauro, Andy H., Andy W., Sion, Corey, Alex, Lewis, James, Yashar, Tom, Mohammed H., Mohammed B., Ali, Nuha, Seni and the countless undergraduates who've come and gone: thanks for everything.

Thank you to my friends outside of the department for their support, especially when they had no idea what I was talking about: Tom, Steve, Dan, Adam, Craig, Sam, Kat, Amy, George and Steph.

To Martyn, I couldn't wish for a better brother. If it's listening to me grumble down the phone, proof-reading documents or trekking through Norway, you're always there when I need you. And thank you Malen, for lending me Martyn.

To my wife Sarah, who has taken the lion's share of the stress, late arrivals, apologies and peace offerings, I cannot thank you enough for your love, support and patience. You've gone far beyond what anyone could expect of a partner and I truly am grateful to have you in my life. *Ti'n fy nghariad am byth.*

Finally, to Mum and Dad, for encouraging me to go my own way from my very first step.

'Difficulties are just things to overcome, after all.'

- Ernest Shackleton (1874- 1922)

Contents

Abstract.....	iii
Acknowledgements.....	iv
Contents.....	vi
Abbreviations.....	xii
Chapter 1: Molecular imaging for diagnosis and designed therapy.....	1
1.1 Introduction.....	1
1.2 Cancer – diagnosis, treatment, morbidity and mortality.....	1
1.3 Monoclonal antibody (mAb) therapy.....	2
1.4 Molecular imaging, contrast agents and multi-modal approaches.....	4
1.5 Positron Emission Tomography.....	7
1.6 Magnetic resonance imaging.....	12
1.7 PET/MRI bimodal imaging and agents.....	17
1.8 Summary.....	21
1.9 References.....	22
Chapter 2: Synthesis, coating and characterisation of water soluble superparamagnetic iron oxide nanoparticles (SPION).....	25
2.1 Introduction.....	25
2.1.1 SPION structure and characteristics.....	25
2.1.2 Methods of SPION synthesis.....	28
2.1.3 Coating materials.....	32
2.1.4 Applications of SPION: <i>in vivo</i> , <i>in vitro</i> and beyond biomedicine.....	35
2.1.5 Characterisation of nanoparticles.....	37
2.1.6 Aims and objectives.....	45
2.2 Experimental.....	46
2.2.1 Material and methods.....	46
2.2.2 Synthesis and analytical techniques.....	46
2.3 Results and discussion.....	51

2.3.1	Synthesis and characterisation of APTES@SPION and ⁸⁹ Zr-APTES@SPION.....	51
2.3.2	Summary for APTES@SPION and ⁸⁹ Zr-APTES@SPION	62
2.3.3	Synthesis and characterisation of CMD@SPION and ⁸⁹ Zr-CMD@SPION.....	63
2.3.4	Summary for CMD@SPION and ⁸⁹ Zr-CMD@SPION	66
2.3.5	Synthesis, dispersion and relaxometry studies of OA@SPION.....	66
2.4	Conclusion.....	70
2.5	References.....	71
Chapter 3: Bioconjugation of enzymes and antibodies with APTES@SPION		74
3.1	Introduction.....	74
3.1.1	The reactions of bioconjugation.....	75
3.1.2	Homo- and heterobifunctional crosslinkers	77
3.1.3	Glutaraldehyde as a crosslinker	78
3.1.4	Enzymes in bioconjugation.....	79
3.1.5	Enzyme structure and mechanism	79
3.1.6	‘Unit’, ‘specific activity’ and issues pertaining to immobilised enzymes.....	80
3.1.7	Horseradish Peroxidase (HRP).....	81
3.1.8	Alkaline phosphatase.....	83
3.1.9	Purifying and characterising proteins and bioconjugate species.....	83
3.1.10	Aims and objectives.....	88
3.2	Experimental	89
3.2.1	Materials and Methods.....	89
3.2.2	Synthesis and analytical techniques	89
3.3	Results and discussion.....	94
3.3.1	Glutaraldehyde activation and immobilisation of HRP.....	94
3.3.2	Immobilisation of HRP via reductive amination	103
3.3.3	Conjugation of HRP and trastuzumab	109
3.3.4	Immobilisation of the HRP-trastuzumab conjugate via reductive amination	115
3.4	Conclusion.....	121
3.5	References.....	122

Chapter 4: <i>In vitro</i> and <i>in vivo</i> validation of Trastuzumab-conjugated SPION.....	124
4.1 Introduction.....	124
4.1.1 Clinical use of Trastuzumab.....	124
4.1.2 PET isotope production, handling and storage	126
4.1.3 Cell culture and xenotransplantation	128
4.1.4 Fluorescence- dyes, microscopy and FACS for <i>in vitro</i> cell studies	132
4.1.5 Aims and objectives.....	137
4.2 Experimental	138
4.2.1 Material and methods.....	138
4.2.2 Synthesis and analytical techniques	138
4.3 Results and discussion.....	144
4.3.1 FITC labelling of trastuzumab.....	144
4.3.2 Immobilisation of FITC-Trastuzumab on APTES@SPION and the synthesis of FITC-APTES@SPION as a control species	147
4.3.3 Flow cytometry and <i>in vitro</i> validation.....	149
4.3.4 Fluorescence microscopy	157
4.3.5 Synthesis of ⁸⁹ Zr-radiolabelled FITC-Trastuzumab-APTES@SPION.....	159
4.3.6 <i>In vivo</i> biodistribution of radiolabelled SPION.....	162
4.4 Conclusion	174
4.5 References.....	176
Chapter 5: The design and synthesis of Cu-ATSM-like complexes for use as haptens in custom antibody production	179
5.1 Introduction.....	179
5.1.1 Angiogenesis and hypoxia (reduced oxygen content) in cancer	179
5.1.2 ⁶⁴ Cu-ATSM – a hypoxia selective PET imaging agent.....	181
5.1.3 The mechanism of Cu-ATSM's hypoxia selectivity.....	184
5.1.4 The use of haptens in polyclonal antibody development	187
5.1.5 Enzymes, catalytic antibodies and the proposed use of M-BTSC complexes as haptens.....	187

5.1.6	Aims and objectives.....	191
5.2	Experimental	192
5.2.1	Materials and Methods.....	192
5.2.2	Synthesis and analytical techniques	192
5.3	Results and discussion.....	202
5.3.1	Preparation and characterisation of complexes.....	202
5.3.2	NMR Spectroscopy	202
5.3.3	IR Spectroscopy.....	203
5.3.4	UV-Vis Spectroscopy.....	204
5.3.5	Cyclic voltammetry.....	209
5.3.6	Crystallography.....	211
5.3.7	Stability under deprotection conditions	214
5.3.8	Anti-bacterial MIC assessments.....	214
5.3.9	Anti-parasitic assessments	217
5.4	Conclusion.....	221
5.5	References.....	222
	Chapter 6: Concluding remarks	225
	Additional Experimental Section I: Selected attempted methods of synthesising APTES@SPION.....	228
1.1	Introduction.....	228
1.2	Experimental	229
1.2.1	Methods and materials	229
1.2.2	Synthesis and analytical techniques	229
	Additional Experimental Section II – Novel naphthalimide species synthesised for use as fluorescent dyes.....	231
1.1	Introduction.....	231
1.2	Naphthalimide fluorophores in bioconjugate chemistry	231
1.3	Experimental	233
1.3.1	Materials and Methods.....	233

1.3.2	Synthesis and analytical techniques	233
1.4	Results and discussion.....	242
1.4.1	Direct labelling of nanoparticles.....	242
1.4.2	Naphthalimide derivatives of APTES	243
1.4.3	Naphthalimides for bioconjugation	246
1.5	Conclusion.....	253
1.6	References.....	254
Additional Experimental Section III - Small molecules arising from the study of bis(thiosemicarbazone) ligands and complexes		255
1.1	Introduction.....	255
1.2	Experimental	255
1.2.1	Materials and Methods.....	255
1.2.2	Synthesis and analytical techniques	255
1.3	Results and discussion.....	262
1.3.1	Attempted deprotection of ligands	262
1.3.2	The use of a diaminohexane-based side arm- H ₂ L ⁵	263
1.3.3	A chiral side arm- H ₂ L ⁶ and its complexes	264
1.3.4	Attempted synthesis of complex HgL ¹	264
1.3.5	Attempted synthesis of a fluorescent bis(thiosemicarbazone), leading to an unusual cyclic structure	265
1.4	References.....	268
Appendix I: PETIC Standard Operating Procedures for ⁸⁹Zr production and purification		269
Appendix II: Calculations of relative enzyme activity values.....		277
1	Calculation of activities of free HRP	277
2	Calculation of relative activities for gluteraldehyde immobilised HRP	278
3	Calculation of relative activities for reductive amination immobilised HRP	280
4	Calculation of relative activities for reductive amination formed HRP-trastuzumab conjugates, free form and immobilised.....	282

Appendix III: Crystallographic data	284
1 Crystallographic data for naphthalimide (9).....	284
2 Crystallographic data for naphthalimide (10)	285
3 Crystallographic data for complex ZnL ¹	286
4 Crystallographic data for complex CdL ¹	288

Abbreviations

Spectroscopy and techniques

CD	Circular Dichroism
CFU	Colony Forming Units
C_{MR}	Mean Residue Concentration
CT	Computerised Tomography
CV	Cyclic Voltammetry
CVD	Chemical Vapour Deposition
DLS	Dynamic Light Scattering
EC	Electron Capture
ELISA	Enzyme-Linked Immunosorbent Assay
ES	Excited State
ESI	Electrospray Ionisation
ϵ	Extinction coefficient, $\text{mol}^{-1} \cdot \text{L} \cdot \text{cm}^{-1}$
eV	Electron Volts
FACS	Fluorescence Activated Cell Sorting
FFC	Fast Field Cycling
FSC	Front Scatter
FWHM	Full Width at Half Maximum
GS	Ground State
HMBC	Heteronuclear Multiple Bond Correlation
HOMO	Highest Occupied Molecular Orbital
HR	High Resolution
IC	Internal Conversion
IMAC	Immobilised Metal Affinity Chromatography
IR	Infra-Red
ISC	Inter-System Crossing
IT	Isomeric Transition
LFSE	Ligand Field Stabilisation Energy
LUMO	Lowest Unoccupied Molecular Orbital
MALDI	Matrix Assisted Laser Desorption Ionisation
MHz	Megahertz, frequency of NMR spectrophotometer
MIC	Minimum Inhibitory Concentration
MR	Magnetic Resonance
MRI	Magnetic Resonance Imaging
MS	Mass Spectrometry
m/z	Mass/Charge ratio
MWCO	Molecular Weight Cut Off
NIR	Near Infra-Red
NMR	Nuclear Magnetic Resonance
NMRD	Nuclear Magnetic Resonance Dispersion
PET	Positron Emission Tomography
RF	Radiofrequency
SEC	Size Exclusion Chromatography

SSC	Side Scatter
SPECT	Single Photon Emission Computed Tomography
TEM	Transmission Electron Microscopy
TLC	Thin Layer Chromatography
UV-Vis	Ultraviolet-Visible
XRD	X-Ray Diffraction
ν	Frequency
λ	Wavelength

Miscellaneous

ADCC	Antibody Dependant Cellular Cytotoxicity
ALARA	As Low As Reasonably Achievable
ATCC	American Type Culture Collection
EPR	Enhanced Permeability and Retention
FDA	U.S. Food and Drug Administration
HEPA	High Efficiency Particulate Air
NCIMB	National Collection of Industrial Food and Marine Bacteria
NCTC	National Collection of Type Cultures
PETIC	PET Imaging Centre, University Hospital of Wales, Cardiff
PPE	Personal Protective Equipment
RES	Reticuloendothelial System
ROI	Region of Interest
ROS	Reactive Oxygen Species
SOP	Standard Operating Procedure

Units

Å	Angstrom, 1×10^{-10} m
Da	Dalton, atomic mass unit
g	Gram, 1×10^{-3} kg
MBq	Megabecquerel, 1×10^6 Bq
mg	Milligram, 1×10^{-6} kg
mL	Millilitre, 1×10^{-3} L
nm	Nanometre, 1×10^{-9} m
ns	Nanosecond, 1×10^{-9} s
μ s	Microsecond, 1×10^{-6} s
μ L	Microlitre, 1×10^{-6} L

Solvents, chemicals and compounds

AMCA	Aminomethylcoumarin
AP	Alkaline Phosphatase
APTES	3-Aminopropyltriethoxysilane
ATSM	Diacetyl-bis(4-methylthiosemicarbazone)
Boc	<i>Tert</i> -butoxycarbonyl
Boc ₂ O	Di- <i>tert</i> -butyl Dicarboxylate

BSA	Bovine Serum Albumin
BTSC	Bisthiosemicarbazone
BT-474	Human Breast Cancer Cell Line, Her-2 overexpressing
^t Bu	<i>Tert</i> -butyl
CHCl ₃	Chloroform
CMD	Carboxymethyl-dextran
DAPI	4', 6-diamidino-2-phenylindole
DCM	Dichloromethane
DMF	Dimethylformamide
DMSO	Dimethylsulfoxide
DNA	Deoxyribonucleic Acid
D ₂ O	Deuterium Oxide
DFO	Desferrioxamine
DMEM	Dulbecco's Modified Eagle's Medium
DOTA	1,4,7,10-tetraazacyclododecane-1,4,7,10-tetraacetic Acid
DPDP	Dipyridoxyl Diphosphate
DTPA	Diethylenetriaminepentaacetic Acid
EDC	(1-ethyl-3-(3-dimethylaminopropyl)carbodiimide Hydrochloride
EGFR	Epidermal Growth Factor Receptor
EPI	Epiisopiloturine
Et ₂ O	Diethyl Ether
EtOH	Ethanol
Fab	Fragment Antigen Binding
Fc	Fragment Crystallisable
FDG	Fludeoxyglucose
FITC	Fluorescein Isothiocyanate
GTSM	Glyoxal-bis(4-methylthiosemicarbazone)
HCl	Hydrochloric Acid
H ₂ O	Water
H ₂ O ₂	Hydrogen Peroxide
HRP	Horseradish Peroxidase
H ₂ SO ₄	Sulfuric Acid
IgG	Immunoglobulin G
KLH	Keyhole Limpet Hemocyanin
mAb	Monoclonal Antibody
MBS	n-Maleimidobenzoyl-N-hydroxysuccinimide ester
MDA-MB-468	Human Breast Cancer Cell Line
MeCN	Acetonitrile
MeOH	Methanol
NaOH	Sodium Hydroxide
Na ₂ CO ₃	Sodium Carbonate
NaBH ₄	Sodium Borohydride
NaCNBH ₃	Sodium Cyanoborohydride
NaCl	Sodium Chloride
NEt ₃	Triethylamine
NHS	N-Hydroxysuccinimide

NaIO ₄	Sodium Periodate
N ₂	Nitrogen
NOTA	1, 4, 7-Triazacyclononane-N, N', N''-triacetic acid
NTA	Nitrilotriacetic Acid
OA	Oleic Acid
PAA	Poly(acrylic acid)
PBS	Phosphate Buffered Saline
PF ₆	Hexafluorophosphate
RPMI	Roswell Park Memorial Institute Medium
SPDP	Succinimidyl 3-(2-pyridyldithio)propionate
SPION	Superparamagnetic Iron Oxide Nanoparticle(s)
THF	Tetrahydrofuran
TFA	Trifluoroacetic Acid
TMB	3, 3', 5, 5'-tetramethylbenzidine
TRITC	Tetramethylrhodamine Isothiocyanate

Chapter 1: Molecular imaging for diagnosis and designed therapy

1.1 Introduction

Superparamagnetic iron oxide nanoparticles (SPION) have been known since the early 1980s,¹ and a number of SPION-based species are now used clinically for the imaging of disease.² They have been the study of much research in a variety of contexts; their ability to adsorb and incorporate heavy metal atoms has already been reported in environmental clean-up,³⁻⁵ but is still relatively unexplored in terms of radiolabelled nanoparticles with medical applications.^{6,7} Similarly, although biomolecules have been immobilised onto the surface of such nanoparticles, reported approaches have tended to be quite distinct from one another, and discerning trends to inform design is difficult. In this thesis, a proof of concept will be demonstrated: biomolecule functionalised iron oxide nanoparticles, synthesised reproducibly on a large scale and radiolabelled with the medically relevant isotope ⁸⁹Zr. The progression to an *in vivo* study from nanoparticle formation via the validation of bioconjugate methodologies bears evidence to how inorganic chemistry can fit into the future of medicine.

1.2 Cancer – diagnosis, treatment, morbidity and mortality

In 2012, published projections of cancer prevalence in the UK predicted that the number of people living with cancer will increase by approximately 1 million per decade to 5.3 million in 2040.⁸ By 2021, the cost to the UK for the diagnosis and treatment of cancer is predicted to rise to £ 15.3 billion.⁹ In cases where cancer is allowed to become metastatic, survival rates are significantly depressed (Fig. 1).³ Early detection, characterisation and treatment is key in improving survival rates among cancer patients, selecting the most appropriate treatment regimen is crucial.

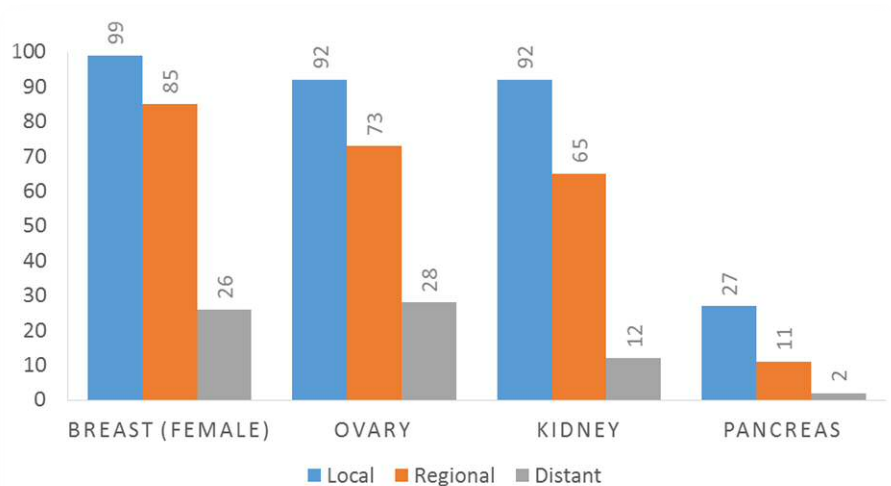


Figure 1. Five Year relative survival rates (%) for selected forms of cancer. Local describes a tumour confined to the organ of origin. Regional describes a tumour that has spread to neighbouring organs, tissues and/or local lymph nodes. Distant refers to a tumour that has spread to regions distant to the organ of origin.¹⁰

There are a wide range of therapies available- depending on the form of cancer, most patients will have a combination of two or more. These may include surgery, radiotherapy, chemotherapy and hormone therapy. Radiotherapy and chemotherapy (the use of radiation and small molecule chemical species respectively to treat cancer or ease symptoms) can be effective but have common side-effects which can diminish patient quality-of-life.¹¹ One of the greatest medical success stories of the past century is the development of immunotherapy, the use of antibodies to treat diseases including many forms of cancer. However, the expense of immunotherapeutic drugs and the ever-increasing population of cancer patients have contributed to a need to refine how patients are selected to receive treatment. It will become necessary to stratify potential patients based on their likely response to immunotherapy.¹² In recent years, there has a been great interest in the development of imaging agents based on immunotherapeutics to achieve this.¹²

1.3 Monoclonal antibody (mAb) therapy

In 1906, the German scientist Paul Ehrlich hypothesised that a chemical stain which showed selectivity for a given bacteria could also be used to deliver a toxic agent to kill its target, acting in effect as a ‘magic bullet’.¹³ Antibodies (part of the body’s immune response to foreign antigens) seemed like an obvious candidate for the development of an arsenal of ‘magic bullets’; however, antibodies are naturally heterogeneous and offer a variety of binding responses to a target antigen. The development of methods to produce homogeneous antibodies sample from a single source (i.e. monoclonal antibodies) along with subsequent

humanisation of murine antibodies made Ehrlich's dream a reality and in the 1990s FDA-approval was granted for Rituximab,¹² leading to clinical success for a number of mAb-based therapies.⁶

Antibodies are large immunoglobulin proteins, consisting of at least 4 subunits. They are produced as part of the body's immune response to foreign macromolecules. There are five classes of antibodies: IgG, IgM, IgA, IgD and IgE.¹⁴ IgG is the most common immunoglobulin class in the body and is the most frequently used in cancer immunotherapy, and will therefore be the focus of the discussion below. Such mAbs consist of 2 identical approximately 23 kDa domains known as 'light chains', and 2 identical 53-75 kDa heavy chains, arranged in the familiar Y-shape (Fig. 2). The subunits associate with each other via disulphide bonds along with local non-covalent interactions. The 'arms' of the molecule consist of two identical 'Fragment antigen binding' (Fab) regions, while the 'stem' consists of the 'Fragment crystallisable' (Fc) region. The Fc regions of different antibodies are largely constant within a given host.

Selectivity of these antibodies is controlled primarily by the antigen binding sites of the light and heavy chains.¹⁴ Variation in the amino acid sequences of antibodies ('hypervariable sequences') occurs predominantly in three flexible loops at the end of the chains, allowing specific antigen binding. The Fc region may bind to effector molecules as part of an immune response; glycosylation in this region is a common post-translational modification, and is believed to play an important part in mediating the effect of the antibody.^{7,8}

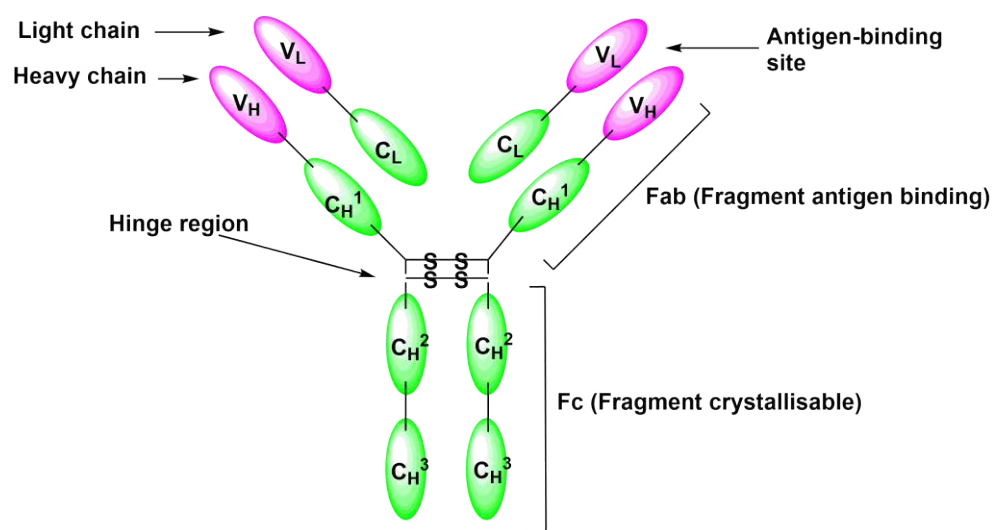


Figure 2. Simplified structure of a typical mAb. Not shown are regions of folding, N- and C-terminals, glycosylation and disulphide bonds between light and heavy chains.

Administration of mAb therapies is now commonplace, with many new mAb species being granted FDA approval every year.^{13,14} A 2015 report on the global market for mAb products hypothesised that with a conservative FDA-approval rate of approximately 4 therapeutic formulations per year, by 2020 the global market will be worth \$125 billion.¹⁵ Many mAb-based therapies are so-called ‘block-buster drugs’, with their efficacy leading to significant profits for the parent company. As an example, trastuzumab (Herceptin[®]) is a mAb preparation which binds to the Her-2 receptor which is over-expressed in approximately 25 % of breast cancers.¹⁶ Although its specific mode of action is still a subject of some debate, dramatic reductions in tumour size have been reported, leading to trastuzumab therapy being recommended for first-time, re-current and metastatic breast cancers.¹⁶ Breast cancer is the most common form of cancer in women worldwide, and trastuzumab is the world’s best-selling breast cancer drug. With a year of trastuzumab treatment typically costing over \$50,000, the cost to healthcare systems for breast cancer treatment alone runs into the billions of dollars.⁹

While remarkable clinical successes have been shown, poor patient-to-patient performance has been reported for some mAb-based treatments. In the case of trastuzumab, Her-2 overexpression in a patient’s tumour may be determined histologically, but does not give an accurate indication of the likely efficacy of trastuzumab. Concurrently, side effects including dose-independent cardiac dysfunction has been reported.¹⁷ There is a need to develop methods of pre-selecting patients for mAb therapy. The benefits of improved patient stratification and selection are manifold; not only is the healthcare system spared the expense of administering a drug that may be of limited effect, but the patient is more quickly referred to the most suitable treatment regimen for them, improving their chances of a successful outcome.¹² The modification of an already clinically approved mAb agent to act as an imaging agent would be an elegant solution. Depending on the imaging mode used (see below), an imaging dose would be a pharmacologically insignificant, limiting cost and side effects while allowing the observation of *in vivo* behaviour and assessment of mAb therapy suitability. Additionally, the path to FDA-approval may prove easier given the prior use of the parent species.

1.4 Molecular imaging, contrast agents and multi-modal approaches

The non-invasive visualisation of biological processes and targets at the molecular level *in vivo* has revolutionised the diagnosis of disease, with a positive effect on patient survival rates and quality of life. There are a range of established and emerging imaging modalities available to the researcher or clinician and almost all require the use of an administered chemical

species (known as a contrast agent) to either create or enhance contrast between tissues of interest and the background to allow the diagnosis of disease. Novel imaging agents based on molecules which exhibit a behaviour in response to external stimuli (e.g. magnetic particles in an applied magnetic field, or fluorescent molecules under irradiation with specific wavelengths of light) provide innovative approaches to better understand biological processes within tissues and to aid diagnosis. Together with the need to improve on current agents, there is a demand for chemists to design and synthesise novel species in response to the increased understanding of disease pathologies.^{18,19}

Unfortunately, no single mode of imaging is perfect, with each having specific advantages and disadvantages (see Table 1).¹⁹ Those with high resolution usually show low sensitivity, while high sensitivity is generally associated with poor spatial resolution. Depth of penetration can severely limit a technique's application. It is now universally accepted that the best approach is to interrogate a biological subject with two or more imaging modes, using their complementary abilities in a synergistic manner to overcome their individual disadvantages. Administering a single agent, active in multiple imaging modes, is preferable to administering several singly active species. Fewer clinical interventions, reduced biological disruption and ensured co-localisation are just a few benefits of using a multi-modal agent.¹⁸ Although the scientific literature contains numerous examples of bimodal imaging agents, a full discussion of all possible combinations of modalities would be inappropriate, and the interested reader is referred to some of the many excellent reviews published to date.¹⁸⁻²¹ Attention in the current instance will be focussed on the individual modes of PET and MRI, the development of combined PET/MRI agents (due to the large potential benefits to be gained from combining high sensitivity and high resolution), and how this has led to SPION being at the forefront of the field.

Modality	Typical agents	Physical basis	Advantages	Disadvantages
CT	Iodine- or barium-containing agents	X ray detection and computer analysis	Deep penetration, high resolution	Low sensitivity, ionising radiation
MRI	Gd chelates, SPION	Differences in water proton relaxivity in a magnetic field	Deep penetration, high resolution, no ionising radiation	Low sensitivity, expensive set-up costs
PET	Radioisotopes	Detection of γ -rays arising from positron annihilation	Deep penetration, extremely sensitive	Poor resolution, ionising radiation, expensive set-up
SPECT	Radioisotopes	Detection of γ -rays	Deep penetration, extremely sensitive	Poor resolution, ionising radiation, expensive set-up
Optical Imaging	Lumophores	Detection of emitted visible/NIR photons	Inexpensive, short timescale of observation	Shallow penetration, autofluorescence

Table 1. Comparison of some common imaging modalities.¹⁹

1.5 Positron Emission Tomography

Positron Emission Tomography (PET) is a non-invasive molecular imaging technique based on the decay of positron emitting radionuclides within a living target. The collision of emitted positrons with endogenous electrons results in an annihilation event and the emission of gamma rays that are detected and which inform the observer of the site of annihilation. It is relatively commonly used in a clinical setting worldwide. In contrast to other diagnostic techniques (e.g. Computerised Tomography (CT) or Magnetic Resonance Imaging (MRI)) a contrast agent is always necessary, as there are no naturally occurring sources of positrons within the human body. This naturally low background contributes to the excellent sensitivity of PET (blood-agent concentrations as low as 10^{-12} mol.L⁻¹ yield sufficient contrast).¹⁹ Such high sensitivity explains the prevalence of PET; although the cost of establishing a PET centre is high due to the requirement for a small medical cyclotron and laboratories suitable for radiochemical work, it is outweighed by the quality of the information to be gained from PET imaging with small quantities of agent. The exposure of the patient to ionising radiation is less than for CT.²² PET contrast agents can be designed to accumulate at biological targets of interest, such as those associated with disease; up-regulated glucose metabolism,²³ over-expressed cell surface receptors²⁴ and hypoxic cell environments²⁵ are all indicative of forms of cancer.

PET isotopes are synthesised by the use of a cyclotron. A target consisting of a naturally occurring element is bombarded by high energy protons, deuterons or helium particles. The bombarding particle combines with the target nucleus to give a compound nucleus of the radioisotope in an unstable, energetically excited state which is isolated and incorporated into an imaging probe for rapid use.^{26,27} Decay of unstable nuclei can occur via multiple pathways, but 'PET active' nuclei decay mainly by the conversion of an extra proton to give a neutron, a neutrino, and an emitted positron, β^+ , the equivalent antiparticle of an electron. Inelastic interactions with surrounding species cause rapid slowing of the positron until collision with an electron occurs (an 'annihilation' event). The conservation of momentum and energy results in the remaining mass of the positron and the electron being converted to two 511 keV photons, emitted at 180 ° to each other as gamma rays.²¹ PET scanners consist of concentric, closed circle detectors enclosing a subject. The impact of gamma rays on the detectors is converted first to an electrical signal, then to a sinogram, then correlated to a tomographic image to give a corrected representation of the source of the gamma rays. This allows the approximate anatomical locale of the tracer to be determined. As the annihilation event occurs at a point distinct from the emission of the positron, PET suffers from limited

resolution; the mean free path of the positron is on the mm scale.²⁸ Different PET active isotopes have different positron ranges which can effect resolution (see Fig. 3c).²⁹

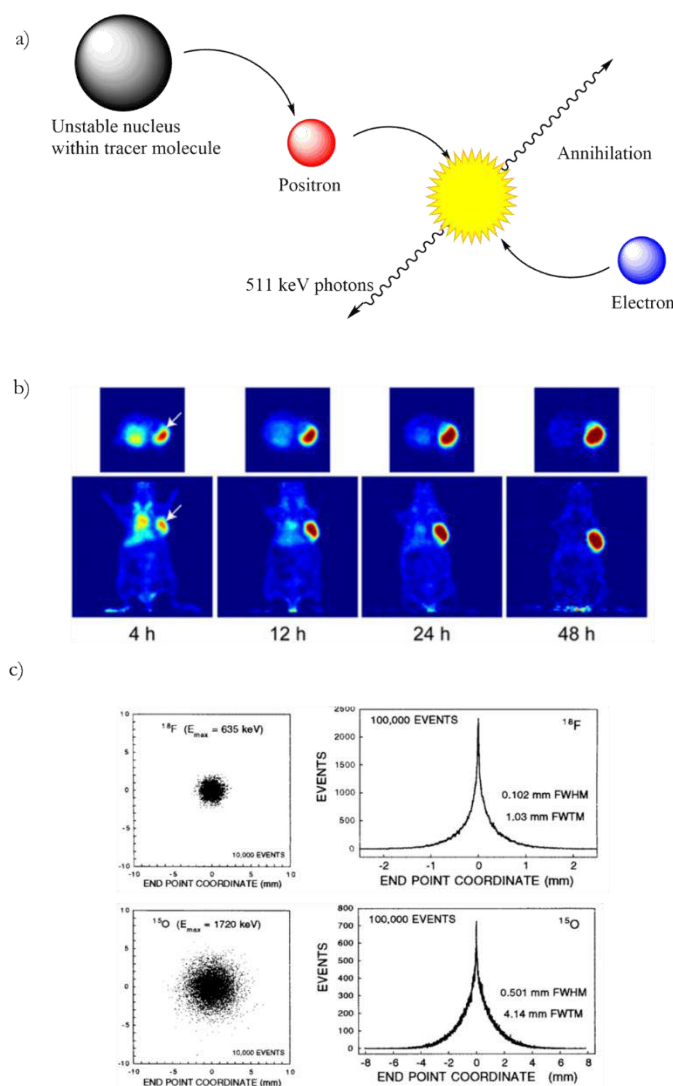


Figure 3a. Schematic of events giving rise to gamma ray emission for detection. **b.** Small animal PET images showing accumulation of tracer in a tumour, adapted from Zeglis et al.³⁰ **c.** Comparison of end-point-coordinates for the decay of different isotopes.²⁹

Historically, the most commonly used radioisotope for clinical PET has been ^{18}F ($t_{1/2} = 109.7 \text{ min}$; $\beta^+ = 0.64 \text{ MeV}$), most regularly as ^{18}F -fluorodeoxyglucose (FDG). Although ideal for visualising the location of upregulated glucose metabolism, this fluorinated sugar is not directed to cancer specific markers, so may accumulate in healthy tissues with high metabolic need and may not accumulate in slow growing tumours.^{16, 23} The short radioactive half-life of ^{18}F limits its practical use to almost immediately upon production, and renders it not suitable for use with longer time-scale biological processes, such as with slow-clearing high molecular weight biomolecules (e.g. mAbs). In the last decade, there has been an effort within the research community to develop PET agents utilising long half-life metallic radioisotopes

which are better suited to investigating long time-scale processes. As a result of the increasing number of small medical cyclotrons in clinical settings, a range of isotopes are available to today's researchers, allowing properties such as physical half-life or emission energy to be selected to complement the biological half-life of the target or delivery vector. The loss of signal of a radiopharmaceutical is affected by radiological (t_r) and biological (t_b) half-lives, and so the agent has an effective half-life, t_e :

Contrast agents with rapid clearance can be labelled with ^{68}Ga ($t_{1/2} \sim 68$ min), whereas species which accumulate or which are slower to clear molecules such as mAbs (e.g. biological half-life of cetuximab is 114 h)³⁰ may be labelled with ^{89}Zr ($t_{1/2} = 78.5$ h) to give a desirable t_e .^{32,33}

<i>Isotope</i>	Half-life/h	Source	Production reaction	Decay mode (% branching ratio)	Common oxidation states	Common coordination numbers
^{18}F	1.8	Cyclotron	$^{18}\text{O}(p, n)^{18}\text{F}$	β^+ (97) EC (3)	1-	1
^{61}Cu	3.3	Cyclotron	$^{61}\text{Ni}(p, n)^{61}\text{Cu}$	β^+ (62) EC (38)	1+, 2+	4, 5, 6
^{64}Cu	12.7	Cyclotron	$^{64}\text{Ni}(p, n)^{64}\text{Cu}$	β^+ (19) EC (41) β^- (40)	1+, 2+	4, 5, 6
^{66}Ga	9.5	Cyclotron	$^{63}\text{Cu}(\alpha, n\gamma)^{66}\text{Ga}$	β^+ (56) EC (44)	3+	4, 5, 6
^{86}Y	14.7	Cyclotron	$^{86}\text{Sr}(p, n)^{86}\text{Y}$	β^+ (33) EC (66)	3+	8, 9
^{89}Zr	78.5	Cyclotron	$^{89}\text{Y}(p, n)^{89}\text{Zr}$	β^+ (23) EC (77)	4+	8

Table 2. Physical characteristics of some common metallic radioisotopes; ^{18}F included for comparison. Data adapted and combined from multiple sources.^{26,32,34}

To date, ^{89}Zr has become the favoured isotope for the purpose of radiolabelling mAbs, a field known as immunoPET.^{12,35–37} The long half-life of the isotope is not only on a similar timescale to whole antibody circulation times, but it allows for production at a location distant to the point of administration to a patient, so the isotope is available commercially.³⁸ Shorter lived isotopes (e.g. ^{64}Cu) are better suited to antibody fragments or small molecules.³⁶ Positrons emitted from ^{89}Zr have relatively low energy ($E_{\text{mean}} = 395 \text{ keV}$) which yields high resolution images.³⁷ The chemistry of zirconium in its +IV oxidation state is also important to understand its popularity for immunoPET- the ion is relatively large for a hard cation, allowing it to accommodate up to eight of its favoured anionic oxygen donors. This has been exploited in the past in nuclear fuel recovery by the use of derivatives of a naturally occurring bacterial iron chelator, desferrioxamine (DFO), which has six hydroxamate groups with which to coordinate Zr^{4+} in a highly stable manner (two water molecules complete the coordination sphere) necessary to maximise retention of the radioisotope by the vector molecule and to aid the analysis of resultant PET scans. Derivatives of DFO are still commonly employed in immunoPET but toxicity issues arising from release of ^{89}Zr and subsequent sequestration in bone has led to the search for improved methods of radiolabelling mAbs.^{36,37}

The development of bifunctional chelators which conjugate to biomolecules and coordinate metal centres has given rise to a degree of modularity. Biomolecules can be rapidly prepared for radiolabelling by the use of commercially available species (e.g. the DFO based Df-Bz-NCS (Fig. 4)^{39,40} or the more stable HOPO-Bz-NCS developed by Lewis *et al.*)^{41,42} Versatile chelators such as DTPA, DOTA and NOTA (Fig. 5) have the ability to coordinate to different metals, such that the radiometal may be exchanged (without need to change the synthesis of the bioconjugate) to give imaging and therapeutic companion agents.³² An imaging agent can be structurally identical to a therapeutic analogue, differing only in the nature of the coordinated metal. However, regardless of the nature of the group or the metal centre, the number of chelating groups that may be introduced per biomolecule is limited by the need to not change the *in vivo* behaviour of the vector.^{39,43} The process of radiometal coordination is typically rapid, requiring mild conditions and relatively facile purification methods. By contrast, organic radioisotopes normally require harsh, multistep reaction schemes with complicated purifications, increasing the complexity of the operation and eating into the usable time of the unstable isotopes.³²

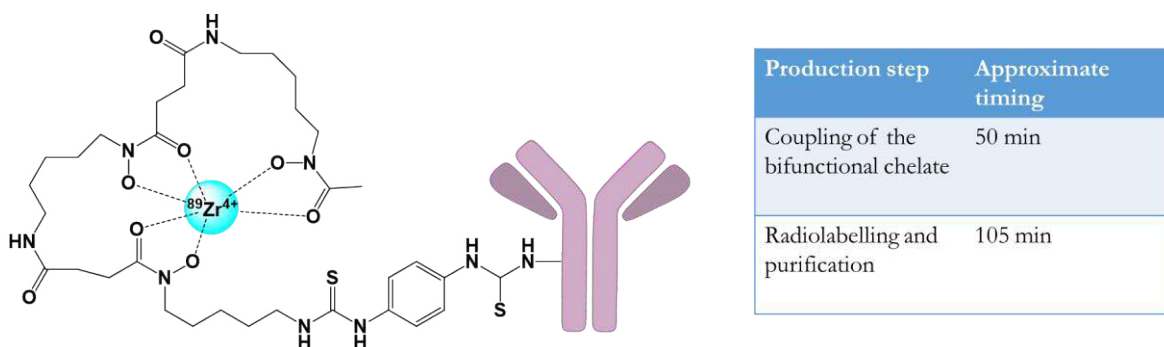


Figure 4. Simplified depiction of Df-Bz-NCS, a metal-coordinating ligand based on DFO, coordinating ^{89}Zr and coupled directly to a mAb. Note the short timeframe of the synthesis. Adapted from Vosjan et al.⁴⁰

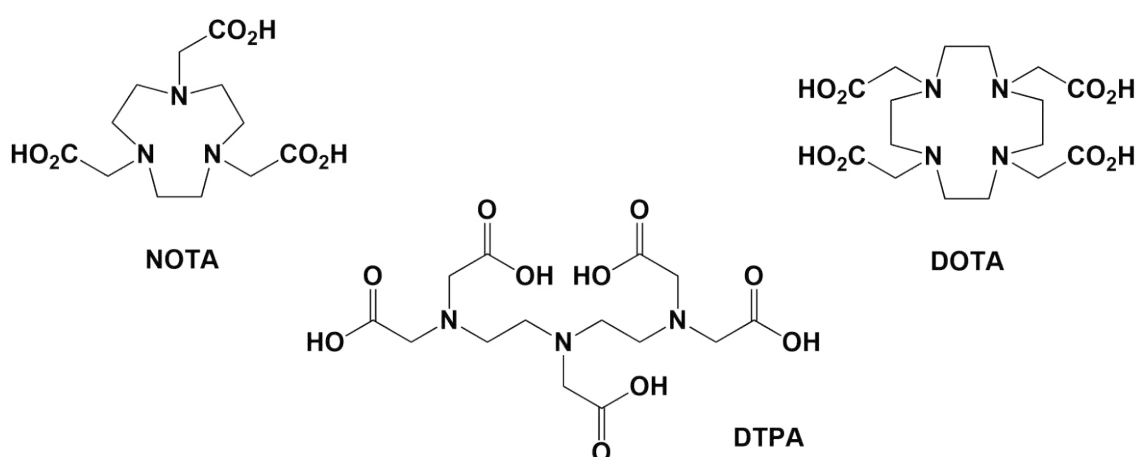


Figure 5. Common chelating moieties within inorganic radiochemistry.

A final desirable characteristic of radiometals is their tendency to residualise in target cells.³⁷ Retention at the target site and long radioactive half-lives gives the opportunity for sequential scans of a subject over long periods of time (multiple half-lives). This allows for the real-time imaging of disease development and/or treatment, with a minimum of interventions, but must be considered against the inherent risks of radiodrugs e.g. cytotoxicity.³²

Several radiometal agents are used in clinical PET imaging today, and two are of direct relevance to the current work. ^{89}Zr -based immunoPET imaging will be discussed further in Chapter 4. The agent ^{64}Cu -ATSM has been used for the PET imaging of hypoxia (indicative of a cancerous cell environment) since 2002.⁴⁴ The interesting chemistry of this agent and the chemical family to which it belongs is discussed in Chapter 5.

1.6 Magnetic resonance imaging

Magnetic resonance imaging (MRI) is one of the most commonly used imaging modes in healthcare systems around the world, offering unlimited depth of penetrations, high spatial resolution (< 1 mm in clinical contexts) and potentially real-time observation of cellular behaviour. However, it displays poor sensitivity, with large quantities of contrast agents being required to achieve contrast sufficient to aid diagnosis.²¹ To understand how contrast is enhanced by chemical agents such as SPION requires a brief description of the fundamentals of the technique. The reader is referred to literature for further information beyond the scope of this introduction.⁴⁵⁻⁴⁷

MRI is based upon the concept of the nuclear spin of hydrogen atoms (protons) present in water molecules in living tissue.^{45,46} Protons are considered as rotating, charged particles, and therefore have a magnetic moment (B) with vector properties. In the absence of an external magnetic field, a sample consists of an equal number of α - and β -spins (spin-up and spin-down respectively) with random orientation in space and zero net magnetisation. The energies of the two spin states change when an external magnetic field (B_0) is applied, as does the population at equilibrium (as predicted by a Boltzmann distribution for a given temperature and field strength), resulting in a small majority of the lower energy α -spins aligning parallel to the field and giving a net longitudinal magnetisation, M_z . A smaller number of higher energy β -spins align anti-parallel to the field. Both spin states precess about the z-direction (Fig. 6).

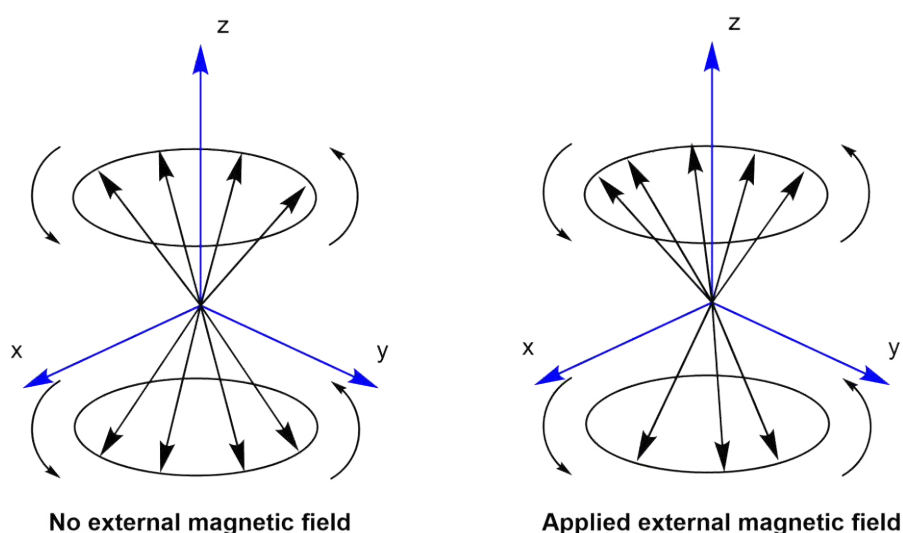


Figure 6. In the presence of an applied magnetic field (B_0) in the z-direction, a small majority of spins align and precess about the z-direction to give a net magnetisation, M_z .

Precession about the z-axis occurs at a rate dependent upon the strength of the applied field and the gyromagnetic ratio of the proton. This rate is the Larmor frequency and is given by the Larmor equation:

where ω_0 is the Larmor frequency in MHz, γ_0 is the gyromagnetic ratio for protons, $42.577 \text{ MHz}\cdot\text{T}^{-1}$, and B_0 is the strength of the magnetic field in Tesla.^{45,46}

Exciting a sample with radio waves equal to the Larmor frequency for a sufficient time tips the longitudinal magnetisation into the xy-plane (a 90° radiofrequency (RF) pulse), giving transverse magnetisation, M_{xy} . Precession in this plane about the z-axis induces a voltage in receiver coils set up around the direction of magnetisation, which is interpreted as an MR signal.

The signal intensity at any point following excitation depends on the degree of transverse magnetisation, and is related to proton density and relaxation rates. Following the 90° RF pulse, the transmitter is turned off. The spins now existing in an excited state seek to relax by dissipating energy. Realignment with the applied field causes a decrease in M_{xy} and free induction decay in the intensity of the MR signal.

Three relaxation mechanisms contribute to decay in the M_{xy} and therefore loss of signal intensity. Realignment of the spins with the z-direction is known as ‘longitudinal’ or ‘spin-lattice’ relaxation (Fig. 7), and has an exponential time constant T_1 . Energy is lost from the spins to their surroundings, allowing recovery of M_z . The time T_1 is the length of time taken for a 63 % recovery, and is generally of the order of seconds at 1.5 T for water in biological tissues. It is dependent on B_0 and Brownian motion within the sample.

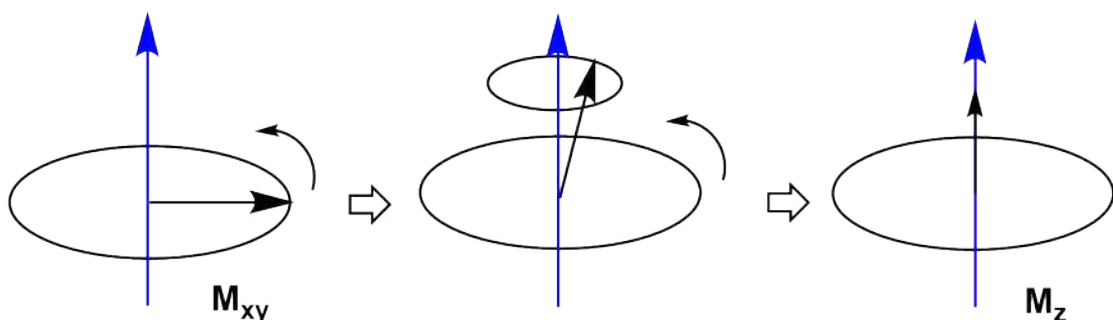


Figure 7. T_1 Relaxation – realignment of spins with field direction.

‘Spin-spin’ or ‘transverse’ relaxation causes signal decay due to loss of phase coherence (Fig. 8). Following the 90° RF pulse, all the proton spins in a sample are initially aligned in the transverse direction coherently, i.e. in the same place in the precessional path around the z-axis. Spins are able to exchange energy with each other, leading to different precessional rates, eventually causing proton spins to go ‘out of phase’. The individual magnetisation vectors no longer sum to give a net magnetisation in one direction, and the measured signal decays with exponential time constant T_2 (the ‘transverse relaxation time’, the time taken for 63 % loss of transverse magnetisation). Transverse relaxation occurs in the first few hundred milliseconds after the 90° RF pulse, before longitudinal relaxation has occurred to a significant degree.

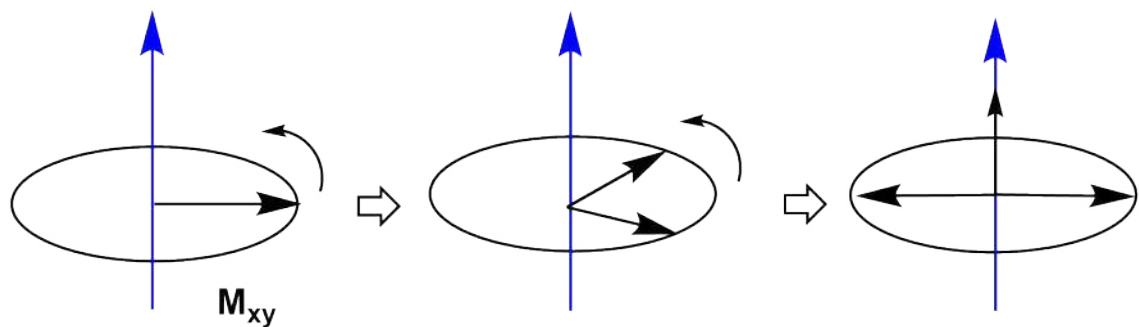


Figure 8. T_2/T_2^* Relaxation – loss of phase coherence between spins.

Local field inhomogeneities also result in different spins having different precession rates, but can be compensated for. The properties of an individual scanner or patient can affect dephasing and loss of MR signal with time constant T_2^* (the ‘effective transverse relaxation time’), but this may be limited by appropriate experiment design. The three relaxation mechanisms occur simultaneously but independently.⁴⁶

Protons in water in different tissues have different T_1 and T_2 relaxation rates. At a given time following a 90° RF pulse their respective MR signals will have different intensities, leading to contrast in reconstructed images. An image can be weighted to achieve maximum contrast by highlighting T_1 or T_2 differences (i.e. if tissues have similar T_1 times, using T_2 differences to generate contrast may be more useful diagnostically) (see Fig. 9b).⁴⁸ A T_1 -weighted image is obtained by using a repetition time (time between RF excitations) that is shorter than the T_1 times of the tissues being contrasted. A fast recovering spin (short T_1) will have a larger transverse magnetisation component following the second RF pulse than a slow recovering spin, leading to a more intense, brighter signal on the MRI image.⁴⁶ A T_2 -weighted image is derived using a gated technique; a short interval of time (echo time) separates the excitation

pulse and collection of the MR signal, during which time loss of phase coherence has occurred to different degrees in different environments. A short T_2 time results in a greater loss of signal (darker image) than a longer T_2 time.⁴⁶

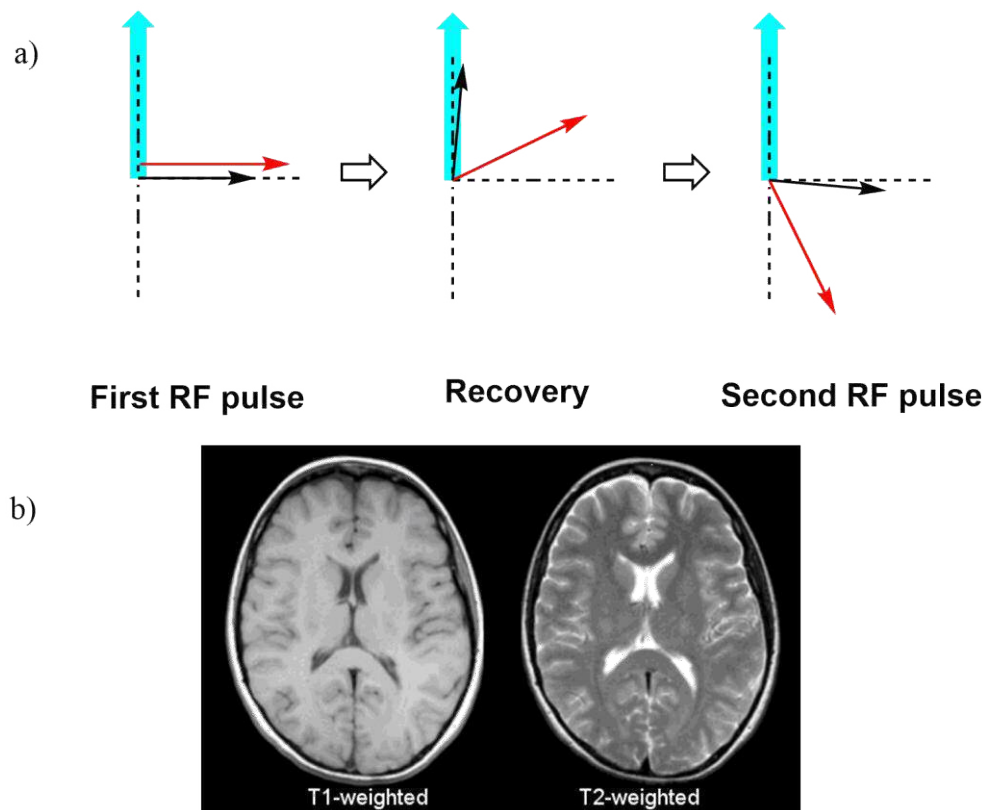


Figure 9a. T_1 weighted images show contrast based on T_1 times. Here, the black vector represents a spin with short T_1 time and the red vector represents a spin with a long T_1 time. The faster relaxing black vector has more longitudinal magnetisation before the second 90° RF pulse, and so more transverse magnetisation afterward, giving a brighter signal.⁴⁵ **b.** Comparison between T_1 - and T_2 -weighted images.⁴⁸

Natural contrast between different tissues is often not sufficient to allow clear imaging. MR contrast media are molecules that have characteristics that make them useful in enhancing contrast: controlled/predictable biodistribution, low toxicity and excretability, and high molar relaxivity.⁴⁵ Most common MR contrast agents are based on paramagnetic or superparamagnetic metal systems where unpaired electronic spins of the metal atoms generate a magnetic moment that when appropriately functionalised cause an enhancement/acceleration of water proton relaxation rates in the target tissue.^{45,46,49} ‘Relaxivity’ is a measure of the efficiency with which a contrast agent enhances T_1 or T_2 relaxation times, based on its concentration and the observed increase in relaxation rates.⁴⁵ The values of the relaxivity quantities R_1 and R_2 can be measured and are known to relate to T_1 and T_2 :

where R has units s^{-1} .⁴⁶ The higher the relaxivity of the agent, the faster the rate of relaxation of the proton, which underlies signal intensity in both T_1 and T_2 weighted images.⁴⁶ Changing signal intensity inherently affects contrast between tissues. Often relaxivities of agents are quoted as r_x with units of $L \cdot mmol^{-1} \cdot s^{-1}$ at a given temperature, and so measured values of R_x and agent concentration c are related by the equation:⁵⁰

There are multiple contributing mechanisms to the relaxivity induced by the use of contrast agents. In a tissue, the local magnetic field experienced by protons is dependent on the applied field and fluctuations arising from the tumbling of nearby molecules with a magnetic moment. The speed of molecular tumbling affects the efficiency of relaxation processes. For both paramagnetic and superparamagnetic contrast agents, T_1 and T_2 relaxation rates can be enhanced by the agent changing the local magnetic field and slowing water tumbling in the inner and outer coordination spheres. Agents are often referred to as T_1 - or T_2 agents based upon the relaxation mode upon which they have most effect. Paramagnetic MRI contrast agents will typically consist of a metal ion with unpaired electrons, coordinated to a ligand that allows exchange of coordinated water with the surroundings. The most common metals used in this context are Gd in its +III oxidation state and Mn in its +II oxidation state, having 7 and 5 unpaired electrons respectively. Such agents are administered to patients in gram quantities, but there has been a desire to develop alternatives to the use of gadolinium species due to their association with nephrogenic systemic fibrosis.⁵¹ Manganese species have also been plagued by toxicity issues,⁵² despite the metal being present as a trace mineral in the body used in metabolism, nerve function and in other roles.^{52,53} Nevertheless, several species have been FDA-approved, from the simple salt $MnCl_2$ (as ‘Lumenhance’) to complex ions such as Mn-DPDP (‘Teslascan’).

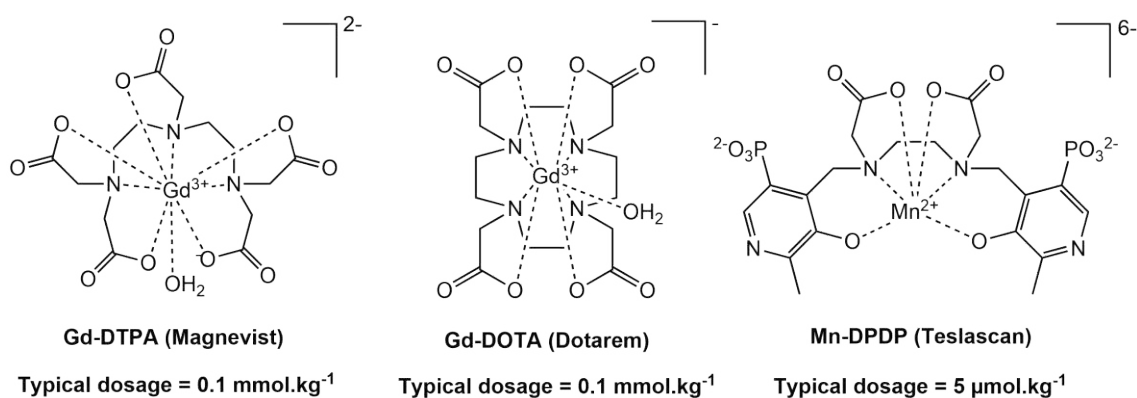


Figure 10. Three FDA-approved paramagnetic MRI contrast agents. The use of Gd and Mn can cause toxicity issues in some patients.^{51–53}

Iron-based contrast agents are particularly desirable for several reasons. Iron is present in the body in large quantities and has low toxicity; iron oxides are known to degrade in the body with few repercussions due to the existing mechanisms of iron metabolism (e.g. ferritin), although a target of research is to optimise the biological lifetime of the agent so that it is excreted before significant degradation occurs.²⁰ The most successful form of ferrous contrast agents to date are superparamagnetic iron oxide nanoparticles. Typically consisting of iron in both its +II and +III oxidation states in a lattice with oxygen, the large number of unpaired spins arising from the metal atoms results in each particle having a net magnetisation vector greater than any individual Gd- or Mn-complex. These particles display superparamagnetism and high relaxivity values, making them excellent MRI contrast agents. A more thorough discussion of SPION and superparamagnetism is given in Chapter 2. The first *in vivo* trials using SPION were carried out in the 1980's,^{32–34} and several SPION-based MRI agents have since been FDA-approved (e.g. Feridex, Resovist and Sinarem).

1.7 PET/MRI bimodal imaging and agents

As has been discussed above, all imaging modes have some limitations, and thus multiple techniques are often used in diagnosis. Since 2001, sales of PET scanners have been overtaken by sales of combined PET/CT scanners, which have become the favoured approach for clinical imaging.^{54,55} CT compensates for the poor resolution of PET, but both result in exposure to radiation. MRI can be viewed as a superior alternative; the use of suitable agents increases contrast relative to CT and radiation dosage is lessened.^{55–57} Modern PET/MRI combined scanners can provide anatomical and functional information via both imaging modes.⁵⁷ For widespread acceptance and integration of PET/MRI over PET/CT or separate, sequential scanning in different modes, PET/MRI must meet unmet clinical needs or provide significant advantages. Some of these advantages are inherent to the technique;

for example, MRI is superior to CT for the imaging of liver, bone and brain cancers. Simultaneous acquisition allows for more accurate analysis of *in vivo* behaviour and distribution,⁵⁷ and PET/MRI may also be more suitable where there are concerns over the ionising radiation used in CT scanning.⁵⁶ To take full advantage of the techniques' synergy the contrast agent administered must be active in both imaging modes, but the markedly different sensitivities of the two techniques imposes a design limitation; as MRI is less sensitive, the addition of a small quantity of PET isotope to an MRI agent is required, rather than the addition of an MRI active group to a PET agent.⁵⁸

PET/MRI bimodal agents can be divided into two categories- small molecule species and nanomaterials. The first species to be reported that displayed MRI and PET activity was in the 2010 publication by Caravan *et al.*, a Gd-DOTA complex with fluorinated moiety (see Fig. 11).⁵⁹ Although other species have been reported since,⁶⁰ research into small molecules for PET/MRI has somewhat stagnated. Research into nanomaterials has dominated the field due to the many advantages they offer: their sizes and surface areas can be easily modified, the surfaces can be functionalised with multiple chemical groups of interest, and many nanomaterials have inherent characteristics that make them suitable.⁵⁵

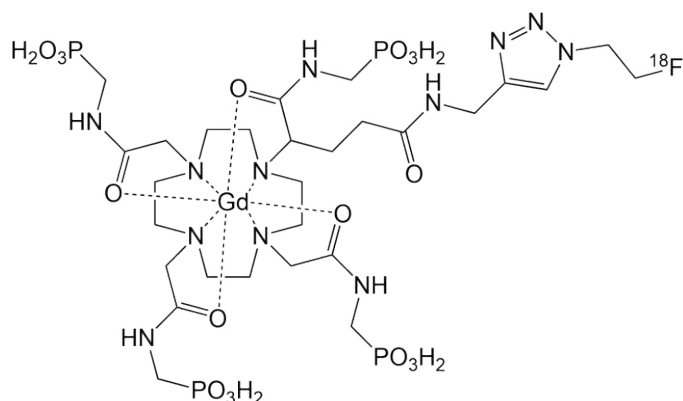


Figure 11. The inclusion of a ¹⁸F bearing moiety via 'click chemistry' imbues PET activity on an MRI agent that was previously known to offer pH sensitivity. Adapted from Caravan *et al.*⁵⁹

Nanomaterials have already seen use as contrast agents in particular imaging modes e.g. SPION for MRI. They have large surface areas which can be functionalised with multiple moieties per nanoparticle. They can also be designed as responsive agents; for example, releasing drugs or contrast agents as a response to specific stimuli (internal or external).^{2,61} Designing a bimodal agent based on an existing nanomaterial agent effectively gives researchers an advantage over small molecule design from first principles.⁵⁵

There are four commonly reported methods for incorporating radionuclides into nanomaterials summarised in Table 3. The ideal method of the future will have high radioactive yields, generate stable products, have short preparation and purification time, and, importantly, ensure low exposure to radiation for the researcher or technician performing the reaction.⁶²

Method	Advantage	Disadvantage	Ref.
<p>Surface chelation</p> <p>Surface groups coordinate a radioisotope directly.</p>	Simple, efficient, inexpensive.	Dissociation of the isotope can limit analysis and can have health impact.	63,64
<p>Post-synthesis proton/neutron bombardment</p> <p>Nanomaterials are synthesised ‘cold’, then subjected to bombardment in a cyclotron.</p>	Stable species limits loss of radioactivity.	Expensive, requiring dedicated instrumentation	65,66
<p>Use of radioactive precursors</p> <p>Nanomaterials are synthesised using radioactive materials in early stages of synthesis</p>	Typically highly stable species.	Often associated with high radiation exposure during production.	67,68
<p>Post-synthesis absorption or exchange</p> <p>Radiometal ions adsorb to the surface of the nanomaterial directly without additional chelating groups</p>	Inexpensive and simple.	Currently limited to certain species; poor stability and yields.	6,69

Table 3. Four common methods for incorporating radioisotopes in nanomaterials.⁵⁵

Although agents based on other nanomaterials have been reported, SPION have been the most popular foundation for PET/MRI species, and have been functionalised with a range of PET isotopes.^{63,64,70–72} This has typically been via conjugation or derivatisation of the surface coating, although some notable cases stand out: the adsorption of radio-arsenic⁶ and -germanium⁷ isotopes onto the iron oxide surface of poly(acrylic acid) coated SPION illustrate not only the issue of coating porosity, but also the potential to directly label the inorganic core of the particles themselves with a range of medically significant radioisotopes. This concept will be discussed further in Chapter 2. When designing immunoPET agents the number of chelating species (ergo, the number of radioisotopes) per antibody must be limited to prevent changes to the structure and pharmacokinetics, but the large size and surface area of a nanoparticle allow for the accommodation of significantly more radioisotopes, increasing the sensitivity and contrast to be observed per molecule while decreasing the need for excretion events.⁷³ While PET/MRI is an exciting area of research which will surely become more common in clinics, what has already been reported in the literature presents an intriguing question: can radiolabelled SPION be linked to clinical mAbs to give a novel immunoPET agent that avoids the limitations of directly radiolabelled mAbs, and which offers flexibility in terms of number and nature of radioisotopes?

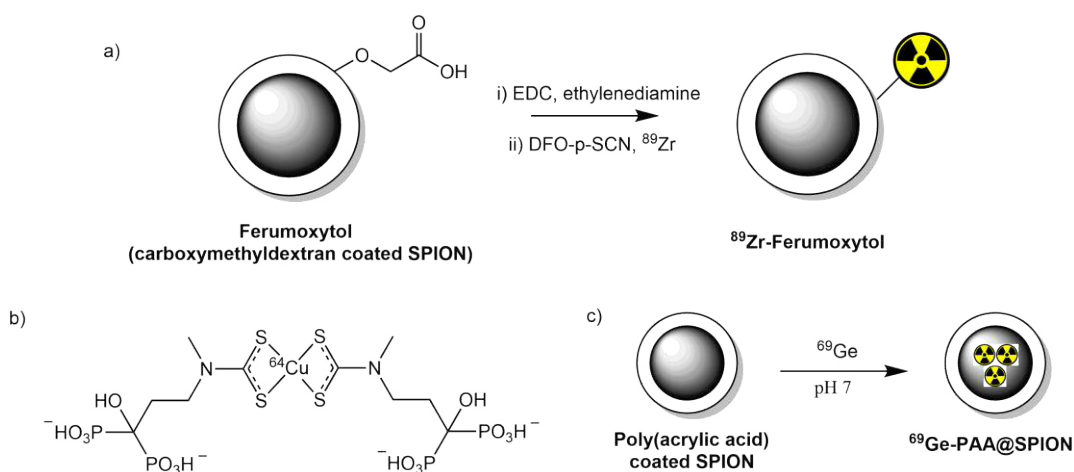


Figure 12a. Cross-reaction between the FDA-approved Ferumoxytol and the commercially available DFO-p-SCN allows for direct labelling with a radioisotope.⁶³ **b.** A ⁶⁴Cu coordination complex (shown) has been used to bind to the surface of the dextran-coated species Endorem via pendant bisphosphonates.⁷¹ **c.** pH dependant adsorption of ⁶⁹Ge to iron oxide allowed a chelator-free synthesis of a PET/MRI active species.⁷

1.8 Summary

The western world faces an epidemic of diseases arising from lifestyle and longevity. The use of monoclonal antibodies in therapy has been increasing annually since the approval of the first generation of agents in the 1990s and will continue to increase as new antibody based agents are developed, new disease-specific targets become known, and more people develop illnesses that require their use. The need for personalised treatment regimens will grow ever greater and so the development of novel imaging probes to stratify patients and aid in diagnosis is crucial.⁷⁴ The design of immunoPET agents incorporating long half-life metallic radioisotopes, such as ⁸⁹Zr, has already been validated by preclinical and clinical studies and is a thriving area of research.^{75,76}

At the same time, the use of bimodal imaging to take advantage of synergistic qualities of different imaging modes will increase; the benefits are clear and the disadvantages few. Combined PET/CT scanners have already largely replaced individual PET and CD machines, and PET/MRI is likely to become more common going forwards, for the reasons discussed above.⁵⁵⁻⁵⁷ Superparamagnetic iron oxide nanoparticles, already established as MRI contrast agents in the clinic, have been at the forefront of PET/MRI agent research and have shown their suitability for further study.

The following chapters describe the design and synthesis of SPION nanoparticles with useful surface functionality that allow for the immobilisation of biomolecules including clinically relevant monoclonal antibodies. These nanoparticles were first synthesised 'cold' in the chemistry laboratory in order to characterise the surface species, stability and retained biological activity of the immobilised enzymes and mAbs. The *in vitro* validation of SPION bearing the Her-2 targeting mAb trastuzumab by FACS and confocal microscopy is shown to lead to *in vivo* studies where immuno-SPION species were radiolabelled with ⁸⁹Zr to give a novel immunoPET and which were applied to nude mice bearing Her-2 positive and Her-2 negative xenograft tumours. In addition to this, the development of novel ligands (based on Cu-ATSM) for use as haptens in catalytic antibody development is described and discussed.

1.9 References

- 1 R. Massart, *IEEE Trans. Magn.*, 1981, **17**, 1247–1248.
- 2 M. Mahmoudi, S. Sant, B. Wang, S. Laurent and T. Sen, *Adv. Drug Deliv. Rev.*, 2011, **63**, 24–46.
- 3 M. r. Lasheen, I. Y. El-Sherif, D. Y. Sabry, S. t. El-Wakeel and M. f. El-Shahat, *Desalination Water Treat.*, 2016, **57**, 17421–17429.
- 4 Y. C. Sharma, V. Srivastava, V. K. Singh, S. N. Kaul and C. H. Weng, *Environ. Technol.*, 2009, **30**, 583–609.
- 5 T. Burks, A. Uheida, M. Saleemi, M. Eita, M. S. Toprak and M. Muhammed, *Sep. Sci. Technol.*, 2013, **48**, 1243–1251.
- 6 F. Chen, P. A. Ellison, C. M. Lewis, H. Hong, Y. Zhang, S. Shi, R. Hernandez, M. E. Meyerand, T. E. Barnhart and W. Cai, *Angew. Chem. Int. Ed.*, 2013, **52**, 13319–13323.
- 7 R. Chakravarty, H. F. Valdovinos, F. Chen, C. M. Lewis, P. A. Ellison, H. Luo, M. E. Meyerand, R. J. Nickles and W. Cai, *Adv. Mater.*, 2014, **26**, 5119–5123.
- 8 J. Maddams, M. Utley and H. Møller, *Br. J. Cancer*, 2012, **107**, 1195–1202.
- 9 'M. F. UK Manor Farm Offices, Biddestone, Chippenham, Wiltshire, Cancer Diagnosis and Treatment', <http://www.healthcare-today.co.uk/news/cancer-diagnosis-and-treatment-a-2021-projection/20626/>, (accessed 10 November 2016).
- 10 'Cancer Facts and Figures 2016', <http://www.cancer.org/research/cancerfactsstatistics/cancerfactsfigures2016/> (accessed 19/01/2017)
- 11 A. Urruticoechea, A Alemany, R Balart, J Villanueva, F. Viñals and G. Capellá, *Curr. Pharm. Des.*, **16**, 3–10.
- 12 G. A. M. S. van Dongen, G. W. M. Visser, M. N. L. Hooge, E. G. de Vries and L. R. Perk, *The Oncologist*, 2007, **12**, 1379–1389.
- 13 L. M. Weiner, R. Surana and S. Wang, *Nat. Rev. Immunol.*, 2010, **10**, 317–327.
- 14 D. Voet, J. G. Voet and C. W. Pratt, *Fundamentals of Biochemistry: Life at the Molecular Level*, Wiley, Hoboken, NJ, 2nd edition., 2012.
- 15 D. M. Ecker, S. D. Jones and H. L. Levine, *mAbs*, 2015, **7**, 9–14.
- 16 R. Nahta and F. J. Esteva, *Cancer Lett.*, 2006, **232**, 123–138.
- 17 N. Patani and K. Mokbel, *Surg. Oncol.*, 2010, **19**, e11–e21.
- 18 L. E. Jennings and N. J. Long, *Chem. Commun.*, 2009, 3511–3524.
- 19 F. L. Thorp-Greenwood and M. P. Coogan, *Dalton Trans.*, 2011, **40**, 6129–6143.
- 20 A. Louie, *Chem. Rev.*, 2010, **110**, 3146–3195.
- 21 M. L. James and S. S. Gambhir, *Physiol. Rev.*, 2012, **92**, 897–965.
- 22 D. Delbeke, R. E. Coleman, M. J. Guiberteau, M. L. Brown, H. D. Royal, B. A. Siegel, D. W. Townsend, L. L. Berland, J. A. Parker, K. Hubner, M. G. Stabin, G. Zubal, M. Kachelriess, V. Cronin and S. Holbrook, *J. Nucl. Med.*, 2006, **47**, 885–895.
- 23 J. C. Knight, M. Wuest, F. A. Saad, M. Wang, D. W. Chapman, H.-S. Jans, S. E. Lapi, B. M. Kariuki, A. J. Amoroso and F. Wuest, *Dalton Trans.*, 2013, **42**, 12005–12014.
- 24 J. Mendelsohn and J. Baselga, *Oncogene*, 2000, **19**, 6550–6565.
- 25 H. Minn, A. C. Clavo and R. L. Wahl, *Nucl. Med. Biol.*, 1996, **23**, 941–946.
- 26 S. M. Qaim, in *Handbook of Nuclear Chemistry*, eds. A. Vértes, S. Nagy, Z. Klencsár, R. G. Lovas and F. Rösch, Springer US, Boston, MA, 2011, pp. 1903–1933.
- 27 'Cyclotron Produced Radionuclides: Physical Characteristics and Production Methods', <http://www-pub.iaea.org/books/IAEABooks/7892/Cyclotron-Produced-Radionuclides-Physical-Characteristics-and-Production-Methods>, (accessed 3 August 2017).
- 28 W. W. Moses, *Nucl. Instrum. Methods Phys. Res. Sect. Accel. Spectrometers Detect. Assoc. Equip.*, 2011, **648 Supplement 1**, S236–S240.
- 29 C. S. Levin and E. J. Hoffman, *Phys. Med. Biol.*, 1999, **44**, 781–799.

- 30 B. M. Zeglis, K. K. Sevak, T. Reiner, P. Mohindra, S. D. Carlin, P. Zanzonico, R. Weissleder and J. S. Lewis, *J. Nucl. Med.*, 2013, **54**, 1389–1396.
- 31 S. L. Rice, C. A. Roney, P. Daumar and J. S. Lewis, *Semin. Nucl. Med.*, 2011, **41**, 265–282.
- 32 B. M. Zeglis, J. L. Houghton, M. J. Evans, N. Viola-Villegas and J. S. Lewis, *Inorg. Chem.*, 2013, **53**, 1880–1899.
- 33 R. Chakravarty, S. Goel, H. F. Valdovinos, R. Hernandez, H. Hong, R. J. Nickles and W. Cai, *Bioconjug. Chem.*, 2014, **25**, 2197–2204.
- 34 T. J. Wadas, E. H. Wong, G. R. Weisman and C. J. Anderson, *Chem. Rev.*, 2010, **110**, 2858–2902.
- 35 M. A. Deri, B. M. Zeglis, L. C. Francesconi and J. S. Lewis, *Nucl. Med. Biol.*, 2013, **40**, 3–14.
- 36 A. C. Freise and A. M. Wu, *Mol. Immunol.*, 2015, **67**, 142–152.
- 37 S. Heskamp, R. Raavé, O. C. Boerman, M. Rijpkema, V. Goncalves and F. Denat, *Bioconjug. Chem.*, 2017, **28**, 2211–2223.
- 38 'Zirconium-89', http://www.cyclotron.nl/2_3_1, (accessed 4 August 2017).
- 39 L. R. Perk, M. J. W. D. Vosjan, G. W. M. Visser, M. Budde, P. Jurek, G. E. Kiefer and G. A. M. S. van Dongen, *Eur. J. Nucl. Med. Mol. Imaging*, 2010, **37**, 250–259.
- 40 M. J. W. D. Vosjan, L. R. Perk, G. W. M. Visser, M. Budde, P. Jurek, G. E. Kiefer and G. A. M. S. van Dongen, *Nat. Protoc.*, 2010, **5**, 739–743.
- 41 M. A. Deri, S. Ponnala, P. Kozlowski, B. P. Burton-Pye, H. T. Cicek, C. Hu, J. S. Lewis and L. C. Francesconi, *Bioconjug. Chem.*, 2015, **26**, 2579–2591.
- 42 M. A. Deri, S. Ponnala, B. M. Zeglis, G. Pohl, J. J. Dannenberg, J. S. Lewis and L. C. Francesconi, *J. Med. Chem.*, 2014, **57**, 4849–4860.
- 43 D. L. Kukis, G. L. DeNardo, S. J. DeNardo, G. R. Mirick, L. A. Miers, D. P. Greiner and C. F. Meares, *Cancer Res.*, 1995, **55**, 878–884.
- 44 J. L. Dearling, J. S. Lewis, G. E. Mullen, M. J. Welch and P. J. Blower, *JBIC J. Biol. Inorg. Chem.*, 2002, **7**, 249–259.
- 45 C. Westbrook, C. K. Roth and J. Talbot, *MRI in Practice*, Wiley-Blackwell, Chichester, West Sussex; Malden, MA, 4th edition., 2011.
- 46 D. Weishaupt, V. D. Kochli and B. Marincek, *How does MRI work?: An Introduction to the Physics and Function of Magnetic Resonance Imaging*, Springer Berlin Heidelberg, Berlin ; New York, 2nd edition., 2008.
- 47 M. Rudin, *Molecular imaging: Basic principles and applications in biomedical research*, Imperial College Press, London, UK, 2nd edition., 2013.
- 48 MRI Basics ,
<http://casemed.case.edu/clerkships/neurology/Web%20Neurorad/MRI%20Basics.htm>, (accessed 3 August 2017).
- 49 W. Xu, K. Kattel, J. Y. Park, Y. Chang, T. J. Kim and G. H. Lee, *Phys. Chem. Chem. Phys.*, 2012, **14**, 12687–12700.
- 50 M. Rohrer, H. Bauer, J. Mintorovitch, M. Requardt and H.-J. Weinmann, *Invest. Radiol.*, 2005, **40**, 715–724.
- 51 H. S. Thomsen, S. K. Morcos, T. Almén, M.-F. Bellin, M. Bertolotto, G. Bongartz, O. Clement, P. Leander, G. Heinz-Peer, P. Reimer, F. Stacul, A. van der Molen, J. A. W. Webb and ESUR Contrast Medium Safety Committee, *Eur. Radiol.*, 2013, **23**, 307–318.
- 52 D. Pan, A. H. Schmieder, S. A. Wickline and G. M. Lanza, *Tetrahedron*, 2011, **67**, 8431–8444.
- 53 J. Crossgrove and W. Zheng, *NMR Biomed.*, 2004, **17**, 544–553.
- 54 D. W. Townsend, *Semin. Ultrasound CT MRI*, 2008, **29**, 232–235.
- 55 D. Chen, C. A. Dougherty, D. Yang, H. Wu and H. Hong, *Tomogr. J. Imaging Res.*, 2016, **2**, 3–16.
- 56 Z. Hu, W. Yang, H. Liu, K. Wang, C. Bao, T. Song, J. Wang and J. Tian, *Mol. Pharm.*, 2014, **11**, 3798–3809.
- 57 B. J. Pichler, A. Kolb, T. Nägele and H.-P. Schlemmer, *J. Nucl. Med.*, 2010, **51**, 333–336.

- 58 R. T. M. de Rosales, *J. Label. Compd. Radiopharm.*, 2014, **57**, 298–303.
- 59 L. Frullano, C. Catana, T. Benner, A. D. Sherry and P. Caravan, *Angew. Chem. Int. Ed Engl.*, 2010, **49**, 2382–2384.
- 60 J. Notni, P. Hermann, I. Dregely and H.-J. Wester, *Chem. – Eur. J.*, 2013, **19**, 12602–12606.
- 61 S. Chandra, S. Mehta, S. Nigam and D. Bahadur, *New J. Chem.*, 2010, **34**, 648–655.
- 62 X. Sun, W. Cai and X. Chen, *Acc. Chem. Res.*, 2015, **48**, 286–294.
- 63 D. L. J. Thorek, D. Ulmert, N.-F. M. Diop, M. E. Lupu, M. G. Doran, R. Huang, D. S. Abou, S. M. Larson and J. Grimm, *Nat. Commun.*, 2014, **5**, 3097.
- 64 H.-Y. Lee, Z. Li, K. Chen, A. R. Hsu, C. Xu, J. Xie, S. Sun and X. Chen, *J. Nucl. Med.*, 2008, **49**, 1371–1379.
- 65 N. Gibson, U. Holzwarth, K. Abbas, F. Simonelli, J. Kozempel, I. Cydzik, G. Cotogno, A. Bulgheroni, D. Gilliland, J. Ponti, F. Franchini, P. Marmorato, H. Stamm, W. Kreyling, A. Wenk, M. Semmler-Behnke, S. Buono, L. Maciocco and N. Burgio, *Arch. Toxicol.*, 2011, **85**, 751–773.
- 66 C. Pérez-Campaña, V. Gómez-Vallejo, M. Puigivila, A. Martín, T. Calvo-Fernández, S. E. Moya, R. F. Ziolo, T. Reese and J. Llop, *ACS Nano*, 2013, **7**, 3498–3505.
- 67 K. C. L. Black, Y. Wang, H. P. Luehmann, X. Cai, W. Xing, B. Pang, Y. Zhao, C. S. Cutler, L. V. Wang, Y. Liu and Y. Xia, *ACS Nano*, 2014, **8**, 4385–4394.
- 68 Y. Wang, Y. Liu, H. Luehmann, X. Xia, D. Wan, C. Cutler and Y. Xia, *Nano Lett.*, 2013, **13**, 581–585.
- 69 H. Hu, P. Huang, O. J. Weiss, X. Yan, X. Yue, M. G. Zhang, Y. Tang, L. Nie, Y. Ma, G. Niu, K. Wu and X. Chen, *Biomaterials*, 2014, **35**, 9868–9876.
- 70 J. Choi, J. C. Park, H. Nah, S. Woo, J. Oh, K. M. Kim, G. J. Cheon, Y. Chang, J. Yoo and J. Cheon, *Angew. Chem. Int. Ed.*, 2008, **47**, 6259–6262.
- 71 R. Torres Martin de Rosales, R. Tavaré, R. L. Paul, M. Jauregui-Osoro, A. Protti, A. Glaria, G. Varma, I. Szanda and P. J. Blower, *Angew. Chem. Int. Ed.*, 2011, **50**, 5509–5513.
- 72 X. Yang, H. Hong, J. J. Grailer, I. J. Rowland, A. Javadi, S. A. Hurley, Y. Xiao, Y. Yang, Y. Zhang, R. J. Nickles, W. Cai, D. A. Steeber and S. Gong, *Biomaterials*, 2011, **32**, 4151–4160.
- 73 J. Kim, P. Chhour, J. Hsu, H. I. Litt, V. A. Ferrari, R. Popovtzer and D. P. Cormode, *Bioconjug. Chem.*, 2017, **28**, 1581–1597.
- 74 A. Beck, T. Wurch, C. Bailly and N. Corvaia, *Nat. Rev. Immunol.*, 2010, **10**, 345–352.
- 75 O. C. Boerman and W. J. G. Oyen, *J. Nucl. Med.*, 2011, **52**, 1171–1172.
- 76 B. D. Wright and S. E. Lapi, *J. Nucl. Med.*, 2013, **54**, 1171–1174.

Chapter 2: Synthesis, coating and characterisation of water soluble superparamagnetic iron oxide nanoparticles (SPION)

2.1 Introduction

Superparamagnetic iron oxide nanoparticles (SPION) have been used clinically as T₂ contrast agents in MRI. They typically consist of an inorganic core of Fe₃O₄ with an organic coating that imbues solubility in a given solvent and which can give a basis for the inclusion of functional groups on the particle surface. Since the first published synthesis of SPION by Massart,¹ there have been thousands of publications describing the synthesis, coating or functionalisation of iron oxide nanoparticles. Many review articles with differing emphases have also been written and the reader is invited to refer to these for more information on particular aspects and routes.²⁻¹⁰ In this chapter, the syntheses and characterisation of two forms of biocompatible SPION are reported, along with initial experiments to incorporate PET-active radiotracers into such particles. The criteria by which such material should be judged if they are to be used as foundations for *in vivo* agents are discussed.

2.1.1 SPION structure and characteristics

While there are many iron oxides and hydroxides found in nature, only two species are commonly encountered within the context of molecular imaging. Magnetite (Fe₃O₄) is the more commonly reported form and is more strongly magnetic as a bulk material but can be oxidised to the less common, less strongly magnetic maghemite (γ-Fe₂O₃). This review will focus on the former and except where explicitly stated will use ‘iron oxide’ and ‘magnetite’ interchangeably.

The terms ‘magnet’ and ‘magnetite’ share a common origin in the observation of attractive forces between stones from ‘Magnesia’, as the magnetite-rich region of western Turkey was known to the Ancient Greeks. Magnetite as a bulk mineral exhibits a permanent (or ‘remanent’) form of ‘cooperative’ magnetism called ‘ferrimagnetism’.¹¹ All forms of magnetism are ultimately derived from the behaviour of electrons in materials and Fe₃O₄ is no exception. Fe²⁺ and Fe³⁺ are d⁶ and d⁵ metal centres respectively and when coordinated in high spin octahedral complexes can have multiple unpaired electrons and large magnetic dipole moments as paramagnetic centres (Fig. 1).

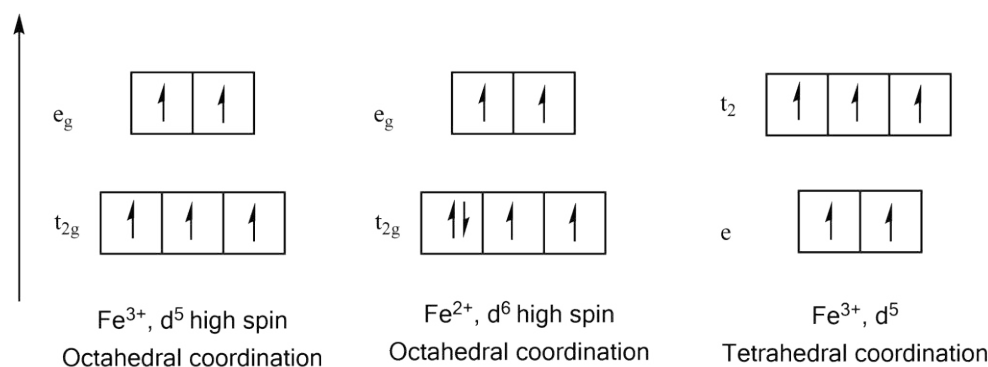


Figure 1. Electronic configurations of iron centres in different oxidation states and coordination geometries.

Fe_3O_4 consists of an ‘inverse spinel’ structure where tetrahedral sites are occupied by Fe^{3+} and octahedral sites are occupied equally by Fe^{3+} and Fe^{2+} (Fig. 2).¹² The two sub-lattices are not equivalent and contain differing numbers of atoms. Coupling between atoms within the sub-lattices to minimise energy results in all of the spins within each sub-lattice aligning parallel to each other but anti-parallel to the other lattice. The Fe^{3+} ions in the sub-lattices counteract each other but the Fe^{2+} ions are uncompensated for, resulting in a net magnetisation vector.

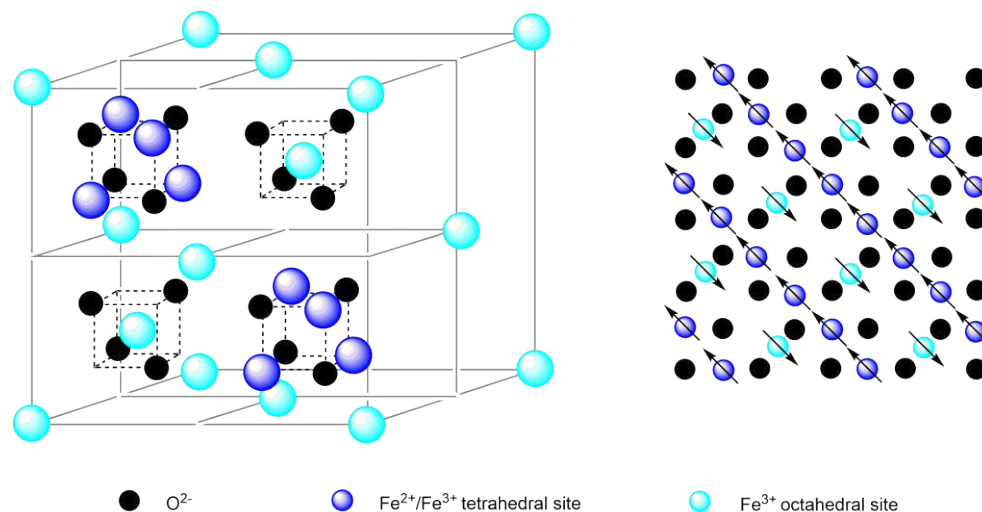


Figure 2. The inverse spinel structure of Fe_3O_4 (left) and the ferrimagnetic coupling observed in a $[1,1,1]$ plane of the same (right). Adapted from Gossuin et al.¹²

The bulk material is divided into regions called Weiss domains as a result of the spontaneous ordering of the spins. Within Weiss domains, spins are aligned to give a net vector but the vectors of different domains may be random. The bulk material is ferrimagnetic because most vectors are approximately aligned. However, if a sample of Fe_3O_4 is smaller than the

Weiss domain limit of the bulk mineral (~ 100 nm), then the sample will behave as a single domain with a random moment orientation. A population of nanoparticles is therefore a population of single domains that do not interact with each other to give ordered magnetism as in the bulk material. They can align with applied magnetic fields, but in the absence of such a field the random orientation of moments results in zero magnetic remanence. This is termed ‘superparamagnetism’ as the behaviour is analogous to paramagnetism but for particles on a nanometre scale rather than small molecules measured in Angstroms.

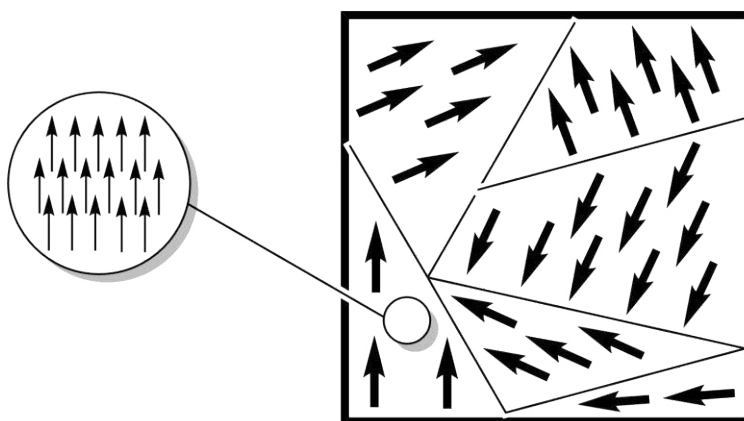


Figure 3. Simplified depiction of Weiss domains within bulk Fe_3O_4 . As the nanoparticle (the small sphere) is smaller than a Weiss domain, it exhibits superparamagnetism.

Superparamagnetism allows SPION to be used as MRI contrast agents. Contrast in MRI images is derived from differences in the relaxation rates of the protons in water in different chemical environments. When administered to a patient, SPION will preferentially accumulate in a target environment. When an external magnetic field is applied, the nanoparticles’ magnetic moments align with it, creating a difference in the local magnetic field strength in their locality. The protons in water molecules are affected by this with a resulting change in the efficiency of relaxation rates.³ Because of the particles’ high values of magnetisation their effect on relaxation rates is large, requiring smaller quantities of SPION to be administered to achieve contrast than for paramagnetic complexes. The magnetic behaviour of SPION samples and their relaxivity at different field strengths may be studied using Fast Field Cycling (FFC) relaxometry (discussed below) to give an NMRD (nuclear magnetic relaxation dispersion) profile for the agent.¹³ Characterisation methods for crystallite size and shape (discussed below) have allowed for mathematical models defining the contribution and effect of particle parameters on relaxation rates to be developed, but are beyond the scope of this project.³

Fe₃O₄ nanoparticles are not stable towards oxidation and aggregation. In an oxygen-rich environment magnetite may be oxidised to maghemite resulting in a loss in magnetic responsiveness.¹⁴ The crystal structure of a nanoparticle of Fe₃O₄ terminates in hydroxyl groups at the surface; as nanoparticles have large surface area:volume ratios, there is a significant contribution from hydroxyl groups to interfacial tension which thermodynamically results in particles aggregating, undergoing dehydration and growing together to minimise interfacial tension (Ostwald ripening).³ Taken to an extreme, the particles may grow larger than the Weiss domain limit and thus become ‘bulk mineral’. Both of these effects can be prevented by incorporating a coating moiety onto the nanoparticle surface either following or during a given synthetic route to stabilise the particles.

2.1.2 Methods of SPION synthesis

There have been hundreds of synthetic accounts to generate SPION reported. Several reviews of SPION syntheses have been published.^{2,4,5,8,14} While some methods are considerably different in their approach to others, most vary in the manipulation of experimental parameters or the use of different solvents or starting materials and fall into one of several groups. The relative merits of some of the more commonly reported approaches are discussed below with a focus on their suitability for use in biomedical contexts. Gas phase methods have also been reported but require specialist equipment and offer low product yields and so are not discussed.¹⁴

Co-precipitation (‘wet’ methods)

The original method reported by Massart is still the most commonly utilised approach.¹ To an aqueous solution of Fe³⁺ and Fe²⁺ salts in a non-oxidising atmosphere is added a strong base:



The uncoated oxide species precipitates as a black solid and may be collected magnetically or by centrifugation and washed prior to stabilisation. The major advantages of this approach are simplicity and scalability. A range of salt precursors and bases may be used, the reaction is quick to perform and the product is relatively easy to isolate and purify. Although the reaction is nominally air-sensitive, oxidation to maghemite is limited even if the experiment is carried out in air, as will be shown in the results section of this chapter. The reaction can be performed from the milligram to the kilogram scale.

Nanoparticle synthesis can be considered as a two-stage process consisting of an initial nucleation step followed by diffusion of ions to the surface of the particles to allow growth.^{2,15} To achieve monodispersity these processes must either be sequential and not simultaneous (i.e. a defined number of particles form and then all have equal time within which to grow to their final size, as described by LaMer (see Fig. 4))¹⁶ or be succeeded by an ‘equilibration’ phase (see below). The original Massart method does not meet either criteria, and so the product particles are inherently polydisperse before stabilisation by coating. Improved methods where the use of size-selection techniques post-coating have been reported but are generally not as commonly utilised as the original approach or syntheses by methods other than co-precipitation.^{17,18}

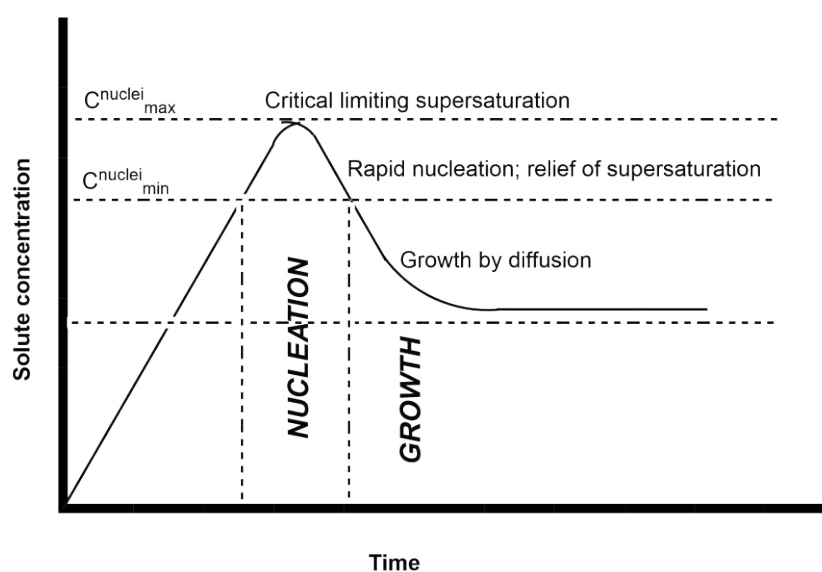


Figure 4. LaMer diagram depicting the ideal case of sequential nucleation and growth of nanoparticles. Adapted from LaMer and Dinegar.¹⁶

Although the particles produced by co-precipitation are polydisperse, the effect of numerous parameters (e.g. pH, ionic strength and reactant concentration) on average particle size, shape and constitution have been determined such that by changing experimental parameters, one can alter average particle size from between 2 and 20 nm.² Formation via co-precipitation is most desirable when the nanoparticles are required to be of a given average size and when the quantity of the product is more important than monodispersity. Particles formed by co-precipitation have previously been used in commercial products such as Feridex[®].¹⁹

The co-precipitation method may be modified to substitute other heavy metals (e.g. Mn, Co) into the inverse spinel structure of Fe_3O_4 without significant effects on size or magnetic behaviour and with high efficiency of doping (isomorphous substitution).^{20,21} As the levels

of dopant metal needed to achieve a stoichiometric labelling are much higher than would be practically used when considering radiolabelling nanoparticles, the co-precipitation method lends itself well to the idea of incorporating radiotracers into SPION.

High-temperature formation ('thermal' methods)

Numerous methods of synthesising highly crystalline, highly monodisperse Fe_3O_4 nanoparticles have been reported where precursor species (e.g. iron oleate, iron acetylacetonate, iron pentacarbonyl) undergo decomposition at elevated temperatures and pressures in an organic solvent and in the presence of a capping agent.²²⁻²⁵ Often the nature of the capping agent results in the particles being coated and stabilised but hydrophobic and incompatible with biological systems.²⁵ Additional steps such as the replacement of the coating or the use of surfactants are required to make them hydrophilic.

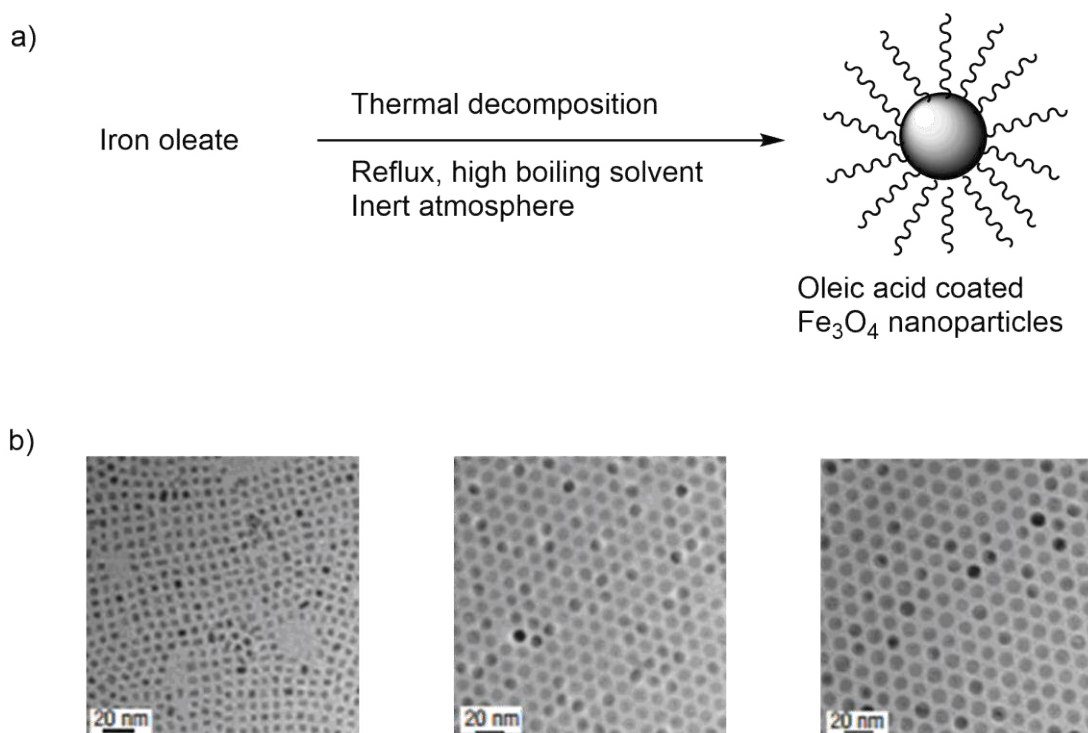


Figure 5a. Schematic depiction of monodisperse SPION formation via thermal decomposition of iron oleate, adapted from Park et al.²² **b.** Left to right, 5, 9 and 12 nm nanoparticles formed as described above using increasing reaction temperature.²²

The high temperatures used (e.g. 300 °C) results in monodispersity. Particle nucleation and growth processes compete for materials from solution and their rates would appear to have different temperature dependencies with the latter taking precedence at high temperature.²⁶ It is also possible that both processes are in a state of equilibrium with decomposition at high temperatures. The monodispersity of the hydrothermal product can be speculated to derive

from an ‘averaging’ of particle size by the interplay of nucleation, decomposition and growth over relatively long reaction times. The particles formed by this method could be viewed as a ‘thermodynamic’ product in contrast to the ‘kinetic’ products formed by co-precipitation.

The size and morphology of the particles made by these methods are easily modified by the manipulation of experimental parameters. For example, in the work by Sun *et al.* the size of the oleic acid-coated product is increased by changing the solvent and therefore increasing the temperature at which reflux is achieved.²³ The ability to control the average size of a highly monodisperse sample is the major advantage of thermal decomposition methods. Thermal decomposition approaches are generally more reproducible than co-precipitation methods as the extreme conditions used generally out-compete the more subtle factors affecting low temperature methods, but due to the high temperatures used air-sensitive techniques must be rigorously adhered to or else the reaction will not yield a strongly magnetic product. Safety issues arising from the high temperatures and flammable solvents contribute to the limited scale upon which these reactions are performed. Equipment is required that is commonplace in the chemistry laboratory but which are not easily transferred to or used in other contexts such as ‘hot cells’ used in radioactive work.

Synthesis in constrained environments

The synthesis of SPION in constrained environments can be considered an overarching term for a number of different routes such as sol-gel syntheses,^{27,28} microemulsions¹⁹ and bacteriological approaches.⁸ All attempt to limit the volume and time within which particles can form. The monodispersity achieved by these methods is not as high as that achieved by thermal decomposition methods and the yields are generally low compared to co-precipitation methods.^{19,29} The syntheses are also subject to a wide variety of parameters that affect the characteristics and behaviour of the product particles, which require strict control to achieve reproducibility and may require purification procedures to render particle surfaces suitable for further synthetic steps.³⁰

The use of flow injection techniques to achieve rapid mixing has previously been reported to give greater control over particle size and polydispersity.^{30–34} Rapid mixing of reagents in a known volume over a known time act as confinements on experimental parameters that may be difficult to control when performing a classical ‘Massart’ approach. In the work by Liu *et al.*, the use of a rapid mixing head gave magnetite particles with an average core size of 8.5 nm and which could be coated with biologically useful species shortly after collection from the reactor.³¹ Reproducing such experiments requires specialist equipment that is not

easily obtained. In Additional Experimental Section I of this thesis, an attempt to use a custom-built injector with limited success is described.

2.1.3 Coating materials

SPION are coated to prevent oxidation and aggregation, to imbue solubility and stability in media and to provide functional groups for covalent modification.^{2,4,8} Coating can either occur in the same reaction step as particle formation or as an additional step following collection and washing of the uncoated particles. Any species used to coat SPION serves to stabilise the particles in terms of sterics and/or electrostatics by preventing the iron oxide surfaces of the particles from coming into contact and combining. For biological purposes steric stabilisation is preferred to electrostatic stabilisation as the latter is more strongly influenced by the properties of the medium the particles are dispersed in.³⁵ A wide range of species have been used to stabilise SPION (Table 1) and the properties of the coating species (e.g. solubility in organic or aqueous solvents) contributes to the properties of the coated particles. Not all are of immediate use in biological contexts and some are more desirable than others when considering later bioconjugation. Nanoparticles are typically described as ‘Coating agent@SPION’ when coated with a particular species e.g. Dextran@SPION.

Organic species that yield solubility in non-polar solvents require an additional surfactant species to make them biocompatible, introducing an additional step into the synthetic pathway. Many organic monomeric and polymeric species are associated with the surface of SPION via non-covalent interactions and can be made to desorb from the magnetite surface under certain conditions.² Nevertheless, dextran and carboxymethyl-dextran (CMD) (Fig. 6) have seen use in commercially available SPION-based contrast agents and are still commonly used in novel agent development with the latter offering a carboxylate group as a target for further reaction.³⁶

Class	Examples	Notes	Ref.
Organic, monomeric species	Oleic acid, oleylamine	Product not water soluble; unsuitable for biological use without an additional surfactant.	23
	Dimercaptosuccinic acid	Water soluble product with up to two targets for bioconjugation.	37,38
	Citric acid	Product is water soluble; increasing citrate concentration controls size and dispersity.	18
Organic, polymeric species	Dextran	Soluble in aqueous media over a range of pH values. Hydroxyl groups used in bioconjugation.	39,40
	Poly(vinyl alcohol)	Nanoparticles have low toxicity when assessed by cell viability.	41,42
Inorganic species	Silica/silane species	Silica layer forms by condensation reactions between monomers and surface hydroxyl groups. Easily modified for bioconjugation.	43–45
	Gold	Deposition of gold gives a surface with a high affinity for thiol groups, allowing direct immobilisation of proteins.	46

Table 1. Examples of SPION coating species reported in the literature with some relevant literature examples.

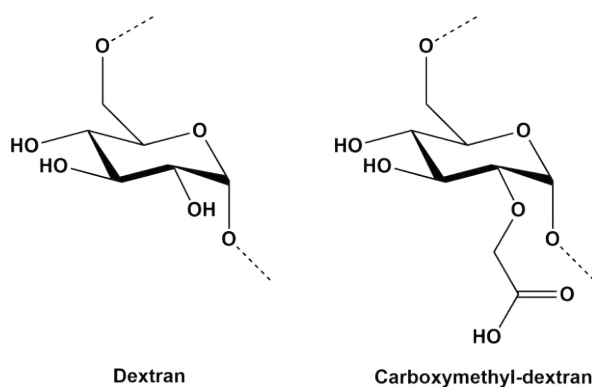


Figure 6. Monomers of dextran and carboxymethyl-dextran (CMD), common reagents used to stabilise SPION for biological uses.

Silica and silane species are among the most commonly reported methods of stabilising and functionalising SPION with 3-Aminopropyltriethoxysilane (APTES) being of particular note.^{47,48} It has also seen use commercially in the synthesis of a number of assay platforms.^{47,49} Like many silanes used in surface modification or bioconjugation, APTES has unstable ether groups that can be hydrolysed under heat or in aqueous conditions to generate reactive silanol groups. These groups react with neighbouring APTES monomers or with hydroxyl groups on surfaces (e.g. silica nanoparticles, glass, uncoated SPION) to form covalent links. The process of surface attachment is commonly referred to as silanisation. When APTES is used the surface becomes amino-functionalised.⁴⁷ Amine groups are a common motif within bioconjugation with a variety of methods available to achieve surface modification.⁴⁸ The chemistry of bioconjugation is discussed in more detail in Chapter 3. From the perspective of SPION biocompatibility, surface amines may be protonated under acidic aqueous conditions, rendering such particles soluble.

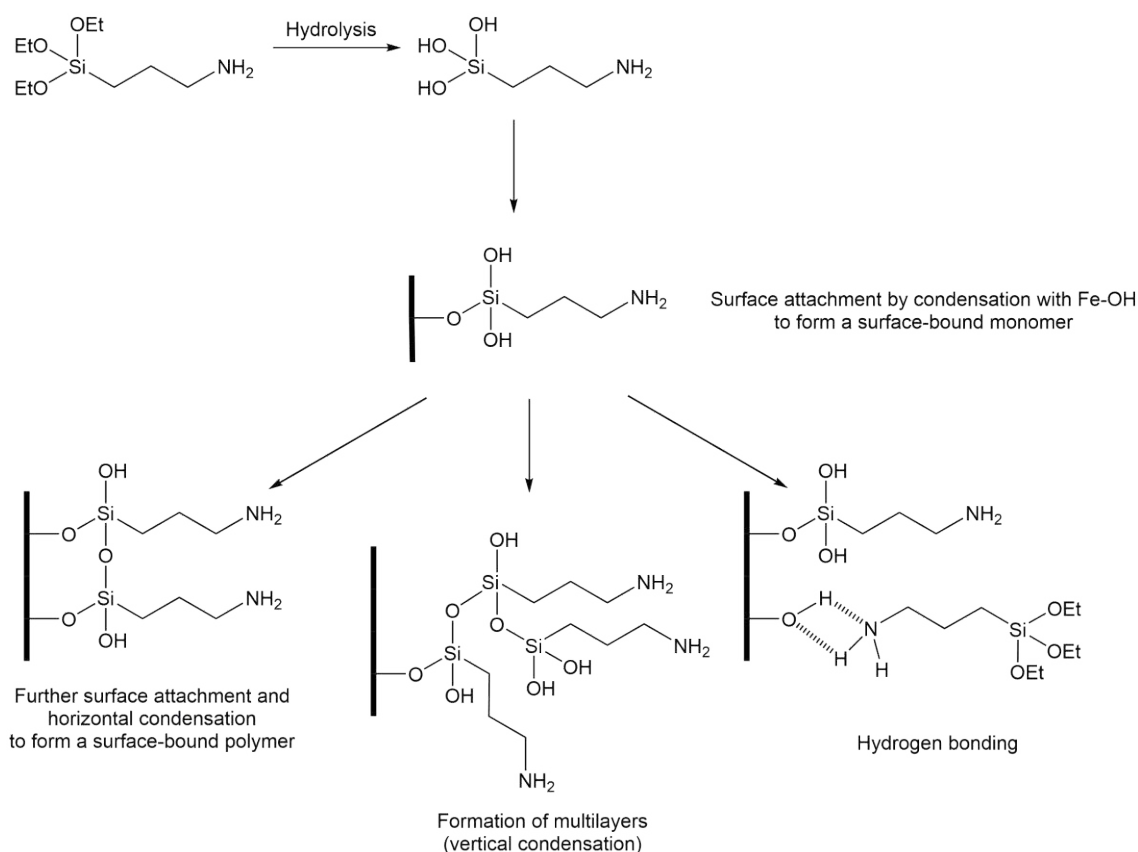


Figure 7. Three mechanisms by which APTES can be bound to a hydroxyl functionalised surface. Note that horizontal (left) and vertical (central) polymerisations are not mutually exclusive.

Silanisation commences with the hydrolysis of the ethoxy groups of APTES. APTES monomers covalently bind to a hydroxy-functionalised surface via dehydration and undergo horizontal polymerisation giving a monolayer of crosslinked APTES on the surface.⁵⁰ They may also undergo vertical polymerisation with APTES monomers that are not directly associated with the surface, allowing for multilayers to build away from the initial surface.⁴⁵

Silanisation is a complex process that is heavily influenced by reaction conditions. For example, when a monolayer is desired the concentration of APTES in dry organic solvents such as toluene must be tightly controlled along with reaction time and temperature.⁴⁷ Reported methods of APTES-coating can be grouped into ‘wet chemical’ or ‘chemical vapour deposition’ (CVD) methods and the former may be sub-divided into organic and aqueous silanisation methods. Aqueous silanisation methods are more likely to generate multilayers but are generally preferred for the coating of SPION due to their relative simplicity.^{45,51–53}

While the kinetics of APTES silanisation are still the subject of research, the amine-functionalising of surfaces has been proven and utilised in multiple bioconjugate contexts: antibodies for ELISA assays,⁵⁴ monoclonal antibodies for biorecognition⁵⁵ and numerous enzyme species have all been immobilised to APTES-functionalised SPION using typical bioconjugation methods.

2.1.4 Applications of SPION: *in vivo*, *in vitro* and beyond biomedicine

While the best known application of SPION to date has been the *in vivo* enhancement of contrast in MRI scans, molecular imaging can be viewed as the tip of the iceberg in terms of the potential uses of such particles. Early research showed that particles with a biocompatible coating were well-suited to imaging of the liver and lymph nodes due to their tendency to accumulate in these organs in the absence of additional directing functionalities.^{36,56} Intravenous administration is followed by rapid absorption of the particles by the reticuloendothelial system (RES) and subsequent accumulation at the liver, spleen and lymphatic system.⁵⁷ The characteristics of FDA-approved agents can be markedly different: Feridex[®] consists of particles coated with dextran with hydrodynamic radii of between 120-180 nm, while Resovist[®] consists of carboxydextran coated particles with 45-60 nm hydrodynamic radii.³⁶ The two agents may be used in broadly similar contexts and it may be concluded that the prediction of a potential agent’s utility based on physical characteristics alone is not advisable.



Figure 8. Contrast observed in the liver due to the effects of Feridex[®], an FDA-approved SPION agent. Adapted from Edmundson et al.⁵⁸

More recently, the immobilisation of biomolecules on biocompatible SPION species has allowed for directed imaging both *in vivo* and *in vitro* of a multitude of biological markers e.g. amyloid plaques in Alzheimer’s Disease,^{59,60} apoptotic cells⁶¹ and different forms of cancer by use of immobilised antibodies.^{62,63}

SPION have also been used to achieve therapeutic benefit. The coating layer of biocompatible SPION may be modified to incorporate drug molecules which may be delivered via the nanoparticle to a site within the body where they are most effective in the treatment of disease. Targeting may be achieved either by including a biological vector on the particle surface or by control of the physical properties of the nanoparticles. Targeted drug delivery is desirable because it can reduce systemic side effects of a therapy while improving local treatment, as well as improving the biophysical characteristics of a drug molecule such as circulation time.³⁵

Drug release can be designed to be responsive to stimuli, e.g. the presence of a magnetic field or an increase in temperature⁶⁴ and is often discussed alongside hyperthermia therapy, with which synergistic advantages can be obtained. Hyperthermia therapy is the use of elevated temperatures to destroy diseased cells. Cancer cells are known to be more sensitive to heat than healthy cells and significant cell death can be achieved when a tumour is heated to 42-46 °C.³⁵ Hyperthermia can also disrupt drug resistance mechanisms.⁶⁴ SPION may accumulate at a given tumour within a patient due to a targeting functionality or due to the EPR effect (‘Enhanced Permeability and Retention’ i.e. extravasation through ‘leaky’ blood vessels). The magnetic moments of the particles align with an applied external magnetic field. When the field direction is flipped the nanoparticles must realign, resulting in some loss of

energy as heat to the particle's surroundings. Realignment can be achieved by the flipping of the magnetic moment (Néel relaxation) or by the physical rotation of the particle (Brownian relaxation); in the latter heat is transferred to the fluid surroundings (essentially by friction) and in the former heat is transferred directly to the solid lattice of the tumour cell.⁶⁵ Brownian relaxation can be prevented by restricting the particle's movement (e.g. by cellular uptake or by binding to a cell surface)⁶⁶ increasing the efficiency with which energy can be passed to the solid cell or tumour. If the external field is made to oscillate rapidly the particles can cause significant tissue damage through the generation of heat.^{67,68}

SPION have not only been of interest to scientists developing novel methods of imaging and treating disease. As stated in Chapter 1, the adsorption of a variety of heavy metal ions by SPION in environmental clean-up has been well-reported; electrostatic attraction between ions such as Co^{2+} , Cu^{2+} , Cr^{6+} and SPION allow for the facile removal of these pollutants from industrial effluent due to efficient adsorption and the ease with which magnetic particles can be abstracted from solution.⁶⁹ The promiscuous nature of SPION as adsorbent surfaces has also been investigated for the uptake of PET active radioisotopes of arsenic and germanium.^{70,71} A study of chelator free ^{89}Zr -labelled mesoporous silica nanoparticles concluded that the presence of O^- species enabled the efficient binding of the hard metal cation⁷² which is similar to the likely mechanism of iron oxide's ability to adsorb heavy metals, but to date no study of chelator free ^{89}Zr -labelling of SPION has been reported in the literature. It was observed that ^{89}Zr can be detached *in vivo* from the surface of dense silica nanoparticles by the action of endogenous chelators due to a reduced number of coordinating groups available on the surface.⁷² In the case of radiolabelling SPION, two methods could be envisaged: adsorption onto preformed particles or incorporation during particle formation. While the high surface area: volume ratio of nanoparticles is of benefit in the context of environmental clean-up, when considering the formation of PET-active SPION it would be preferable to achieve quantitative incorporation with little chance of the radioisotope being released from the particle.

2.1.5 Characterisation of nanoparticles

Methods of characterisation typically used in the study of small molecules are not always available to use in the field of nanotechnology. In the case of biocompatible SPION, the magnetic nature of the iron oxide core prevents the use of NMR spectroscopy to investigate the nature of organic coatings. Mass spectrometry does not yield useful data as even the most monodisperse of samples will have an enormous range of masses present. As a black, highly absorbent material, UV-Vis spectroscopic analysis shows significant absorption at all

wavelengths; indeed, molecules on the surface of the particles with large extinction coefficients (i.e. dyes) can be detected only when present in large numbers and not in a quantitative sense. The characterisation of SPION is focussed mainly on the determination of the size, shape, morphology and surface nature of the particles. Other parameters may be of interest in different contexts and there are many other techniques which can be used to characterise nanomaterials, but the following section will focus on techniques used and discussed later in this chapter. Multiple techniques can be used to determine the same parameter, the comparison of which can be useful in its own right.

Transmission Electron Microscopy (TEM)

TEM is a microscopy technique that uses a beam of short wavelength electrons to visualise high magnification, high resolution images of a target.⁷³ Electrons are emitted from a source at the top of the microscope into a vacuum where they are focussed into a beam by electromagnetic lenses. The incident beam passes through a thin sample before impacting on a detector. Electrons may be stopped or diffracted by the sample material which results in a 'shadow' on the bright image field. How dark a material appears is related to the sample thickness and how efficiently electrons are stopped by it. Heavier atoms scatter electrons more efficiently and appear darker. For iron oxide nanoparticles bearing a coating of significant thickness and with sufficient difference in electron density to the iron oxide core, this can allow the measurement of the core size and the thickness of the coating layer as the two materials will appear markedly different shades (Fig. 9), although instrumental factors can affect this.

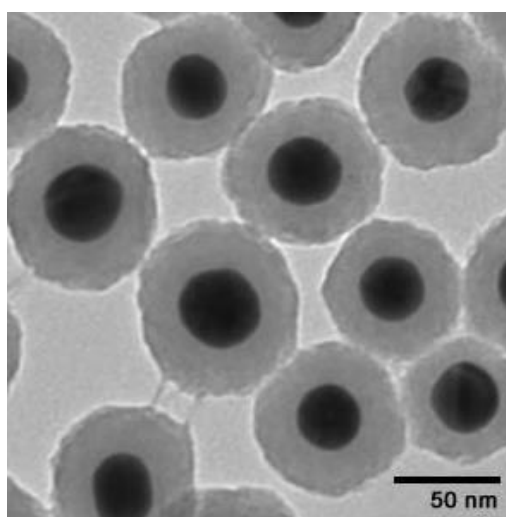


Figure 9. Example TEM image of commercially available silica-coated gold nanoparticles. Note the contrast between the core and surface coating arising from differences in electron density.⁷⁴

Samples are prepared by drying nanoparticles onto a carbon-coated copper grid with known dimensions. Particle sizes are determined by comparison against an internal standard. Although the image obtained by TEM is two dimensional the approximate shape of the particles can be assessed; for SPION, spherical nanoparticles are most common but other structures such as cubes and rods have been reported for other nanomaterials. Image analysis software (such as the software ImageJ⁷⁵) can be used to determine important statistical quantities such as average particle size, size distribution and standard deviation within a population of nanoparticles. These values are important for comparing SPION made using different methodologies and for assessing the reproducibility of a given synthetic approach.

TEM has limitations that should be noted if the particles are intended for biological uses. TEM images show particles in the solid state; how particles dry from the solution phase onto the support in sample preparation is dependent on many factors such that any agglomeration observed cannot be used to assess the behaviour of particles in solution. This is more accurately assessed using dynamic light scattering, discussed below. Particles may sinter together during drying and it may be difficult to determine individual particles. The selection of particles to form part of the statistical population should be made at random and their diameter taken at a fixed angle; over a suitable population size, the resulting statistics can be judged to be representative.

X-Ray Diffraction (XRD)

XRD is the most popular method of identifying an unknown iron oxide. The interaction of electromagnetic radiation with wavelengths (λ) on the order of Angstroms (10^{-10} M) with atoms in a regular solid can allow for the determination of interatomic distances based on the diffraction of these X-rays.⁷⁶ At certain angles of incidence (θ) constructive interference can occur and X-rays can be diffracted from materials in a manner described by Bragg's Law:

where d is the interatomic spacing and n is an integer (constructive interference can only occur when the extra distance travelled by one photon is equal to an integer number of wavelengths). Plotting diffraction intensity against the angle θ yields a diffractogram that is unique to a given arrangement of atoms in a solid and which functions as a 'fingerprint' of the form of iron oxide present in a sample of SPION. XRD only considers the iron oxide core of the particle.

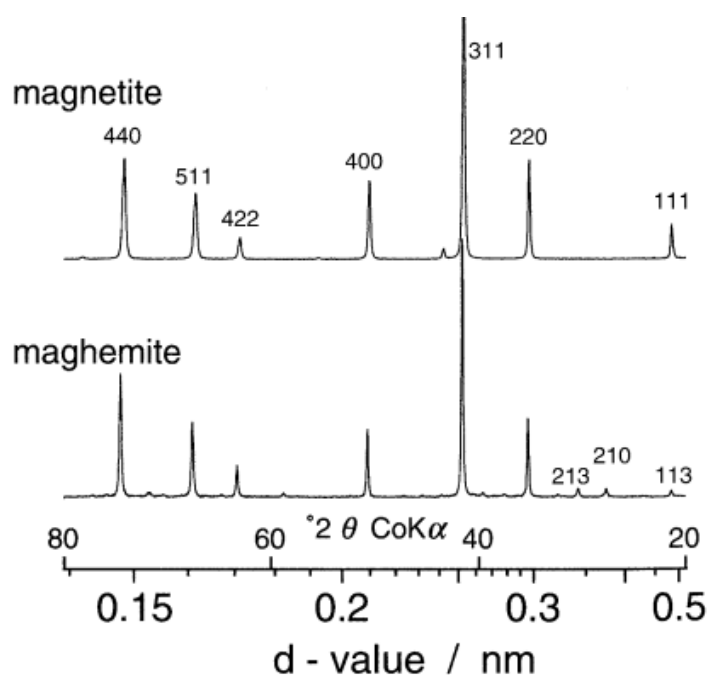


Figure 10. Comparison of standard diffractograms of magnetite and maghemite. Although peaks occur at similar values, relative intensities can be used to unequivocally identify unknown samples. Adapted from Cornell and Schwertmann.⁷⁷

Comparison to standard diffractograms can allow the assessment of proportions of different oxides in a mixture. Diffractograms can also allow the assessment of crystal size (i.e. nanoparticle size) from the broadening of XRD peaks by application of the Scherrer equation:^{76,77}

where K is a shape factor of 0.9 for spherical crystallites, λ is the wavelength of the X-rays used (determined from their source material), θ is the angle of incidence in radians for the peak in question, and $B_{\text{structural}}$ is the instrument broadening for the peak in question determined by:

where B_{observed} is the ‘full width at half maximum’ (FWHM) of the sample peak in radians and B_{standard} is the FWHM in radians of the Si(111) peak from a SiO₂ standard for the apparatus used. The crystallite size determined using the Scherrer equation is a volume average for the sample being studied but gives no information on polydispersity or deviation within the sample. The value can be of use in assessing the reproducibility of a synthetic route however.

Dynamic Light Scattering (DLS)

Dynamic light scattering (DLS) measures the size and polydispersity of nanoparticles in solution or suspension. A typical experimental set up is shown in Fig. 11a. For a full mathematical approach to DLS, the reader is directed to dedicated articles;^{78,79} in practice, all calculations are performed by DLS equipment and/or software.

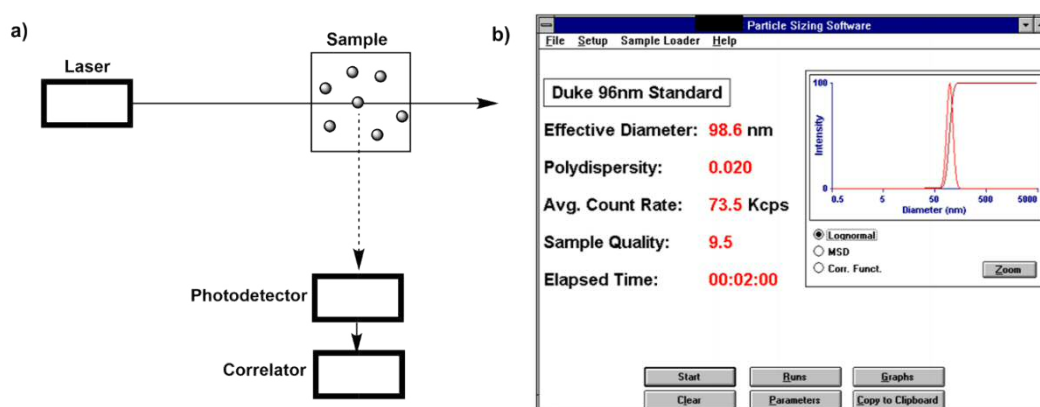


Figure 11a. Typical experimental set-up for DLS analysis, adapted from Goldberg.⁷⁸ **b.** Example output screen, showing diameter and dispersity for a known standard.

Lasers undergo Rayleigh scattering upon interaction with particles on the nanoscale. A photodetector positioned at 90 ° to the incident laser beam will only detect light scattered from a sample. Nanoparticles in solution undergo Brownian motion; as particles move through solution and cross the laser beam, the intensity of scattered light fluctuates.⁷⁹ The

decay of scattered light intensity as particles diffuse out of the beam path is exponential and the decay rate can be used to give the particles' translational diffusion coefficient (D_T). The movement of particles through solution is affected by the temperature of the solution (T), solution viscosity (η), Boltzmann's constant (k_B) and their translational diffusion coefficient (D_T) and can be correlated to their size by the Stokes-Einstein equation:

where D_h is the hydrodynamic diameter i.e. the diameter of a theoretical sphere that diffuses in the same manner as the sample particle.⁸⁰ As particles are solvated, D_h is not a 'true' measure of the particle size and is often an overestimation.^{79,80} This effect can be compounded if the particle is not a perfect sphere or if the sample particles are flocculating in solution. As the value of D_h is a mean average, the presence of aggregate species can skew D_h to much higher values than the actual dimensions of the nanoparticle.

Infra-red Spectroscopy (IR)

The most rapid method of characterising the surface nature of a nanoparticle is IR spectroscopy, familiar to all chemical scientists. Magnetite consists almost entirely of Fe-O-Fe bonds, and so the IR spectrum of uncoated SPION is dominated by absorptions associated with these bonds at approximately 580 cm^{-1} .⁷⁷ When a coating agent is applied, the presence of other bonds (e.g. Si-O-Si, N-H in the case of APTES) can be determined spectroscopically by IR. The shortcoming of this technique is that the information gained is qualitative; IR spectroscopy cannot determine coating thickness, extent of coating (i.e. coverage) or the exact functional nature of the surface groups.

Biocompatible (i.e. hydrophilic) SPION have typically been investigated in the pursuit of novel MRI-active contrast agents and are often characterised by FFC relaxometry. An aqueous sample of SPION of known concentration is transferred into a relaxometer and the T_1 relaxation rates of the protons in the water molecules determined at different applied field strengths, allowing for the calculation of the molar relaxivity r_1 which is crucial to describing the efficacy of the species as a contrast agent.¹³ The technique is also known as Nuclear Magnetic Relaxation Dispersion (NMRD) Spectroscopy and the data as an NMRD profile.

NMRD profiles cover field strengths from MHz to KHz. In the case of weak, fixed field strength NMR, signal detection can be poor due to a loss of sensitivity. This is overcome by field cycling where the field strength is rapidly (on the order of milliseconds) modulated electromagnetically throughout the experiment. T_1 relaxation times are determined via inversion recovery using pulse sequences. Under a magnetic field, almost all spins will align with the direction of the magnetic field, the z -axis. Applying a 180° RF pulse results in an inversion of the net magnetisation. After a delay period (τ) during which the spins start to realign with the applied field, a 90° RF pulse is applied which causes the net magnetisation to align either above or below the xy -plane (i.e. transverse magnetisation that generates signal, see Chapter 1). As the delay period varies, the degree of transverse magnetisation (hence signal intensity) varies; plotting τ against signal intensity allows the calculation of T_1 and R_1 .

At low field strengths, the population of spins initially aligned with the applied magnetic field direction will not produce sufficient signal following the pulse sequence to allow for calculation of T_1 . Field cycling overcomes this by initially using a strong field, B_p , to 'pre-align' or polarise the spins (see Fig. 12a). The field strength is rapidly lowered to the required value at which relaxation is to occur, B_r . The field strength is then increased to a significantly higher value (B_d) at which the desired RF pulse sequence is applied, signal monitored and relaxation times calculated. The field strength returns to B_p for a delay to allow complete realignment and the process repeated.

An example NMRD profile for SPION in aqueous solution is shown in Fig. 12b. NMRD profiles can be analysed via mathematical models to yield a value for average particle radius,² but this is uncommon in the literature.

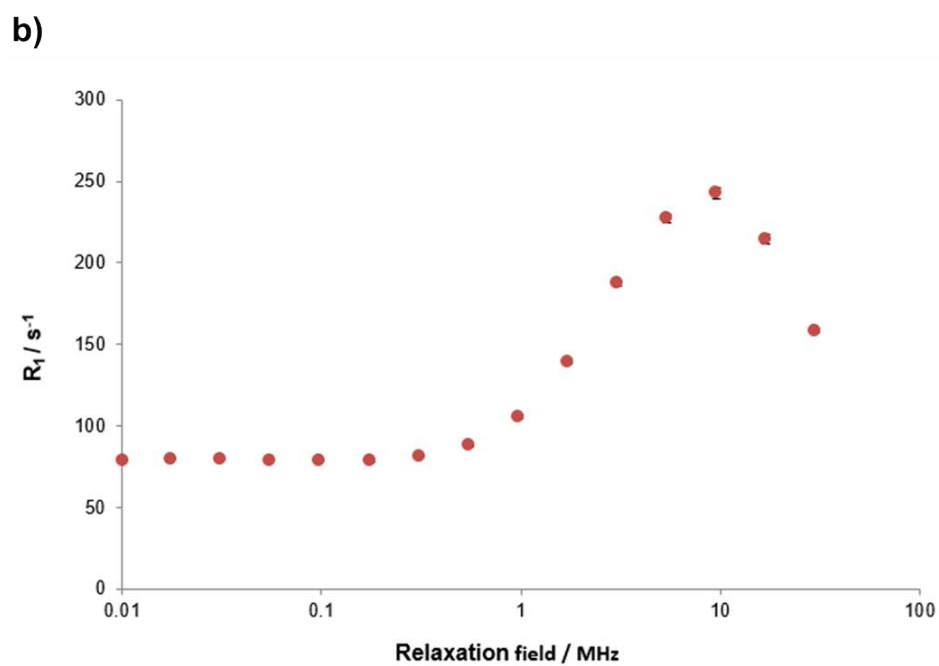
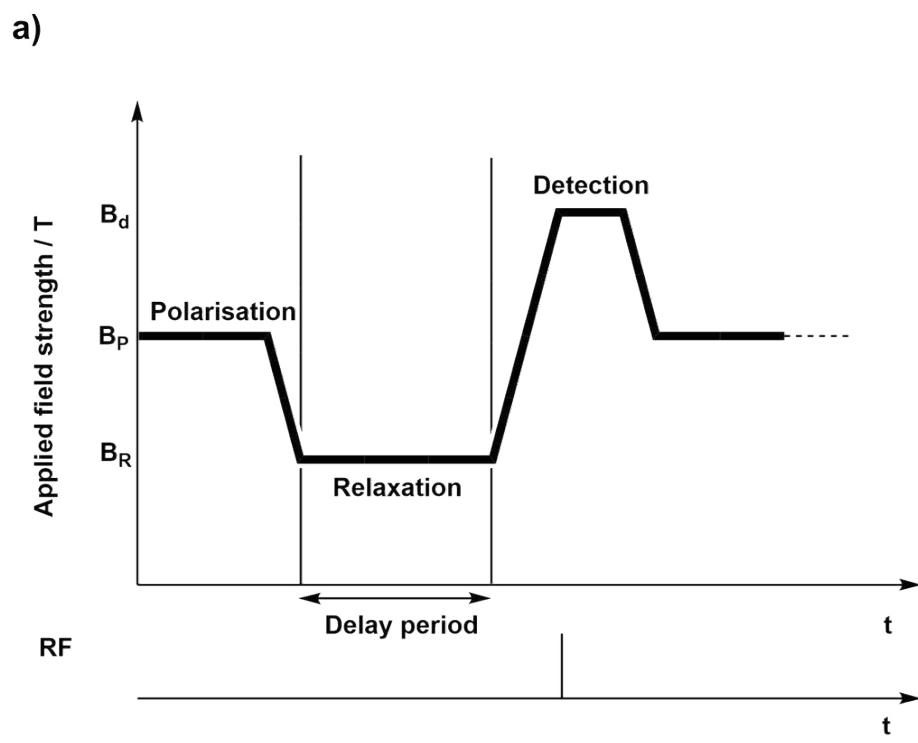


Figure 12a. Schematic representation of a typical FFC-NMRD experimental approach. Adapted from Kimmich and Anoardo.¹³ **b.** Example NMRD profile of SPION in aqueous solution.

2.1.6 Aims and objectives

The development of SPION can be viewed as a modern incarnation of our ancient fascination with magnetism. From their clinical use as MRI contrast agents to more novel applications such as hyperthermia therapy^{67,68} and drug delivery,^{64,81} SPION research is a rich and varied field. While there are many methods of synthesising SPION, when direct radiolabelling of nanoparticles with PET-active radiotracers is desired only co-precipitation methods are truly practicable at the time of writing. Thermal decomposition approaches require rigorously inert conditions which are achievable in a dedicated chemistry laboratory but are not easily maintained in a hot cell using radioactive materials. Other methods of SPION synthesis require specialist equipment that introduce additional cost and which limit the scale on which particles can be produced. Although co-precipitation techniques have limitations, they can be made to be satisfactorily reproducible under controlled conditions. Subsequent silanisation with APTES is an ideal next step due to the elegance by which stability, solubility and reactivity are introduced simultaneously. The ultimate aim of this research was therefore to develop a reproducible method of generating biocompatible SPION in a manner which could be transferred for use in a hot cell.

In the results and discussion section below, the method by which APTES was immobilised on SPION to give a stable, water-dispersible entity is discussed and such nanoparticles characterised. In addition, the use of carboxymethyl-dextran (CMD) as a coating agent is described and evaluated. The radiolabelling of SPION coated with APTES or CMD is discussed. Efforts to render hydrophobic nanoparticles (synthesised by thermal decomposition of an organometallic precursor) soluble in water by the use of common surfactants are reported.

Standard operating protocols for the production, storage, handling and use of radioisotopes for PETIC, University Hospital Wales, Cardiff are included as Appendix I to this thesis. As the pre-requisite for nanoparticles intended for introduction into biological systems is water-solubility, multiple approaches based on literature methods that gave nanoparticles that were not suitably water-soluble and which were not characterised fully are described in Additional Experimental Section I.

2.2 Experimental

2.2.1 Material and methods

Reactions were performed with the use of vacuum line and Schlenk techniques where appropriate. Reagents were commercial grade and were used without further purification. All reagents and solvents were purchased from Alfa Aesar or Sigma Aldrich, except APTES which was purchased from TCI Chemicals. $\text{FeCl}_2 \cdot 4\text{H}_2\text{O}$ and APTES were stored under inert atmospheres. Powder X-Ray diffraction was performed on an X'Pert PRO analytical using a Cu radiation source and analysed using X'Pert Highscore Plus. IR spectra were recorded as solid samples on a Shimadzu IRAffinity-1 FTIR spectrometer. Transmission electron microscopy was carried out on a Philips CM12 Transmission Electron Microscope; 80kV. Digital photomicrographs were captured with a Megaview III digital TEM camera and iTEM software (Soft Imaging System GmbH, Münster, Germany) and analysed using ImageJ. Dynamic light scattering analysis was performed on a Brookhaven Instruments Corporation 'Zetaplus'. Relaxometry was performed on a Stelar FFC-2000 fast field cycling NMR spectrometer. Radioactivity was assessed using a Capintec CRC[®]-25 PET dose calibrator. Radiolabelling was performed in the research laboratory of PETIC, University Hospital of Wales, Cardiff.

2.2.2 Synthesis and analytical techniques

APTES@SPION (1) Method adapted from that of Yamaura et al.⁴⁵

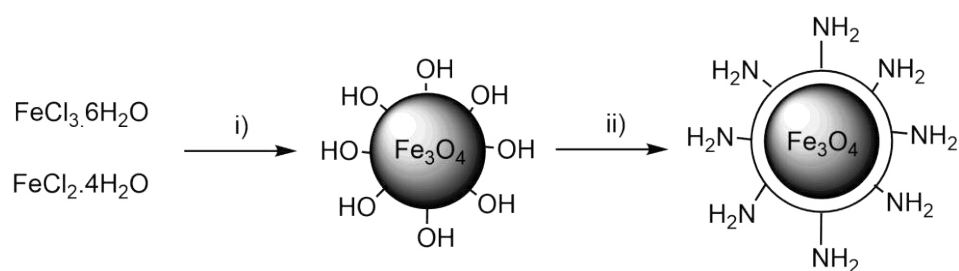


Figure 13. Synthetic route for APTES@SPION. i) 5 M NaOH (5 mL), H_2O (10 mL), room temperature, 5 min. ii) Glycerol (3 mL), APTES (0.8 mL), H_2O (7.2 mL), Acetic acid (0.8 mL), 75 °C, 3 h.

$\text{FeCl}_2 \cdot 4\text{H}_2\text{O}$ (0.5 g, 2.5 mmol) and $\text{FeCl}_3 \cdot 6\text{H}_2\text{O}$ (1.352 g, 5 mmol) were dissolved in H_2O (10 mL) and the solution stirred. 5M NaOH (5 mL) was added and the reaction mixture stirred for 5 mins at room temperature. The precipitated nanoparticles were collected using a permanent magnet (1 T) and washed with distilled water until the pH of the washings were

pH 7. As much water as possible was removed by use of a permanent magnet and a pipette prior to the next step. Glycerol (3 mL) was added and the reaction mixture homogenised. APTES (0.8 mL, 3.4 mmol) was added to water (7.2 mL) and the pH adjusted to 4 with glacial acetic acid (0.8 mL) and then added to the nanoparticle dispersion. The reaction mixture was stirred at 75 °C for 3 h. The reaction mixture was allowed to cool and then transferred to a volumetric flask and made up to 50 mL with H₂O. Adding this solution to MeCN (75 mL) caused the coated nanoparticles to precipitate. The particles were collected magnetically and were washed with fresh, cold MeCN (3 × 10 mL) and then dried *in vacuo* to give the *title product* as a black powder (0.53 g). XRD analysis confirmed phase identity as magnetite, average crystalline size = 6.5 nm. TEM analysis showed approximately spherical nanoparticles, average diameter = 8.1 ± 1.7 nm. DLS analysis showed aggregate species, hydrodynamic diameter = 264.1 nm, polydispersity = 0.245. IR (ATP) ν = 1541 (NH₂ bending), 1404 (CH₂ bending), 1098 (Si-OH), 1050 (Si-OH), 962 (Si-O-Si), 570 (Fe-O) cm⁻¹.

⁸⁹Zr-APTES@SPION (2)

FeCl₂·4H₂O (0.1 g, 0.5 mmol) and FeCl₃·6H₂O (0.270 g, 1 mmol) were dissolved in H₂O (2 mL) and the solution stirred. ⁸⁹Zr oxalate solution* (100 μL, 6.50 MBq) was brought to pH 7 by addition of saturated Na₂CO₃ solution and was added to the iron-containing solution. 5M NaOH (1 mL) was added, and the reaction mixture stirred for 5 mins at room temperature. The precipitated nanoparticles were collected using a permanent magnet (1 T) and washed with distilled water until the pH of the washings were pH 7. As much water as possible was removed by use of a permanent magnet and a pipette prior to the next step. Glycerol (0.6 mL) was added and the reaction stirred to homogenise. APTES (160 μL) was added to water (1.44 mL) and the pH adjusted to 4 with glacial acetic acid (160 μL), and then added to the nanoparticle dispersion. The reaction mixture was stirred at 75 °C for 3 h. After 3 hours the reaction mixture was allowed to cool, transferred to a volumetric flask and made up to 10 mL with H₂O. Adding this solution to MeCN (15 mL) caused the coated nanoparticles to precipitate. These were washed with cold MeCN (3 × 5 mL) and then dried in air to give the *title product* as a black powder (0.138 g, 4.70 MBq, 72 % radiolabelling efficiency). TEM analysis showed approximately spherical nanoparticles, average diameter = 9.3 ± 2.0 nm. DLS analysis showed aggregate species, hydrodynamic diameter = 254.5 nm, polydispersity

* Radioisotope production and purification is described in Appendix I of this thesis and discussed in greater detail in Chapter 4.

= 0.257. IR (ATP) $\nu = 1540$ (NH₂ bending), 1404 (CH₂ bending), 1094 (Si-OH), 1047 (Si-OH), 962 (Si-O-Si), 571 (Fe-O) cm⁻¹.

CMD@SPION (3) Method adapted from that of Pardoe et al.⁸²

FeCl₃.6H₂O (0.068 g, 0.28 mmol) and FeCl₂.4H₂O (0.028 g, 0.14 mmol) was dissolved in H₂O (1 mL). Carboxymethyl-dextran sodium salt (100 mg) was dissolved in H₂O (1 mL) and added to the iron solution. The mixture was shaken and observed to congeal. 1M NaOH solution (1 mL) was added and the reaction mixture vortexed in an Eppendorf thermomixer (15 min., 60 °C, 550 rpm). EtOH (3 mL) was added to precipitate the coated nanoparticles and vortexing continued (1 min., 60 °C, 550 rpm). The reaction mixture was centrifuged (5 min., 21 °C, 900 rpm) and the supernatant decanted. The pellet was then dissolved in PBS buffer, pH 7.4 (5 mL). The solution was centrifuged to remove insoluble material (5 min., 21 °C, 900 rpm). The supernatant was decanted to give the *title compound* as a solution in PBS buffer. TEM analysis showed approximately spherical nanoparticles, average diameter = 7.6 ± 1.8 nm. DLS analysis showed aggregate species, hydrodynamic diameter = 141.3 nm, polydispersity = 0.257. IR (ATP) $\nu = \nu = 3589$ -3000 (OH stretching), 2920 (CH₂ stretching), 1593 (CH₂ bending), 1415 (CH₂ bending), 1002 (C-OH stretching), 568 (Fe-O), 527 (Fe-O) cm⁻¹.

⁸⁹Zr-CMD@SPION (4)

FeCl₃.6H₂O (0.068 g, 0.28 mmol) and FeCl₂.4H₂O (0.028 g, 0.14 mmol) was dissolved in H₂O (1 mL). ⁸⁹Zr oxalate solution (75 μL, 9.90 MBq) was added, and the mixture homogenised. Carboxymethyl-dextran sodium salt (100 mg) was dissolved in H₂O (1 mL) and added to the iron solution. The mixture was shaken, and observed to congeal. 1M NaOH solution (1 mL) was added, and the reaction mixture vortexed in an Eppendorf thermomixer (15 min., 60 °C, 550 rpm). EtOH (3 mL) was added to precipitate the coated nanoparticles and vortexing continued (1 min., 60 °C, 550 rpm). The reaction mixture was centrifuged (5 min., 21 °C, 900 rpm) and the supernatant decanted. The activity of the pellet was measured (9.24 MBq) and the pellet was then dissolved in PBS buffer, pH 7.4 (5 mL). The solution was centrifuged to remove insoluble material (5 min., 21 °C, 900 rpm). The supernatant was decanted and the activity measured (9.00 MBq, 91 % radiolabelling efficiency) to give the *title compound* as a solution in PBS buffer. Characterisation data could not be obtained due to the radioactive nature of the particles.

Iron (III) acetylacetonate ($Fe(acac)_3$) (5)

$FeCl_3 \cdot 6H_2O$ (12.43 g, 46 mmol) was dissolved in water (100 mL). KOH (20 % aqueous solution) was added dropwise with stirring until pH 8. The brown precipitate formed was left to settle and was then removed by filtration under suction, washed with ice cold water and left to dry on the pump overnight. The brown solid was transferred to a conical flask and acetylacetonone (15.8 mL, 154 mmol) added. The reaction mixture was stirred at room temperature for 30 minutes, then chilled for 1 hour without stirring. A crimson solid was isolated by filtration under suction and dried *in vacuo*. The solid was dissolved in a minimum of hot chloroform and the bright orange solution filtered while hot. The filtered solution was warmed to 50 °C and room temperature hexane was added until crystallisation was observed. The reaction mixture was left to crystallise overnight. Bright red crystals formed and were isolated by filtration under suction and dried on the pump. The crude solid was recrystallised from hot methanol and room temperature water. The product was isolated by filtration under suction and dried on the pump to give the *title compound* as a red powder (8.04 g, 22.8 mmol, 50 %); IR (ATP) $\nu = 1566$ (CO), 1520 (CO), 1420 (CO), 1352 (CC), 1273 (CC), 1188 (CC), 1015 (CC), 928(CC), 800 (CH), 770 (CH), 665 (CH), 653 (CH).

Oleic acid@SPION (OA@SPION) (6) Method adapted from that of Sun et al.²³

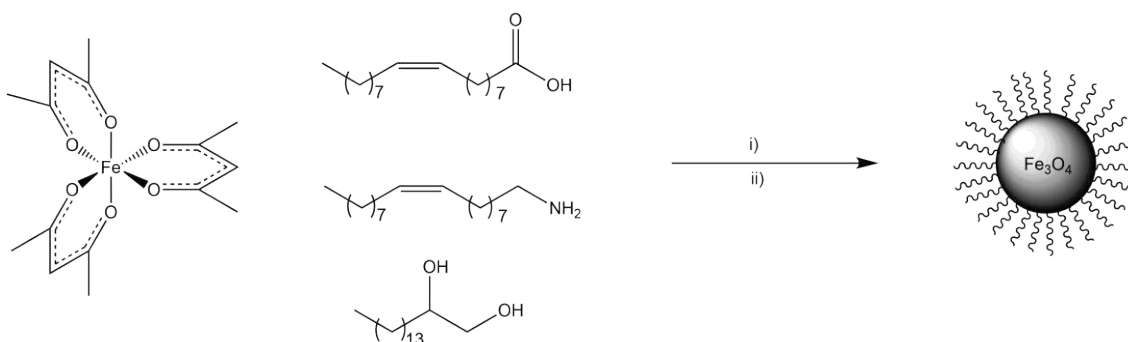


Figure 14. Synthetic scheme for thermal decomposition of $[Fe(acac)_3]$ to give OA@SPION. i) Phenyl ether, 200 °C, 30 min, $N_2(g)$. ii) Phenyl ether, reflux, 30 min, $N_2(g)$.

Crystalline $[Fe(acac)_3]$ was finely powdered using a pestle and mortar. $Fe(acac)_3$ (0.706 g, 2 mmol), 1,2-hexadecanediol (2.58 g, 10 mmol), oleic acid (1.94 mL, 6 mmol) and oleylamine (2.04 mL, 6 mmol) were mixed in phenyl ether (20 mL) and stirred under inert conditions in a Schlenk tube. The reaction mixture was heated to 200 °C by use of an oil bath for 30 minutes, then heated to reflux under nitrogen by use of a Bunsen burner for 30 minutes. The solution was seen to turn black. The reaction mixture was allowed to cool to room temperature. Ethanol (40 mL) was added to encourage precipitation. The mixture was shaken

and left to settle for 1 hour. Solvent was removed until approximately 20 mL remained and the precipitate re-suspended. The precipitate was separated through centrifugation (6000 rpm, 10 minutes) and left to dry overnight, then dissolved in hexane (20 mL) in the presence of oleic acid (0.05 mL) and oleylamine (0.05 mL). The solution was centrifuged (8000 rpm, 10 minutes) and any pellet discarded. The supernatant was kept and the product precipitated by addition of ethanol (20 mL). The product was isolated by centrifugation (13200 rpm, 10 minutes) to give superparamagnetic iron oxide nanoparticles as a black powder (0.196 g, 76 %). TEM analysis showed approximately spherical nanoparticles, average diameter = 4.3 ± 0.4 nm.

Dispersion of OA@SPION using commercial surfactants

A solution of OA@SPION in Et₂O (2 mL, 5 mg.mL⁻¹) was added to an aqueous solution of one of nine surfactants (Brij[®]-35, Brij[®]-98 or Triton[™] X-100, 2 mL, 25 mM; and Brij[®]-30, Brij[®]-56, Brij[®]-96, Tween[®] 20, 2mL, 50 mM). The two phase system was sonicated and allowed to settle. The ether layer was allowed to evaporate slowly over three hours with regular sonication to ensure dispersion of SPION into the aqueous layer and addition of small quantities of diethyl ether to redisperse precipitated nanoparticles to give brown solutions of surfactant-dispersed OA@SPION in water (5 mg.mL⁻¹) in the cases of Brij[®]-35, Brij[®]-96 and Tween[®] 20. These suspensions were characterised by FFC-NMRD relaxometry.

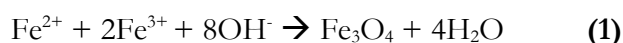
2.3 Results and discussion

2.3.1 Synthesis and characterisation of APTES@SPION and ⁸⁹Zr-APTES@SPION

Synthetic considerations

In the work published by Yamaura *et al.*,⁴⁵ SPION were prepared by a co-precipitation method from hydrated iron chloride salt solutions by the addition of a strong base. The particles were washed thoroughly before glycerol was added as a co-solvent and the particles heated to 70 °C for 3 h in the presence of a freshly prepared APTES aqueous solution (pH 4). This procedure did not specify a reaction time allowed for the initial formation of the nanoparticles. The particles were characterised by XRD, TEM and IR. Analysis of the diffractograms of APTES@SPION using the Scherrer equation allowed the calculation of an average core size of 12 nm, while TEM images gave a value of 15 nm, which the authors concluded as signifying an APTES coating layer 3 nm thick. The IR spectrum showed multiple peaks between 1100 and 900 cm⁻¹ corresponding to Si-O-Si and Si-O-H bonds, but perhaps the most indicative of the success of the coating step would be the bands at 3417 and 1625 cm⁻¹ for NH stretching and NH₂ bending respectively.

For any technique developed on the lab bench to be transferable to the ‘hot cells’ of a PET research laboratory, it must be reproducible, reliable and relatively simple to perform by use of remote manipulators. It must also be able to be scaled down without affecting the kinetics of the reaction. The formation of magnetite nanoparticles (described in Equation 1) could not require the use of rigorously inert conditions that could not be attained in the hot cell.



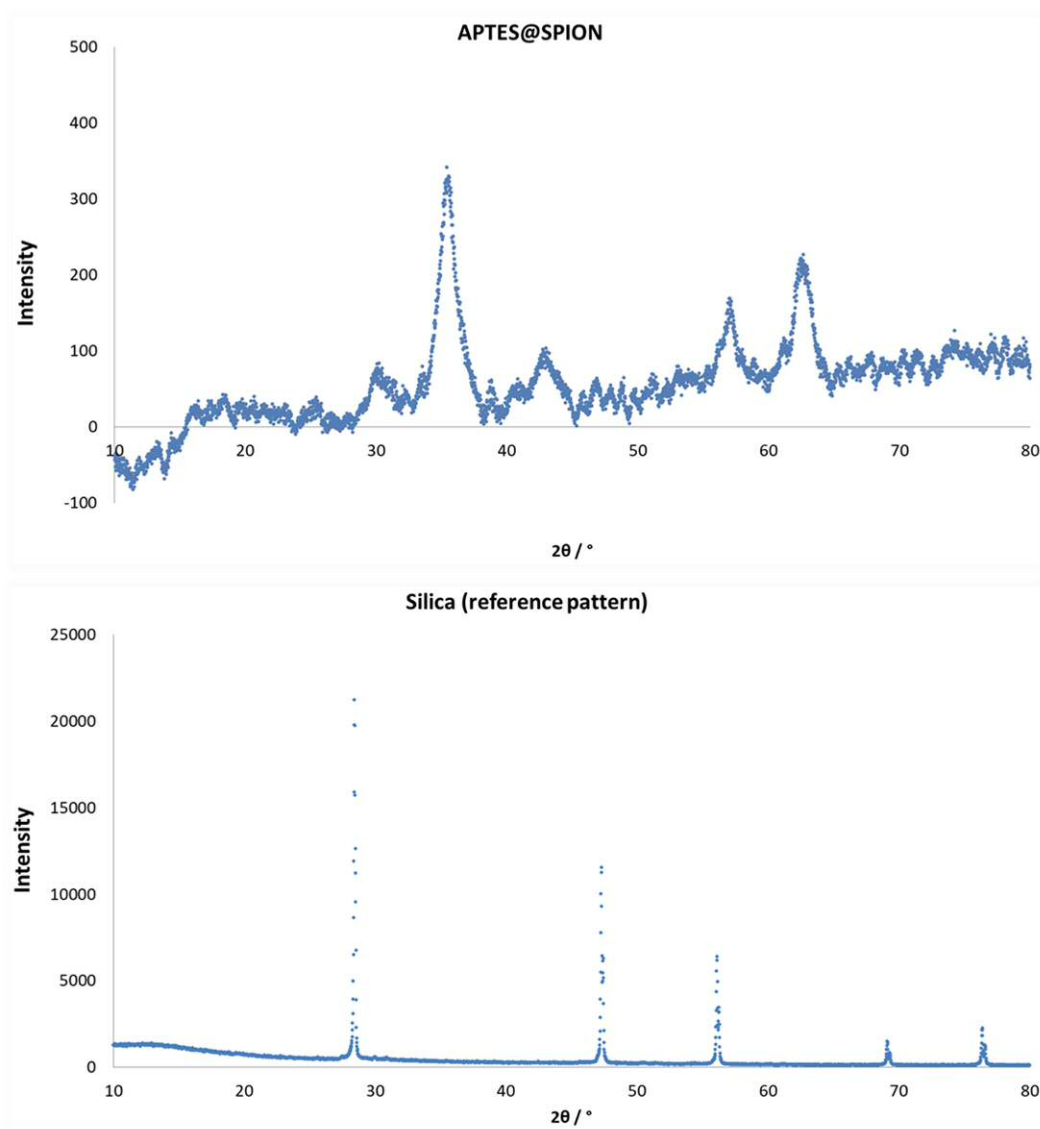
Therefore, initial attempts to repeat the work of Yamaura *et al.* had to ignore the stated need to maintain inert conditions throughout the synthesis to prevent oxidation of magnetite to maghemite (Fe₂O₃). To limit the extent of oxidation in the reaction system, the reaction was performed as quickly as possible. The Fe²⁺ salt was added to the reaction mixture almost immediately before the addition of the base. Reaction time (i.e. the delay between adding the base and magnetic collection and washing of the particles) was kept low at 5 min.

Following the coating step, the particles were dried *in vacuo* and appeared as a black solid that showed a strong attraction to a permanent magnet. Reaction yields were consistent at a given reaction scale; as reaction scale was varied, yield varied linearly. The product particles were characterised and observed to be of comparable dimensions (see below).

XRD Analysis

Initial analysis of diffraction patterns yielded phase identification that showed that Fe_3O_4 was the major constituent of the coated particles' core. No peaks corresponding to other iron oxide phases could be determined against background noise. Diffractograms were analysed using the Scherrer equation:

$B_{\text{structural}}$ was found by subtracting the FWHM of the 111 peak of SiO_2 at $2\theta = 28.4^\circ$ from the FWHM of the magnetite 311 peak at $2\theta = 35.5^\circ$.⁸³ For spherical nanoparticles $K = 0.9$, and the Cu source used emitted X-rays with $\lambda = 1.542 \text{ \AA}$. Fig. 15 shows a typical measured diffractogram, the standard silica diffractogram used to determine $B_{\text{structural}}$ for all samples, and the derivation of the average crystallite size of the shown sample. Average values and absolute error were determined by taking multiple calculations of B_{observed} at FWHM utilising outlying values of θ . Table 2 shows calculated average crystallite sizes for multiple samples of APTES@SPION prepared as described and on a larger scale.



Maximum intensity(SPION(311))	335 ($2\theta = 35.5^\circ$)
Half maximum(SPION(311))	167.5 ($2\theta = 35.5^\circ$)
FWHM(SPION(311))	$36.1 - 34.7 = 1.4^\circ = 2.44 \times 10^{-2}$ rad
FWHM(Si(111))	2.16×10^{-3} rad
$B_{\text{structural}}$	2.22×10^{-2} rad
Average crystallite size (\AA)	65 \AA

Figure 15. XRD patterns of APTES@SPION (Sample 1), silica reference, and the derivation of average crystallite size for Sample 1.

APTES@SPION Sample No. (Reaction scale)	Calculated crystallite size \pm error / nm
1 (5 mmol of FeCl ₃ .6H ₂ O)	6.5 \pm 0.4
2 (5 mmol of FeCl ₃ .6H ₂ O)	6.3 \pm 0.6
3 (5 mmol of FeCl ₃ .6H ₂ O)	6.3 \pm 0.4
4 (5 mmol of FeCl ₃ .6H ₂ O)	6.2 \pm 0.7
5 (25 mmol of FeCl ₃ .6H ₂ O)	7.6 \pm 0.8
6 (25 mmol of FeCl ₃ .6H ₂ O)	9.1 \pm 0.9
7 (25 mmol of FeCl ₃ .6H ₂ O)	9.1 \pm 0.8

Table 2. Calculated average crystallite sizes of APTES@SPION samples synthesised on different reaction scales.

Taking the values of the samples produced on the ‘5 mmol’ scale, the size of particles range from 5.5 to 6.9 nm with most being approximately 6.3 nm. Although this value is approximately half of the value calculated from XRD data by Yamaura *et al.*,⁴⁵ it is likely that the 5 minute reaction time used here is less than for the published work; a longer reaction time would allow for more Ostwald ripening within the reaction system and an increase in average particle size. When performed on a larger scale, the synthetic approach described yields particles with a larger average size and with a greater deviation in calculated values. This may be due to the longer time required to wash the greater mass of particles until the washings were of pH 7, allowing for more particle growth.

During the synthesis of ⁸⁹Zr-radiolabelled particles (described as **(2)** in the accompanying experimental section), to achieve a maximum radiolabel loading of the particles while maintaining safety and to facilitate synthesis the scale of the reaction was decreased by a factor of five. The mass of nanoparticles obtained per experiment was insufficient to allow XRD analysis; however, based on the XRD data above and data from other techniques discussed below, it would be expected that the core sizes would be approximately 7-8 nm.

TEM Image Analysis

Select samples of APTES@SPION synthesised cold in the chemistry laboratory and samples of ^{89}Zr -labelled APTES@SPION (suitably decayed as to render them safe for transit and study) were dispersed in distilled water and dried onto a suitable support prior to microscopy. Digital images were taken and analysed using the software package ImageJ. The scale was set by reference to the internal standard and a square grid pattern was overlaid onto the image. Where the vertical and horizontal grid markings intersected on top of a particle, the particle was selected to be part of a statistical population of 30 particles per sample and the horizontal diameter of the particle measured based on contrast to the field. The average particle size and standard deviation per population were then calculated (see Table 3).

For APTES@SPION, an approximate value for coating thickness can be found by subtracting TEM-observed diameter from the calculated core diameter from XRD analysis, which yields values between 1.5 and 1.8 nm. This method was applied by Yamaura *et al.* and gave an estimated value of 3 nm for 12 nm iron oxide core;⁴⁵ the particles described here can be estimated as having a 1.5 nm coating on a 6.5 nm core. Limited resolution in the TEM images does not allow for the clear visualisation of the coating layer. Based on typical bond lengths and taking into account experimental error and the movement of atoms within molecules this thickness would be the approximate equivalent of two monomers of APTES (see Fig. 16).

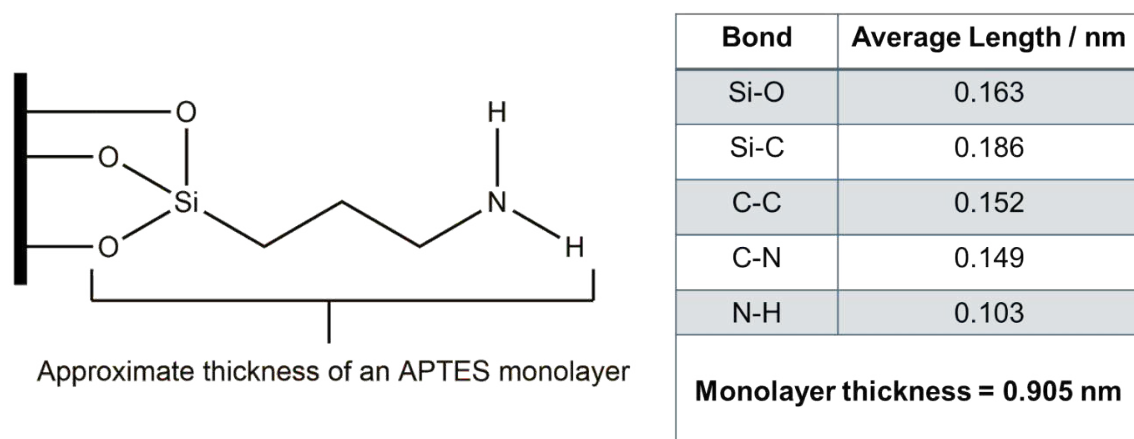


Figure 16. Calculation of approximate monolayer thickness based on average bond lengths.⁸⁴

APTES@SPION Sample No. (Reaction scale)	Average diameter \pm S.D. / nm ($n = 30$)	Approx. coating thickness / nm
1 (5 mmol of FeCl ₃ .6H ₂ O)	8.1 \pm 1.7	1.6
2 (5 mmol of FeCl ₃ .6H ₂ O)	7.8 \pm 1.7	1.5
3 (5 mmol of FeCl ₃ .6H ₂ O)	8.0 \pm 1.2	1.7
4 (5 mmol of FeCl ₃ .6H ₂ O)	8.0 \pm 1.3	1.8
⁸⁹ Zr-APTES@SPION Sample No. (Reaction scale)	Average diameter \pm S.D. / nm ($n = 30$)	Approx. coating thickness / nm
1 (1 mmol of FeCl ₃ .6H ₂ O)	9.3 \pm 2.0	N/A
2 (1 mmol of FeCl ₃ .6H ₂ O)	8.7 \pm 1.5	N/A
3 (1 mmol of FeCl ₃ .6H ₂ O)	8.7 \pm 1.9	N/A

Table 3. Average diameters of APTES@SPION and ⁸⁹Zr-APTES@SPION as determined from TEM analysis. Approximate coating thickness calculated by comparison of TEM and XRD determined diameters. For ⁸⁹Zr-APTES@SPION, sample masses were insufficient to obtain XRD data, hence coating thickness is not provided.

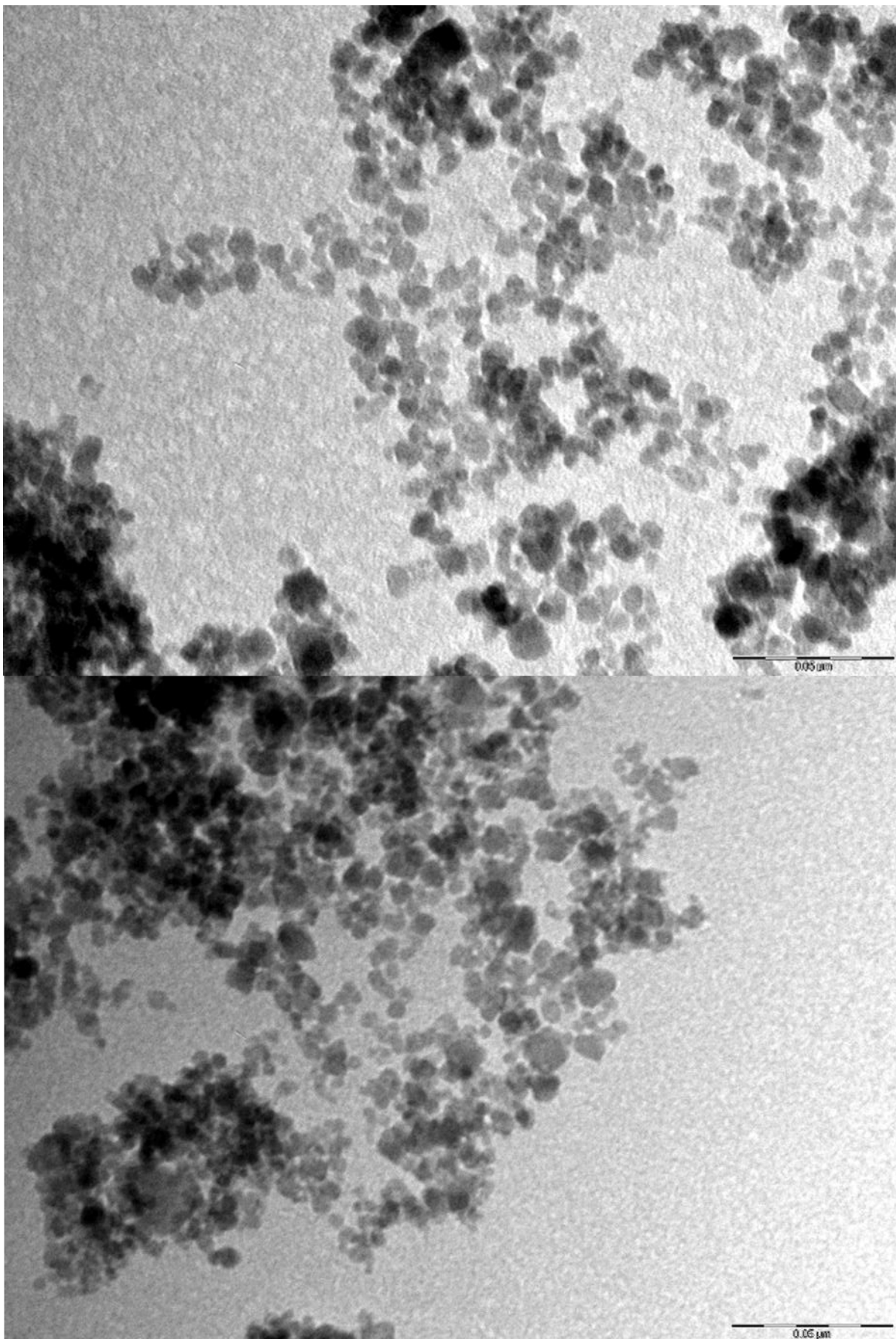


Figure 17. TEM images of APTES@SPION, average size = 8.1 ± 1.7 nm. Scale bar in both images corresponds to 50 nm. Polydispersity (from DLS, see below) = 0.245.

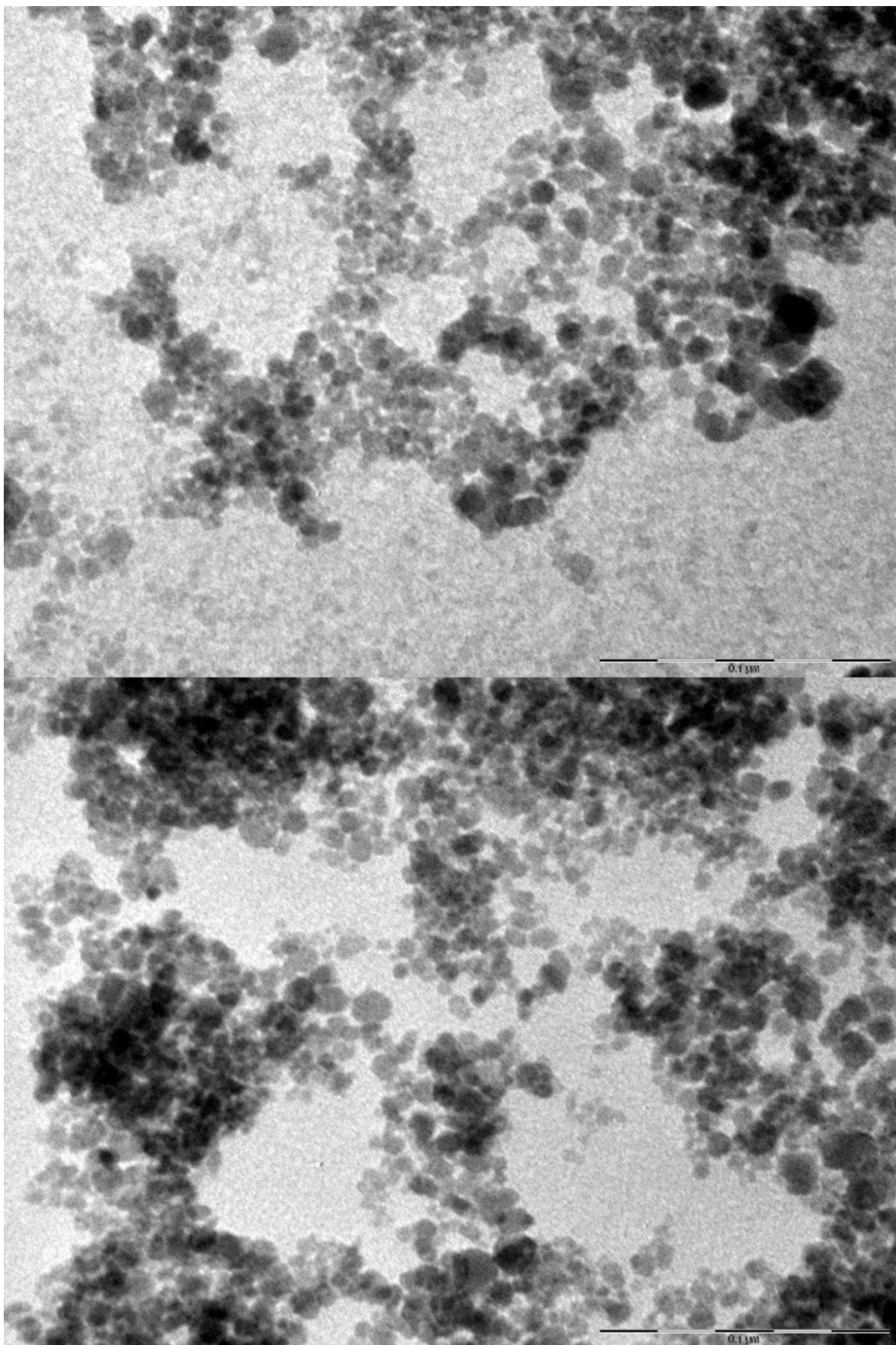


Figure 18. TEM images of $^{89}\text{Zr-APTES@SPION}$, average size = 9.3 ± 2.0 nm. Scale bar in both images corresponds to 100 nm. Polydispersity (from DLS, see below) = 0.257.

The radiolabelled particles would be expected to have a greater average particle size and greater standard deviation than the unlabelled particles as a result of the more accurate temperature control available due to the apparatus used in the hot cell and a longer period of time prior to coating during which Ostwald ripening can occur. The differences in calculated average diameter sizes between the classes of samples was typically within one standard deviation and can be determined to be statistically insignificant. The methodology was highly reproducible and any sample could be used in subsequent experiments with reasonable confidence that it was representative in terms of particle size.

Dynamic Light Scattering analysis

Samples of APTES@SPION synthesised cold in the chemistry laboratory and samples of ⁸⁹Zr-labelled APTES@SPION were dispersed in distilled water at a concentration of 0.1 mg.mL⁻¹ and analysed by DLS at 25 °C (see Table 4). More concentrated and more dilute solutions were unsuitable as they did not yield reliable data. Under the conditions used, all samples had hydrodynamic radii much greater than the particle diameter determined from TEM image analysis, showing aggregation between particles although the dispersions appeared stable to the eye over 48 hrs.

For the SPION dispersions studied, the measured value of hydrodynamic diameter is highly dependent on the conditions of the sample and degree of aggregation. This could be varied by sonicating a sample and disturbing the aggregate species; the measured diameters would vary markedly for a short period of time before equilibrium would be restored and the diameters would again be consistent with the aggregation of the particles. It can be concluded that the data shown below describes an equilibrium state of aggregation that occurs under the conditions used and can therefore only truly be used to make qualitative statements about the behaviour of different samples. More accurate data about individual particles may be obtained by changing the conditions (e.g. lowering pH to increase the charge on particle surfaces) but this was not achieved. All samples were seen to behave similarly, forming large aggregates of between 10 and 20 nanoparticles with a polydispersity of between 0.24 and 0.28, indicating that the aggregates are not monodisperse but are not so polydisperse as to be unsuitable for DLS analysis.⁸⁰ The behaviour of the radiolabelled particles was analogous to that of the unlabelled particles. It can be concluded that bioconjugation experiments performed using unlabelled particles would yield results that could be used to make predictions about the behaviour of labelled particles in similar experiments as long as care is taken to counteract aggregation which may limit reaction rates.

APTES@SPION Sample No. (Reaction scale)	Hydrodynamic diameter \pm S.E. / nm ($n = 3$)	Half width \pm S.E. / nm	Polydispersity
1 (5 mmol of FeCl₃·6H₂O)	264.1 \pm 1.0	130.7 \pm 0.9	0.245
2 (5 mmol of FeCl₃·6H₂O)	250.2 \pm 1.8	128.1 \pm 1.7	0.263
3 (5 mmol of FeCl₃·6H₂O)	224.5 \pm 2.0	109.8 \pm 1.3	0.240
4 (5 mmol of FeCl₃·6H₂O)	172.5 \pm 1.2	83.8 \pm 0.9	0.236
⁸⁹Zr-APTES@SPION Sample No. (Reaction scale)	Hydrodynamic diameter \pm S.E. / nm ($n = 3$)	Half width \pm S.E. / nm	Polydispersity
1 (5 mmol of FeCl₃·6H₂O)	254.5 \pm 1.6	129.0 \pm 1.3	0.257
2 (5 mmol of FeCl₃·6H₂O)	291.9 \pm 6.4	154.6 \pm 3.9	0.281
3 (5 mmol of FeCl₃·6H₂O)	208.5 \pm 2.6	102.3 \pm 2.7	0.240

Table 4. DLS data for APTES@SPION and ⁸⁹Zr-APTES@SPION. It is likely that these values reflect aggregate species and not truly colloidal stabilised dispersions.

IR Spectroscopy

All samples of APTES@SPION and ^{89}Zr -APTES@SPION gave almost identical IR spectra; a typical spectrum is shown with that of an uncoated SPION sample for comparison (Fig. 19). A broad peak at 570 cm^{-1} arises due to the Fe-O bonds of magnetite in both spectra.⁷⁷ For the coated species, peaks can be observed at 1098 , 1050 and 962 cm^{-1} corresponding to Si-O-H and Si-O-Si bond.⁴⁵ Peaks observed at 1541 and 1404 cm^{-1} correspond to NH_2 and CH_2 bending and are prominent and indicative of the success of coating. NH_2 stretching at $\sim 3400\text{ cm}^{-1}$ can be difficult to observe due to the hygroscopic nature of the particles.

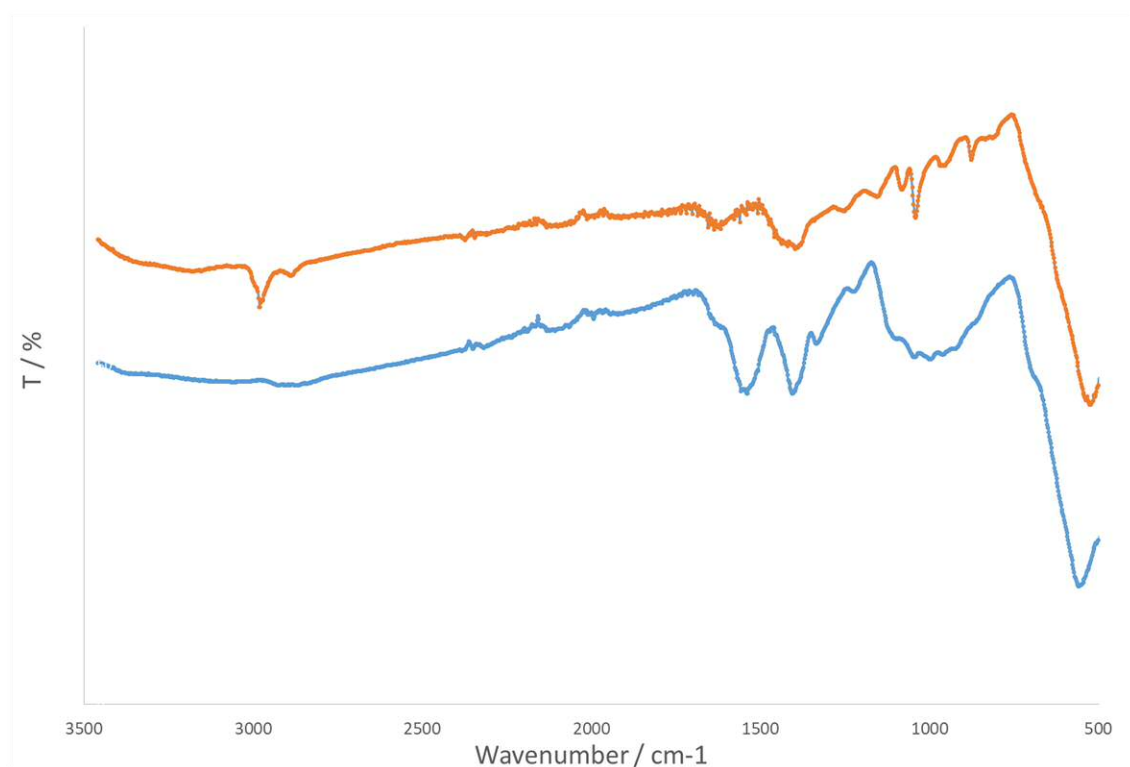


Figure 19. IR spectra of APTES@SPION (blue) and uncoated SPION prepared by coprecipitation (orange)

2.3.2 Summary for APTES@SPION and ⁸⁹Zr-APTES@SPION

APTES@SPION were synthesised ‘cold’ and initially characterised by IR (to confirm the nature of the coating) and XRD to observe the effect of reaction scale on the core size. Performing the reaction on the smaller scale gave a smaller average core size with a narrower size distribution and it was concluded that the synthesis of a radiolabelled analogue should be performed on a small scale to minimise polydispersity. TEM image analysis showed no significant difference in average particle diameter between ‘cold’ particles prepared on a ‘5 mmol’ scale and the radiolabelled species prepared on a ‘1 mmol’ scale and the calculated coating thicknesses of an ‘average particle’ were similar in all samples. DLS analysis allowed for a qualitative assessment of the stability of a dispersion of such particles and insight into their behaviour under certain conditions. It was concluded that the cold APTES@SPION synthesised could be used as model systems in protocol development with confidence that any methods could be successfully adapted for use with radiolabelled particles.

Combined Data for APTES@SPION, Sample 1		
Core diameter \pm error / nm	Total diameter \pm S.D. / nm	Hydrodynamic diameter \pm S.E. / nm
6.5 \pm 0.4	8.1 \pm 1.7	264.1 \pm 1.0

Table 5. APTES@SPION, Sample 1 was selected for protocol development described in Chapter 3 and 4 due to its representative physical characteristics. The hydrodynamic diameter reflects aggregation is occurring.

All samples, regardless of reaction scale or their degree of radiolabelling, showed comparable physical characteristics and gave stable dispersions in water and physiologically relevant buffers. The incorporation of ⁸⁹Zr into uncoated SPION was initially quantitative; a decrease in final radiolabelling efficiency to 72 % was due primarily to the loss of labelled particles during washing and drying steps mainly due to difficulties using remote manipulators. Given the amine-functionality present on the surface of APTES@SPION, it was judged that the method reliably gave a nanoparticle species that could be radiolabelled with high efficiency and which bore surface functionalities suitable for bioconjugation. Due to technical difficulties, relaxometry studies were not performed for these particles.

2.3.3 Synthesis and characterisation of CMD@SPION and ⁸⁹Zr-CMD@SPION

Synthetic considerations

CMD-coated SPION were synthesised in a manner based on that described by Pardoe *et al.*⁸² Stabilisation occurred immediately upon formation due to the presence of CMD in solution that adsorbed onto the hydroxylated surface of magnetite. The resulting particles were well dispersed in distilled water, pH 7.4 buffer and Dulbecco's Modified Eagle Medium (DMEM). When the reaction was performed in the presence of radiotracers for incorporation into the iron oxide lattice, radiolabelling occurred with 91 % efficiency with most losses due to transfer during isolation and purification of the produce particles. In comparison to the method described for the synthesis of ⁸⁹Zr-APTES@SPION, the preparation of ⁸⁹Zr-CMD@SPION was considerably more time efficient, easier to perform when using remote manipulators and occurred with higher radiolabelling efficiency.

However, this method is not as desirable for the synthesis of bioconjugates. CMD@SPION are negatively charged and cells have a negatively charged surface, potentially limiting the adsorption of nanoparticles.⁸⁵ This could impact on the binding ability of an immobilised antibody and/or prevent internalisation. Also, although carboxylic acid groups are used in bioconjugation (discussed in Chapter 3), they are generally not as common as other functionalities (e.g. amines, thiols) because of their need for carbodiimides and/or active ester intermediates. Most troublingly, the method described was found to be unreliable in terms of yield and magnetic responsiveness of the particles when the reaction scale was altered, and once the particles were dispersed in a suitable medium they could not be precipitated and re-dispersed. The particles formed on the scale described were analysed by TEM, DLS and IR, but at the scale used final masses were insufficient to allow XRD analysis. As is shown below, they are physically of a similar size to APTES@SPION and appear to behave somewhat similarly in solution, but the practical limitations of their use in method development render them undesirable for further study in a bioconjugate context.

The radiolabelled species could not be characterised until sufficiently decayed. Upon return, the particles were visibly aggregated and showed little magnetic response. Characterisation was not performed.

TEM Image Analysis

Samples were prepared, treated and analysed analogously to the APTES-coated particles discussed above. The particles were observed to be approximately spherical, with an average size of 7.6 ± 1.8 nm ($n = 30$). The CMD@SPION are comparable in solid state diameter to

APTES@SPION, although qualitatively they have a greater tendency to aggregate into tightly packed structures during TEM sample preparation. It may be this tendency that prevents the redispersal of precipitated nanoparticles and which limits the usefulness of these particles for the synthesis of magnetically responsive bioconjugate species.

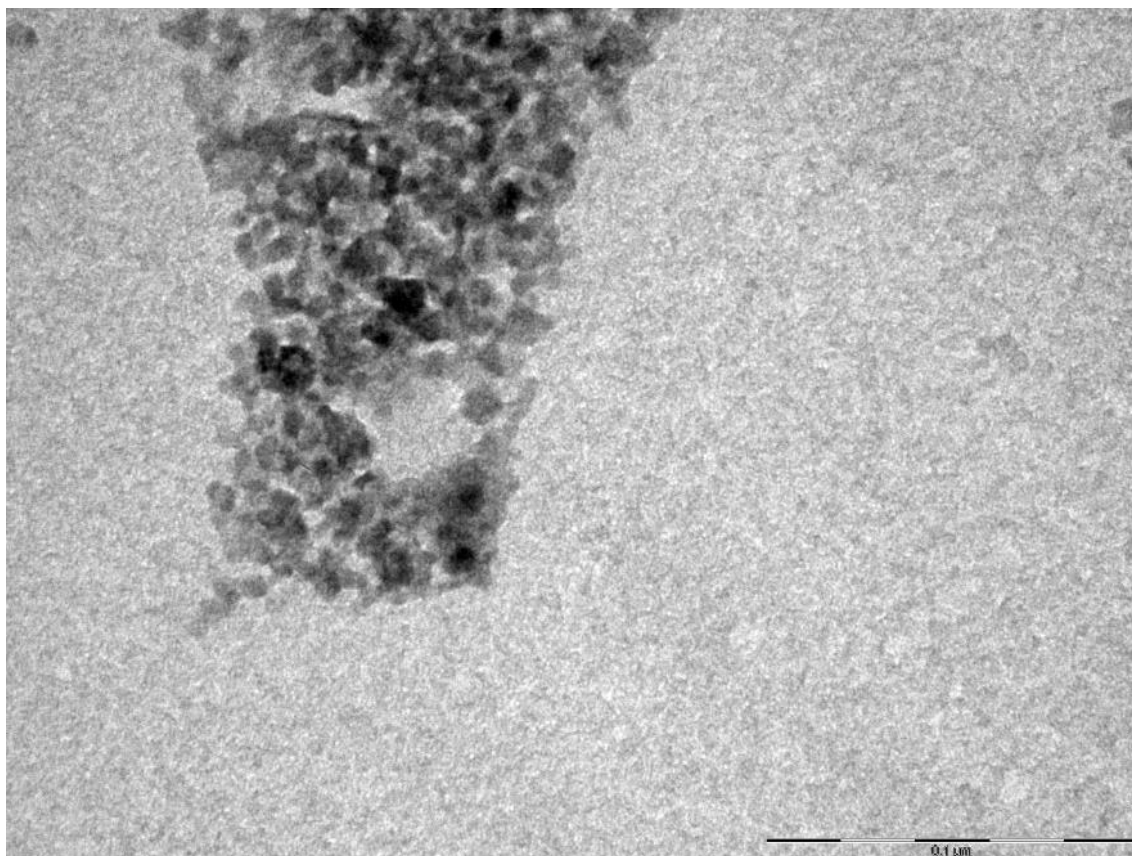


Figure 20. TEM images of CMD@SPION, average size = 7.6 ± 1.8 nm. Scale bar corresponds to 100 nm.

Dynamic Light Scattering analysis

Because a known mass of CMD@SPION could not be dissolved to a known concentration due to the difficulty of redispersing precipitated particles, aqueous samples were prepared by dilution to an estimated concentration of $0.1 \text{ mg}\cdot\text{mL}^{-1}$ based on expected yields and analysed by DLS at $25 \text{ }^\circ\text{C}$. As was observed for APTES@SPION, all samples had hydrodynamic radii much greater than the particle diameter determined from TEM image analysis (typically values are between approximately 140 and 190 nm) and for a given sample analysed multiple times the standard error was typically greater than APTES@SPION. Given the sensitivity of DLS to environmental conditions it is difficult to draw any conclusions from this data other than the seemingly reproducible behaviour in solution of nanoparticles prepared as similarly as possible.

CMD@SPION Sample No.	Hydrodynamic diameter \pm S.E. / nm ($n = 3$)	Half width \pm S.E. / nm	Polydispersity
1	141.3 \pm 5.8	71.4 \pm 1.5	0.257
2	138.2 \pm 3.4	68.2 \pm 0.6	0.245
3	188.1 \pm 3.4	96.6 \pm 0.6	0.264

Table 6. DLS data for CMD@SPION. It is likely that these values reflect aggregate species and not truly colloidal stabilised dispersions.

IR Spectroscopy

The IR spectra of CMD@SPION is markedly different from that of uncoated magnetite but similar to spectra reported elsewhere in the literature, confirming the *in situ* adsorption of the biopolymer following nanoparticle formation.^{86,87} The broad band between 3589 and 3000 cm^{-1} is indicative of the O-H stretch of the hydroxyl groups of the sugar, while the broadened peak centred at 2920 cm^{-1} is due to CH_2 stretching. The carboxylic acid group would be expected to give absorbance around 1700 cm^{-1} but this was not seen, probably due to their relatively low quantity relative to other functional groups. The two absorbances at 1593 and 1415 cm^{-1} are due to CH_2 bending forms, while the most prominent peak centred around 1002 cm^{-1} is due to the C-O stretch of the sugar ether groups.⁸⁷

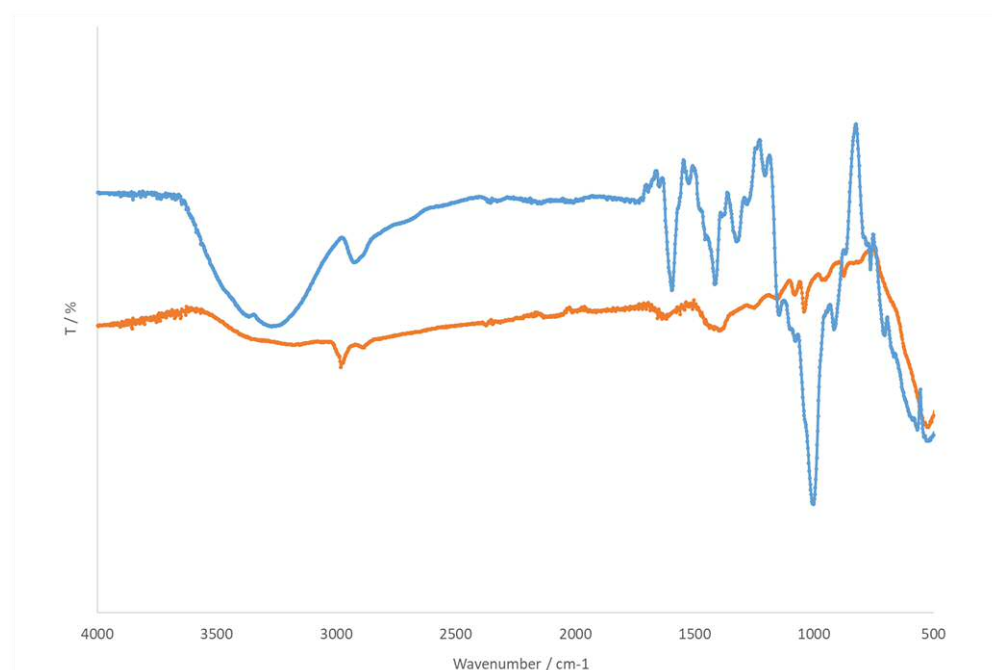


Figure 21. IR spectra of CMD@SPION (blue) and uncoated SPION prepared by co-precipitation (orange).

2.3.4 Summary for CMD@SPION and ⁸⁹Zr-CMD@SPION

The synthesis of CMD@SPION had several practical advantages over the synthesis of the amine-functionalised APTES@SPION. However, the physical characteristics and behaviour of the end particles rendered them less attractive for use as a foundation upon which to design bioconjugate species. Further research could find a use for these particles; for example, incorporating a second coating layer on top of the CMD layer may aid the stability of these particles and give them preferable surface characteristics while retaining the relative ease and efficiency with which radiolabelled particles can be synthesised.

2.3.5 Synthesis, dispersion and relaxometry studies of OA@SPION

Oleic acid coated SPION were synthesised from [Fe(acac)₃] via the highly cited method described by Sun *et al.*²³ The hydrophobic particles were characterised by TEM image analysis to have an average diameter of 4.3 ± 0.4 nm and can be seen to not form large aggregate 'islands' as observed for APTES- and CMD-coated particles.

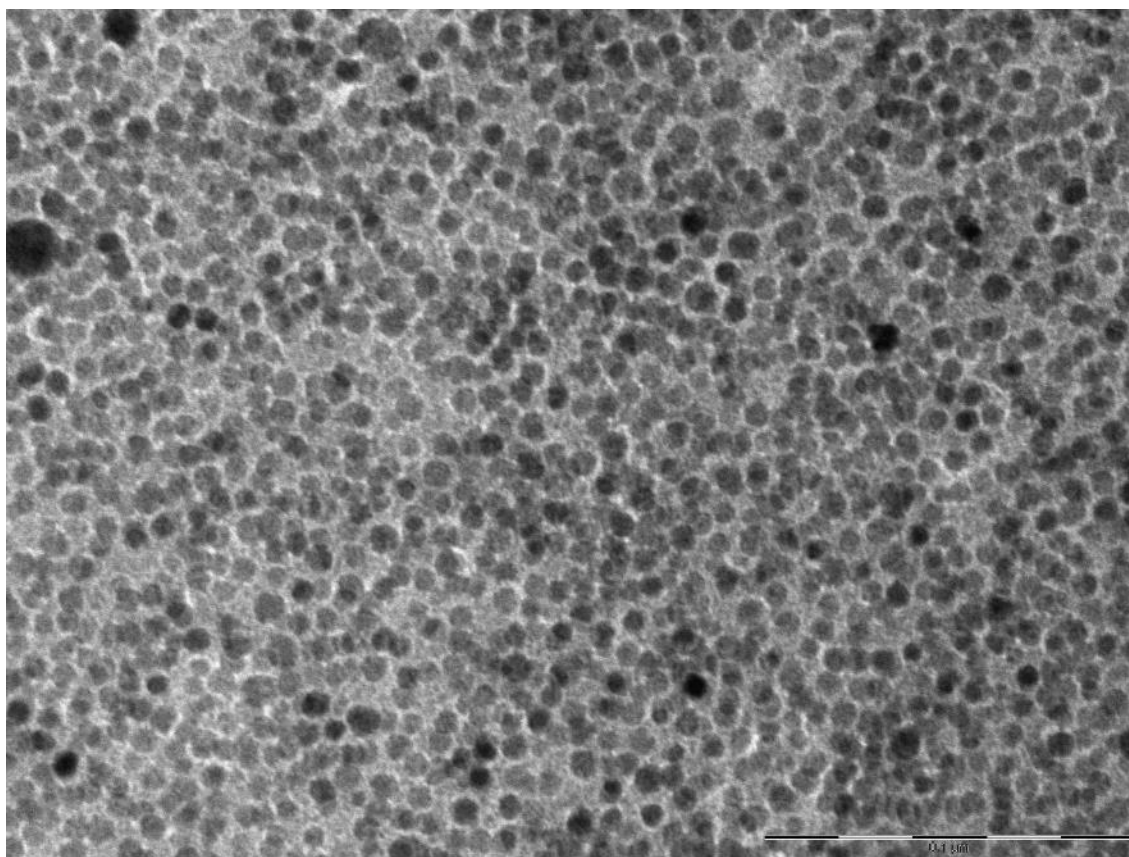


Figure 22. TEM images of OA@SPION, average size = 4.3 ± 0.4 nm. Scale bar corresponds to 100 nm.

As part of the current work, several common non-ionic surfactant species were investigated to assess their ability to render hydrophobic OA@SPION dispersible in water to give a monodisperse species that could form a basis for bioconjugation or for a drug delivery system. All of the species (shown in Fig. 23) were commercially available and used without further purification.

Complete solubilisation of OA@SPION was observed with Brij[®]-35, Brij[®]-96 and Tween[®] 20. Brij[®] and Tween[®] species have low toxicity and have been studied in a drug-delivery context previously.⁸⁸ The dispersions were stable over 72 h. DLS analysis did not yield useful data, possibly because the species in solution were not aggregating and the spectrometer used could not analyse the monomeric species due to the limits of detection. The dispersions were studied by relaxometry to provide evidence of the solubilisation of OA@SPION and to assess the relaxivity of the particles.

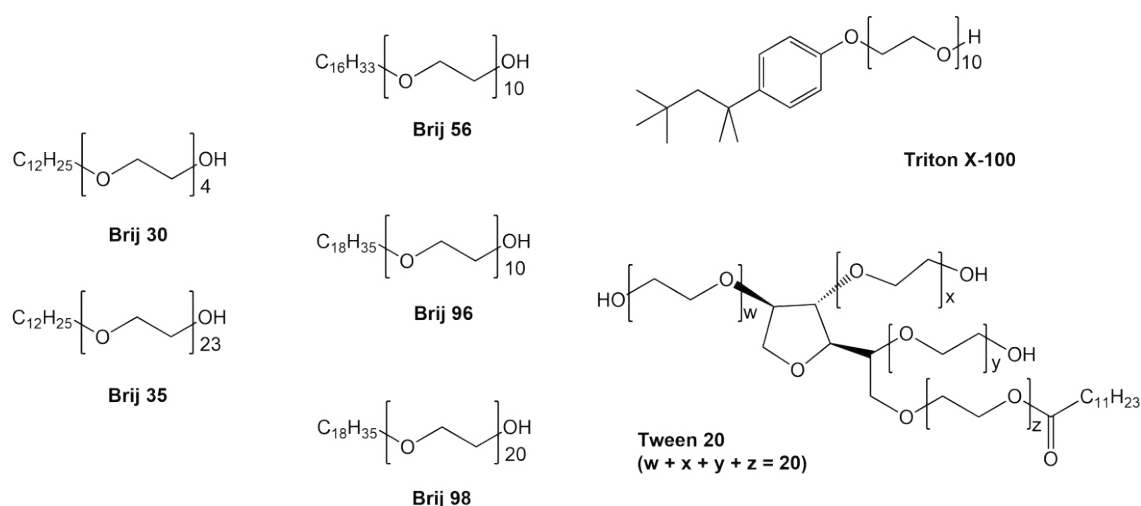


Figure 23. Non-ionic surfactants studied as part of OA@SPION solubilisation experiments. Complete solubilisation occurred with Brij[®]-35, Brij[®]-96 and Tween[®]-20.

All of the surfactant species consist of a hydrophobic tail and a polar head group. As the ether layer evaporates, OA@SPION becomes concentrated and the formation of emulsion droplets by sonication allows for the insertion of the surfactant alkyl chains into the hydrophobic coating of the nanoparticles. Comparing the surfactant species it would be expected that when the hydrophobic tail groups are common (as between Brij[®]-30 and Brij[®]-35), the more efficient surfactant will have the more polar head group. Under the conditions trialled, the remaining surfactants (Brij[®]-30, Brij[®]-56, Brij[®]-98 and Triton[™]-X-100) did not solubilise OA@SPION completely and did not allow for the accurate measuring of relaxivity values for a known mass of particles (hence molar relaxivity). Further experiments could

optimise the approach taken to find the conditions under which these species may solubilise OA@SPION.

The NMRD profiles below show that when experimental temperature increases, the measured maximum value of R_1 for a sample decreases as temperature influences the rate of diffusion within the sample, which limits the ability of a contrast agent to slow molecular tumbling.⁸⁹ As the quantity of iron oxide present in the samples is identical, and the particles present were taken from the same initial stock, differences in the shown NMRD profiles (Fig. 24-26) arise as a result of how solubilisation using the different surfactants affects the efficiency with which the nanoparticles increase relaxation rates. In each studied dispersion of 2 mL volume, 10 mg of OA@SPION were dispersed; reported analysis of similar particles allow an estimation of inorganic content of 70 % such that in each sample 7 mg of Fe_3O_4 , corresponding to 9×10^{-2} mmol of Fe is present.⁹⁰ The concentration of Fe is therefore 45.3 mmol.L⁻¹, and the values of r_1 (the molar relaxivity) in Table 7 can be calculated according to the equation:

Where c is the concentration of the contrast agent (here the iron within the nanoparticles).

Surfactant used ([Fe] / mmol.L ⁻¹)	$r_1 \pm \text{error} / \text{L.mmol}^{-1}.\text{s}^{-1}$ (T = 25 °C, B = 10 MHz)	$r_1 \pm \text{error} / \text{L.mmol}^{-1}.\text{s}^{-1}$ (T = 37 °C, B = 10 MHz)
Brij [®] -35 (45.3)	5.18 ± 0.13	4.82 ± 0.03
Brij [®] -96 (45.3)	7.02 ± 0.10	6.61 ± 0.03
Tween [®] 20 (45.3)	4.82 ± 0.03	4.49 ± 0.03
Commercial species	$r_1 \pm \text{error} / \text{L.mmol}^{-1}.\text{s}^{-1}$ (T = 37 °C, B = 20 MHz)	
Feridex [®]	4.7 ± 0.30	
Resovist [®]	8.7 ± 0.50	

Table 7. Calculated values of r_1 at 10 MHz for OA@SPION solubilised using commercially available non-ionic surfactants. Relaxivity values for commercially available SPION-based species are shown for comparison.⁹¹

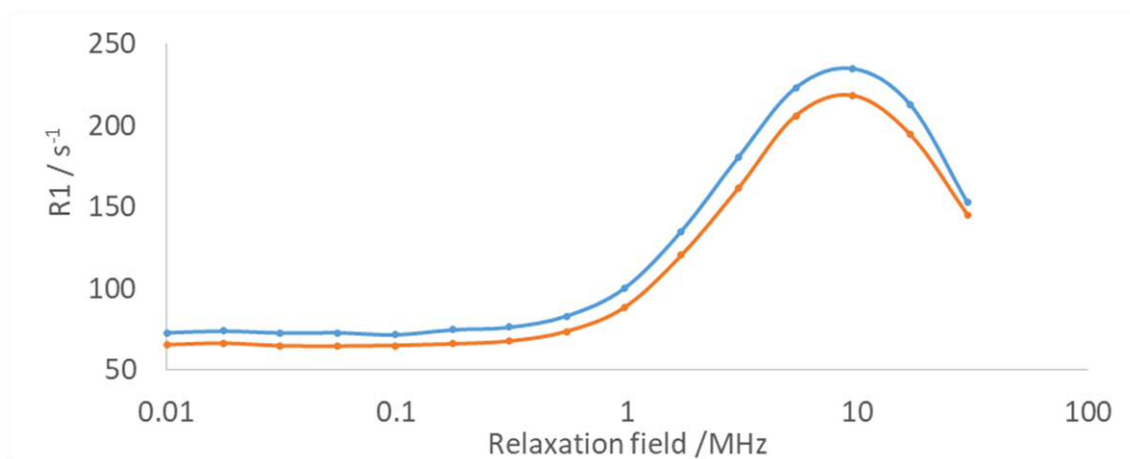


Figure 24. NMRD profiles of Brij 35-solubilised OA@SPION in water (5 mg.mL^{-1}) at 25 °C (blue) and 37 °C (orange).

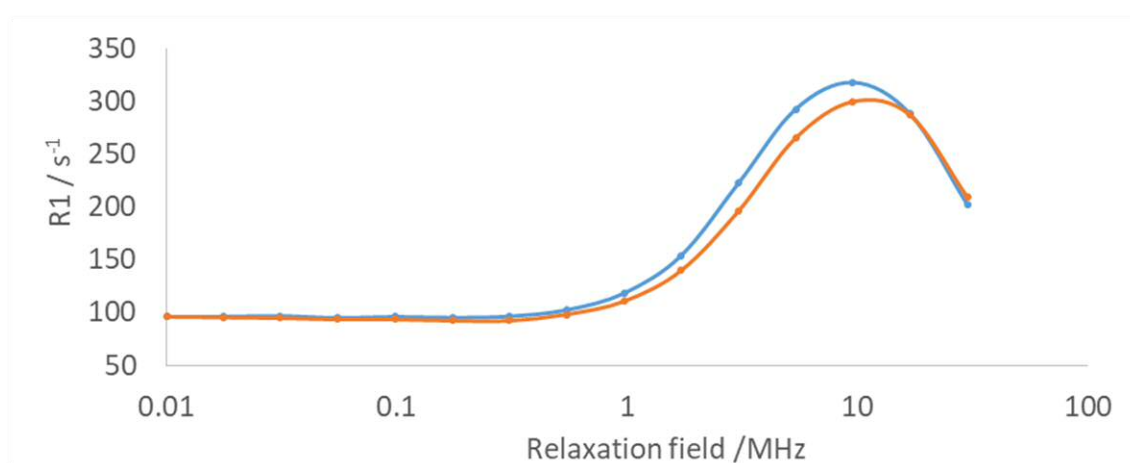


Figure 25. NMRD profiles of Brij 96-solubilised OA@SPION in water (5 mg.mL^{-1}) at 25 °C (blue) and 37 °C (orange).

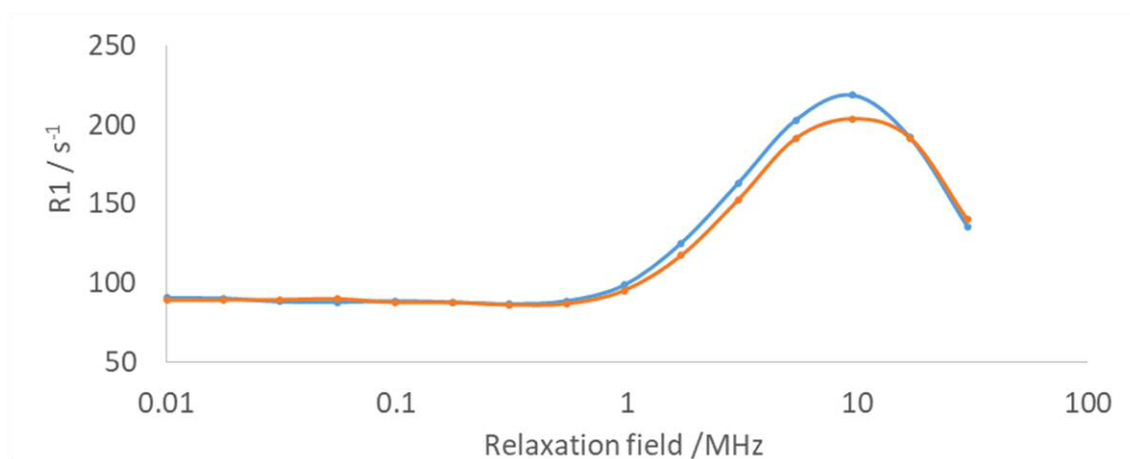


Figure 26. NMRD profiles of Tween-20-solubilised OA@SPION in water (5 mg.mL^{-1}) at 25 °C (blue) and 37 °C (orange).

The calculated relaxivity values compare favourably to values for commercial SPION-based contrast agents under similar conditions (Table 7).⁹¹ Further experiments could be performed to further optimise stability of the dispersion, to investigate methods of enhancing relaxivity further and to explore how values of r_1 for such species would change *in vivo*. In terms of drug delivery, the ability of dispersed particles to respond to an oscillating magnetic field as used in therapeutic hyperthermia would be of great interest. From a bioconjugation perspective, OA@SPION solubilised by surfactant materials do not make for an immediately attractive foundation species, especially when considering the possibility of radiolabelling.

2.4 Conclusion

Three methods of preparing water-dispersible SPION have been discussed in the above pages. Thermal decomposition of an organometallic precursor yields monodisperse hydrophobic particles that can be solubilised in water by use of surfactant species but the methodology is not transferrable to a hot cell. SPION can be coated *in situ* with CMD to yield highly water soluble species and the technique can be readily modified to enable radiolabelling, but the product particles are not suitable for further bioconjugation experiments because they cannot be manipulated with accuracy. SPION coated with APTES are water dispersible, have a desirable surface functionality for bioconjugation, can be manipulated post-synthesis easily, can be radiolabelled with high efficiency and the synthetic approach can be deemed to be highly reproducible and transferrable to hot cells with minimal risk to the researcher. APTES@SPION synthesised in the manner described above appears to be an ideal candidate for further study in the design and development of bioconjugated, radiolabelled nanoparticles.

2.5 References

- 1 R. Massart, *IEEE Trans. Magn.*, 1981, **17**, 1247–1248.
- 2 S. Laurent, D. Forge, M. Port, A. Roch, C. Robic, L. Vander Elst and R. N. Muller, *Chem. Rev.*, 2008, **108**, 2064–2110.
- 3 S. Laurent, L. V. Elst and R. N. Muller, in *The Chemistry of Contrast Agents in Medical Magnetic Resonance Imaging*, eds. A. Merbach, L. Helm and É. Tóth, John Wiley & Sons, Ltd, 2013, pp. 427–447.
- 4 M. Mahmoudi, S. Sant, B. Wang, S. Laurent and T. Sen, *Adv. Drug Deliv. Rev.*, 2011, **63**, 24–46.
- 5 L. H. Reddy, J. L. Arias, J. Nicolas and P. Couvreur, *Chem. Rev.*, 2012, **112**, 5818–5878.
- 6 S. Sharifi, H. Seyednejad, S. Laurent, F. Atyabi, A. A. Saei and M. Mahmoudi, *Contrast Media Mol. Imaging*, 2015, **10**, 329–355.
- 7 J. R. McCarthy and R. Weissleder, *Adv. Drug Deliv. Rev.*, 2008, **60**, 1241–1251.
- 8 A. K. Gupta and M. Gupta, *Biomaterials*, 2005, **26**, 3995–4021.
- 9 H. Lee, T.-H. Shin, J. Cheon and R. Weissleder, *Chem. Rev.*, 2015, **115**, 10690–10724.
- 10 W. Wu, Z. Wu, T. Yu, C. Jiang and W.-S. Kim, *Sci. Technol. Adv. Mater.*, 2015, **16**, 023501.
- 11 A. F. Orchard, *Magnetochemistry*, Oxford University Press, U.S.A., Oxford ; New York, 2003.
- 12 Y. Gossuin, P. Gillis, A. Hocq, Q. L. Vuong and A. Roch, *Wiley Interdiscip. Rev. Nanomed. Nanobiotechnol.*, 2009, **1**, 299–310.
- 13 R. Kimmich and E. Anoardo, *Prog. Nucl. Magn. Reson. Spectrosc.*, 2004, **44**, 257–320.
- 14 A. S. Teja and P.-Y. Koh, *Prog. Cryst. Growth Charact. Mater.*, 2009, **55**, 22–45.
- 15 J. Baumgartner, A. Dey, P. H. H. Bomans, C. Le Coadou, P. Fratzl, N. A. J. M. Sommerdijk and D. Faivre, *Nat. Mater.*, 2013, **12**, 310–314.
- 16 V. K. LaMer and R. H. Dinegar, *J. Am. Chem. Soc.*, 1950, **72**, 4847–4854.
- 17 R. Massart, E. Dubois, V. Cabuil and E. Hasmonay, *J. Magn. Magn. Mater.*, 1995, **149**, 1–5.
- 18 A. Bee, R. Massart and S. Neveu, *J. Magn. Magn. Mater.*, 1995, **149**, 6–9.
- 19 M. H. El-Dakdouki, K. El-Boubbou, J. Xia, H. Kavunja and X. Huang, in *Chemistry of Bioconjugates*, ed. R. Narain, John Wiley & Sons, Inc., 2014, pp. 281–314.
- 20 Fallis Group, unpublished work .
- 21 U. Schwertmann and R. M. Cornell, *Iron Oxides in the Laboratory: Preparation and Characterization*, Wiley VCH, Weinheim ; New York, 2nd edition., 2000.
- 22 J. Park, K. An, Y. Hwang, J.-G. Park, H.-J. Noh, J.-Y. Kim, J.-H. Park, N.-M. Hwang and T. Hyeon, *Nat. Mater.*, 2004, **3**, 891–895.
- 23 S. Sun, H. Zeng, D. B. Robinson, S. Raoux, P. M. Rice, S. X. Wang and G. Li, *J. Am. Chem. Soc.*, 2004, **126**, 273–279.
- 24 T. Hyeon, S. S. Lee, J. Park, Y. Chung and H. B. Na, *J. Am. Chem. Soc.*, 2001, **123**, 12798–12801.
- 25 N. Pinna, S. Grancharov, P. Beato, P. Bonville, M. Antonietti and M. Niederberger, *Chem. Mater.*, 2005, **17**, 3044–3049.
- 26 S. Sato, T. Murakata, H. Yanagi, F. Miyasaka and S. Iwaya, *J. Mater. Sci.*, 1994, **29**, 5657–5663.
- 27 L. Durães, B. F. O. Costa, J. Vasques, J. Campos and A. Portugal, *Mater. Lett.*, 2005, **59**, 859–863.
- 28 Z. Dai, F. Meiser and H. Möhwald, *J. Colloid Interface Sci.*, 2005, **288**, 298–300.
- 29 A. Zarepour, A. Zarrabi and A. Khosravi, *SPIONs as Nano-Theranostics Agents*, Springer Singapore, 2017.
- 30 G. Salazar-Alvarez, M. Muhammed and A. A. Zagorodni, *Chem. Eng. Sci.*, 2006, **61**, 4625–4633.
- 31 D. Liu, A. M. Pourrahimi, L. K. H. Pallon, R. L. Andersson, M. S. Hedenqvist, U. W. Gedde and R. T. Olsson, *RSC Adv.*, 2015, **5**, 48094–48103.

- 32 V. Ström, R. T. Olsson and K. V. Rao, *J. Mater. Chem.*, 2010, **20**, 4168–4175.
- 33 M. Fang, V. Ström, R. T. Olsson, L. Belova and K. V. Rao, *Nanotechnology*, 2012, **23**, 145601.
- 34 M. Fang, V. Ström, R. T. Olsson, L. Belova and K. V. Rao, *Appl. Phys. Lett.*, 2011, **99**, 222501.
- 35 P. Majewski and B. Thierry, *Crit. Rev. Solid State Mater. Sci.*, 2007, **32**, 203–215.
- 36 Y.-X. J. Wang, *Quant. Imaging Med. Surg.*, 2011, **1**, 35–40.
- 37 F. Bertorelle, C. Wilhelm, J. Roger, F. Gazeau, C. Ménager and V. Cabuil, *Langmuir*, 2006, **22**, 5385–5391.
- 38 Fauconnier, Pons, Roger and Bee, *J. Colloid Interface Sci.*, 1997, **194**, 427–433.
- 39 R. S. Molday and D. MacKenzie, *J. Immunol. Methods*, 1982, **52**, 353–367.
- 40 F. Yu and V. C. Yang, *J. Biomed. Mater. Res. A*, 2010, **92**, 1468–1475.
- 41 M. Mahmoudi, A. Simchi, A. S. Milani and P. Stroeve, *J. Colloid Interface Sci.*, 2009, **336**, 510–518.
- 42 M. Mahmoudi, A. Simchi, M. Imani, M. A. Shokrgozard, A. S. Milani, U. O. Haefeli and P. Stroeve, *Colloids Surf. B-Biointerfaces*, 2010, **75**, 300–309.
- 43 S. H. Im, T. Herricks, Y. T. Lee and Y. Xia, *Chem. Phys. Lett.*, 2005, **401**, 19–23.
- 44 B. K. Sodipo and A. A. Aziz, *J. Magn. Magn. Mater.*, 2016, **416**, 275–291.
- 45 M. Yamaura, R. L. Camilo, L. C. Sampaio, M. A. Macêdo, M. Nakamura and H. E. Toma, *J. Magn. Magn. Mater.*, 2004, **279**, 210–217.
- 46 M. P. Cude and C. D. Gwenin, *ECS Trans.*, 2011, **33**, 79–89.
- 47 S. K. Vashist, E. Lam, S. Hrapovic, K. B. Male and J. H. T. Luong, *Chem. Rev.*, 2014, **114**, 11083–11130.
- 48 G. T. Hermanson, *Bioconjugate Techniques*, Academic Press, London ; Waltham, MA, 3rd edition., 2013.
- 49 C. K. Dixit, S. K. Vashist, B. D. MacCraith and R. O’Kennedy, *Nat. Protoc.*, 2011, **6**, 439–445.
- 50 E. Asenath Smith and W. Chen, *Langmuir*, 2008, **24**, 12405–12409.
- 51 A. C. A. Roque, A. Bicho, I. L. Batalha, A. S. Cardoso and A. Hussain, *J. Biotechnol.*, 2009, **144**, 313–320.
- 52 Y. Liu, Y. Li, X.-M. Li and T. He, *Langmuir*, 2013, **29**, 15275–15282.
- 53 I. J. Bruce and T. Sen, *Langmuir*, 2005, **21**, 7029–7035.
- 54 S. H. North, E. H. Lock, C. J. Cooper, J. B. Franek, C. R. Taitt and S. G. Walton, *ACS Appl. Mater. Interfaces*, 2010, **2**, 2884–2891.
- 55 J. Joo, D. Kwon, H. H. Shin, K.-H. Park, H. J. Cha and S. Jeon, *Sens. Actuators B Chem.*, 2013, **188**, 1250–1254.
- 56 Y.-X. J. Wang, S. M. Hussain and G. P. Krestin, *Eur. Radiol.*, 2001, **11**, 2319–2331.
- 57 S. Wilhelm, A. J. Tavares, Q. Dai, S. Ohta, J. Audet, H. F. Dvorak and W. C. W. Chan, *Nat. Rev. Mater.*, 2016, **1**, 1–12.
- 58 M. Edmundson, N. T. Thanh and B. Song, *Theranostics*, 2013, **3**, 573–582.
- 59 Y. Z. Wadghiri, E. M. Sigurdsson, M. Sadowski, J. I. Elliott, Y. Li, H. Scholtzova, C. Y. Tang, G. Aguinaldo, M. Pappolla, K. Duff, T. Wisniewski and D. H. Turnbull, *Magn. Reson. Med.*, 2003, **50**, 293–302.
- 60 L. O. Sillerud, N. O. Solberg, R. Chamberlain, R. A. Orlando, J. E. Heidrich, D. C. Brown, C. I. Brady, T. A. Vander Jagt, M. Garwood and D. L. Vander Jagt, *J. Alzheimers Dis. JAD*, 2013, **34**, 349–365.
- 61 H. Jung, M. I. Kettunen, B. Davletov and K. M. Brindle, *Bioconjug. Chem.*, 2004, **15**, 983–987.
- 62 I. Hilger, R. Trost, J. R. Reichenbach, W. Linß, M.-R. Lisy, A. Berndt and W. A. Kaiser, *Nanotechnology*, 2007, **18**, 135103.
- 63 M. Suzuki, M. Shinkai, M. Kamihira and T. Kobayashi, *Biotechnol. Appl. Biochem.*, 1995, **21**, 335–345.

- 64 K. Ulbrich, K. Holá, V. Šubr, A. Bakandritsos, J. Tuček and R. Zbořil, *Chem. Rev.*, 2016, **116**, 5338–5431.
- 65 P. F. de Châtel, I. Nándori, J. Hakl, S. Mészáros and K. Vad, *J. Phys. Condens. Matter*, 2009, **21**, 124202.
- 66 J.-P. Fortin, F. Gazeau and C. Wilhelm, *Eur. Biophys. J. EBJ*, 2008, **37**, 223–228.
- 67 A. B. Salunkhe, V. M. Khot and S. H. Pawar, *Curr. Top. Med. Chem.*, 2014, **14**, 572–594.
- 68 I. M. Obaidat, B. Issa and Y. Haik, *Nanomater. Basel Switz.*, 2015, **5**, 63–89.
- 69 Y. C. Sharma, V. Srivastava, V. K. Singh, S. N. Kaul and C. H. Weng, *Environ. Technol.*, 2009, **30**, 583–609.
- 70 F. Chen, P. A. Ellison, C. M. Lewis, H. Hong, Y. Zhang, S. Shi, R. Hernandez, M. E. Meyerand, T. E. Barnhart and W. Cai, *Angew. Chem. Int. Ed.*, 2013, **52**, 13319–13323.
- 71 R. Chakravarty, H. F. Valdovinos, F. Chen, C. M. Lewis, P. A. Ellison, H. Luo, M. E. Meyerand, R. J. Nickles and W. Cai, *Adv. Mater.*, 2014, **26**, 5119–5123.
- 72 F. Chen, S. Goel, H. F. Valdovinos, H. Luo, R. Hernandez, T. E. Barnhart and W. Cai, *ACS Nano*, 2015, **9**, 7950–7959.
- 73 'Transmission Electron Microscopy (TEM)', <https://www.nottingham.ac.uk/isac/facilities/tem.aspx>, (accessed 17 August 2017).
- 74 'Gold Colloid', <https://nanocomposix.com/pages/gold-colloid>, (accessed 17 August 2017).
- 75 'ImageJ', <https://imagej.nih.gov/ij/index.html>, (accessed 17 August 2017).
- 76 B. Ingham, *Crystallogr. Rev.*, 2015, **21**, 229–303.
- 77 R. M. Cornell and U. Schwertmann, *The Iron Oxides: Structure, Properties, Reactions, Occurrences and Uses*, John Wiley & Sons, Hoboken, NJ, 2006.
- 78 W. I. Goldberg, *Am. J. Phys.*, 1999, **67**, 1152–1160.
- 79 'Dynamic Light Scattering for Nanoparticle Size Analysis', <http://www.horiba.com/scientific/products/particle-characterization/technology/dynamic-light-scattering/>, (accessed 17 August 2017).
- 80 'Dynamic light scattering - common terms defined', <https://www.malvern.com/en/support/resource-center/Whitepapers/WP111214DLSTermsDefined>, (accessed 17 August 2017).
- 81 J. Huang, Y. Li, A. Orza, Q. Lu, P. Guo, L. Wang, L. Yang and H. Mao, *Adv. Funct. Mater.*, 2016, **26**, 3818–3836.
- 82 H. Pardoe, W. Chua-anusorn, T. G. St. Pierre and J. Dobson, *J. Magn. Magn. Mater.*, 2001, **225**, 41–46.
- 83 P. C. Burns, F. C. Hawthorne, E. Libowitzky, N. Bordes and R. C. Ewing, *Neues Jahrb. Mineral.-Monatshefte*, 1997, 163–174.
- 84 W. M. Haynes, Ed., *CRC Handbook of Chemistry and Physics*, CRC Press, Boca Raton; London; New York, 95th edition., 2014.
- 85 B. Chen, W. Le, Y. Wang, Z. Li, D. Wang, L. Ren, L. Lin, S. Cui, J. J. Hu, Y. Hu, P. Yang, R. C. Ewing, D. Shi and Z. Cui, *Theranostics*, 2016, **6**, 1887–1898.
- 86 M. Khalkhali, K. Rostamizadeh, S. Sadighian, F. Khoeini, M. Naghibi and M. Hamidi, *DARU J. Pharm. Sci.*, 2015, **23**, 45.
- 87 G.-C. Han, Y. Ouyang, X.-Y. Long, Y. Zhou, M. Li, Y.-N. Liu and H.-B. Kraatz, *Eur. J. Inorg. Chem.*, 2010, **2010**, 5455–5461.
- 88 I. Ullah, M. K. Baloch and G. F. Durrani, *J. Solut. Chem.*, 2011, **40**, 1341.
- 89 R. B. Lauffer, *Chem. Rev.*, 1987, **87**, 901–927.
- 90 J. Salado, M. Insausti, L. Lezama, I. Gil de Muro, E. Goikolea and T. Rojo, *Chem. Mater.*, 2011, **23**, 2879–2885.
- 91 M. Rohrer, H. Bauer, J. Mintorovitch, M. Requardt and H.-J. Weinmann, *Invest. Radiol.*, 2005, **40**, 715–724.

Chapter 3: Bioconjugation of enzymes and antibodies with APTES@SPION

3.1 Introduction

In this chapter, different approaches to the immobilisation of biomolecules (enzymes, antibodies and conjugates thereof) on APTES@SPION synthesised as described in Chapter 2 will be discussed.

Bioconjugation is the attachment of one molecule to another, typically through covalent bond formation, where at least one molecule is a biomolecule e.g. an enzyme or antibody.¹ The other may be a second biomolecule,² a small molecule that imbues a particular functionality on the product conjugate,³ or a surface (referred to as ‘immobilisation’, even when the surface in question is a mobile nanoparticle).^{4,5} Linking is often achieved via crosslinking agents that react in reliable ways to particular functionalities present in the molecules to be conjugated. The field of bioconjugation is dominated by a relatively limited number of reactive groups and approaches to achieve linking which are discussed below.

A crucial consideration in the synthesis of a nanoparticle agent incorporating a monoclonal antibody is the effect of immobilisation; the product must retain the function of its parent species and antibodies, as proteins, are susceptible to denaturation.⁶ Changes to their tertiary structures, specifically in their antigen binding sites, will limit or remove their ability to selectively bind their target. Any immobilisation reaction used must be shown to not have an excessively deleterious effect on the antibody’s function. The heterogeneous nature of nanoparticles in general and the UV-Vis absorption profile of SPION in particular render many common methods of interrogating protein structure unusable. The inclusion of a dye would serve to locate the antibody but would give no information on its condition,⁷ and the use of cell line studies is arguably inappropriate as an initial method of characterisation.

In chemical biology the actions and activities of enzymes are often followed spectroscopically. A colorimetric assay can give kinetic data which may be related back to known standards, giving an indication of the environment or condition of an enzyme.^{8,9} While enzymes are not perfect models, they may be susceptible to the same conditions that can cause denaturation in antibodies. It was hypothesised that a method developed to immobilise enzymes onto SPION with limited effect on function could be transferred to achieve the immobilisation of antibodies in a similar way.

3.1.1 The reactions of bioconjugation

In 'Bioconjugate Techniques' by Greg Hermanson, to which the reader is directed for a thorough introduction to the theory and typical protocols of bioconjugation, it is stated that there are less than ten reactive groups used commonly in the construction of the majority of bioconjugates.¹ Although there are hundreds of commercially available crosslinkers, the novelty of their design is in their physical properties (e.g. solubility, stability to different conditions, linker length) not their targeted functionalities.

The functional groups that underpin most bioconjugate syntheses are amines, thiols, carboxylic acids, hydroxyls, aldehydes and ketones.^{1,2} All are commonly found in peptides, proteins, carbohydrates and nucleic acids or can be relatively easily introduced without detriment to the molecule's function. Examples of how these groups typically react are shown below.

Amine reactions

Nearly all biomolecules will have at least one reactive amine residue available for reaction. As an example, the Fab region of cetuximab has been shown to have 23 amine-bearing lysine residues in its primary structure, including a single lysine in the antigen binding region.¹¹ Because amines are common, reactive groups sensitive to them (e.g. isothiocyanates, succinimidyl esters) are the most common functionalities incorporated into cross linkers. Amines typically couple rapidly via alkylation or acylation, giving secondary amines or amides (Fig. 1a).

Thiol reactions

Thiol-sensitive reactive groups are the second most common functionalities seen in crosslinkers.¹ Thiols typically react via alkylation or disulphide interchange, often in a two-step process. The thioether and disulphide bonds that result from these reactions are stable (Fig. 1b).

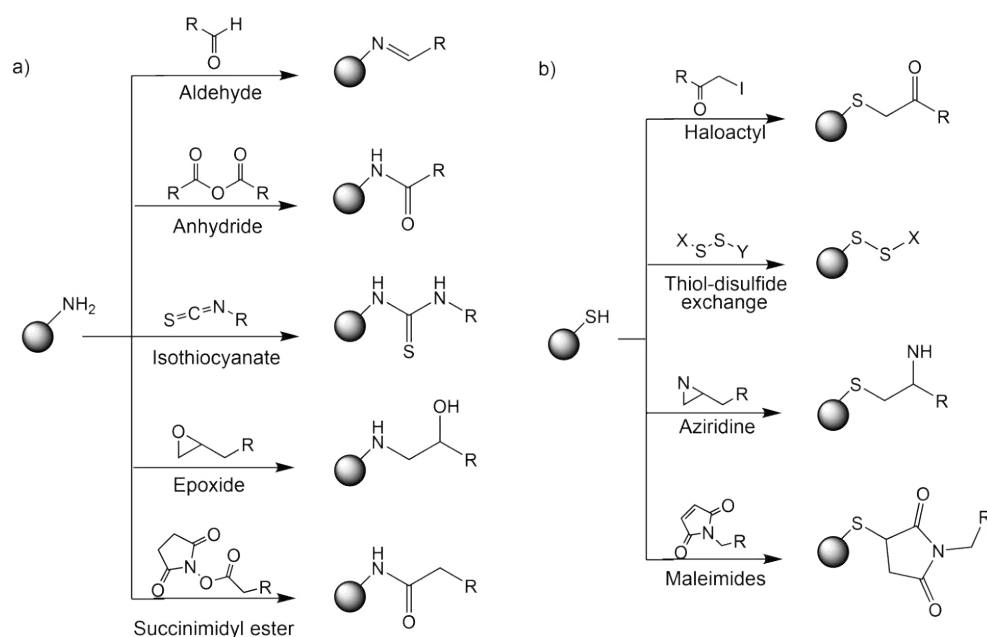


Figure 1. Selected typical (a) amine and (b) thiol reactions for bioconjugation.

Carboxylic acid reactions

Carboxylate groups in aqueous solution are relatively poor targets for nucleophiles. Their use in bioconjugation is dominated by the need to activate them and enhance their reactivity to nucleophiles. Carbodiimides are commonly used to facilitate amine-to-acid linking (Fig. 2), although other species are available.¹ They can be used on their own or to produce active ester groups (e.g. with N-hydroxysuccinimide), yielding an intermediate with increased stability to hydrolysis and enhancing reactivity against amines.

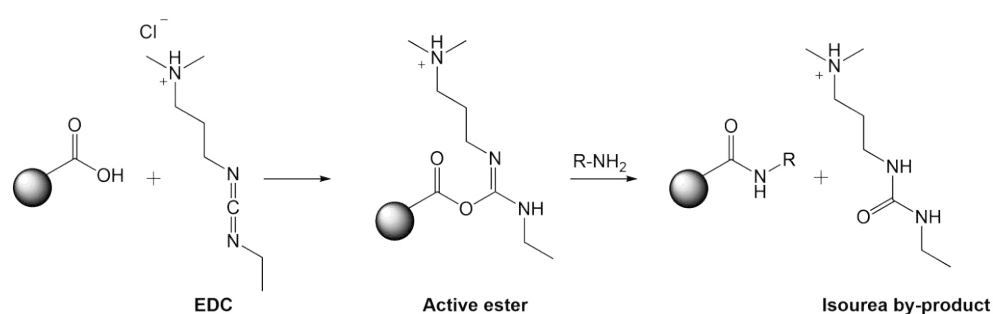


Figure 2. Structural mechanism for amine-to-acid linking facilitated by carbodiimides. Although EDC is shown here, the mechanism is general to all such species.

Hydroxyl-reactive species are available not only for direct reaction with hydroxyls but also for the activation of the group to a more reactive form e.g. aldehydes or ketones. These groups are not commonly found in native proteins or biomolecules but are often introduced deliberately to achieve a desired linkage. Of most relevance to the current work is the ability to oxidise a hydroxyl group of a biomolecule (e.g. a sugar or sugar side chain) to give aldehyde functionalities that can react with amines (Fig. 3a). The Schiff base formed may be reduced to a secondary amine to stabilise the linkage, a protocol described as reductive amination (Fig. 3b).¹

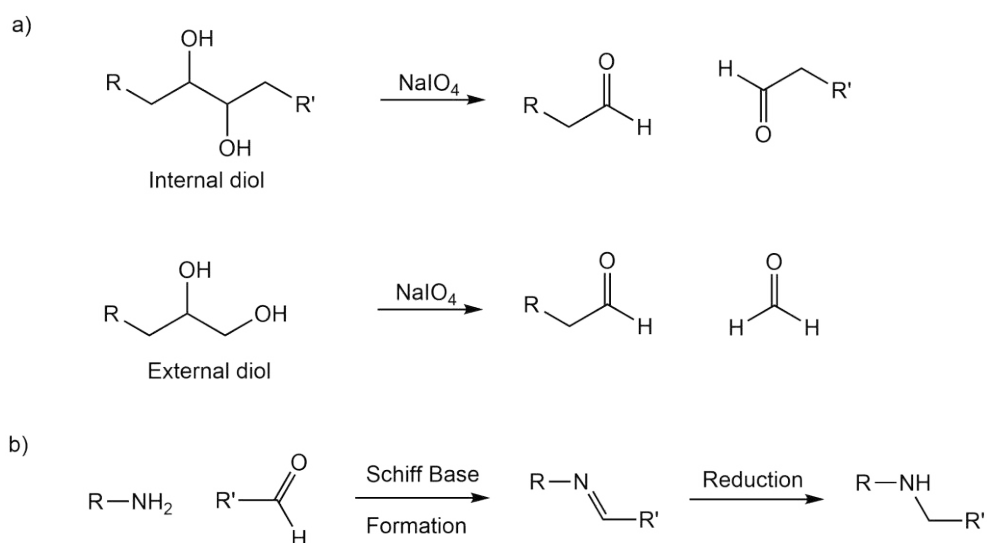


Figure 3a. Depending on the nature of the diol, oxidation with sodium periodate can yield different results. **b.** Reduction of the Schiff base formed by reaction between aldehydes and amines is necessary to prevent hydrolysis in aqueous conditions.

Reductive amination has been a popular method for the synthesis of enzyme-antibody conjugates^{12,13} and for immobilising antibodies on nanoparticles.¹⁴ The immobilisation of antibodies on dextran-functionalised nanoparticles has been reported, where the internal diol of the nanoparticles' carbohydrate surface coating is the subject of oxidation.¹⁵

3.1.2 Homo- and heterobifunctional crosslinkers

Bioconjugation almost always uses some form of crosslinking agent. These may form a physical link between the two molecules in the final product or may be used to activate a functionality for reaction. Crosslinkers may be divided broadly into two classes, homobifunctional and heterobifunctional. Homobifunctional species are symmetrical and have two reactive groups designed to react with the same class of target; a classic example

would be glutaraldehyde (Fig. 4a) which is discussed in detail below. While they are inexpensive, the main disadvantage of homobifunctional linkers is the limited control available to the researcher even over multi-step procedures. The result can often be a heterogeneous mixture of poorly defined species.

Heterobifunctional chelators such as SPDP (Fig. 4b) have two reactive ends designed to react with two different functional groups on proteins or macromolecules (e.g. amine-to-thiol crosslinking). The use of heterobifunctional species typically requires multistep reactions and the careful manipulation of reaction conditions but offers greater control and improved reaction outcomes. Correspondingly, they can be very expensive when considering the quantities needed for method development. The most populous group of heterobifunctional crosslinkers are amine-to-thiol species, typically expressing amine reactive active ester groups for amide bond formation and an alkylating agent capable of forming disulphide or thioether bonds.¹ The greater stability of the sulfhydryl-reactive group relative to the amine-reactive ester allows for control over crosslinking.

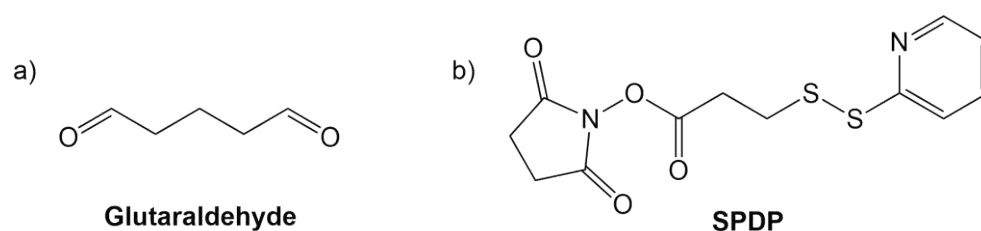


Figure 4a. Glutaraldehyde has two aldehyde groups, and is able to react with two amine groups. **b.** SPDP has an NHS-ester group (amine-reactive) and a 2-pyridyldithiol group (thiol-reactive).

3.1.3 Glutaraldehyde as a crosslinker

Glutaraldehyde has become a work-horse within the field of bioconjugation. Because of its multitude of uses outside of research it is produced on an industrial scale and is inexpensive in large quantities.¹⁶ It is common to find glutaraldehyde used as a crosslinker despite the drawbacks inherent with homobifunctional species and its complex aqueous chemistry; glutaraldehyde exists not just as a monomer but has many possible forms in aqueous solution which can react differently depending on reaction conditions.¹⁶ Glutaraldehyde's reactivity can be difficult to predict or reproduce. In its simplest form, the linear dialdehyde would be expected to react with two amine groups to give Schiff bases. Reduction of the Schiff bases would be required to stabilise them to hydrolysis but this is often not carried out. Rather, it is believed that the glutaraldehyde forms a cyclic hemiacetal at acidic and neutral pH values

which reacts with amines by nucleophilic substitution (see Fig. 5), explaining the increased stability of glutaraldehyde-conjugates over what would be expected in the absence of reduction.^{8, 9} The tendency of glutaraldehyde to polymerise and/or form crosslinked aggregates make it a difficult reagent to control but nevertheless a useful tool with which to commence experiments in bioconjugation.

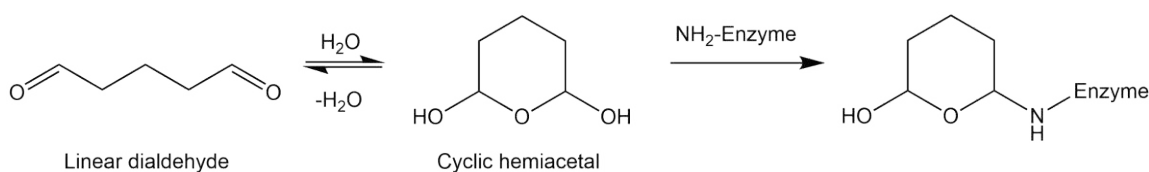


Figure 5. Proposed reaction between cyclic form of glutaraldehyde with amine-containing groups at acidic and neutral pH.¹⁶

3.1.4 Enzymes in bioconjugation

Enzymes are biological catalysts that carry out a range of reactions *in vivo*. While the study of the role and activity of enzymes in living systems has been instrumental in our understanding of biology, enzymes are now routinely used *ex vivo* in biotechnology. One of the most well-known applications is ELISA (enzyme-linked immunosorbent assay), where an enzyme's action on a substrate gives a colorimetric response to indicate the presence of an analyte to which the enzyme has been bound.¹⁸ The two enzymes most commonly used for ELISA are also the most commonly found enzymes in bioconjugate chemistry and are discussed below.

3.1.5 Enzyme structure and mechanism

A brief overview of how enzymes perform their function is necessary to understand how they may be of use to researchers and why care must be taken with experiment design. For further detail, introductory texts abound.¹⁹

Enzymes are proteins, having a primary structure (their amino acid sequence), a secondary structure (regions of local order) and a tertiary structure (a three-dimensional shape arising from how the separate regions interact). A quaternary structure may be present where an enzyme consists of 'subunits' of associated polypeptide chains. The tertiary structure throughout a protein is formed by Van der Waals forces, hydrogen bonding, electrostatics and hydrophobic interactions. Most significantly in the case of enzymes is the inclusion of a region in the 3D structure described as an 'active site' that is near complementary to the shape of a substrate molecule and which can form necessary non-covalent interactions with the substrate.²⁰ The site undergoes conformational change upon binding to give the necessary

specificity for enzymatic catalysis, described as an induced fit. The ability of the active site to change shape explains why enzymes can have multiple substrates with different structures rather than a single exact match. Once bound, the substrate undergoes whichever reaction the enzyme in question catalyses. In the case of metalloenzymes, metals are coordinated within the active site in a deliberately strained (or 'entatic') state with sufficient transferrable energy to essentially preform the transition state of the reaction, achieving efficient catalysis under relatively mild conditions.²¹

The active site can be changed by environmental conditions: changes in pH, temperature, ionic strength or the presence of other chemicals can break the non-covalent interactions giving its shape. This 'denaturing' results in partial or total loss of the enzyme's ability to perform its function. Enzymes have optimum conditions which are typically similar to their natural environment, where activity is maximised due to maintenance of the active site. Catalytic activity can be used as a proxy-measurement for the condition of an enzyme; a significant decrease in catalytic rates from optimal figures when other factors are controlled can signify loss of active site shape.

3.1.6 'Unit', 'specific activity' and issues pertaining to immobilised enzymes

Within enzymology, there are several units of which researchers must be aware. An enzyme 'unit' is defined as the amount of enzyme required to convert 1 μmol of a given substrate to product per minute. While concentration of proteins is typically quoted in milligrams per millilitre ($\text{mg}\cdot\text{mL}^{-1}$), the ratio of the number of units in a sample to its concentration gives $\text{units}\cdot\text{mg}^{-1}$, a quantity known as 'specific activity'. The 'turnover number' is defined as the number of μmoles of substrate converted, per μmole of enzyme, per second.²⁰ It is important to distinguish between the non-specific term 'activity' meaning 'enzyme action in a sample' and the defined quantity 'specific activity'.

In the present work, the protein concentration of dispersions of enzyme-functionalised nanoparticles cannot be determined spectroscopically due to the presence of the nanoparticles and therefore the specific activity cannot be calculated. While a value of 'units' could be determined for the free- and for the nanoparticle-conjugated- enzyme, the definition of unit does not take into account that an immobilised enzyme is in effect a different species and the absolute value of units cannot be fairly compared. A calculation of units per milligram of solid support is also of limited use.

For reaction rates to be used as a proxy measurement for the effect of immobilisation on enzyme shape, they must be normalised against the number of enzyme molecules present in

a sample.⁹ Given certain assumptions which are discussed in the ‘Results’ section of this chapter, judgements can be made as to the approximate number of enzymes immobilised in a sample and their condition and therefore the suitability of the immobilisation method for transfer to monoclonal antibody immobilisation.

3.1.7 Horseradish Peroxidase (HRP)

Horseradish peroxidase (HRP) is a 44 kDa protein with a diameter of approximately 3 nm,²² that catalyses the reduction of H₂O₂ when in the presence of an electron donor:

where AH₂ is a reducing substrate and AH· is the radical product.²³ Many donors are commercially available which when oxidised give a coloured product which strongly absorbs in the UV region. HRP is a robust and stable enzyme; although the pH optimum for the enzyme’s activity is 7.0, activity can be observed at higher and lower pH values and purified species can be stored for months at 4 °C with limited loss of activity through degradation.¹ The most common isoform has pI = 5.7.²⁴

HRP contains two types of metal centres: iron present in heme (making the enzyme a hemoprotein) and two seven-coordinate calcium ions.²³ All contribute to giving the active site its shape, but only the redox active iron centre contributes to the catalytic pathway proposed in Fig. 6,²⁵ the exact details of which are beyond the scope of this discussion but which is included for completeness.

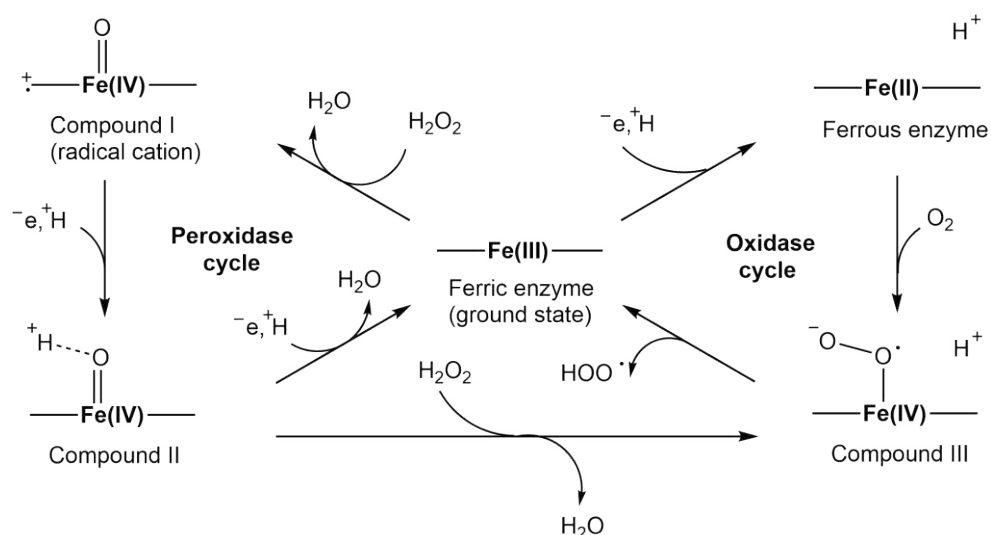


Figure 6. Proposed catalytic mechanisms for HRP activity, showing the peroxidase cycle (on the left) and the oxidase cycle (on the right) which occurs in the presence of excess peroxide. Both Compounds I and II are strong oxidants. Combined and adapted from Berglund et al and Veitch.^{23,25}

Multiple substrates exist for use with HRP in both colorimetric and chemiluminescent assays such that depending on experiment design one substrate may be preferred over others. 3, 3', 5, 5'-tetramethylbenzidine (TMB) is a common substrate which gives a blue colour as a result of HRP activity (see Fig. 7). The blue dimer produced has two absorbance maxima at 370 nm and 652 nm. The addition of acid stops the reaction and gives a yellow colour that can be measured at 420 nm.²⁶

HRP has just two amine groups from lysine residues that are free to react which is extremely low for a protein and which can limit the use of amine-reactive crosslinkers with HRP.¹ Glutaraldehyde is still often used to achieve conjugation,²⁷ but is not ideal for the reasons discussed above. In addition, glutaraldehyde is an inhibitor of HRP and excess reagent must be removed prior to kinetic studies on a modified enzyme.²⁸ HRP is a glycoprotein, bearing sugar side chains attached to eight asparagine residues, although the exact quantity and nature of these sugars varies between isoenzymes and samples.²³ This renders it suitable for conjugation via reductive amination following oxidation of a sugar chain.

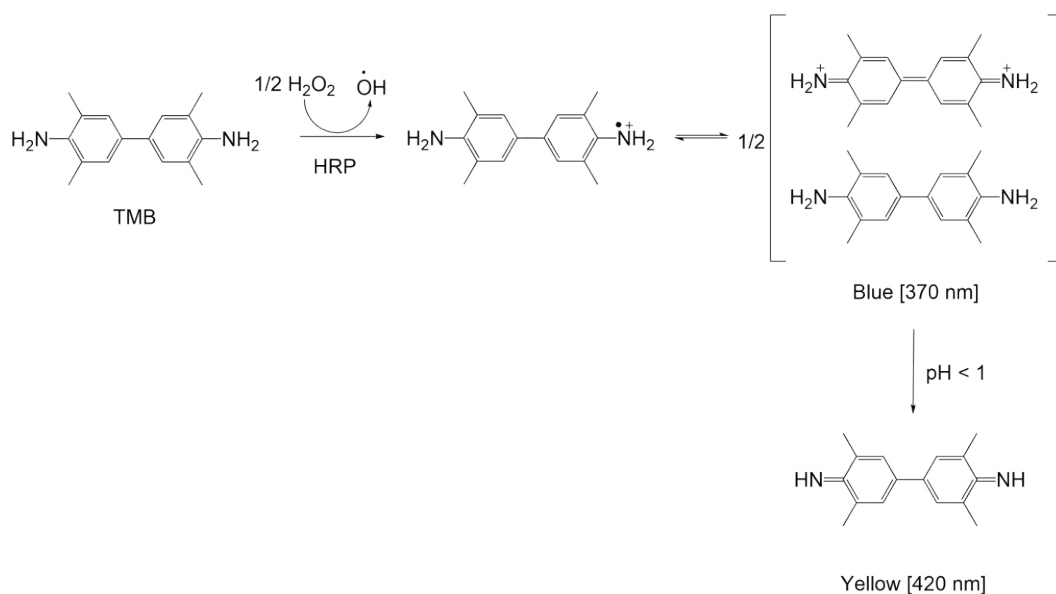


Figure 7. Scheme of formation of coloured species by sequential oxidation of TMB.

HRP's robust nature, long term stability, relatively low molecular weight and high activity even upon modification has resulted in it being the most popular enzyme for use in bioconjugate systems, used in approximately 80 % of antibody-enzyme conjugates.¹

The conjugation of HRP to other biomolecules has most commonly been achieved via glutaraldehyde- or periodate-mediated approaches with the latter typically giving products with higher retained enzymatic activities.^{1,29,30} The immobilisation of the enzyme on

nanomaterials using glutaraldehyde has been reported²⁷ along with non-covalent methods of attachment e.g. adsorption, although the effects of non-covalent immobilisation upon enzymatic activity vary between sources.^{31–33}

3.1.8 Alkaline phosphatase

The Alkaline phosphatases are a large family of related enzymes. Mammals express two forms of AP, both having optimal activity at pH 8-10, both being activated by divalent cations and both being inhibited by similar species e.g. phosphate ions.^{1,33} The most commonly encountered form of AP, Calf Intestinal AP, is the second most common used enzyme in commercial conjugate species but is generally not as desirable as HRP. Modification of the enzyme with crosslinker molecules or when forming conjugate species lowers enzyme activity significantly even when following known methods.^{1,9,34} AP's lack of reliability in this sense make it a poor species for method development.

3.1.9 Purifying and characterising proteins and bioconjugate species

An overview of bioconjugate technology would be incomplete without discussing methods of purifying and characterising bioconjugate species. The approach taken is largely dictated by the nature of the desired product. However, the potential for denaturation introduces limitations to the techniques and conditions which may be used. The manipulation of proteins is dominated by chromatographic methods; the techniques used in the current work are discussed below.

Size-exclusion chromatography (SEC)

The separation of molecules based on their molecular weight or molecular size is a fundamental technique of biochemistry. While it may be used as an analytical method for the determination of the size of an unknown protein, it is most commonly encountered as a preparative method to separate large biomolecules from small molecules, for buffer exchange or for de-salting.³⁵ A diagram of how size-exclusion or gel-filtration chromatography works is shown in Fig. 8. A column consists of a solid phase of porous beads. Small molecules and/or salts are able to enter the pores of the beads such that when an eluting medium is applied to the solid phase, the small molecules experience a greater column volume than large molecules that cannot enter the pores. The large molecules move through the interstitial spaces between beads and are eluted before the small molecules.³⁶

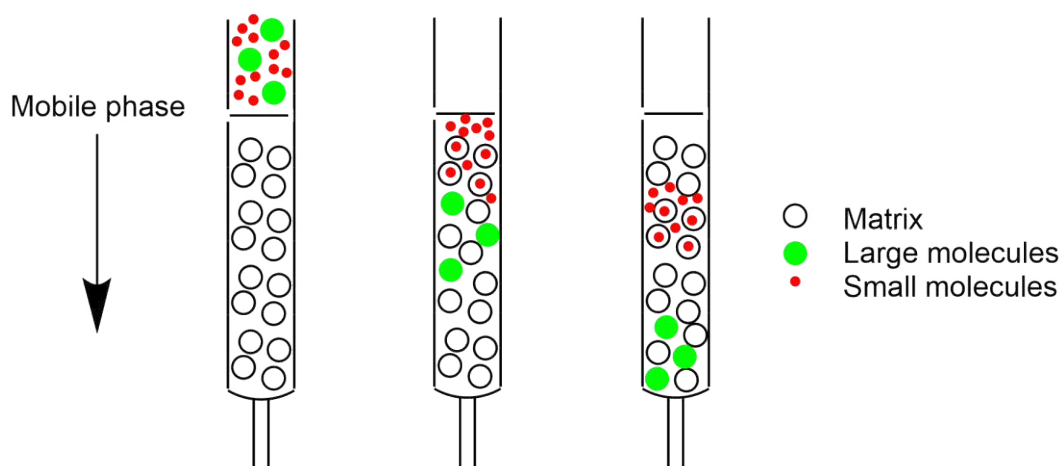


Figure 8. Size exclusion chromatography. Large molecules cannot enter pores, and so elute first.

SEC column media can be purchased from commercial suppliers for the preparation of bespoke columns, although pre-packaged columns such as PD-10 desalting columns containing crosslinked porous dextran gel are common.³⁷ These columns can be used with gravity and with centrifugation and have well-defined elution profiles.

The eluted protein fractions of size-exclusion columns (and the fractions of IMAC chromatography discussed below) are often dilute and require concentration prior to use or storage. Although multiple methods for protein concentration exist (such as dialysis) a fast method which also allows for buffer exchange is the use of protein concentrator 'spin columns'. These consist of a centrifuge tube divided into upper and lower compartments separated by a semi-permeable membrane with a defined molecular weight cut-off (MWCO). Upon centrifugation, molecules with a higher mass than the MWCO remain in the upper compartment while smaller molecules pass through the membrane and collect below.

Immobilised metal affinity chromatography (IMAC)

This method of purifying biomolecules is common in the synthesis of custom peptide sequences but is also used in the purification of mAb-based species.¹ For example, in the synthesis of enzyme-antibody conjugates such as for ELISA assays, an excess of enzyme is used relative to the amount of antibody. As the product and excess starter molecules are large, pre-packed SEC columns may give insufficient separation which can affect the study of the final sample. A more effective method utilises a form of affinity chromatography where the solid phase media consists of a matrix bearing chelating groups which coordinate a metal ion but which do not fill the coordination sphere. While several metal ions have been reported (e.g. Co^{2+} , Ni^{2+} , Cu^{2+} , Zn^{2+}),³⁸ the most commonly used matrix-metal couplings

today are nickel-nitrilotriacetic acid (Ni^{2+} -NTA)³⁹ and cobalt-carboxymethylaspartate (Co^{2+} -CMA).⁴⁰ Both matrices fill four coordination sites on the approximately octahedral metal centres, leaving two sites available to allow the binding of a biomolecule of interest (see Fig. 9).³⁸ The molecule to be purified is often modified by the inclusion of a stretch of six histidine residues at the N- or C-terminal termed a His-tag. For the purification of His-tagged proteins or peptides Ni^{2+} -NTA is typically used as nickel forms strong interactions with the imidazole side chain of histidine residues such that the binding is specific, but which are not strong enough to prevent relatively facile elution of the protein with only minor changes to buffer conditions.³⁶ Ni^{2+} -NTA can be viewed as a 'general purpose' IMAC media because while other metal-matrix pairings may give superior recovery or purification for a given protein or peptide, their use would require optimisation of conditions. Generally, Cu^{2+} is too strongly binding and Co^{2+} too weak, while Co^{3+} (as a d^6 metal centre) would form a low spin kinetically inert complex from which the protein could not be recovered.^{40,41} Ni^{2+} is a d^8 metal and does not form kinetically inert octahedral complexes, allowing for ligand substitution and protein recovery to occur at useful rates under experimentally achievable conditions. NTA is the preferred matrix because it is associated with reduced metal leaching into the final sample and greater end purity.⁴²

IMAC has been shown to be applicable to IgG-class antibodies and enzyme-antibody conjugates because of a common histidine rich sequence in the Fc region of the antibody that functions similarly to a His-tag.^{21,22} When applied to the column, antibody-containing species become bound to the stationary phase and excess enzymes or small molecules may be washed away. Elution of the bound species can be achieved by applying an elution buffer which changes the pH, increases the ionic strength or which includes a competitive species (such as imidazole) which can displace the histidines.

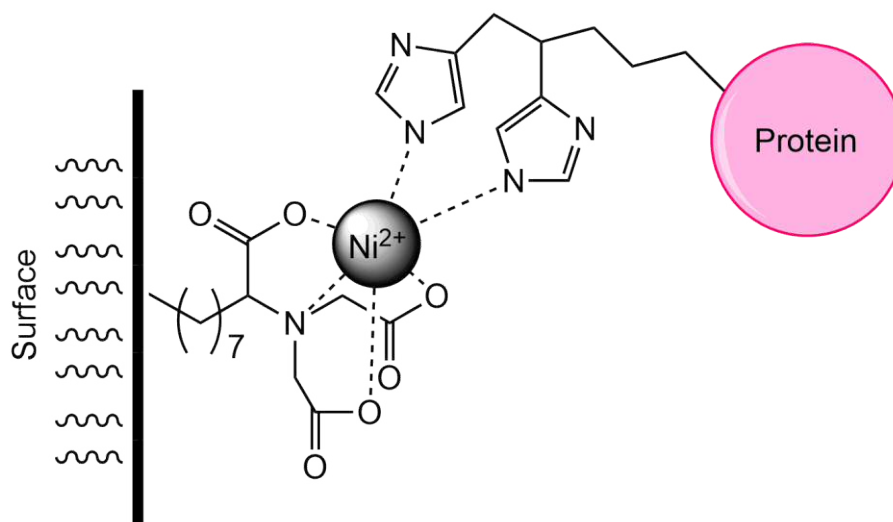


Figure 9. Diagram showing the interaction between the approximately octahedral immobilised Ni²⁺ ion of a Ni-NTA resin and histidine residues on a suitably tagged protein (whole His-tag not shown). Adapted from Block et al.⁴²

Measuring protein concentration

Protein concentration within a sample may be determined spectroscopically.⁴⁵ This is crucial for determining reaction stoichiometry. Proteins absorb at 280 nm due to the aromatic amino acids tyrosine and tryptophan and disulphide bonds present in their structure. Absorbance at a wavelength is related to concentration by the Beer-Lambert law:

where A is absorbance, ϵ is the molar extinction coefficient, c is the concentration of the species, and l is the experimental pathlength (typically 1 cm). The molar absorptivity at 280 nm, or ϵ_{280} , can be calculated if the protein structure is known:

where the number of each group in the protein is multiplied by an estimated molar extinction coefficient. The values of ϵ_{280} for common proteins such as HRP are known and can be referred to as standards. In the case of monoclonal antibodies, the number of groups that absorb at 280 nm do not differ greatly between given species and so average or typical values may be used with confidence. The concentration of a protein sample may be found using a UV-spectrometer or by the use of a 'NanoDrop'-type microvolume spectrophotometer.⁴⁶ The latter, although less accurate, is able to determine trends over eluted column fractions. As micro-volumes are used it is ideal for use in an on-going experiment.

Circular dichroism

Many techniques for the characterisation of proteins exist. One which is less commonly applied outside of the study of biomolecules is circular dichroism (CD) spectroscopy, the specifics of which are outside the scope of the current work.^{36,47-49}

Briefly, a plane of polarised light can be considered as two components of equal magnitude but with opposite circular polarisation (counter clockwise or left-handed and clockwise or right-handed). Absorption of both components equally by a sample would give an incident beam of the same initial polarity. Chiral chromophores absorb left- and right-handed radiation differently, such that the incident beam is distorted away from the initial plane of polarity; an effect known as ‘elliptical polarisation’.⁴⁷ The ability of a compound to absorb with different intensity at a given wavelength depending on chirality is known as circular dichroism (CD) and may be calculated by:

where A is absorbance, λ is the wavelength and L and R refer to the direction of polarisation. CD spectroscopy measures the value of CD over a range of wavelengths, converts this value to ‘ellipticity’ and then normalises it by considering concentration and the number of amino acid residues in the protein to give the mean residue ellipticity, θ_{MR} , allowing comparisons between proteins of different sizes.

As CD arises as the result of chirality, CD spectroscopy is well suited to measure the secondary and tertiary structures of proteins which make these biomolecules chiral. As α -helices, β -sheets and other features of a protein’s structure can have signature effects on the CD spectrum (Fig. 10), information derived from CD spectroscopy can be used to estimate protein structure,⁴⁹ or as a method of checking on the structural integrity of a known protein. Denaturation causes significant differences in the CD spectrum of a protein, while minor modifications may be difficult to observe.⁴⁸

In the context of the current work, CD spectroscopy can be of use confirming the retention of structure following bioconjugation of two proteins (e.g. an antibody-enzyme conjugate) or following fluorescent labelling of a protein. Unfortunately, because of the absorbance properties of SPION, CD spectroscopy cannot be used to characterise immobilised proteins.

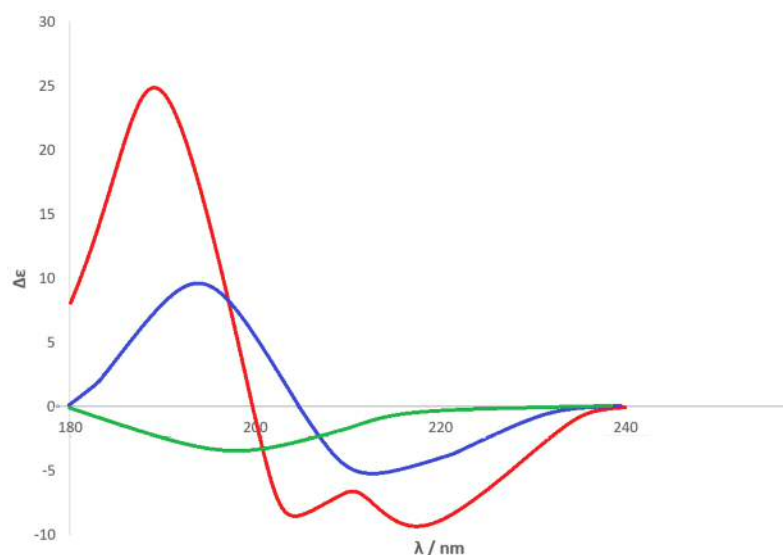


Figure 10. CD signatures of selected structural elements: α -helix (red), β -sheet (blue), denatured protein (green).⁴⁸

3.1.10 Aims and objectives

'Bioconjugation' is where chemical biology and synthetic chemistry meet. Although still a relatively young field of research, its impact has been huge and continues to grow. The present work was intended to answer the following three questions:

- How can biomolecules be immobilised on SPION?
- How can their structural integrity post-immobilisation be assessed??
- How many should be immobilised onto nanoparticles to maximise effect in later *in vitro* and *in vivo* experiments?

The solutions to the above questions form a synthetic approach to a radiolabelled, antibody-directed nanoparticle species. The discussion in the preceding pages provides the context to how these questions were addressed experimentally, the results of which are discussed below.

3.2 Experimental

3.2.1 Materials and Methods

All reactions were performed with the use of vacuum line and Schlenk techniques where appropriate. Reagents were commercial grade and were used without further purification. All reagents and solvents were purchased from Alfa Aesar or Sigma Aldrich. HRP was of commercial grade and was stored as lyophilised solids at -4 °C prior to use. The antibody trastuzumab was obtained via generous donation from Velindre Cancer Centre, Cardiff, and were stored as solutions of 21 mg.mL⁻¹ in a suitable buffer at 4 °C. UV-Vis studies were performed on a Jasco V-570 spectrophotometer in H₂O or in a suitable aqueous buffer. Enzymatic activity studies were carried out on a BMG LabTech FLUOstar Omega plate reader. All absorbance experiments were carried out in triplicate, at 298 K, and the results averaged. Protein concentrations were determined spectroscopically by A₂₈₀ on a Thermo Scientific NanoDrop 1000 UV-Vis Spectrophotometer. CD spectroscopy was carried out on an Applied Photophysics Chirascan CD spectrometer and analysed with Chirascan software. Dynamic light scattering analysis was performed on a Brookhaven Instruments Corporation 'Zetaplus'. HisPur Ni-NTA IMAC column media was purchased from ThermoFisher and was used without modification according to typical protocols.

3.2.2 Synthesis and analytical techniques

Preparation of TMB assay solution

3, 3', 5, 5'-tetramethylbenzidine (TMB) was dissolved in DMSO (1 mg.mL⁻¹) and was diluted tenfold in a volumetric flask with pH 5 phosphate citrate buffer to give the inactive assay solution. The assay solution was activated immediately prior to use by addition of 30 % H₂O₂ (2 μL).

Assessment of free HRP activity

Horseradish peroxidase, type I (M_w = 44 kDa) was dissolved in 0.1 M sodium phosphate buffer, 0.15 M NaCl, pH 6.8 (10 mg.mL⁻¹). The concentration was reduced to 1 × 10⁻⁴ mg.mL⁻¹ by serial dilution. 20 μL of the dilute enzyme solution was added to each well of a 96-well plate. Active TMB assay solution (180 μL) was added with mixing in a plate reader to each well in sequence. The absorbance of each well at 370 nm was measured over 10 min to assess the activity of the fresh free enzyme.

Analogous experiments were carried out using HRP that had been dissolved 24 hours prior to reaction with TMB assay solution to assess how enzyme activity changes over time when there is no addition of reactant species.

Assessment of glutaraldehyde-activated HRP activity

To a fresh solution of HRP in 0.1 M sodium phosphate buffer, 0.15 M NaCl, pH 6.8 (100 μL , 10 $\text{mg}\cdot\text{mL}^{-1}$) was added glutaraldehyde, 50 % wt. in water (2.52 μL). The reaction mixture was mixed for 24 hours at room temperature. The solution was transferred to a centrifuge tube and centrifuged (1 min, 13200 rpm) to remove any insoluble precipitates. The solution was diluted to $1 \times 10^{-4} \text{mg}\cdot\text{mL}^{-1}$, and 20 μL added to each of three wells prior to the addition of TMB assay (180 μL). Analysis was carried out as for fresh HRP, described above.

Assessment of reduced HRP activity

To a fresh solution of HRP in 0.1 M sodium phosphate buffer, 0.15 M NaCl, pH 6.8 (100 μL , 10 $\text{mg}\cdot\text{mL}^{-1}$) was added NaBH_4 to a final concentration of 26 $\text{mg}\cdot\text{mL}^{-1}$. The reaction mixture was vortexed gently and allowed to react at 4 °C for 1 h. Excess reductant was removed via desalting by use of a protein concentrator column (30 kDa MWCO) and washing with fresh buffer ($3 \times 1 \text{ mL}$). The reaction mixture was concentrated, the protein concentration measured from A_{280} , and an aliquot taken and diluted by serial dilution to $1 \times 10^{-4} \text{mg}\cdot\text{mL}^{-1}$. To each of three wells was added 20 μL prior to the addition of TMB assay (180 μL). Analysis was carried out as for fresh HRP, described above.

Synthesis of HRP-APTES@SPION by use of glutaraldehyde

HRP was dissolved in 0.1 M sodium phosphate buffer, 0.15 M NaCl, pH 6.8 (1 mL, 10 $\text{mg}\cdot\text{mL}^{-1}$). Glutaraldehyde, 50 % wt. in H_2O was added to a final percentage of 1.25 % of the crosslinker (26.1 μL) and the reaction mixture stirred overnight at room temperature. After 24 h, the reaction mixture was purified by size-exclusion chromatography on a PD-10 desalting column using 0.1 M sodium phosphate buffer, 0.15 M NaCl, pH 6.8 as an elution buffer. Elution yielded activated enzyme solution (3.5 mL, 2.86 $\text{mg}\cdot\text{mL}^{-1}$). Centrifugation was applied to remove the insoluble glutaraldehyde-based polymers (2 min, 13200 rpm). APTES@SPION was dispersed in 0.1 M sodium phosphate buffer, 0.15 M NaCl pH 6.8 (10 $\text{mg}\cdot\text{mL}^{-1}$). Differing volumes of nanoparticles suspension and enzyme solutions were mixed to achieve differing maximum loadings of enzyme per nanoparticle (see below). The reaction mixtures were mixed overnight at 4 °C by use of an inverting carousel mixer. To each was added NaBH_4 in 0.1 M sodium phosphate buffer, 0.15 M NaCl, pH 6.8 (200 μL , 20 $\text{mg}\cdot\text{mL}^{-1}$) and the mixture stirred for 1 h at 4 °C to reduce Schiff bases. The particles were collected

by centrifugation (2 min, 13200 rpm) and washed with distilled water (5×1 mL) to remove unbound enzyme. The particles were dispersed in 0.1 M sodium phosphate buffer, 0.15 M NaCl, pH 6.8 (1 mL), homogenised and diluted 100-fold. 20 μ L of each dispersion was transferred to a well of a 96-well plate. Active TMB assay solution (180 μ L) was added to each with mixing and the absorbance at 370 nm measured over an hour. All experiments were carried out in triplicate. The enzymatic activity of each sample was determined based on the estimated number of particles in the well and the initial reaction stoichiometry. DLS studies yielded inconclusive data.

Synthesis of HRP-APTES@SPION via reductive amination

HRP was dissolved in 0.1 M sodium phosphate buffer, 0.15 M NaCl, pH 7.2 (10 mg.mL⁻¹). NaIO₄ (22 mg) was dissolved in H₂O (1 mL, 88 mM) in the dark. 100 μ L of the periodate solution was added per 1 mL of enzyme solution. The reaction mixture was mixed and allowed to react in the dark for 20 min. Excess NaIO₄ was quenched by addition of Na₂SO₃ (2.5 molar equivalents). A PD-10 column was equilibrated using 0.1 M sodium phosphate buffer, 0.15 M NaCl, pH 7.2, and the reaction mixture applied. Elution was achieved using aliquots of buffer (0.5 mL). The concentration of the activated enzyme was determined spectroscopically and the most concentrated fraction selected for use in immobilisation. APTES@SPION was dispersed in H₂O (10 mg.mL⁻¹). Differing volumes of nanoparticle suspension and enzyme solution were mixed to achieve differing loadings of enzyme per nanoparticle (see below), and allowed to react at room temperature for 2 h. 5 M NaCNBH₃ in 1M NaOH was added (10 μ L per 1 mL of reaction mixture) to reduce Schiff bases by reaction at room temperature for 30 min. 1 M ethanolamine, pH 9.6 (50 μ L per 1 mL of reaction mixture) was added and reaction continued at room temperature for 30 min. The particles were collected by centrifugation (2 min, 13200 rpm) and washed with distilled water (5×1 mL) to remove any unbound enzyme. For all samples, the particles were dispersed in H₂O (1 mL), homogenised, and a sample diluted 1000-fold. 20 μ L of each sample dispersion was transferred to a well of a 96-well plate. Active TMB assay solution (180 μ L) was added to each with mixing and A₃₇₀ measured over an hour. All experiments were carried out in triplicate. The enzymatic activity of each sample was determined based on the estimated number of particles in the well and the initial reaction stoichiometry. DLS studies yielded inconclusive data.

Conjugation of HRP and trastuzumab by reductive amination

Trastuzumab was dissolved in 10 mM sodium phosphate, 0.15 M NaCl, pH 7.2 (10 mg.mL⁻¹). NaIO₄ (22 mg) was dissolved in H₂O (1 mL) in the dark and 100 μ L of the periodate

solution added per 1 mL of the antibody solution. The mixture was allowed to react in the dark at room temperature for 20 min, and the excess periodate quenched by the addition of Na₂SO₃ (2.5 molar equivalents). The reaction mixture was applied to a PD-10 column equilibrated with 100 mM sodium phosphate, 0.15 M NaCl, pH 7.2, and the activated antibody collected by elution in the same buffer using fractions of 0.5 mL. A₂₈₀ was used to monitor antibody concentration and the activated antibody was used immediately. HRP was dissolved in 0.2 M sodium carbonate buffer, pH 9.6 (10 mg.mL⁻¹). The enzyme solution was added to the antibody solution to achieve a 15-fold molar excess of the enzyme. The mixture was allowed to react for 2 h at room temperature. 5 M NaCNBH₃ in 1 M NaOH was added (10 µL per 1 mL) and allowed to mix for 30 min at room temperature. Excess aldehyde groups were blocked by the addition of 1 M ethanolamine, pH 9.6 (50 µL per 1 mL) and allowed to react for 30 min at room temperature. The reaction solution was then applied to a PD-10 column equilibrated with 10 mM sodium phosphate, 0.15 M NaCl, pH 7.2, and elution carried out with the same buffer using 1.0 mL fractions. The absorbance at 280 nm was monitored to determine the most concentrated fractions, which were combined. HisPur Ni-NTA resin was used to ensure separation of the conjugate species from excess enzyme. Briefly, a short column (2 mL) was prepared and washed with H₂O (10 × 2 mL) to remove storage buffer, then equilibrated with 10 mM sodium phosphate, 0.15 M NaCl, pH 7.0 (3 × 2 mL). The reaction mixture (2 mL) was applied to the resin and the eluent discarded. The resin was washed with 0.15 M NaCl (10 × 2 mL) until the absorbance of the fractions at 280 nm was negligible. The bound immunoconjugate species was eluted by the addition of 100 mM sodium phosphate, 0.5 M NaCl, pH 5.0 (10 × 1 mL). The most concentrated fractions were determined spectroscopically, combined, buffer exchanged into 100 mM sodium phosphate, 0.15 M NaCl and concentrated by use of a protein concentrator (10,000 MWCO) to ~5 mg.mL⁻¹ as determined by A₂₈₀. Circular dichroism spectroscopy suggested a 1:1 conjugate species (see below). The enzymatic activity of the conjugate was determined similarly to the free enzyme above.

Immobilisation of HRP-trastuzumab conjugates on APTES@SPION

To HRP-trastuzumab in 100 mM sodium phosphate, 0.15 M NaCl, pH 7.2 was added a periodate solution (100 µL per 1 mL of antibody solution) prepared by dissolving NaIO₄ (22 mg) in H₂O (1 mL) in the dark. The reaction was allowed to proceed for 20 min, then excess periodate was quenched with Na₂SO₃ (2.5 molar equivalents). A PD-10 column was equilibrated with 100 mM sodium phosphate, 0.15 M NaCl, pH 7.2, and the reaction mixture applied. The same buffer was used for elution in fractions of 0.5 mL. A₂₈₀ was used to determine the most concentrated sample, which was selected for the next step of the

reaction. APTES@SPION was dispersed in H₂O (10 mg.mL⁻¹), and quantities of the activated immuno-conjugate solution added to achieve the desired stoichiometric loading of the product particles (see section 3.3.4). The reaction was allowed to mix at room temperature for 2 h. 5 M NaCNBH₃ in 1 M NaOH was added (10 μL per 1 mL) and reaction allowed to proceed for 30 min at room temperature. 1 M ethanolamine, pH 9.6 was added (50 μL per 1 mL) and reaction allowed to proceed for 30 min at room temperature. The particles were collected by centrifugation (1 min, 1000 rpm), and washed with 10 mM sodium phosphate, 0.15 M NaCl, pH 7.2 (5 × 1 mL). The particles were dispersed in H₂O (1 mL), homogenised, and a sample diluted a 1000-fold. 20 μL of each sample dispersion was transferred to a well of a 96-well plate. Active TMB assay solution (180 μL) was added to each with mixing and the absorbance at 370 nm measured over an hour. All experiments were carried out in triplicate. The enzymatic activity of each sample was determined based on the estimated number of particles in the well and the initial reaction stoichiometry. DLS studies yielded inconclusive data.

3.3 Results and discussion

3.3.1 Glutaraldehyde activation and immobilisation of HRP

Free' HRP activity measurements

As stated above, HRP has an unusually low number of free amine groups available for reaction with glutaraldehyde; just two for a protein of over 300 amino acid residues.¹ This has been shown to be sufficient to allow bioconjugation via the homobifunctional agent glutaraldehyde, and given the ready availability of the agent, use of glutaraldehyde is a clear starting point for the development of methods of immobilisation.

As the structure of enzymes immobilised on SPION cannot be studied directly, how catalytic activity is changed post-immobilisation serves as a measure of the 'health' of the protein. Initial experiments focussed on measuring the catalytic activity of the free enzyme in a range of conditions: prepared freshly before reaction, after 24 h in solution, after 24 h incubation with glutaraldehyde and after reduction by NaBH₄. The measured enzymatic activity of the different samples were compared to the free, freshly prepared enzyme to determine the effects of different treatments on the enzyme in a manner similar to that reported by Mark *et al.*⁹ HRP was dissolved in a suitable buffer at 10 mg.mL⁻¹, diluted by serial dilution to 1 × 10⁻⁴ mg.mL⁻¹, then 20 μL of this solution diluted to 1 × 10⁻⁵ mg.mL⁻¹ in the wells of the 96 well plate by addition of the TMB assay solution. All samples were treated analogously. A negative control consisting of glutaraldehyde with no HRP present gave no measurable increase in A₃₇₀ over the time scale of the experiments and is not discussed in the figures below.

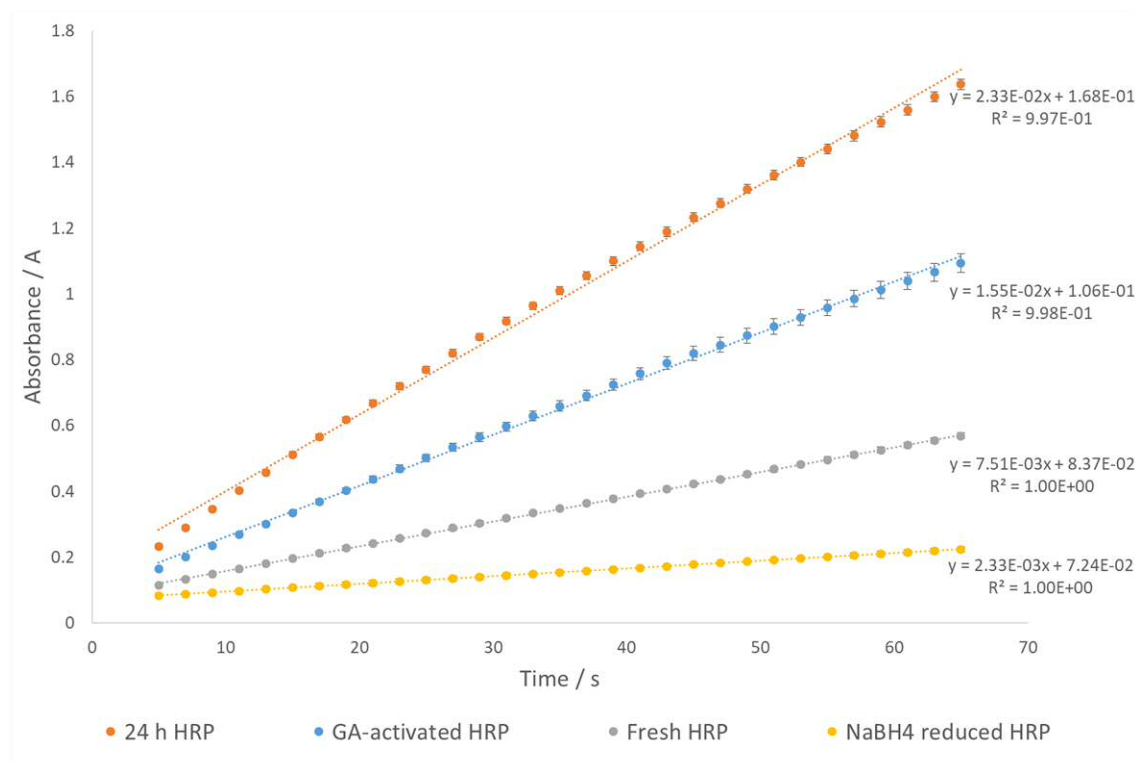


Figure 11. Absorbance at 370 nm versus time for HRP in different states (freshly prepared, glutaraldehyde (GA) activated, NaBH₄-reduced and 24 hours post-preparation). Error bars show standard error ($n = 3$).

Measuring A_{370} over time allowed the determination of the rate of formation of the blue TMB dimer in units of $A \cdot s^{-1}$ (Fig. 11). The number of enzyme molecules per well can be calculated from concentration and molecular mass:

The contribution to the observed rate per enzyme molecule present can then be calculated and used as a point of reference for similar calculations to be performed as part of later experiments. Full calculations are shown in section 1 of Appendix II.

	Observed rate \pm S.E. / A.s ⁻¹	Rate per enzyme \pm S.E. / A.s ⁻¹ .enz ⁻¹	Activity relative to freshly prepared, free HRP (%)
Freshly prepared HRP	$7.51 \pm 0.11 \times 10^{-3}$	$2.74 \pm 0.04 \times 10^{-13}$	100
24 hour post-preparation HRP	$2.33 \pm 0.02 \times 10^{-2}$	$8.50 \pm 0.07 \times 10^{-13}$	310 ± 3
GA-activated HRP	$1.55 \pm 0.04 \times 10^{-2}$	$5.66 \pm 0.15 \times 10^{-13}$	207 ± 6
NaBH₄-reduced HRP	$2.33 \pm 0.08 \times 10^{-3}$	$8.50 \pm 0.27 \times 10^{-14}$	31 ± 1

Table 1. Rates and relative activities of samples of free HRP. Standard deviation of mean observed rates used to determine variance in calculated quantities. Activity of freshly prepared HRP set at an absolute value of $2.74 \times 10^{-13} \text{ A.s}^{-1}.\text{enz}^{-1}$ for expediency of later analysis. ($n = 3$)

The relative activity of HRP dissolved in a suitable buffer 24 hours prior to study is over three times that of HRP dissolved immediately prior (see Table 1). When HRP has been incubated with glutaraldehyde for 24 hours, activity is increased approximately twofold relative to freshly dissolved HRP. In the proposed mechanism given in Fig. 6, oxidation of the iron centre of the ‘ground state’ enzyme from Fe³⁺ to Fe⁴⁺ (formally Fe⁵⁺) in an oxyferryl centre (‘Compound I’) is the first step.²⁵ When freshly dissolved HRP is used in the method described, the initial oxidation occurs by action of H₂O₂. When in solution for an extended period of time oxidation can occur due to O₂ in solution prior to addition of the assay solution. Numerous oxidants with less oxidising power than O₂ have been shown to initiate catalysis by HRP.^{30,31} The effect is similar to what would be observed if a greater quantity of oxidant were added to ‘activate’ the TMB assay solution. A greater proportion of the enzyme molecules are activated away from the ground state and are able to catalyse TMB dimerisation, leading to a higher measured rate while the smaller increase observed after 24 hour in solution with glutaraldehyde is likely due to some denaturation and/or the action of glutaraldehyde as an inhibitor of HRP.²⁸ The inverse is seen following incubation with the reductant NaBH₄. The relative activity measured is less than a third of the value observed for freshly prepared HRP in its native state.

Incubation of HRP with glutaraldehyde does not result in a complete denaturation of the enzyme. Qualitatively, aggregation is not observed although the observed decrease in activity may be due to crosslinking between enzyme molecules on a microscopic scale. Loss at this point is not so severe as to prevent attempts at immobilisation. NaBH₄ results in a loss of relative enzymatic activity (expected from the proposed catalytic mechanism) but not so much as to preclude the use of this reducing agent in the synthesis of bioconjugates incorporating HRP. The use of freshly prepared HRP as the control to which later experiments are referenced may be justified when considering that the degree of oxidation that occurs over 24 hours in solution may differ between samples despite attempts to limit such differences.

Calculation of immobilisation stoichiometry

The immobilisation protocol used was based on a two-step glutaraldehyde-mediated method first reported by Avrameas and Ternynck.⁵² Overnight incubation of the enzyme with the crosslinker was followed by size exclusion chromatography and centrifugation to remove any insoluble precipitates. The concentration of the activated enzyme was measured spectroscopically prior to addition to a dispersion of nanoparticles. Using characterisation data described in Chapter 2 of the present work, the number of nanoparticles per mg solid could be estimated; assuming spherical particles of diameter equivalent to the experimental determined average and with equal surface coverage with APTES allows an approximate reaction stoichiometry to be determined. The polydisperse nature of the nanoparticles means that a ‘theoretical average’ particle must be used in the calculations in Table 2 below, which describe the approach used in designing these experiments.

The APTES@SPION sample used in all experiments was characterised to have an average inorganic (Fe₃O₄) core diameter of 6.5 ± 0.4 nm by application of the Scherrer equation to the Powder X-Ray diffraction pattern. Random selection of a cohort of 30 particles from TEM images gave an average whole particle diameter of 8.1 ± 1.7 nm (see Chapter 2). The ‘theoretical average’ particle used has a whole diameter of 8.1 nm and a Fe₃O₄ core diameter of 6.5 nm, with the difference due to SiO₂ coating. Standard densities of these materials were used to calculate the mass of the ‘theoretical average particle’.

Taking into account the deviation in particle size parameters when estimating ‘particles per milligram’ introduces considerable variance (over 50 % relative to the value stated below and used in this work). For the sake of clarity this is omitted, however the reader should note that the stoichiometric labelling described below as enzyme:nanoparticle ratios and percentage labelling are *not* absolute values, but are reflective of the changing quantities of

protein (either enzyme or antibody) being used relative to an ideal population of ‘theoretical average particles’. As all experiments were performed in triplicate and good agreement in quantitative data was observed (see below), this approach would appear sound.

$$d(\text{SiO}_2) = 2.00 \text{ g.cm}^{-3}, d(\text{Fe}_3\text{O}_4) = 5.17 \text{ g.cm}^{-3} \text{ }^{53,54}$$

8.1 nm SiO ₂ Sphere	6.5 nm SiO ₂ Sphere	6.5 nm Fe ₃ O ₄ Sphere
—	—	—
<p>For an 8.1 nm nanoparticle having a 6.5 nm Fe₃O₄ core, the remainder being assumed to be of comparable density to SiO₂:</p> <hr style="width: 30%; margin: 20px auto;"/>		

Table 2. Calculating approximate number of nanoparticles per mg solid for reaction stoichiometry.

Table 3 shows how the desired reaction stoichiometries were achieved. The diameter of HRP is approximately 3 nm; if the immobilisation of biomolecules on a surface is approached as a sphere packing problem and the enzyme HRP is considered as a sphere with a ‘footprint’ of 7 nm², then an approximately spherical nanoparticle with a diameter of 8.1 nm and with a surface area of 206 nm² could theoretically accommodate a maximum of 22 enzyme molecules with 74 % packing efficiency. However, steric clashes would prevent this maximum from being reached and hindrance between enzymes would have a marked effect at levels well below saturation. For this reason, reaction stoichiometries were kept low so that the effect of increasing the number of singly enzyme-labelled particles in a population (expressed as a percentage) was studied. This would exclude the effects of inter-enzyme steric clashes that would not be immediately applicable to antibodies.

V(APTES@SPION) /μL (conc. /mg.mL⁻¹)	No. of nanoparticles	V(HRP) /μL (conc. /mg.mL⁻¹)	No. of enzymes	Enzyme:nanoparticle ratio (% singly labelled)
180 (10)	1.78×10^{15}	20 (0.286)	7.83×10^{13}	1:22 (~ 5 %)
160 (10)	1.58×10^{15}	40 (0.286)	1.57×10^{14}	1:10 (~ 10 %)
140 (10)	1.38×10^{15}	60 (0.286)	2.35×10^{14}	1:6 (~ 17 %)
180 (10)	1.78×10^{15}	20 (2.860)	7.83×10^{14}	1:2.3 (~ 43 %)
160 (10)	1.58×10^{15}	40 (2.860)	1.57×10^{15}	1:1 (~ 100 %)
140 (10)	1.38×10^{15}	60 (2.860)	2.35×10^{15}	1.7:1 (170 % i.e. 70 % bear two enzymes)

Table 3. *Volumes of nanoparticle and HRP solutions and resulting enzyme:nanoparticle ratio (glutaraldehyde method).*

Relative activities of immobilised enzymes

After immobilisation, the coated particles were dispersed in 1 mL of buffer and a sample was diluted 100-fold. 20 μL of this sample was transferred to a well plate for study. From Fig. 12, the initial rates of A_{370} vs. time for the different samples may be derived from the initially linear response.⁵⁵ Mathematical treatment allows the calculation of the theoretical contribution of each enzyme to this figure, assuming the immobilisation step went to completion (see Table 4). Comparison against the relative activity of the freshly prepared, free enzyme (found in Table 1) is achieved by the formula:

$$\frac{A_{\text{immobilised}}}{A_{\text{free}}} = \frac{\text{Rate}_{\text{immobilised}}}{\text{Rate}_{\text{free}}}$$

Full calculations are shown in the Appendix II. As the degree of oxidation within a sample of HRP has been shown to affect activity, great care was taken to ensure that all samples were measured at approximately the same time post-initial dissolution of the solid enzyme in an attempt to ensure that in all samples the degree of oxidation was comparable.

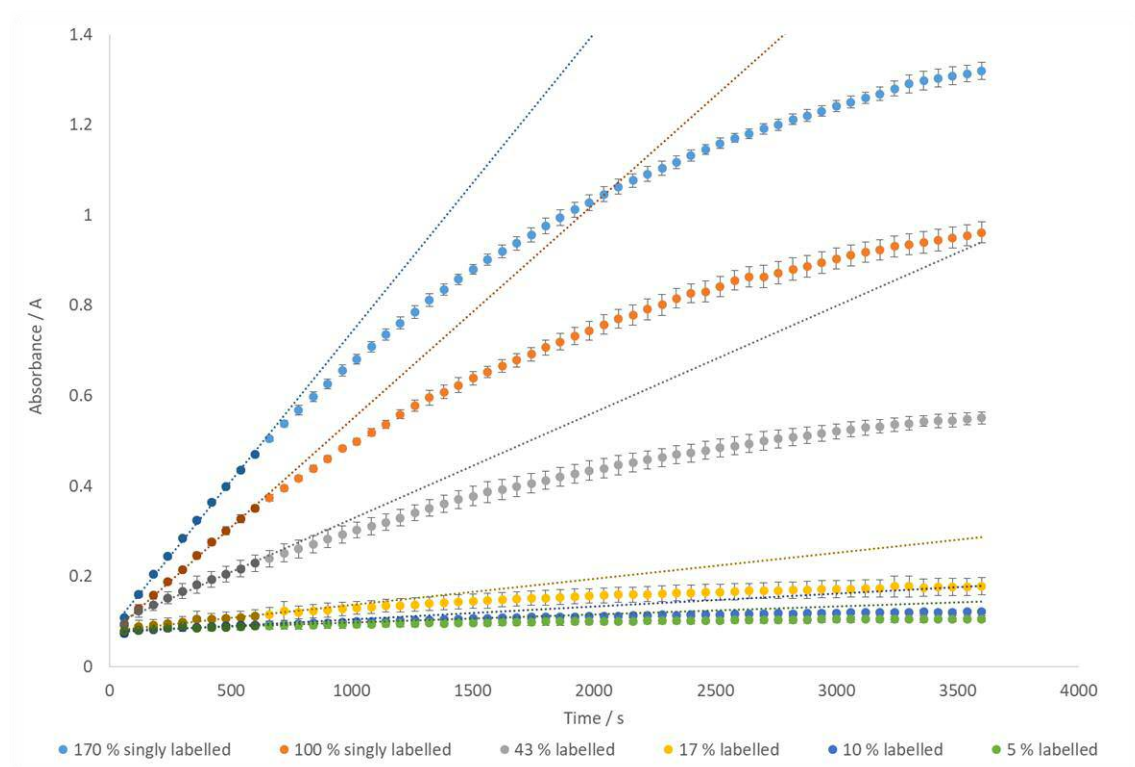


Figure 12. Absorbance vs. time for nanoparticles having different percentage labelling with HRP immobilised via glutaraldehyde. Error bars show standard error ($n = 3$)

Enzyme:nanoparticle ratio (% singly labelled)	Observed rate \pm S.E. / A.s ⁻¹	No. of enzymes	Rate per enzyme \pm S.E. / A.s ⁻¹ .enz ⁻¹	Activity relative to freshly prepared, free HRP \pm S.E. (%)
1:22 (~ 5 %)	$1.77 \pm 0.29 \times 10^{-5}$	1.62×10^{10}	$1.09 \pm 0.18 \times 10^{-15}$	0.40 ± 0.07
1:10 (~ 10 %)	$2.86 \pm 0.16 \times 10^{-5}$	3.16×10^{10}	$9.05 \pm 0.51 \times 10^{-16}$	0.33 ± 0.02
1:6 (~ 17 %)	$5.75 \pm 0.32 \times 10^{-5}$	4.68×10^{10}	$1.23 \pm 0.07 \times 10^{-15}$	0.45 ± 0.03
1:2.3 (~ 43 %)	$2.35 \pm 0.01 \times 10^{-4}$	1.54×10^{11}	$1.53 \pm 0.07 \times 10^{-15}$	0.56 ± 0.02
1:1 (~ 100 %)	$4.78 \pm 0.09 \times 10^{-4}$	3.16×10^{11}	$1.51 \pm 0.03 \times 10^{-15}$	0.57 ± 0.01
1.7:1 (170 % i.e. 70 % bear two enzymes)	$6.61 \pm 0.01 \times 10^{-4}$	4.68×10^{11}	$1.41 \pm 0.002 \times 10^{-15}$	0.51 ± 0.001

Table 4. Calculation of immobilised enzyme activity relative to the free species (glutaraldehyde method) ($n = 3$).

The immobilised enzymes gave measurable rates of catalysis at all theoretical loadings (Fig. 12 and Table 4). In all cases the enzymatic activity relative to that of the free enzyme is approximately 0.5 %, representing significant activity loss; no trend in activity can be discerned as initial stoichiometry increases, because the activity is so low that error renders the calculated differences between samples statistically insignificant.

Crosslinking between enzymes prior to immobilisation is not likely to be occurring. The low number of available amine groups on HRP makes cross-reaction with the more numerous surface amine groups of the nanoparticles more likely than either inter- or intra-enzyme crosslinking.

Although glutaraldehyde is known to be an inhibitor of HRP,²⁸ multiple washes post-immobilisation would be expected to have removed excess glutaraldehyde from the active sites. Incubation of HRP overnight in the presence of glutaraldehyde does not have an effect similar to that seen in Table 4; similarly the action of the reductant NaBH₄ diminishes the observed activity of the free enzyme but not to the degree noted for the nanoparticle-immobilised species (see Table 1).

If it is considered that steric hindrance, crosslinking, inhibition, reduction and denaturation are not likely to be the causes of the lowered activity, then it may be that glutaraldehyde is causing the enzyme to bind to the surface in such a way as to impede the formation of a substrate-enzyme complex. HRP is a relatively small protein; glutaraldehyde's short length may cause the active site to be either close to or oriented towards the highly charged, hydrophilic surface of the nanoparticle thus making it difficult for substrate molecules to enter. Antibodies have many lysine residues which would be free to link to the nanoparticle surface; attachment via multiple residues per protein could occur. If the crosslinker's length is the cause of HRP's reduced activity, it would be expected that using glutaraldehyde to achieve antibody immobilisation would result in the mAb being bound tightly to the surface, possibly via multiple points of attachment. If the antigen binding region were to be oriented toward or parallel to the particle surface, this would greatly decrease the ability of the mAb to bind its target receptor.

The approach described above would be unsuitable for mAb immobilisation. Antibodies are significantly larger than HRP (10 nm vs. 3 nm, or a 'spherical footprint' of 78.5 nm² vs. 7 nm²) and so a maximum of two antibodies could be accommodated, although realistically only one per nanoparticle could be achieved. Reduction in the ability of the protein to bind its target on the scale observed for HRP above could not be compensated for by increased loadings of the biomolecule.

3.3.2 Immobilisation of HRP via reductive amination

Mechanism of immobilisation

HRP has up to eight sugar side chains attached to amino acid residues throughout its structure.²³ Treatment of the protein with sodium periodate (NaIO_4) results in the oxidation of these sugars, generating up to two aldehyde groups per sugar monomer. Reaction of these aldehyde groups with deprotonated amines on the surface of the nanoparticles results in Schiff bases that must be stabilised by reduction.

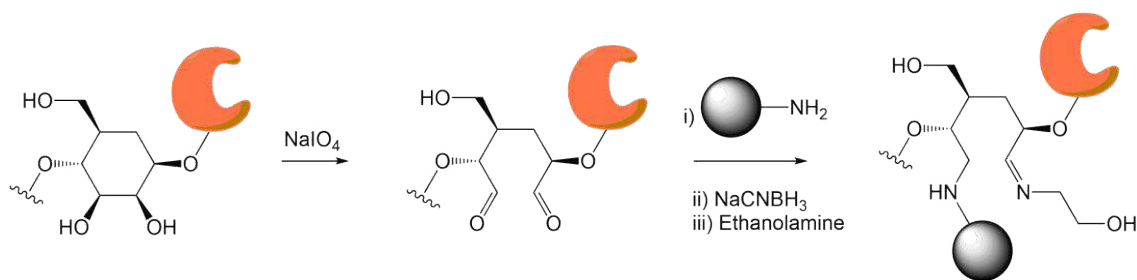


Figure 13. Glycoproteins (e.g. HRP, most mAbs) can be crosslinked to amine containing species, here a nanoparticle, by reductive amination.

This approach has several advantages. First, the oxidised sugar group of HRP will have a large number of aldehyde groups available for reaction with amines, while HRP has only two amine groups for reaction with the aldehydes of glutaraldehyde. Second, the reactive groups exist away from the steric bulk of the protein and so are more able to react. Third, the sugar side chain to be used as a crosslinker between the protein and the nanoparticle will be considerably longer than the crosslink formed by glutaraldehyde. This will allow the enzyme to move more freely in space, increasing the likelihood of substrate binding.

Calculation of immobilisation stoichiometry

The same samples of APTES@SPION were used for immobilisation as described in section 3.8.1 above; taking average values allowed an estimate that 1 mg of solid contained 9.88×10^{14} nanoparticles.

HRP was reacted with an excess of NaIO_4 and the activated protein purified by size exclusion chromatography. The activated protein was eluted from the column in aliquots with a volume of 0.5 mL and the concentration of each fraction was determined spectroscopically from A_{280} by use of a NanoDrop spectrophotometer. The most concentrated fraction was typically the sixth eluted volume and was used immediately in further reactions; volumes of the activated

HRP solution were added to volumes of a nanoparticle dispersion to achieve the desired reaction stoichiometry (see Table 5 below).

Relative activities of immobilised enzymes

Following reaction at room temperature for 2 h, the Schiff bases were reduced by NaCNBH₃ and any remaining aldehyde groups blocked by ethanolamine. Centrifugation and washing of the particles allowed the removal of unbound enzyme and excess reagents. The enzyme coated particles were then dispersed in H₂O (1 mL), diluted 1000-fold and 20 μ L used for studies. As the theoretical number of particles in each volume is known, then assuming complete immobilisation the number of enzymes present is known.

The change in A₃₇₀ due to enzyme activity was measured over 150 seconds. Analysis of the initial rates of reaction were taken from the first 60 seconds of the experiments (Fig. 14). Activities relative to free HRP were then be calculated (Table 6). An example approach is shown in section 3 of Appendix II.

Plotting the relative activities of the immobilised enzymes against the percentage of particles bearing an enzyme moiety yields the decay curve in Fig. 15 with equation:

Plotting log₁₀(relative activity) against log₁₀(% nanoparticles singly labelled) results in the straight line observed in the inset figure with equation:

which allows for the analysis of the relationship between activity and stoichiometry; the decay curve has a monomial formula where activity (y) is essentially (within error) inversely proportional (-1.164) to the percentage of nanoparticles bearing a biomolecule (x). Additional data would be required for greater confidence in the absolute value of the index.

As well as allowing the estimation of the expected relative activities for samples having different initial reaction stoichiometries to those studied, this relationship shows that as the number of particles bearing an enzyme increases, the ability of the enzymes to function decreases in a non-linear fashion reflecting the multiple factors contributing to activity loss (i.e. change in speed in solution, different orientations upon immobilisation, intra- and inter-particle steric effects and the formation of aggregate species). At the lowest studied percentage of nanoparticles with HRP ($\sim 2\%$), the relative activity is $81.4 \pm 8.0\%$ that of the free, freshly prepared enzyme. The reduction in activity in this case is likely due to the

small HRP enzyme molecule being attached to a large nanoparticle that limits the likelihood of collision with substrate molecules by slowing the motion of the enzyme in solution and by providing a steric hindrance to substrate molecules. The errors in the relative activity values given in Table 6 are sufficient to conclude with 95 % confidence that the trend observed is statistically significant.

As more particles are conjugated to HRP moieties, the relative activity of these enzymes decreases markedly. It is likely that increasing the number of protein species changes the surface character of the particles and increases their propensity to aggregate. In aggregates of multiple particles the enzymes would experience greater steric hindrance, preventing the formation of substrate-enzyme complexes.

When the number of immobilised enzymes in a sample is low the observed relative activity is comparatively high. Immobilisation by reductive amination does not negatively affect enzyme function as severely as immobilisation by use of glutaraldehyde and it can be concluded that the former approach is preferable for attempting antibody immobilisation. As antibodies are several times larger than HRP their effect on surface charge and the stability of the nanoparticle dispersion could be greater and a low biomolecule:nanoparticle ratio is even more important to ensure retention of biomolecule function.

V(APTES@SPION) /μL (conc. /mg.mL⁻¹)	No. of nanoparticles	V(HRP) /μL (conc. /mg.mL⁻¹)	No. of enzymes	Enzyme:nanoparticle ratio (% singly labelled)
500 (10)	4.95×10^{15}	2.08 (3.14)	8.94×10^{13}	1:55 (~2 %)
500 (10)	4.95×10^{15}	4.15 (3.14)	1.78×10^{14}	1:27 (~4 %)
500 (10)	4.95×10^{15}	10.38 (3.14)	4.46×10^{14}	1:11 (~9 %)
500 (10)	4.95×10^{15}	20.75 (3.14)	8.92×10^{14}	1:6 (~17 %)
500 (10)	4.95×10^{15}	41.50 (3.14)	1.78×10^{15}	1:3 (~33 %)

Table 5. Volumes of nanoparticle and HRP solutions and resulting enzyme:nanoparticle ratio (reductive amination method).

Enzyme:nanoparticle ratio (% singly labelled)	Observed rate \pm S.E. / A.s ⁻¹	No. of enzymes	Rate per enzyme \pm S.E. / A.s ⁻¹ .enz ⁻¹	Activity relative to freshly prepared, free HRP \pm S.E. (%)
1:55 (~2 %)	$3.99 \pm 0.39 \times 10^{-4}$	1.78×10^9	$2.23 \pm 0.22 \times 10^{-13}$	81.4 ± 8.0
1:27 (~4 %)	$4.29 \pm 0.47 \times 10^{-4}$	3.66×10^9	$1.17 \pm 0.13 \times 10^{-13}$	42.7 ± 4.7
1:11 (~9 %)	$3.33 \pm 0.36 \times 10^{-4}$	8.91×10^9	$3.74 \pm 0.40 \times 10^{-14}$	14 ± 1.5
1:6 (~17 %)	$4.51 \pm 0.65 \times 10^{-4}$	1.80×10^{10}	$2.51 \pm 0.36 \times 10^{-14}$	9.2 ± 1.3
1:3 (~33 %)	$2.92 \pm 0.52 \times 10^{-4}$	3.66×10^{10}	$7.97 \pm 1.42 \times 10^{-15}$	2.9 ± 0.5

Table 6. Calculation of immobilised enzyme activity relative to the free species (reductive amination method) ($n = 9$).

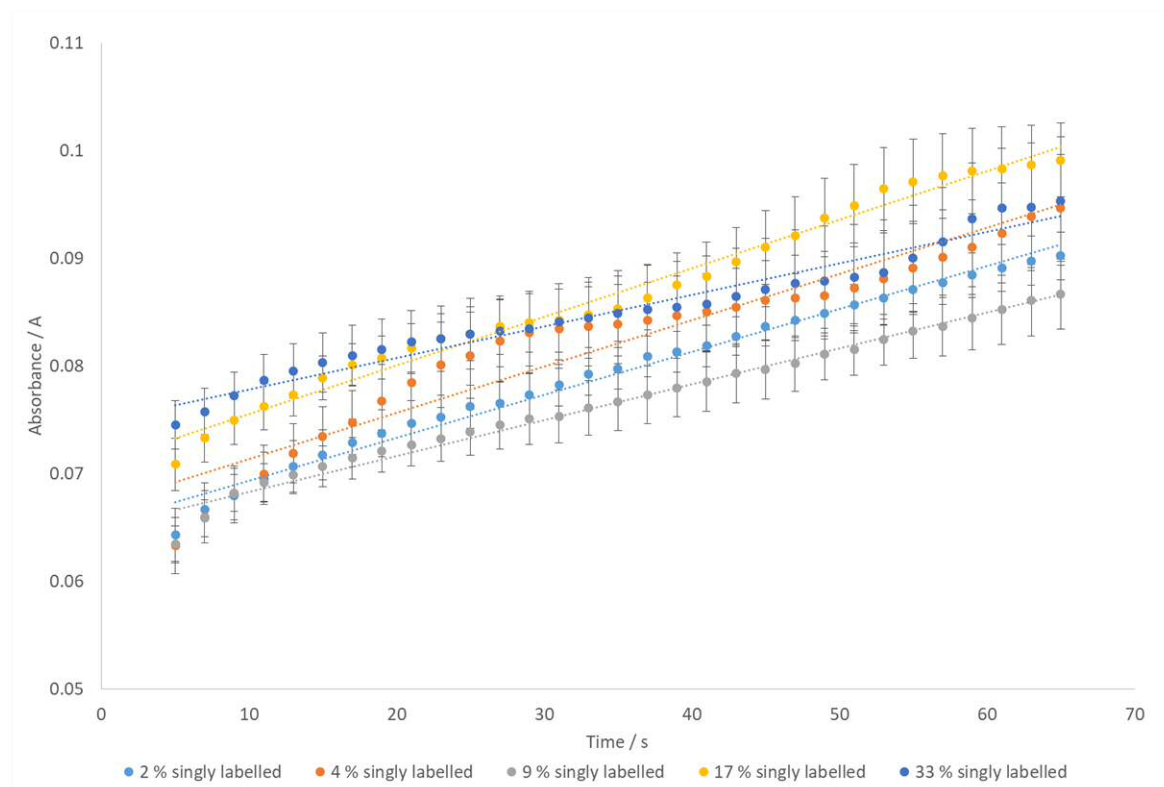


Figure 14. Absorbance vs. time for samples of nanoparticles having different percentages of immobilised HRP (reductive amination method). Error bars show standard error ($n = 9$).

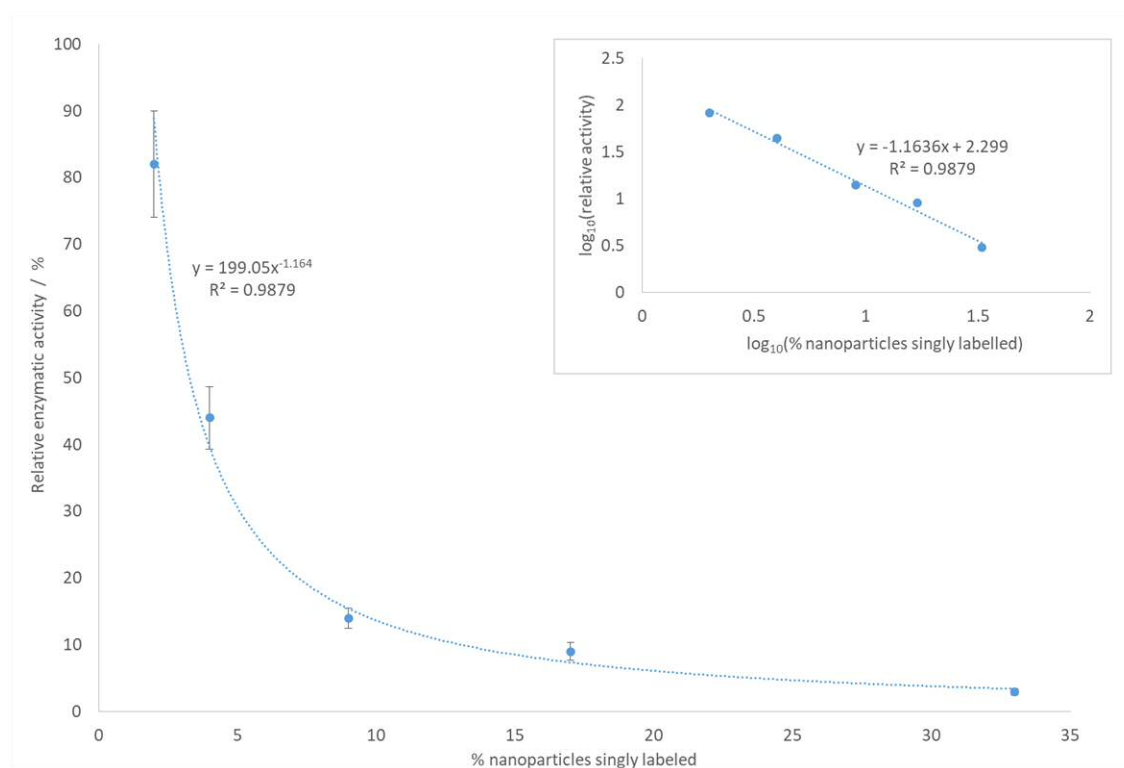


Figure 15. Relative activity plotted against percentage of nanoparticles bearing an HRP moiety. $\log_{10}(\text{activity})$ against $\log_{10}(\% \text{ nanoparticles singly labelled})$ shows a linear relationship (inset). Error bars show standard error ($n = 9$).

3.3.3 Conjugation of HRP and trastuzumab

Trastuzumab (Herceptin[®]) is a clinically approved monoclonal antibody used in the treatment of Her-2 positive breast cancers. A thorough discussion of this antibody is included in Chapter 4. As a glycoprotein bearing a sugar side chain at one N-glycosylation site in the Fc region (Asn297),⁵⁶ immobilisation may occur by reductive amination in a manner analogous to that described for HRP. The determination of the success of the experiment requires modification of the native species by incorporating a tag (e.g. an enzyme or fluorescent dye) that allows tracking of the mAb.

The number of fluorophores that can be conjugated to antibodies must be limited to prevent changing avidity (the antigen-antibody binding strength).⁷ Previous experiments have shown the need to limit the number of biomolecules (and therefore fluorophores) to be immobilised on the nanoparticles; also, the potential for fluorescence signal loss via quenching (see Chapter 4) means that linking the antibody to an enzyme that generates a product that can be observed in UV-Vis spectroscopy would give greater signal and greater tracking sensitivity. Neither approach directly assesses the retained function of the antibody, for which further experiments are required e.g. cell line studies discussed in Chapter 4.

As the antibody has one glycosylated site it is possible to perform a reductive amination reaction with an amine group on HRP, and although the reaction proceeds in the presence of a 15-fold excess of enzyme to take the reaction to completion, the limited number of glycosylation sites on the mAb and the sizes of the proteins theoretically limit the conjugation ratio to 1:1. Affinity chromatography (IMAC) allows for the removal of excess free enzyme moieties from the reaction mixture. The sugars of the enzyme moieties may then be used in a second reductive amination to immobilise the conjugate species on to nanoparticles (Fig. 16). In effect, the enzyme is being used as a crosslinker. Testing for enzymatic activity indicates the attachment of the antibody to the nanoparticle surface.

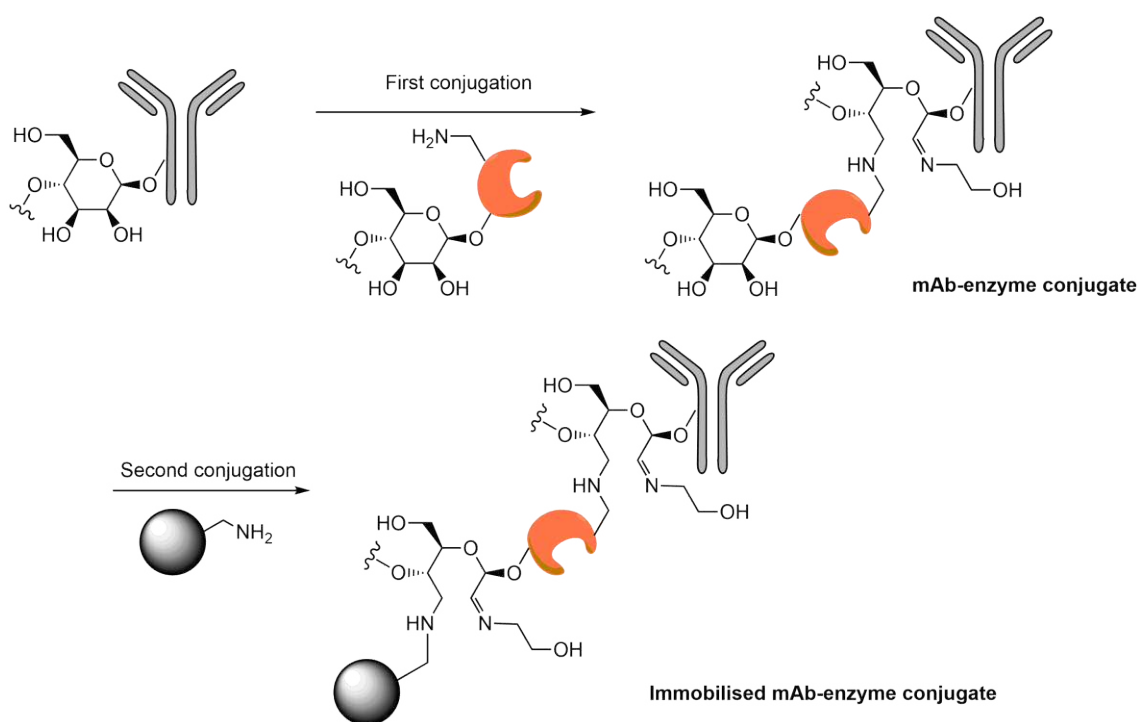


Figure 16. Sequential reductive amination allows the synthesis of a mAb-enzyme conjugate and its immobilisation on an amine-functionalised nanoparticle. Not to scale.

Circular dichroism spectroscopy

The 1:1 conjugate of HRP ($M_w = 44,000 \text{ g.mol}^{-1}$) and trastuzumab ($M_w = 145,421.5 \text{ g.mol}^{-1}$, $148,400 \text{ g.mol}^{-1}$ glycosylated) would have a M_w of approximately $192,400 \text{ g.mol}^{-1}$. Mass spectrometry of proteins often requires specialist techniques and/or equipment; in the current case, a representative mass spectrum could not be obtained. CD spectroscopy can be used to assess the structure of a conjugate species. The CD spectra of the enzyme, antibody and conjugate species were measured in millidegrees of ellipticity by dilution of stock solutions. By reference to the number of amino acid residues, degrees of ellipticity can be converted to mean residue ellipticity as discussed in the introduction to this chapter.

HRP ($M_w = 44,000$ Da)	Trastuzumab ($M_w = 145,421.5$ Da)	HRP-mAb conjugate ($M_w \approx 192,400$ Da)
[Stock] = 10 mg.mL^{-1} $= 2.27 \times 10^{-4} \text{ M}$	[Stock] = 21 mg.mL^{-1} $= 1.44 \times 10^{-4} \text{ M}$	[Stock] = 5.18 mg.mL^{-1} $= 2.73 \times 10^{-4} \text{ M}$
10 μL of stock solution diluted to 260 μL in sample.	5 μL of stock solution diluted to 260 μL in sample.	10 μL of stock solution diluted to 260 μL in sample.
\therefore [Sample] = $8.74 \times 10^{-6} \text{ M}$	\therefore [Sample] = $2.78 \times 10^{-6} \text{ M}$	\therefore [Sample] = $1.06 \times 10^{-6} \text{ M}$
N = 308 residues	N = 1330 residues	N = 1638 residues
\therefore $C_{MR} = 2.69 \times 10^{-3} \text{ M.res.}$	\therefore $C_{MR} = 3.69 \times 10^{-3} \text{ M.res.}$	\therefore $C_{MR} = 1.72 \times 10^{-3} \text{ M.res.}$

Table 7. Calculation of C_{MR} for HRP, trastuzumab, and the conjugate thereof.

The CD spectra of HRP, trastuzumab and the conjugate species are shown in Fig. 17. The native proteins have significantly different spectra against which the conjugate can be compared. HRP can be seen to have a greater contribution of α -helices to its CD spectra than the antibody, in agreement with X-ray crystal structure analysis.²³ The CD spectra of the conjugate species has a similar lineshape to the native antibody, but is sufficiently different that it can be judged to be a novel species. The peak at 289 nm seen in HRP's spectrum is not seen in that of the conjugate, implying a low contribution from the α -helices of HRP.

From the masses stated for glycosylated and non-glycosylated trastuzumab, it can be calculated that polysaccharides account for $2978.5 \text{ g.mol}^{-1}$ of the antibody, equivalent to approximately 16.5 glucose monomers per protein (attached in one polymer chain at Asn297). Assuming a linear, non-branched polysaccharide, with a monomer length of approximately 9 Å (based on typical C-C and C-O bond lengths), the sugar side chain would be 149 Å (14.9 nm) in length. In reality such sugars are branched and folded, and would be shorter. Following conjugation to a single 3 nm diameter enzyme ('spherical footprint' of 7 nm^2), subsequent enzymes would be sterically hindered from approaching any remaining aldehyde moieties by the steric bulk of the enzyme and the antibody.

The most likely product of the bioconjugation is a 1:1 species. The CD spectra shown in Fig. 17 below do not allow for the unequivocal assessment of the mAb:enzyme ratio on their own. Taking steric arguments into account and assuming that the reaction stoichiometry (a 15-fold excess of the enzyme) will have been sufficient to take the reaction to completion, the CD spectra of the product is sufficiently unlike that of the enzyme that it can be concluded with confidence that reaction has taken place. Simulated CD spectra for 1:1 and 1:2 species were obtained by addition of the spectra of the free enzyme and antibodies in different proportions; comparison to the experimentally obtained spectrum allows the conclusion that it is highly likely that a 1:1 bioconjugate has been formed (see Fig. 18).

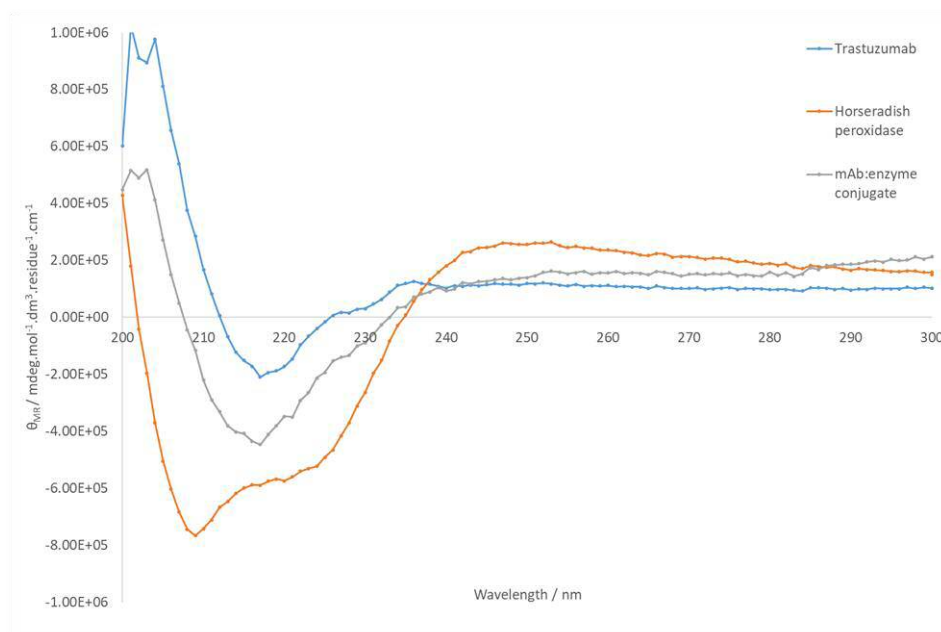


Figure 17. CD spectra of trastuzumab, HRP and the conjugate species. The line shape of the conjugate species is distinct from each of the starting species.

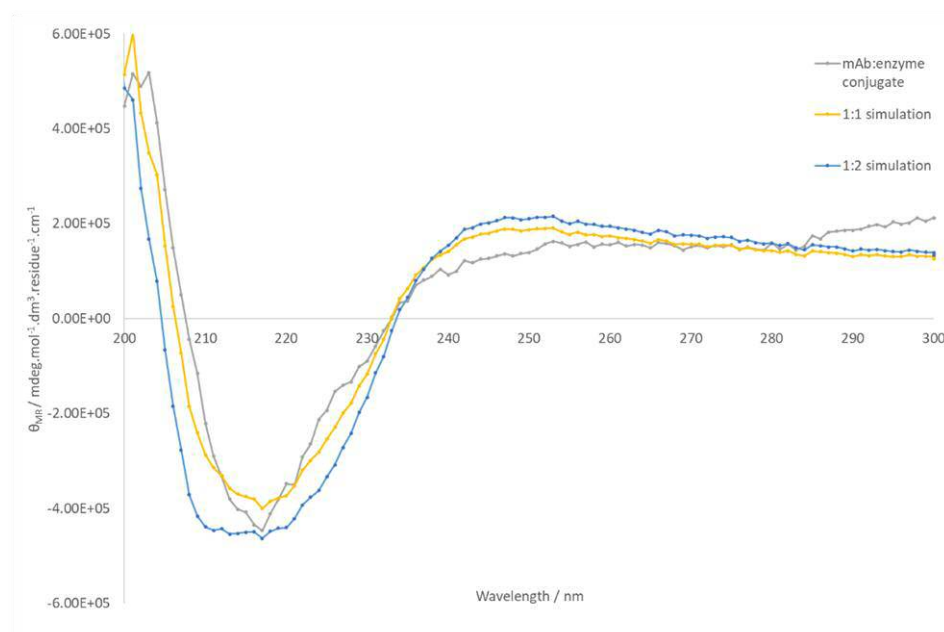


Figure 18. Comparison of the experimentally observed conjugate spectra to simulations allow the conclusion that a 1:1 conjugate has been formed.

Free' HRP-Herceptin conjugate activity measurements

The activity of the conjugate species was determined similarly to the approach taken for the native enzyme. Following chromatographic purification, the fractions containing the conjugate species were combined, concentrated in a protein concentrator 'spin column', and the final concentration made to 3 mg.mL⁻¹ (determined spectroscopically from A₂₈₀). An aliquot was taken and diluted 1000-fold, and 20 μL of this solution transferred to a well plate for study in the plate reader. Taking an approximate mass of 192,400 Da, the number of conjugate species (hence enzyme moieties) per well may be calculated:

Measuring A₃₇₀ against time (Fig. 19) yields an observed rate of $8.46 \pm 0.15 \times 10^{-3} \text{ A.s}^{-1}$ from which the effective contribution per enzyme moiety can be determined as $4.50 \pm 0.08 \times 10^{-14} \text{ A.s}^{-1}.\text{enz}^{-1}$. The activity of the immobilised conjugate can be calculated to be $16.4 \pm 0.3 \%$ relative to that of free, freshly prepared HRP; the low relative activity of the enzyme moiety in the conjugate reflects that it is considerably less able to perform catalysis than the free, native enzyme. Full calculations are shown in section 4 of the Appendix II.

From the decay curve shown in Fig. 15 above, it can be determined that a dispersion of SPION where all nanoparticles bear an HRP moiety would show significantly less enzymatic activity ($< 1\%$ relative to free HRP) than the enzyme-antibody system described here despite the similar sizes of a SPION (~ 8 nm) and an antibody (~ 10 nm). This supports the argument that it is not steric bulk that is limiting activity but another characteristic of the labelled nanoparticles such as an increased propensity to aggregate.

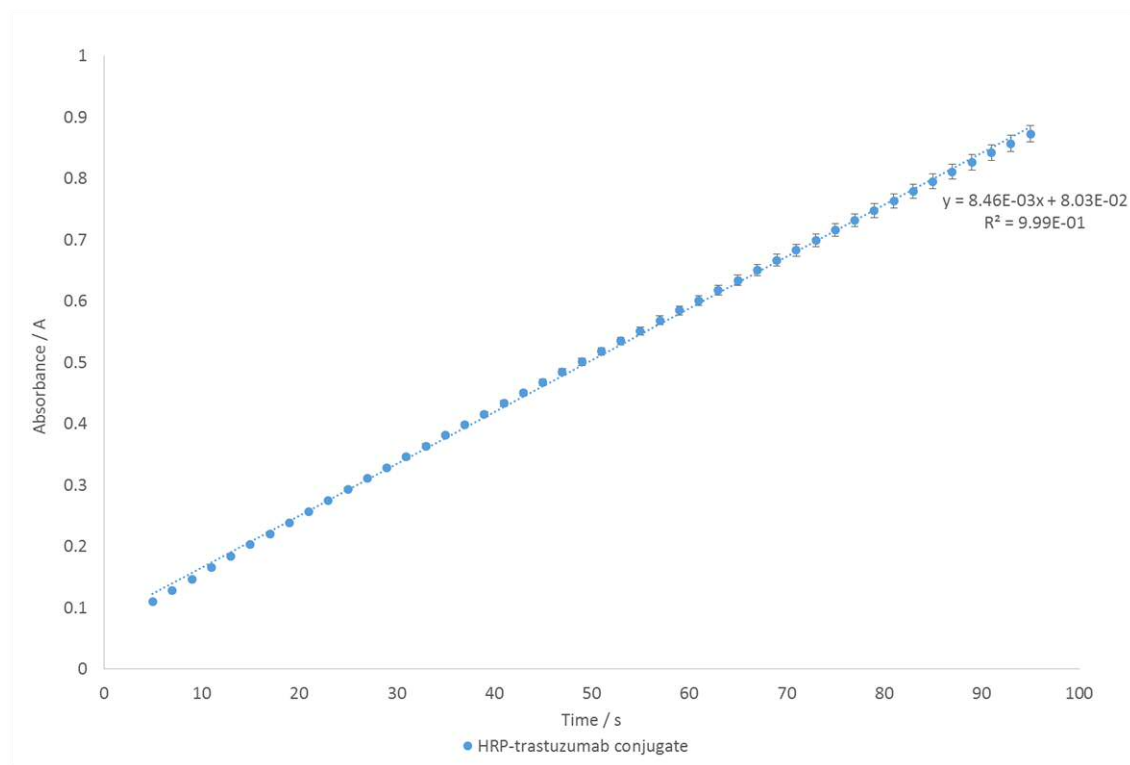


Figure 19. Absorbance at 370 nm versus time for free HRP-trastuzumab conjugate. Error bars show standard error ($n = 6$).

3.3.4 Immobilisation of the HRP-trastuzumab conjugate via reductive amination

It would be expected that immobilisation of the HRP-trastuzumab conjugate species onto SPION via the enzyme moiety's sugar side chain would reduce the observed relative enzymatic activity. The enzyme molecule would essentially exist as a small crosslinking moiety between two large, sterically hindering bodies which would limit collision with substrate molecules. If the presence of protein on nanoparticles is increasing the drive to aggregation, then as the percentage of nanoparticles bearing a conjugate species increases, the effect on activity would be expected to be similar to that observed for HRP alone.

Calculation of immobilisation stoichiometry

Immobilisation was achieved following a modified version of the protocol described by Hermanson, analogously to experiments discussed above.¹ It was again estimated that 1 mg of APTES@SPION contained 9.88×10^{14} 'theoretical average' nanoparticles as described above. Table 8 below shows how different theoretical reaction stoichiometries were achieved.

V(APTES@SPION) /μL (conc. /mg.mL ⁻¹)	No. of nanoparticles	V(Conjugate) /μL (conc. /mg.mL ⁻¹)	No. of enzyme moieties	Conjugate:nanoparticle ratio (% singly labelled)
200 (10)	1.98×10^{15}	8.46 (1.32)	3.506×10^{13}	1:56 (~ 2 %)
200 (10)	1.98×10^{15}	16.92 (1.32)	7.012×10^{13}	1:28 (~ 4 %)
200 (10)	1.98×10^{15}	33.85 (1.32)	1.403×10^{14}	1:14 (~ 7 %)
200 (10)	1.98×10^{15}	42.30 (1.32)	1.753×10^{14}	1:11 (~ 9 %)
200 (10)	1.98×10^{15}	84.60 (1.32)	3.506×10^{14}	1:6 (~ 17 %)

Table 8. Volumes of nanoparticle and HRP-trastuzumab conjugate ($M_w = 192,400$ Da) solutions and resulting conjugate:nanoparticle ratio (reductive amination method).

Relative activities of immobilised enzymes

The functionalised particles were washed to remove excess reagents and centrifuged for collection. They were dispersed in buffer (1 mL), and an aliquot was diluted tenfold. 20 μL of these dispersions were used for activity measurements (performed in triplicate). Fig. 20 shows the average changes in A_{370} observed over the time frame of the experiment.

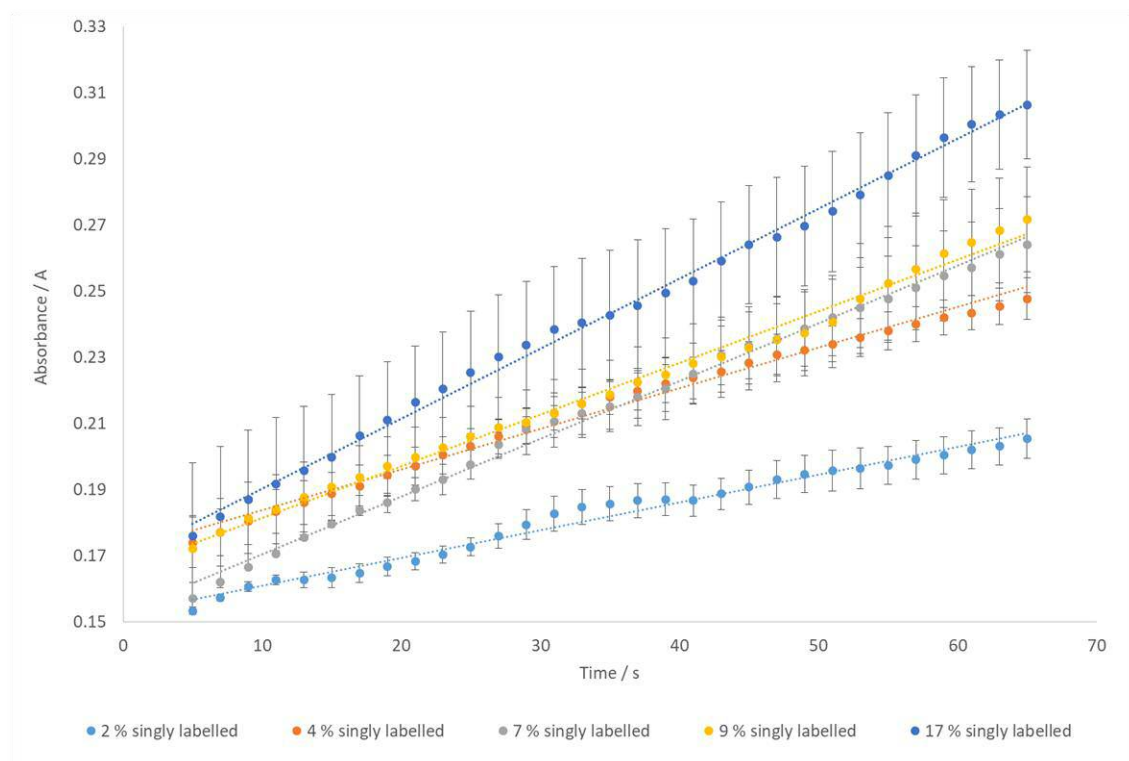


Figure 20. Absorbance vs. time for samples of nanoparticles having different percentages of immobilised HRP-trastuzumab conjugate (reductive amination method). Error bars show standard error ($n = 3$).

The particles were qualitatively observed to have a greater tendency to precipitate out of solution than the HRP-conjugated species studied previously. Differences in observed rates between samples having the same initial stoichiometry may be a result of different degrees of aggregation and precipitation between the identically prepared samples. The difference in qualitative behaviour compared to the enzyme bearing particles prepared by reductive amination (discussed above) and the observed activity of the HRP moiety confirms the presence of the antibody.

Table 9 below shows the observed rate per immobilised enzyme moiety for the above samples when compared to that of the free, native enzyme. From the lowest stoichiometric loading (approximately 2 % of nanoparticles bearing a conjugate species), it can be seen the activity of the HRP moiety is reduced further by immobilisation from 16.4 ± 0.3 % of that

of the free enzyme following conjugation to a mAb to 4.6 ± 0.54 % as a result of the enzyme's active site being subject to greater steric hindrance. As the number of particle-protein conjugates in a sample increases, the value of relative activity for the enzyme moieties present decreases resulting in the decay curve observed in Fig. 21 with equation:

The standard errors calculated and shown on the plot reveal that the differences in relative activity are significant, with the possible exception of the case where approximately 7 per cent of particles bear a conjugate but which may be omitted with limited effect on the observed trend. Plotting $\log_{10}(\text{relative activity})$ against $\log_{10}(\text{initial stoichiometry})$ yields the straight line in the inset figure with equation:

The linear relationship displayed in the log-log plot allows the formula of the decay curve to be seen as a monomial where relative activity (y) is inversely proportional to the percentage of particles bearing a conjugate species raised to the power -0.66. The presence of a fractional power in the formula is indicative of the growing complexity of the system compared to the enzyme-bearing particles studied analogously above. In the current instance, the products can be envisioned as much larger entities with a greater propensity to aggregate and precipitate out of solution. Multiple factors contribute to the systems' drive to aggregate; the value of -0.66 is likely arrived at due to the different contributions of these factors, the elucidation of which is beyond the scope of this work. Again, further experiments would be required for greater confidence in the absolute value of the index.

Increasing the amount of particles bearing HRP-trastuzumab conjugates in a sample results in an increased likelihood of precipitation and a marked decrease in the ability of the enzyme moieties to function. It can be concluded that in terms of the reaction conditions and reagents reductive amination can be used to link antibodies to enzymes and the resulting conjugates to nanoparticles, but the stoichiometry of the immobilisation reaction is crucial to retaining biological functionality in the end product. A compromise must be struck between retaining functionality and maximising the number of biomolecules that are present in a nanoparticle population.

Enzyme:nanoparticle ratio (% singly labelled)	Observed rate \pm S.E. / A.s⁻¹	No. of enzymes	Rate per enzyme \pm S.E. / A.s⁻¹.enz⁻¹	Activity relative to freshly prepared, free HRP \pm S.E. (%)
1:56 (~2 %)	$8.39 \pm 1.00 \times 10^{-4}$	6.73×10^{10}	$1.25 \pm 0.15 \times 10^{-14}$	4.56 ± 0.54
1:28 (~4 %)	$1.23 \pm 0.05 \times 10^{-3}$	1.39×10^{11}	$8.85 \pm 0.36 \times 10^{-15}$	3.23 ± 0.13
1:14 (~7 %)	$1.74 \pm 0.33 \times 10^{-3}$	2.28×10^{11}	$6.28 \pm 1.44 \times 10^{-15}$	2.29 ± 0.53
1:11 (~9 %)	$1.56 \pm 0.22 \times 10^{-3}$	3.48×10^{11}	$4.48 \pm 0.63 \times 10^{-15}$	1.64 ± 0.23
1:6 (~17 %)	$2.12 \pm 0.08 \times 10^{-3}$	7.01×10^{11}	$3.02 \pm 0.11 \times 10^{-15}$	1.10 ± 0.04

Table 9. Calculation of immobilised HRP-trastuzumab conjugate activity relative to the free species (reductive amination method).

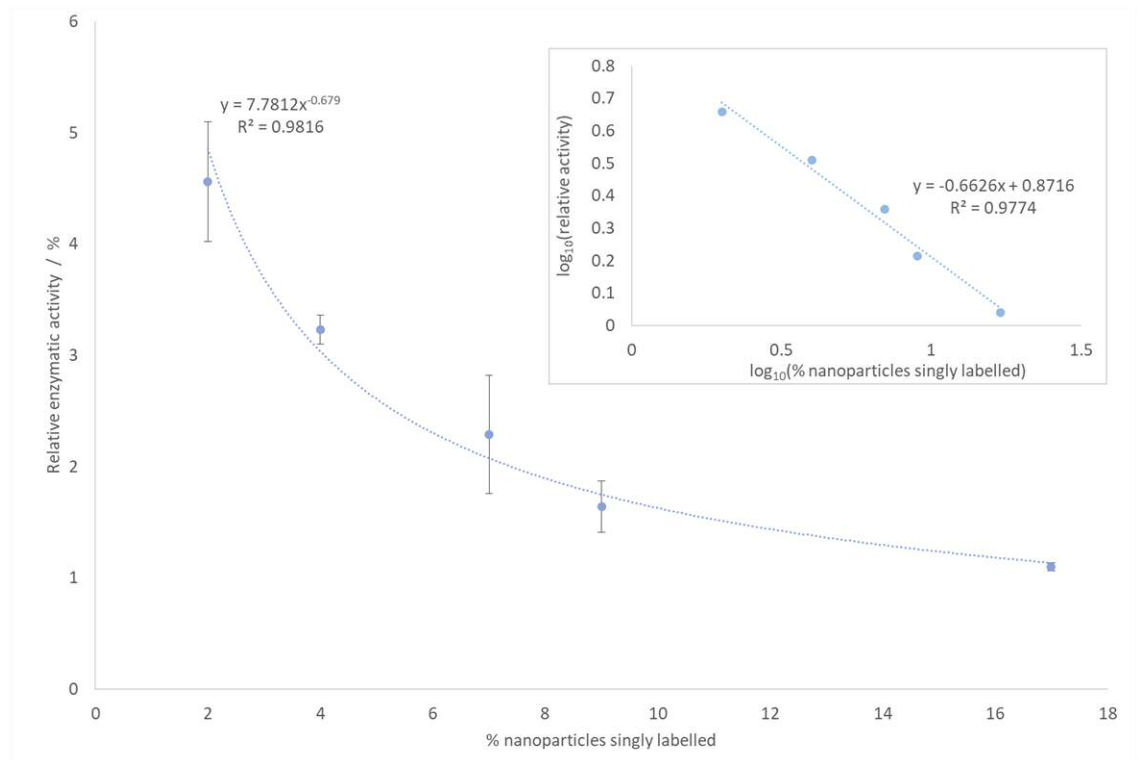


Figure 21. Relative activity plotted against percentage of nanoparticles bearing an HRP-trastuzumab conjugates moiety. $\log_{10}(\text{activity})$ against $\log_{10}(\% \text{ nanoparticles singly labelled})$ shows a linear relationship (inset). Error bars show standard error ($n = 3$).

3.4 Conclusion

APTES@SPION can be bioconjugated by various methods to biomolecules of interest. Although monoclonal antibodies are of clinical significance, their successful immobilisation cannot be directly proven without prior modification. Enzymes can be used as prototypes for antibodies in method development; observing the activity of the enzyme shows its presence and can be used as gauge for the effect of the immobilisation method on the protein's structure.

HRP immobilised on SPION using glutaraldehyde shows a loss of activity relative to the free enzyme of over 99 % across all percentage loadings studied. This technique would appear to be unsuitable for the immobilisation of antibodies; it would likely completely remove the ability of the antibody to bind its target. A major contributing factor to the observed loss would appear to be reaction via one of HRP's few available amine groups. When HRP is conjugated to trastuzumab via an amine group, the activity of the conjugate is 16.4 % of that of the native free enzyme (a loss of 83.6 %). There is a negative effect on the active site and/or the ability of substrate to bind. This likely contributes to the poor activity retained when HRP is immobilised using glutaraldehyde, but is not the sole factor; the tightness of the binding or an enforced orientation may also be limiting functionality.

Greater retention of the enzymatic activity of HRP is observed when conjugation to nanoparticles occurs through the sugar side chain; retained activity is higher when the number of protein-nanoparticles conjugates within a SPION population is low. As the glycan of trastuzumab is on the Fc region and away from the antigen binding site, immobilisation by reductive amination onto SPION would not be expected to prevent antigen binding. Keeping the number of immobilised biomolecules in a nanoparticle population low is desirable; the apparent decreased colloidal stability of SPION following HRP conjugation or HRP-mAb conjugation suggests that as biomolecule size increases, samples may be more likely to aggregate. Unfortunately, DLS studies did not yield representative data on the degree of aggregation within the different samples.

The synthesis of the HRP-trastuzumab conjugate species demonstrates the successful bioconjugation of an antibody via the sugar side chain at Asn297. The immobilisation of HRP by reductive amination shows how immobilisation via a sugar group may have a limited effect on enzyme function when protein content in a sample is low. To confirm that an antibody immobilised on SPION via reductive amination would be able to specifically bind its target cell-surface receptor, *in vitro* cell-line studies are required. The synthesis of such conjugates and their *in vitro* and *in vivo* testing is discussed in Chapter 4.

3.5 References

- 1 G. T. Hermanson, *Bioconjugate Techniques*, Academic Press, London ; Waltham, MA, 3rd edition., 2013.
- 2 H. B. Breitz, P. L. Weiden, P. L. Beaumier, D. B. Axworthy, C. Seiler, F.-M. Su, S. Graves, K. Bryan and J. M. Reno, *J. Nucl. Med.*, 2000, **41**, 131–140.
- 3 S. Panowski, S. Bhakta, H. Raab, P. Polakis and J. R. Junutula, *mAbs*, 2013, **6**, 34–45.
- 4 M. P. Cude and C. D. Gwenin, *ECS Trans.*, 2011, **33**, 79–89.
- 5 S. Ding, A. A. Cargill, I. L. Medintz and J. C. Claussen, *Curr. Opin. Biotechnol.*, 2015, **34**, 242–250.
- 6 K. L. Lazar, T. W. Patapoff and V. K. Sharma, *mAbs*, 2010, **2**, 42–52.
- 7 S. Vira, E. Mekhedov, G. Humphrey and P. S. Blank, *Anal. Biochem.*, 2010, **402**, 146–150.
- 8 B.-W. Park, K.-A. Ko, D.-Y. Yoon and D.-S. Kim, *Enzyme Microb. Technol.*, 2012, **51**, 81–85.
- 9 S. S. Mark, S. I. Stolper, C. Baratti, J. Y. Park, M. A. Taku, J. J. Santiago-Avilés and L. J. Kricka, *Macromol. Biosci.*, 2008, **8**, 484–498.
- 10 R. Narain, Ed., *Chemistry of Bioconjugates: Synthesis, Characterization, and Biomedical Applications*, Wiley-Blackwell, Hoboken, New Jersey, 1st edition., 2014.
- 11 H. J. W. L. Aerts, L. Dubois, T. M. Hackeng, R. Straathof, R. K. Chiu, N. G. Lieuwes, B. Jutten, S. A. Wepler, G. Lammering, B. G. Wouters and P. Lambin, *Radiother. Oncol.*, 2007, **83**, 326–332.
- 12 G. B. Wisdom, in *The Protein Protocols Handbook*, ed. J. Walker, Humana Press, 1996, pp. 273–274.
- 13 G. B. Wisdom, in *Immunochemical Protocols*, ed. R. Burns, Humana Press, 2005, pp. 127–130.
- 14 M. H. El-Dakdouki, K. El-Boubbou, J. Xia, H. Kavunja and X. Huang, in *Chemistry of Bioconjugates*, ed. R. Narain, John Wiley & Sons, Inc., 2014, pp. 281–314.
- 15 S.-H. Tseng, M.-Y. Chou and I.-M. Chu, *Int. J. Nanomedicine*, 2015, **10**, 3663–3685.
- 16 I. Migneault, C. Dartiguenave, M. J. Bertrand and K. C. Waldron, *BioTechniques*, 2004, **37**, 790–796, 798–802.
- 17 O. Barbosa, C. Ortiz, Á. Berenguer-Murcia, R. Torres, R. C. Rodrigues and R. Fernandez-Lafuente, *RSC Adv.*, 2013, **4**, 1583–1600.
- 18 'Overview of ELISA', <http://www.piercenet.com/method/overview-elisa> (accessed 09/02/2017)
- 19 D. Voet, J. G. Voet and C. W. Pratt, *Fundamentals of Biochemistry: Life at the Molecular Level*, Wiley, Hoboken, NJ, 2nd edition., 2012.
- 20 T. D. H. Bugg, *Introduction to Enzyme and Coenzyme Chemistry*, John Wiley & Sons, Hoboken, NJ, 3rd edition., 2012.
- 21 W. Kaim, B. Schwederski and A. Klein, *Bioinorganic Chemistry -- Inorganic Elements in the Chemistry of Life: An Introduction and Guide*, Wiley, Chichester, West Sussex, United Kingdom, 2nd edition., 2013.
- 22 J. I. Herren, K. S. Kunzleman, C. Vocelka, R. P. Cochran and B. D. Spiess, *Stroke*, 1997, **28**, 2025–2030.
- 23 N. C. Veitch, *Phytochemistry*, 2004, **65**, 249–259.
- 24 F. W. Krainer and A. Glieder, *Appl. Microbiol. Biotechnol.*, 2015, **99**, 1611–1625.
- 25 G. I. Berglund, G. H. Carlsson, A. T. Smith, H. Szöke, A. Henriksen and J. Hajdu, *Nature*, 2002, **417**, 463–468.
- 26 'Enzyme Substrates for ELISA', <https://www.thermofisher.com/uk/en/home/life-science/protein-biology/protein-assays-analysis/elisa/elisa-reagents-buffers/enzyme-substrates-elisa.html> (accessed 09.02/2017)
- 27 S. S. Deepthi, E. Prasad, B. V. S. Reddy, B. Sreedhar and A. B. Rao, *Green Sustain. Chem.*, 2014, **04**, 15–19.
- 28 S. Nag, *The Blood-Brain Barrier: Biology and Research Protocols*, Humana Press, Totawa, NJ, 2003.
- 29 A. Jeanson, J. M. Cloes, M. Bouchet and B. Rentier, *J. Immunol. Methods*, 1988, **111**, 261–270.
- 30 J. P. Tresca, R. Ricoux, M. Pontet and R. Engler, *Ann. Biol. Clin. (Paris)*, 1995, **53**, 227–231.

- 31 S. A. Mohamed, M. H. Al-Harbi, Y. Q. Almulaiky, I. H. Ibrahim and R. M. El-Shishtawy, *Electron. J. Biotechnol.*, 2017, **27**, 84–90.
- 32 H. Wu, Y. Liu, M. Li, Y. Chong, M. Zeng, Y. M. Lo and J.-J. Yin, *Nanoscale*, 2015, **7**, 4505–4513.
- 33 Q. Wan, H. Song, H. Shu, Z. Wang, J. Zou and N. Yang, *Colloids Surf. B Biointerfaces*, 2013, **104**, 181–185.
- 34 Z. M. Saiyed, S. Sharma, R. Godawat, S. D. Telang and C. N. Ramchand, *J. Biotechnol.*, 2007, **131**, 240–244.
- 35 'Introduction to Size Exclusion Chromatography', <http://www.bio-rad.com/en-uk/applications-technologies/introduction-size-exclusion-chromatography> (accessed 22/02/2017)
- 36 K. Wilson and J. Walker, Eds., *Principles and Techniques of Biochemistry and Molecular Biology*, Cambridge University Press, Cambridge, UK : New York, 7th edition., 2010.
- 37 'Disposable PD-10 Desalting Columns', <http://www.gelifesciences.com/webapp/wcs/stores/servlet/ProductDisplay?categoryId=11522&catalogId=10101&productId=22954&storeId=12751&langId=-1>, (accessed 22 February 2017).
- 38 J. A. Bornhorst and J. J. Falke, *Methods Enzymol.*, 2000, **326**, 245–254.
- 39 J. Schmitt, H. Hess and H. G. Stunnenberg, *Mol. Biol. Rep.*, 1993, **18**, 223–230.
- 40 G. Chaga, J. Hopp and P. Nelson, *Biotechnol. Appl. Biochem.*, 1999, **29 (Pt 1)**, 19–24.
- 41 N. N. Greenwood and A. Earnshaw, *Chemistry of the Elements*, Butterworth-Heinemann, Oxford ; Boston, 2nd edition., 1997.
- 42 H. Block, B. Maertens, A. Spriestersbach, N. Brinker, J. Kubicek, R. Fabis, J. Labahn and F. Schäfer, *Methods Enzymol.*, 2009, **463**, 439–473.
- 43 US5266686 A, 1993.
- 44 'Antibody Purification Methods', <https://www.thermofisher.com/uk/en/home/life-science/antibodies/antibodies-learning-center/antibodies-resource-library/antibody-methods/antibody-purification-methods.html> (22/02/2017)
- 45 M. H. Simonian, in *Current Protocols in Cell Biology*, John Wiley & Sons, Inc., 2002, p. A.3B.1-A.3B.7.
- 46 'Nanodrop Microvolume Spectrophotometers', <http://www.nanodrop.com/Default.aspx> (accessed 22/02/2017)
- 47 S. M. Kelly, T. J. Jess and N. C. Price, *Biochim. Biophys. Acta BBA - Proteins Proteomics*, 2005, **1751**, 119–139.
- 48 'An Introduction to Circular Dichroism Spectroscopy', <https://www.photophysics.com/resources/introduction-circular-dichroism-spectroscopy> (accessed 23/02/2017)
- 49 N. J. Greenfield, *Nat. Protoc.*, 2006, **1**, 2876–2890.
- 50 P. F. Hollenberg, T. Rand-Meir and L. P. Hager, *J. Biol. Chem.*, 1974, **249**, 5816–5825.
- 51 Y. Hayashi and I. Yamazaki, *J. Biol. Chem.*, 1979, **254**, 9101–9106.
- 52 S. Avrameas and T. Ternynck, *Immunochemistry*, 1971, **8**, 1175–1179.
- 53 T. J. Bruno and P. D. N. Svoronos, *CRC Handbook of Basic Tables for Chemical Analysis*, CRC Press, Boca Raton, FL, 3rd Edition., 2010.
- 54 P. Walker and W. H. Tarn, *CRC Handbook of Metal Etchants*, CRC Press, Boca Raton, FL, 1990.
- 55 R. Eisenthal, Ed., *Enzyme Assays: A Practical Approach*, Oxford University Press, U.S.A., Oxford, 2nd Edition., 2002.
- 56 M. Hamm, Y. Wang and R. R. Rustandi, *Pharmaceuticals*, 2013, **6**, 393–406.

Chapter 4: *In vitro* and *in vivo* validation of Trastuzumab-conjugated SPION

4.1 Introduction

The development of reproducible syntheses of biocompatible SPION with the ability to bear biomolecules discussed in the previous chapters was intended as a precursor to the *in vivo* use of radiolabelled SPION bearing a clinically relevant antibody. Initial experiments were required to optimise the fluorescent labelling of an antibody, which could be immobilised and then followed *in vitro* to observe its' pharmacologic behaviour. *In vitro* validation led to the design of *in vivo* experiments using animal breast cancer models (mice bearing xenograft tumours). Finally, the radiolabelling of APTES@SPION described in Chapter 2 was increased in preparation for the *in vivo* following of the biodistribution of PET active FITC-Trastuzumab-APTES@SPION. This introduction is intended to introduce the antibody being used and the techniques and equipment employed in each step from the bench to the pre-clinical PET scanner.

4.1.1 Clinical use of Trastuzumab

Genetic mutations within cancer cell nuclei often results in the overexpression of growth factors and growth factor receptors; the EGFR (epidermal growth factor receptor) family consists of four related species, of which Her-2 is of great importance. The overexpression of this receptor is relatively common in breast cancers (20-30 %) and is negatively correlated with prognosis and survival.^{1,2} Overexpression can occur at up to one hundred times that of healthy tissues and is common in a high proportion of both primary and metastatic tumour cells, making anti-Her-2 therapy a desirable route for clinical management.¹

Trastuzumab is an FDA-approved recombinant humanised mAb that is indicated for the treatment of adjuvant and metastatic breast cancers shown in *ex vivo* assays to overexpress the Her-2 receptor, although correlations between measured Her-2 overexpression and trastuzumab therapy effectiveness are imperfect.^{3,4} Although costly, when trastuzumab therapy is effective its effects are profound; however severe side effects such as cardiotoxicity occur independently of administered dose⁴ and patients can exhibit or develop trastuzumab resistance.⁵ A more direct and effective method of assessing a patient's likely response to trastuzumab therapies is needed if this antibody is to remain a viable clinical option worldwide.

The mechanism of action of Trastuzumab is still a subject of research, but it seems clear that it downregulates tumour growth via multiple pathways. All members of the EGFR family have extra-cellular domains to which ligands or antibodies can bind. It is proposed that Trastuzumab binds to the extracellular domain of Her-2 and prevents receptor dimerisation and receptor shedding while promoting antibody dependant cell-mediated cytotoxicity (ADCC) and endocytosis, all of which contribute to the dampening of Her-2 mediated cell proliferation.³ The specificity of Trastuzumab for the extracellular domain of the Her-2 receptor and the considerable excess of the latter in cancerous tissues over healthy tissues render this antibody suitable for use in the development of immunoPET agents as discussed in Chapter 1.

Radiolabelling of Trastuzumab- therapy and diagnostics

As was discussed in Chapter 1, long half-life radiometals have become the preferred agents for the radiolabelling of antibodies due to the need to ‘match’ the long biological half-life of the mAb.⁶ Because of its notable clinical successes Trastuzumab is relatively commonly used in the development of radiopharmaceuticals using metal isotopes, examples of which are shown in Table 1.

Radiometal used (half-life)	Method of labelling	Clinical purpose	Sources
¹¹¹ In (67.3 h)	DTPA chelation	SPECT imaging	7,8
⁸⁶ Y (14.7 h)	DTPA chelation	PET imaging	9
^{99m} Tc (6 h)	Direct coordination	SPECT imaging	10
⁸⁹ Zr (78.4 h)	DFO chelation	PET imaging	11
	DOTAGA chelation		12
⁶⁴ Cu (12.7 h)	DOTA chelation	PET imaging	13,14
²¹² Pb (10.6 h)	TCMC chelation	Radiotherapy	15
¹⁷⁷ Lu (159 h)	DOTA chelation	Radiotherapy	16

Table 1. Selected examples of radiometals used to label Trastuzumab for imaging or therapeutic purposes.

The methods described in Table 1 all require the direct radiolabelling of the antibody, an approach which is inherently limited by the need to avoid altering the protein structure by the addition of coordinating groups.¹² This could theoretically be circumvented by conjugating Trastuzumab to a single nanoparticle bearing multiple radioisotopes. Trastuzumab has been the subject of bioconjugation to SPION via various methods reported in the literature,^{17–19} but to date only one research group has reported radiolabelled, Trastuzumab bearing SPION, and radiolabelling of the antibody occurs post-immobilisation.^{20–22} Radiolabelling of SPION with a long half-life radioisotope (such as ⁸⁹Zr) followed by conjugation to Trastuzumab has not previously been reported in the literature.

4.1.2 PET isotope production, handling and storage

In the field of immunoPET, zirconium-89 is king. This isotope has near ideal decay characteristics for use in immunoPET imaging: a long half-life ($t_{1/2} = 78.4$ h), an acceptable percentage of beta decay (22.7 %) and low energy emitted positrons (396 keV, leading to higher resolution).²³ The coordination of zirconium by DFO or by novel ligand systems conjugated to an antibody is commonly reported in the literature and numerous articles reviewing the field exist for the interested reader.^{23–25} Leaching of the isotope from complexes *in vivo* can result in bone sequestration leading to additional radiation exposure for patients, hence the need to develop improved methods of ⁸⁹Zr administration.²³ The methods described in Chapter 2 for the ⁸⁹Zr radiolabelling of APTES@SPION bear more in common with the methods of arsenic- or germanium-labelling SPION reported by the Cai group,^{26,27} who also reported the zirconium labelling of mesoporous silica nanoparticles where deprotected silanol groups act as hard electron donors for the radiometal.²⁸ When the ability of iron oxides to accept other metal ions into the lattice is considered, it would seem that studies of directly ⁸⁹Zr-labelled SPION are long overdue.

⁸⁹Zr production and purification

The production of ⁸⁹Zr most commonly occurs from commercially available, stable ⁸⁹Y foil that is irradiated with a high energy proton beam (≥ 14 MeV).^{23,29} The inclusion of a proton into the nucleus of ⁸⁹Y converts the atom into unstable ⁸⁹Zr (Fig. 1a)

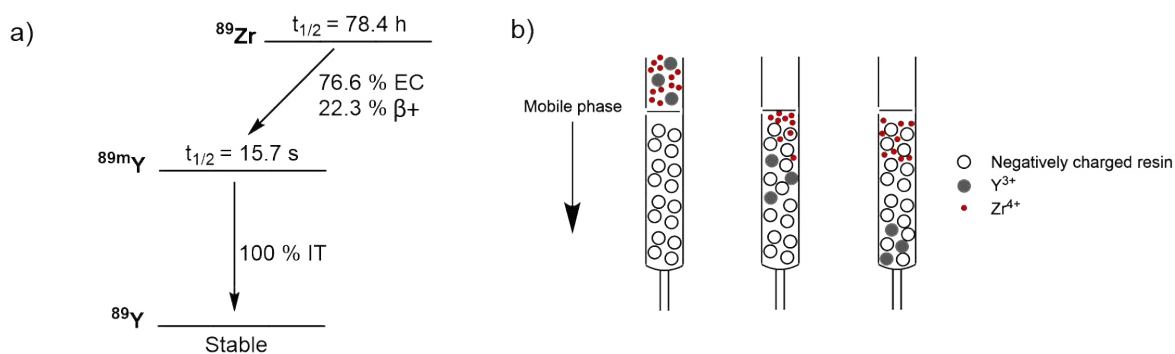


Figure 1a. Simplified decay scheme for ^{89}Zr (EC = electron capture, IT = isomeric transition).²³ **b.** Simplified illustration of Cationic Ion Exchange chromatography.

Purification of the radioisotope from starting materials or impurities arising from side reactions is achieved chromatographically by dissolving the ^{89}Zr enriched target in dilute hydrochloric acid then applying the radioactive solution to a hydroxamate functionalised acidic ion-exchange resin, for which Zr^{4+} has higher affinity than Y^{3+} (Fig. 1b).³⁰ Washing away the starting material leaves the product radioisotope bound; elution is achieved by the application of 1 M oxalic acid.²⁹ Standard operating procedures can be defined for these procedures within an imaging centre (see Appendix I), which can standardise the efficiency and yield of production while minimising operator exposure time (see below).

Safe handling and exposure limits

The use of any radioactive material is strictly controlled and subject to legislation for the protection of the operator and the public at large. In the context of research, facilities must be provided that allows for the safe manipulation of radioactive material. While the levels of radioactivity present in a hot cell or the lab in general should be constantly monitored, it is important that all persons present (especially the primary operator) wear personal dosimeters at all times during experimentation to prevent over-exposure to radiation. For classified radiation workers, the legal exposure limit per annum is 20 mSv.³¹ Local rules are often enforced to prevent workers reaching this limit; in PETIC, University Hospital Wales, an ALARA (As Low As Reasonably Achievable) daily limit of 20 μSv is imposed where if the limit is reached or exceeded regularly, the operator is encouraged to reassess risk and their laboratory practice. For example, increasing distance from a radiation source reduces the received dose according to the relationship:³²

Minimising exposure time and maintaining appropriate shielding also protects the operator. Zirconium-89 requires thicker shielding than the purely positron emitting fluorine-18; the 909 keV gamma rays emitted by the former have a half-value in lead of 10 mm.²³

Radioactivity units

Radioactivity can be measured in multiple units depending on context. The energy that radiation imparts to a biological absorbent is measured in Gray (Gy), where 1 Gy is equivalent to 1 J.kg⁻¹. The unit of absorbed radiation dose is the Sievert (Sv) which is referenced against the biological impact of 1 Gy of X-rays. Dose rates are measured in Sv.h⁻¹ and dosimeters can be calibrated to give an alarm if a safe dose rate is exceeded.³²

From an experimental perspective, the Becquerel (Bq) is used as the SI unit of radioactivity and is equivalent to 1 disintegration per second (and this linked to half-life). The measured activity, A, of a radiolabelled sample can be related to the number of radioisotopes present N:

—

Because radioactive decay follows a natural logarithm, the half-life ($t_{1/2}$) of an isotope in seconds relates to the decay constant λ by:

—

The number of radioisotopes can also be related to the mass of a radiotherapeutic or radiodiagnostic agent in terms of the Specific Activity (S) in units of Bq/g:

—

Where m_{radio} is the mass of the agent. Specific activity should ideally be high for radioimaging because a smaller molar quantity of the agent will be required to meet detection limits, limiting potential toxicity.³²

4.1.3 Cell culture and xenotransplantation

A thorough exploration of the theory and practice of *in vitro* cell culture in medical research is not appropriate to the current discussion but a brief overview is necessary to contextualise the experimental approach taken below. The *in vitro* maintenance of a healthy population of cells derived from living tissue requires careful attention to several key factors:

- The initial population must be pure and sterile (i.e. a monoculture)
- Experimental conditions are optimised for growth of cells
- Appropriate aseptic technique is used at all times to protect the cells.

Typically, cells that express a particular disease characteristic (e.g. the Her-2 over-expressing cell line BT-474 or the 'triple negative' cell line MDA-MB-468)³³ may be purchased in a sterile form from commercial suppliers and stored frozen prior to use.³⁴ Similarly, a range of culture media (which provide nutrients for cell growth and protective broad-spectrum antibiotics) is available to purchase or may be prepared as needed and can be sterilised to avoid the introduction of competitive bacteria into cell culture. Assuming the use of suitable equipment and facilities such as cell culture hoods, incubators and non-porous surfaces (discussed below), the main concern of researchers practicing cell culture is ensuring aseptic technique.

Cell culture equipment

Initial choice of cell-line is dictated by the nature of the research question. Once a cell-line is selected, an initial population is taken from storage (typically at -78 °C) and resuscitated, then transferred to a disposable vessel of tissue-culture grade plastic and given an appropriate volume of a suitable media. All cell manipulations occur under sterile conditions in a laminar flow hood.³² There are three types of hood, designated Class I, II and III; while a Class I hood would be familiar to the chemist, Class II hoods are more commonly used in tissue culture as they provide protection to the operator *and* to the cells as air drawn into the hood is sterilised using a High Efficiency Particulate Air (HEPA) filter prior to being blown onto the cells. Class III hoods are sealed from the outside environment to maximise operator protection.

All surfaces inside the hood are made from non-porous metals and plastics and are sterilised before and after use with 70 % alcohol or 70 % methylated spirits. The operator wears appropriate PPE while working in the hood and sterilises their hands using the same alcoholic solution.

Once work in the hood is completed, the culture vessel is closed and transferred to a water jacketed incubator. Environmental conditions inside the incubator are optimised for cell culture growth by maintaining a temperature of 37 °C, constant humidity, and CO₂-enriched air (5-10 %). The cells are incubated while they fix to the vessel surfaces and divide until they reach a maximum surface coverage. Sub-culturing may be required to maintain growth rates.

This is often performed using the proteolytic enzyme trypsin which breaks the bonds between cells and the vessel walls, allowing for the transfer of cells.³²

Cell cultures may be monitored using optical microscopy, from which much information can be derived; cellular stress responses (e.g. to sub-optimal conditions, lack of nutrients or infection) can be observed and counter-acted rapidly. Throughout the culture stage, the cells should be checked and the media replaced regularly to encourage growth.

Aseptic technique

The first consideration when performing experimental manipulations under sterile conditions is the cleanliness of the facilities; as discussed, cleaning all surfaces inside a Class II fume hood ensures a clean working environment. All media should be prepared in such an environment and all equipment such as pipettes, pipette tips, centrifuge tubes and other vessels should be clean and autoclaved prior to use. All waste, spillages or excess reagents should be disposed of rapidly and the operator should ensure the cleanliness of their hands and lab coat prior to entering the hood.

It is sometimes necessary to perform sterile work at the bench. For example, in the experiments discussed below, the preparation of antibody-nanoparticle conjugates could not be performed in a dedicated sterile lab. In this case, sterility inside the reaction vessel was obtained by virtue of the reagents present (e.g. sodium cyanoborohydride, ethanolamine) and maintained during washing by the use of buffers that had been sterilised in an autoclave. All manipulations were carried out in close proximity to a Bunsen burner on an orange flame. The flame destroys local airborne contaminants and creates a protective updraft.

Cell counting and viability

When a cell culture is ready to use, the sample will be observed microscopically to check for any issues in the health or behaviour of the cells, the cells will be counted and the viability of the sample determined (the percentage of live cells present in the total population). These steps are commonly performed using a haemocytometer, in which a sample of the cell culture of known volume is transferred to a cell following incubation with a dye that colours dead or dying cells.³² A haemocytometer is a glass slide of known volume bearing an etched grid. Each square of the grid represents a volume of 0.1 mm^3 and the number of cells present in this volume can be determined microscopically, allowing for a calculation of cells per unit of volume and the total number of cells in a sample of culture suspension. Within this number, the number of dead cells can be determined following incubation with a dye (e.g. Trypan blue or DAPI) which stains the nuclei of dead cells a different colour to those of living cells.³⁵ The proportion of living cells in a sample is expressed as a percentage quantity referred to as *cell viability*, which can be useful in quantifying how the presence of a drug species or exposure to unfavourable conditions affects the well-being of a cell culture. Cell counting and cell viability assays can be performed together automatically with appropriate equipment.³⁶

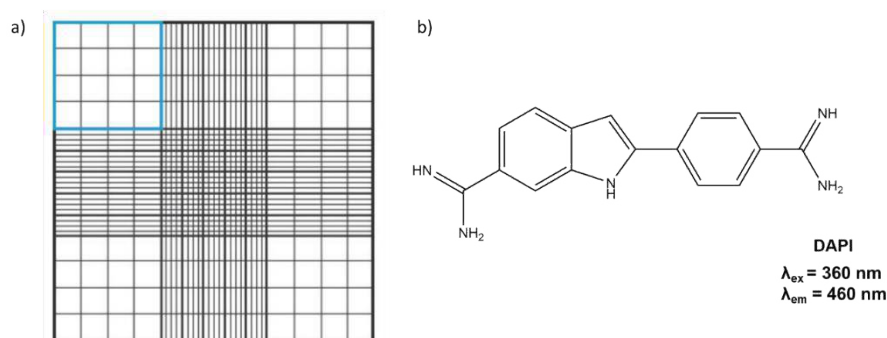


Figure 2a. Haemocytometer grid with a set of 16 squares for counting highlighted.³⁷ **b.** DAPI, a fluorescent stain that preferentially binds to DNA in dead cells; it is excreted by living cells.³⁸

Xenotransplantation

Xenotransplantation is the transfer of living cells, tissues or organs from one species into another. The ability to use animals as models for human diseases has been crucial in the development of drugs and therapies. They provide pharmacologic and toxicological information which can guide research prior to trials in human disease models, although their predictive power is disputed.^{39–41} Rodent models are commonly used in research due to their small size, short breeding cycle and limited cost, with the favoured model, mice, being 95 %

identical to humans on the genomic level.³⁹ Within breast cancer research, the implantation of human breast cancer cells into immunocompromised mice is a common method of investigating the pathology of the disease, often viewed as the gold standard for therapy development.⁴² Cells from immortal cell lines are commonly used, although the use of cells taken directly from a human patient (patient-derived xenografts) is also possible.⁴³ The use of immuno-deficient mice is necessary to ensure xenograft survival by limiting rejection of the foreign cells. In the experiments described below nude (*nu*) mice are used which are athymic and consequently have few or no T-cells which contribute to antibody formation and graft rejection.^{44,45} The most frequently used method of xenotransplantation is the subcutaneous injection into a mouse of a population of cancerous cells suspended in media such as Matrigel, an extracted protein from a murine cancer that is fluid at 4 °C but gels at physiological temperatures. The gelling of Matrigel increases the likelihood that the injected cells will ‘take’ and develop into a solid tumour *in vivo*.⁴⁶

Once xenotransplantation has occurred, the mice must be kept in sterile conditions and cared for while the tumours grow. As part of the ethical guideline imposed on the use of animals in research, it is important to prevent pain and suffering and so regular checking on the overall health of the animals as well as the development of the tumour must be carried out. When undue suffering is identified e.g. the tumour has become necrotic, infected or is severely reducing motility, it is important that the animal in question is euthanised humanely as soon as possible.⁴⁷ Experimental approaches often allow tumours to grow either for a defined period of time or until they reach a defined physical parameter e.g. volume in an effort to prevent this.^{48,49}

Small animals bearing xenotransplant tumours can be administered PET contrast agents and imaged in ‘pre-clinical’ PET-CT scanners in an effort to bridge the gap between *in vitro* validation and use in larger animals and humans.^{50,51} Care must be taken throughout with regards to anaesthesia and environmental conditions; rodents can die within minutes of hypothermia.⁵² As in clinical PET-CT scanners, the overlay of the location of annihilation events onto a reconstructed anatomical image allows for the following of the radioagent through the body, and the extraction of data from defined regions of interest (typically organs).^{52,53}

4.1.4 Fluorescence- dyes, microscopy and FACS for *in vitro* cell studies

To confirm the retention of antibody specificity following modification (e.g. bioconjugation to nanoparticles) requires the use of cell lines expressing the target antigen; for Trastuzumab, BT-474 (Her-2 overexpressing) cells are used. The binding of antibody and antigen can be

visualised directly when the antibody is fluorescently labelled, allowing the use of fluorescence microscopy and Fluorescence Activated Cell Sorting (FACS).

Fluorescence is one of a number of luminescent processes by which a molecule can emit light when it relaxes from an electronically excited state (ES) to a ground state (GS) (see Fig. 3). Because fluorescence imaging is most commonly used in cell studies, other luminescent processes will not be discussed in detail. Fluorescence occurs when the excited electron is spin paired to the ground state electron, relaxation is spin allowed and relaxation is fast (less than 10 ns).⁵⁴

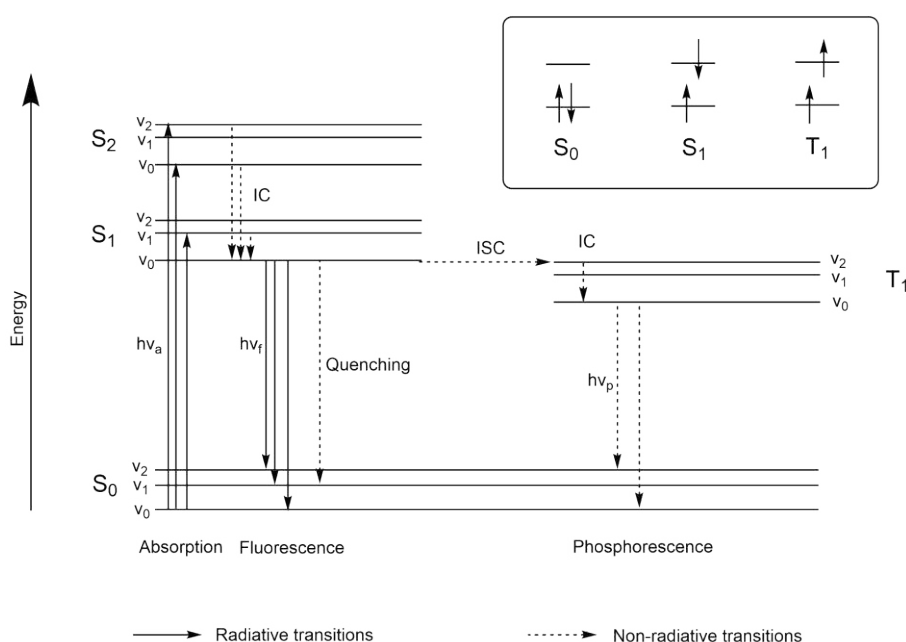


Figure 3. Jablonskii diagram showing the energy levels and transitions available for fluorophores (IC = internal conversion, ISC = inter-system crossing). Adapted from multiple sources.^{32,54}

A molecule at room temperature will typically be in a low electronic (S₀) and vibrational energy level (v₀). The absorption of a photon of light with energy $h\nu_a$ will excite an electron to occupy any of a number of discrete higher electronic and vibrational levels.³² Vibrational relaxation to the ground vibrational level of S₁ (i.e. S₁v₀) occurs rapidly (picosecond timescale) by non-radiative processes called Internal Conversion (IC).⁵⁵ Further non-radiative transition from S₁ to S₀ can occur due to external factors (e.g. quenching, discussed below). The radiative relaxation of the electron from S₁ to S₀ can occur by the emission of a photon with energy $h\nu_f$; this is fluorescence emission. Because energy is lost from the system due to IC, the emitted photon has a longer wavelength than the absorbed photon, a shift towards the red end of the spectrum referred to as a red, bathochromic or Stokes shift.⁵⁵ The Stokes shift

is crucial to emission based technologies because it allows for the use of optical filters to prevent excitation wavelengths reaching the detector, decreasing the background against which fluorescence is detected.⁵⁵ The average time taken for an excited electron to relax back to the ground state by fluorescence is known as the fluorescence lifetime (τ). The ratio of total photon emission over total photon absorption is called the Quantum Yield (Φ), and ranges from 0 to 1 as a measure of the fluorophore's efficiency. An ideal fluorophore for biomolecule labelling will have a large Stokes shift, a lifetime on the order of nanoseconds and a high quantum yield, all of which aid in the *in vitro* detection of the species.⁵⁶

Fluorophore design, selection and photophysical characteristics

Fluorophores are comparatively rare because most molecules are structurally flexible and have vibrational energy levels of the electronic ground state that overlap with the vibrational energy levels of the excited state, permitting complete relaxation by non-radiative transitions. Most commercially available organic fluorescent dyes have rigid aromatic ring systems that prevent this overlap (see Fig. 4).³² A dye's photophysical and chemical properties can be changed by exchanging functional groups around the fluorescent core to optimise their utility in different applications. The reactive groups present on the dyes will be familiar from the discussion of bioconjugation techniques in Chapter 3.

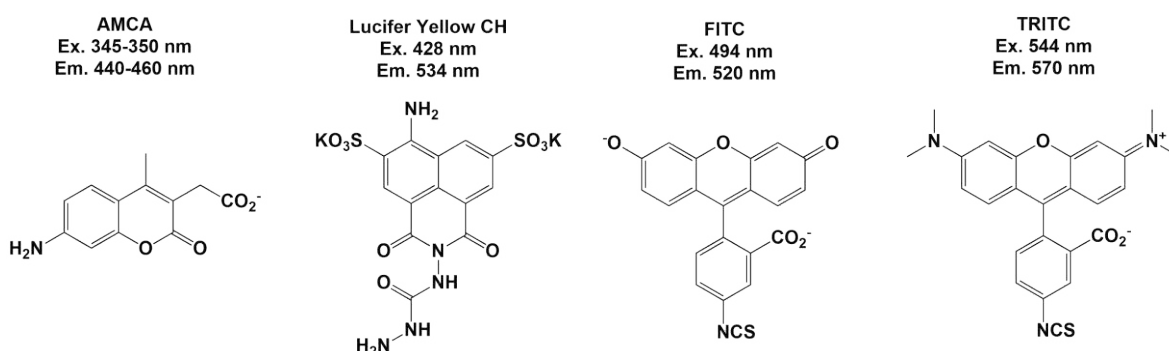


Figure 4. Several commercially available fluorescent dyes commonly used in bioconjugation. Analogues bearing different reactive groups for different coupling methodologies are available.⁵⁶

FITC (Fluorescein isothiocyanate) is one of the most commonly employed amine-reactive dyes for labelling biomolecules; although it is prone to photobleaching (irreversible loss of fluorescence due to chemical changes brought on by excitation),⁵⁵ its photophysical properties, aqueous solubility and well-understood reactivity make it an excellent dye for initial research. Several general protocols for antibody labelling with FITC exist, but modification is required for each biomolecule to optimise the degree of labelling (the F/P

ratio).^{56,57} This can be determined spectroscopically from the ratio of the absorbance of the protein at 280 nm and the fluorophore at 495 nm for FITC-IgG conjugates:

Having selected an appropriate fluorophore, the potential for quenching in the final species should be considered. Quenching is the reduction of fluorescence emission intensity, most commonly due to contact and energy transfer between the excited molecule and another species (collisional quenching). This can be due to dye-dye interactions at high degrees of substitution on a protein,⁵⁶ the presence of molecular oxygen in solution⁵⁵ or the action of uncoated iron oxide nanoparticles.⁵⁸ Coated, stabilised SPION have little quenching effect on fluorophores, so it is more important to ensure that the F/P ratio is optimised to maximise emission intensity while avoiding self-quenching or the altering of the biomolecule's structure and functionality. A 'rule of thumb' is between two and five fluorophores per biomolecule is acceptable, depending on the fluorophore.⁵⁹

Fluorescence microscopy

Fluorescence microscopy is commonly used to visualise fluorescence occurring in cell cultures or in thin tissues. Naturally non-emissive cells can be observed to fluoresce following incubation with dyes or dye-bearing biomolecules and appropriate excitation. This allows for greater signal-to-noise ratios than are available using conventional microscopy.⁵³ Two commonly used forms are epifluorescence (or conventional fluorescence) and confocal fluorescence microscopy, of which the former is relevant here.⁵³ Briefly, a light source is used to illuminate a sample, but with the use of a filter that only lets light with the appropriate excitation wavelength through. This reflects off a dichromatic mirror and is focussed on the subject by the objective lens. The emitted light has a longer wavelength and passes through the dichromatic mirror and an emission filter so that the emitted light is the only signal that forms an image.³² By this method, the binding of a fluorescently labelled antibody to a cell surface receptor can be visualised directly.

FACS

Fluorescent Activated Cell Sorting (FACS) is a technique used to sort live cells based on their fluorescence properties. This occurs by use of a flow cytometer, where cells in an aqueous medium are taken up, aerosolised and passed individually through a chamber where they are excited with light (Fig. 5). The light that is scattered, reflected or emitted by a cell is used to profile it and used to trigger electromagnetic sorting of cells into populations.³² Light

scattered forwards of the incident light beam is deemed ‘Front Scatter’ and gives an indication of cell or particle size; light scattered at 90 ° to the incident light beam (‘Side Scatter’) increases with cell internal granularity and the ‘roughness’ of the cell surface.⁶⁰ This allows not only the type of cells present in a mixture to be identified but also allows live cells, debris, and other solid materials (e.g. nanoparticles) to be distinguished from one another. The presence of a fluorophore on a cell can be determined by irradiating at a suitable excitation wavelength and observing for emission indicative of the fluorophore.

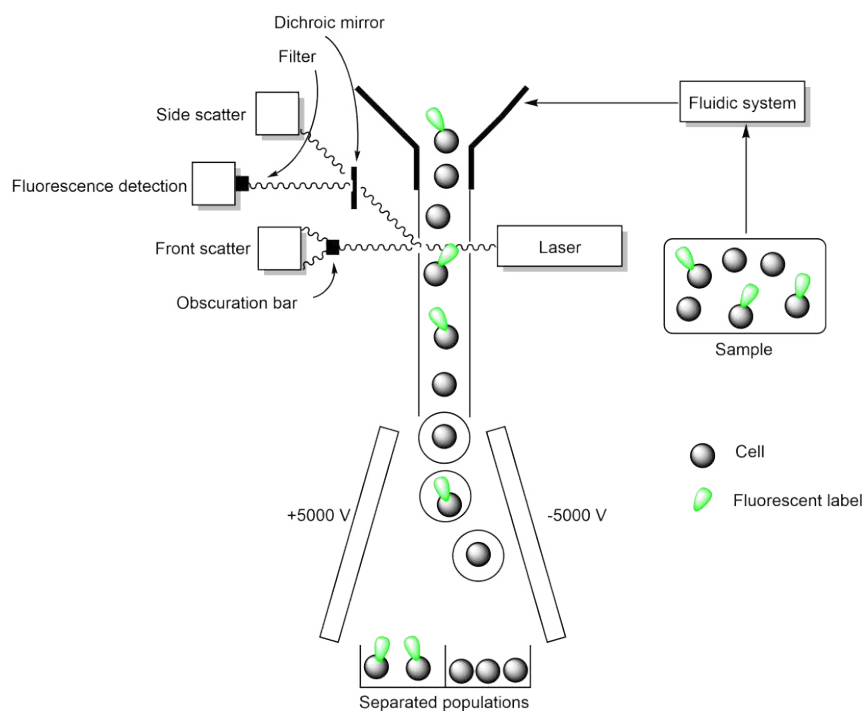


Figure 5. Simplified illustration of FACS. Cells are pumped into a conductive fluid sheath of buffered saline that is broken into droplets by vibration. The flow chamber charges the droplets, allowing for deflection when passing through the charged plates to achieve sorting. Profiling from front scatter, side scatter and fluorescence determine how cells are sorted. Adapted from multiple sources.^{32,60,61}

FACS analysis can be based on multiple parameters such as front scatter, side scatter and fluorescence. Raw data for a sorted cell population is typically expressed as a dot-plot (or two-parameter histogram) of front scatter against side scatter for each cell studied; it is therefore the operator’s responsibility to determine the identity of observed groupings (by use of control and reference populations) and select sub-populations for further analysis (e.g. excitation to confirm fluorescent labelling) by gating.⁶² Because of the flexibility in experimental design, FACS is a common method for the observation of antibody binding *in vitro* with single cell resolution.

4.1.5 Aims and objectives

This introduction has encompassed a broad range of topics needed to contextualise the experiments below. Direct relevance has taken precedence over depth for the sake of brevity, as is often necessary for experiments spanning multiple disciplines. Further information may be found in the referenced works.

Methods of synthesising biocompatible SPION which could be radiolabelled efficiently are discussed in Chapter 2, while Chapter 3 details the design and study of bioconjugate species based on these particles. The aim of the current work was to combine and develop these previously described approaches. Initial efforts were focussed on achieving the fluorescent labelling of trastuzumab and its' immobilisation by reductive amination on SPION. Incubation with breast cancer cell lines *in vitro* followed by FACS analysis and fluorescence microscopy was intended to show the retention of specificity by the mAb for the Her-2 receptor. Finally, the synthesis of analogous bioconjugates based on ^{89}Zr -labelled SPION preceded *in vivo* experiments utilising small animal cancer models that were intended to show directed contrast in the case of mice bearing Her-2 overexpressing solid tumours following administration of mAb-bearing SPION.

Additional Experimental Section II details related work exploring the potential use of novel naphthalimide dyes for labelling antibodies. The synthesis and characterisation of the dyes in question is included, along with an exploration of the failure to achieve suitable levels of bioconjugation.

4.2 Experimental

4.2.1 Material and methods

Reagents were commercial grade and were used without further purification. All reagents and solvents were purchased from Alfa Aesar or Sigma Aldrich. Pharmaceutical grade Herceptin® was obtained by kind gift of Velindre Hospital, Cardiff, Wales. UV-Vis studies were performed on a Jasco V-570 spectrophotometer as solutions (5×10^{-5} M) in CHCl_3 or H_2O . Photophysical data was obtained on a JobinYvon-Horiba Fluorolog spectrometer fitted with a JY-TBX picoseconds photodetection module as CHCl_3 , H_2O or DMSO solutions. Emission spectra were uncorrected and excitation spectra were instrument corrected. The pulsed source was a Nano-LED configured for 355 nm output operating at 1 MHz. Luminescence lifetime profiles were obtained using the JobinYvon-Horiba FluoroHub single photon counting module and the data fitted using DAS6 deconvolution software. BT-474 and MDA-MB-468 cells were obtained by kind gift from the Smalley group, Cardiff School of Biosciences. Cell counting and viability assays were performed on a Chemometec Nucleocounter NC-200. Flow cytometry was performed on a BD FACSAria Fusion and analysed using BD FACSDiva 8.0.1. Fluorescence microscopy was performed and analysed on a Bio-rad ZOE fluorescent cell imager. All animal experiments were performed under protocols approved by the Cardiff School of Biosciences and Cardiff School of Medicine. PET of tumour bearing mice was performed on a pre-clinical Mediso Nanoscan PET/CT and analysed using VivoQuant V2.50(patch 1) to obtain imaging region-of-interest (ROI) derived percentage of activity.

4.2.2 Synthesis and analytical techniques

FITC-labelling of Trastuzumab (1)

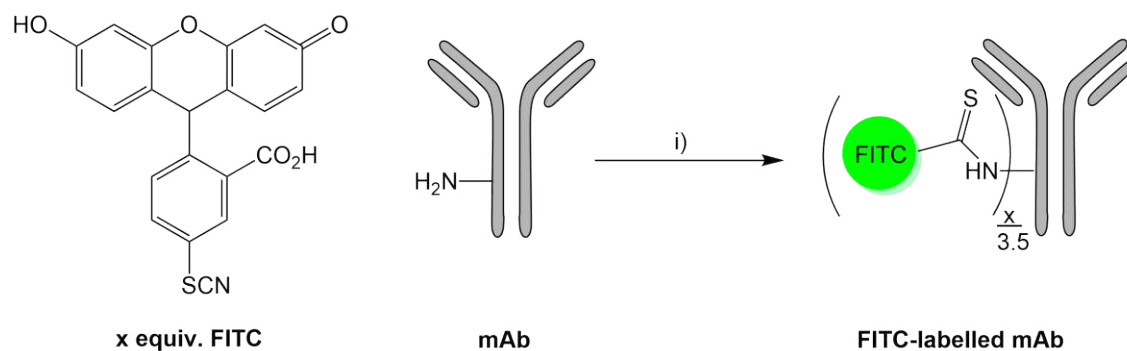


Figure 6. Simplified synthetic scheme for FITC-labelling of Trastuzumab. F/P ratio scales linearly with initial fluorophore excess. i) Overnight, 4 °C, H_2O .

Trastuzumab was dissolved in 0.1 M sodium carbonate buffer at pH 9.0 (5.0 mg.mL⁻¹). FITC was dissolved in dry DMSO (1.0 mg.mL⁻¹). The FITC solution was added to the antibody solution at 200 μ L per 1 mL in the dark, achieving a 15-fold excess of the fluorophore. The reaction was mixed overnight at 4 °C. Excess reagent was quenched by the addition of NH₄Cl to a concentration of 50 mM. The reaction mixture was purified by size exclusion chromatography on a PD-10 column, equilibrated with 10 mM sodium phosphate buffer, 0.15 M NaCl, pH 7.2. Protein concentration was monitored via A₂₈₀, and the most concentrated fractions were combined and concentrated to ~10 mg.mL⁻¹ for storage. UV-Vis spectrometry showed an F/P ratio of 4.2. Emission (H₂O): λ_{em} = 520 nm (3.40 ns, χ^2 = 0.91).

Immobilisation of FITC-Trastuzumab on APTES@SPION (2)

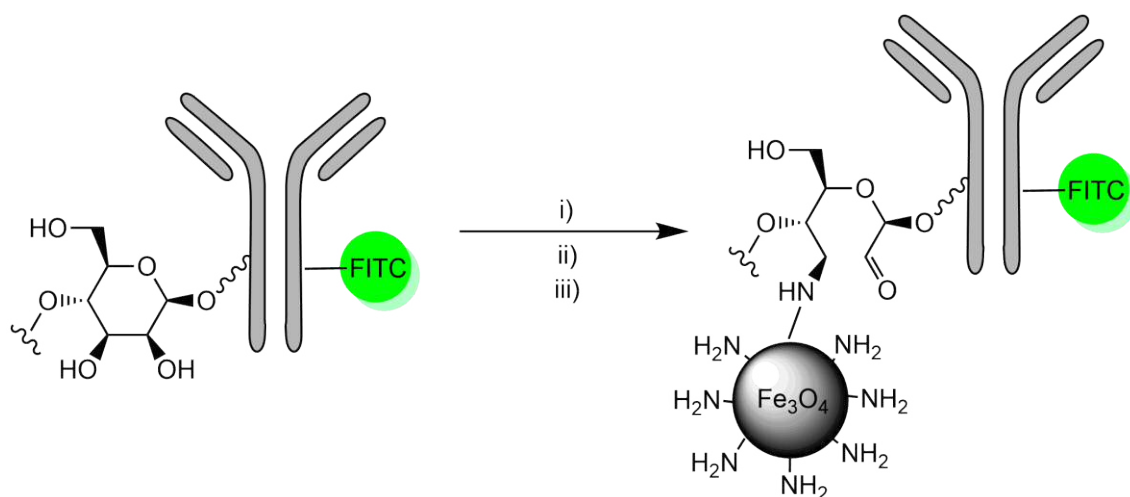


Figure 7. Simplified synthetic scheme for the immobilisation of FITC-Trastuzumab on APTES@SPION by reductive amination. i) NaIO₄, H₂O, RT, 20 min. ii) APTES@SPION, H₂O, RT, 2 h. iii) NaCNBH₃, RT, 30 min.

FITC-Trastuzumab (M_w ~ 150 kDa) (1) was dissolved in 10 mM sodium phosphate buffer, 0.15 M NaCl, pH 7.2 (10 mg.mL⁻¹). NaIO₄ (22 mg) was dissolved in H₂O (1 mL) in the dark. 100 μ L of the periodate solution was added per 1 mL of protein solution. The mixture was allowed to react for 20 min at room temperature in the dark. Excess periodate was quenched by addition of a 2.5-fold excess of Na₂SO₃. The oxidised antibody species was isolated by size exclusion chromatography on a PD-10 column, equilibrated with 100 mM sodium phosphate buffer, 0.15 M NaCl, pH 7.2. The most concentrated fraction was determined by monitoring A₂₈₀, and suitable volumes were added to an aqueous dispersion of APTES@SPION (10 mg.mL⁻¹) to achieve a desired percentage of nanoparticles bearing an antibody conjugate (see Results and Discussion). The reaction was mixed for 2h at room

temperature in the dark. The imine formed was reduced to a secondary amine by the addition of 5 M NaCNBH₃ in 1 M NaOH (10 μ L per 1 mL) and allowed to react for 30 min. Excess NaCNBH₃ was quenched by the addition of 1 M ethanolamine, pH 9.6 (50 μ L per 1 mL) and allowed to react for 30 min. The particles were collected by centrifugation (1 min, 1000 rpm) and washed with 10 mM sodium phosphate buffer, 0.15 M NaCl, pH 7.2 (5 \times 1 mL). The particles were dispersed in 10 mM sodium phosphate buffer, 0.15 M NaCl, pH 7.2 (1 mL) for storage. Emission (H₂O): λ_{em} = 520 nm.

FITC-APTES@SPION (3)

APTES@SPION was dispersed in H₂O (10 mg.mL⁻¹). FITC was dispersed in DMSO (1 mg.mL⁻¹). 11.5 μ L of the fluorescent dye solution was added per 1 mL of nanoparticles, achieving an approximately two-fold excess. The solution was mixed and allowed to react at room temperature for 2 h. Excess FITC was quenched and the particles precipitated by the addition of 1 M ethanolamine, pH 9.6 (50 μ L per 1 mL). The precipitated particles were collected by centrifugation (1 min, 1000 rpm) and washed with 10 mM sodium phosphate buffer, 0.15 M NaCl, pH 7.2 (5 \times 1 mL) to give the *title compound* as a black solid. UV-vis (H₂O): λ_{max} = 495 nm. Emission (H₂O): λ_{em} = 519 nm.

Cell culture and flow cytometry (FACS analysis)

BT-474 cells (Her-2 overexpressing, Trastuzumab sensitive) were cultured in Dulbecco's Modified Eagle Medium (DMEM) until near confluence. The media was removed, and DMEM (1.5 mL) with Trypsin (0.05 %) was added and incubated at 37 °C for 5 min to free cells from the container surface. Excess trypsin was quenched by addition of DMEM (15 mL) and the media filtered with a 40 μ m filter to remove cell aggregates. The cells were collected by centrifugation (5 min, 1200 rpm). The supernatant was removed and L-15 media (10 % serum, 0.0001 % DAPI) added to achieve a concentration of $\sim 5 \times 10^5$ cells.mL⁻¹. FITC-Trastuzumab-APTES@SPION (10 mg.mL⁻¹) was added in excess (500 μ L per 1 mL of cell media). The reaction mixture was incubated with mixing for 30 min at 37 °C and then analysed by flow cytometry. MDA-MB-468 (negative control) cells were treated analogously, but for initial growth in RPMI media. Control experiments were performed analogously but for the use of FITC-APTES@SPION.

Synthesis and purification of ⁸⁹Zr from ⁸⁹Y foil

Adapted from the method described by Walther *et al.*²⁹ and developed into Standard Operating Procedures within PETIC, School of Medicine, Cardiff University (see Appendix I). Briefly, an ⁸⁹Y solid target was placed in an Al support in a cyclotron, and was irradiated

with protons to form a ^{89}Zr -enriched foil. The foil was delivered into an appropriately set-up hot cell and its activity noted at the time of delivery. The foil was placed in a glass beaker and 2 M HCl (3×2 mL) was added slowly. Effervescence subsided to reveal a turbid grey solution. H_2O_2 (0.1 mL) and 6 M HCl (0.5 mL) was added to complete dissolution. The solution was heated to boiling point for 15 min then allowed to cool to room temperature. The solution was delivered by syringe to a lyophilised, hydroxamate functionalised ion exchange column. The column was washed with 2 M HCl (6×2 mL) to remove excess ^{89}Y and by-products then washed with H_2O (2×2 mL). 1 M oxalic acid solution was applied to the column as three fractions of 0.5 mL, 0.5 mL and 1.5 mL, yielding three fractions of ^{89}Zr oxalate, of which the latter was observed to contain the majority of the radioactivity.

^{89}Zr -labelled APTES@SPION (4)



Figure 8. Experimental set-up for ^{89}Zr labelling of APTES@SPION. Care must be taken to arrange hot cell interior prior to introduction of radiation to facilitate ease of manipulation.

^{89}Zr oxalate solution (1.5 mL) was brought to pH 7 by addition of saturated Na_2CO_3 solution. $\text{FeCl}_3 \cdot 6\text{H}_2\text{O}$ (0.135 g, 0.5 mmol) and $\text{FeCl}_2 \cdot 4\text{H}_2\text{O}$ (0.050 g, 0.25 mmol) was dissolved in the ^{89}Zr oxalate solution (1 mL, 802 MBq). 5 M NaOH (0.5 mL) was added, and the solution mixed at 25 °C for 5 min. The black precipitate was collected by use of a permanent magnet and washed with distilled H_2O until the washings were measured to be pH 7. As much solvent was removed as was possible via pipette. Glycerol (0.3 mL) was added. APTES (80 μL) and glacial acetic acid (80 μL) was added to H_2O (0.72 mL) and then added to the glycerol

suspension of bare nanoparticles. The reaction mixture was heated at 75 °C for 3 h. Upon cooling, H₂O (5 mL) was added and the reaction mixture poured into MeCN (10 mL) to cause precipitation. The particles were collected magnetically and washed with fresh MeCN (3 × 5 mL). Dispersion, precipitation and washing was repeated and the particles were dried in air inside the hot cell to give the *title compound* (15.8 mg, 108.4 MBq, 13 % recovery of activity, S = 6.86 GBq.g⁻¹). A significant mass of particles was lost during washing and manipulation.

Immobilisation of FITC-Trastuzumab on ⁸⁹Zr-labelled APTES@SPION (5)

FITC-Trastuzumab (**1**) was dissolved in 10 mM sodium phosphate buffer, 0.15 M NaCl, pH 7.2 (10 mg.mL⁻¹). NaIO₄ (22 mg) was dissolved in H₂O (1 mL) in the dark. 100 µL of the periodate solution was added per 1 mL of protein solution. The mixture was allowed to react for 20 min at room temperature in the dark. Excess periodate was quenched by addition of a 2.5-fold excess of Na₂SO₃. The oxidised antibody species was isolated by size exclusion chromatography on a PD-10 column equilibrated with 100 mM sodium phosphate buffer, 0.15 M NaCl, pH 7.2. The most concentrated fraction was determined by monitoring A₂₈₀ and suitable volumes were added to an aqueous dispersion of ⁸⁹Zr-labelled APTES@SPION (10 mg.mL⁻¹, 1 mL, 65.8 MBq) to achieve the desired percentage of particles bearing an antibody (see Results and Discussion). The reaction was mixed for 2h at room temperature in the dark. The imine formed was reduced to a secondary amine by the addition of 5 M NaCNBH₃ in 1 M NaOH (10 µL per 1 mL) and allowed to react for 30 min. Excess NaCNBH₃ was quenched by the addition of 1 M ethanolamine, pH 9.6 (50 µL per 1 mL) and allowed to react for 30 min. The particles were collected by centrifugation (1 min, 1000 rpm) and washed with 10 mM sodium phosphate buffer, 0.15 M NaCl, pH 7.2 (5 × 1 mL). The particles were stirred in 10 mM sodium phosphate buffer, 0.15 M NaCl, pH 7.2 (5 % EtOH, 2 mL., 60.4 MBq) overnight at room temperature.

In vivo biodistribution of radiolabelled SPION

Animal studies were conducted in accordance with institutional guidelines. Twelve female, nude mice of similar age and weight were selected for inclusion in an *in vivo* study. BT-474 (Her-2 overexpressing, ‘positive’) cells and MDA-MB-468 (‘negative’) cells were cultured on Matrigel at 4 °C (~5 × 10⁶ cells/ 100 µL media). Random selection of the mice gave two populations of six for use respectively as a ‘positive group’ and as a ‘negative group’. 100 µL of the relevant Matrigel suspension was delivered via subcutaneous injection to the right flank of each mouse. The tumours were allowed to grow for 30 days with regular checking

of the tumour size and overall health of the animals prior to the administration of the drug agents.

⁸⁹Zr-labelled APTES@SPION (4) was dispersed with mixing in sterile 10 mM sodium phosphate buffer, 0.15 M NaCl, pH 7.2 (2 mL) overnight as was the FITC-Trastuzumab-⁸⁹Zr-labelled APTES@SPION (5) in pH 7.2 buffer solution. Both samples were allowed to stand with no mixing for 30 min. Upon settling, undissolved aggregates were removed and the supernatant collected. Dissolution in both cases was observed to be poor. The supernatants were diluted to obtain solutions suitable for injection with activity of approximately 0.03 MBq per 100 µL injection volume. 200 µL of the appropriate nanoparticle solution (~0.06 MBq) were injected into each mice via the tail vein. PET-CT scans of the mice were taken at regular intervals over 7 days in a small animal PET-CT scanner. The health of the animals was monitored over this period and where appropriate they were sacrificed via typical humane methods. The PET scans were subjected to region of interest analysis to determine distribution of the nanoparticles *in vivo*. At the end of the experimental period, all remaining mice were euthanised humanely.

4.3 Results and discussion

4.3.1 FITC labelling of trastuzumab

The fluorescent labelling of the clinically used antibody Trastuzumab in different amounts was achieved by the use of different initial excesses of the dye FITC. The protocol used was based on a general procedure described in *Bioconjugate Techniques*,⁵⁶ initial experiments yielded a conjugate species with an F/P value of approximately 2. Subsequent CD analysis (see below) showed that a higher F/P was desirable to maximise fluorescent signal from the immobilised species and could be achieved with little effect on protein structure. F/P for a FITC-IgG conjugate can be determined by:⁵⁷

Increasing the initial excess of FITC over the antibody species results in a near linear increase in the F/P value derived from post-purification spectroscopic analysis (Table 2 and Fig. 9).

Volume of FITC (1 mg.mL⁻¹) added per mL mAb (5 mg.mL⁻¹) / μL	FITC:mAb molar excess	A₂₈₀(Product) / A	A₄₉₅(Product) / A	F/P ratio
100	7.5	0.405	0.235	2.0
150	11.25	0.421	0.327	3.0
200	15	0.438	0.419	4.0

Table 2. Table showing how F/P ratio of product FITC-Trastuzumab conjugate varies with initial stoichiometric excess.

The emission spectra of all FITC-trastuzumab conjugates were essentially identical with no observed effect of increasing F/P on the species' photophysical properties (Fig. 10). Excitation at 495 nm results in an emission profile with maxima at 520 nm (as expected for any FITC-bearing species) and a lifetime of 3.40 ns ($\chi^2 = 0.91$).

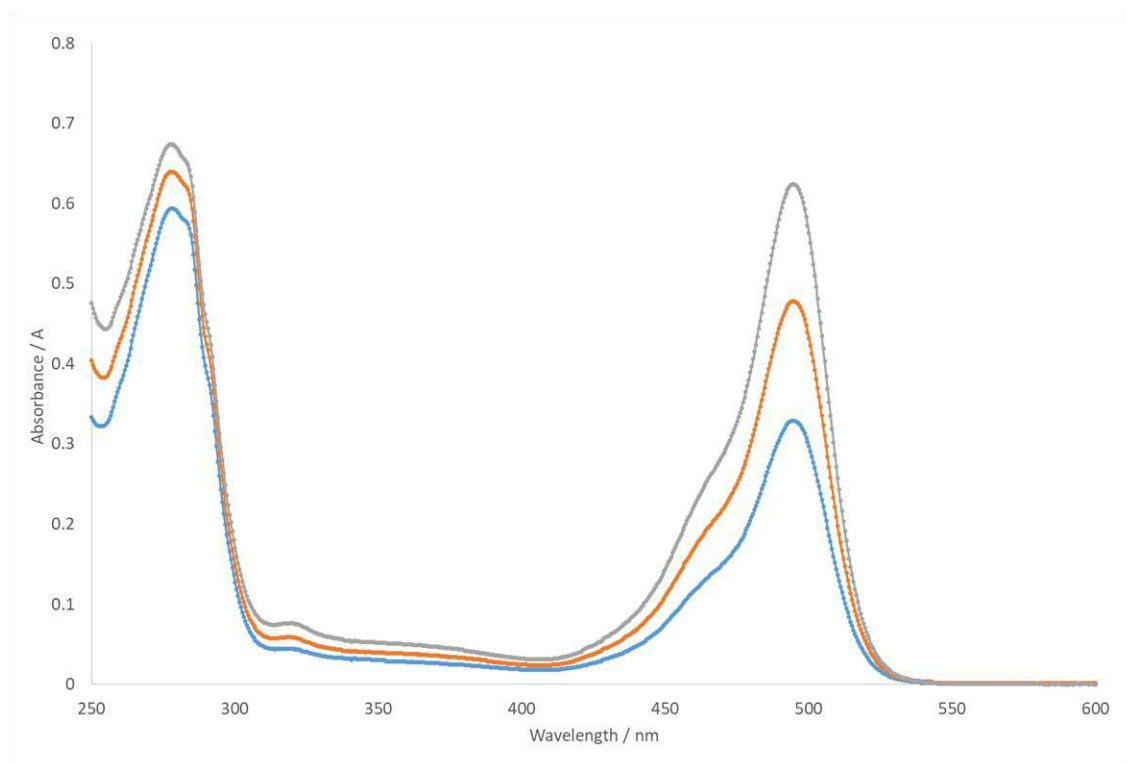


Figure 9. UV-vis spectra of FITC-Trastuzumab conjugates with F/P values of 2 (blue), 3 (orange) and 4 (grey).

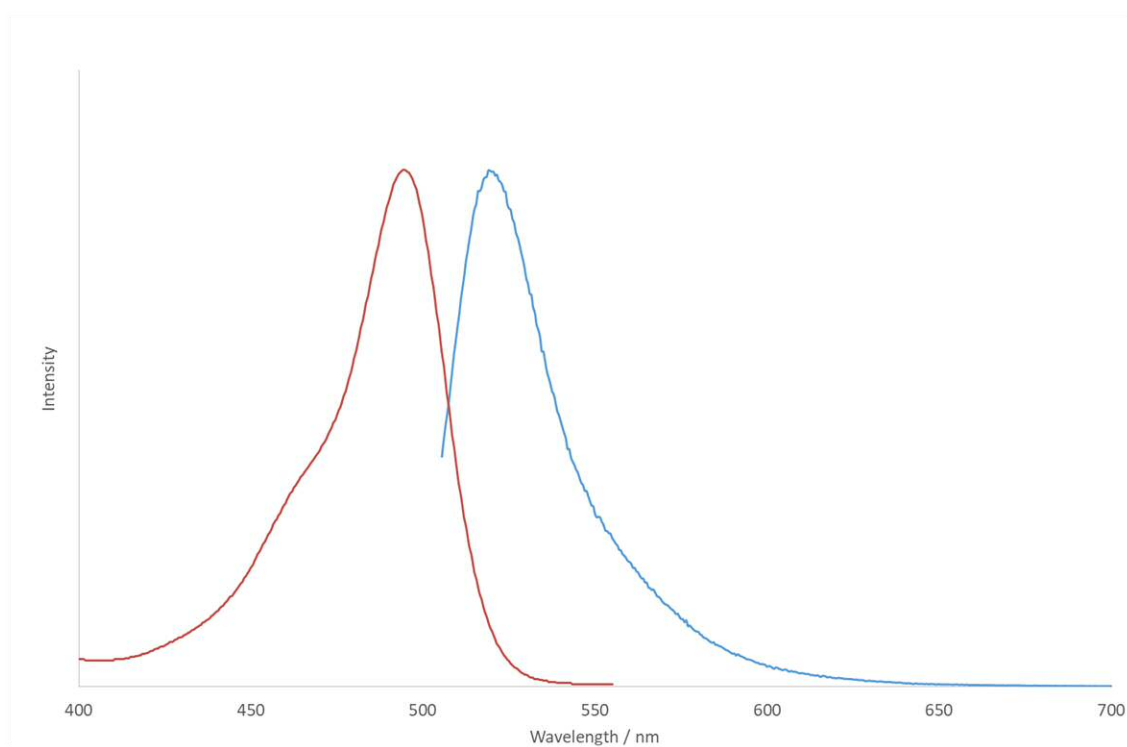


Figure 10. Example excitation (red) and emission spectra (blue) for FITC-Trastuzumab conjugates. Wavelengths below 505 nm were not measured due to the excitation wavelength used ($\lambda_{ex} = 495$ nm).

UV-vis and fluorescence spectroscopy confirmed the success of the reaction methodology and the suitability of FITC as a fluorescent dye on Trastuzumab but gave no indication of the effect of labelling on protein tertiary structure. This was investigated by CD spectroscopy (see Chapter 3). It is generally accepted within the field of bioconjugation that fluorescently-labelling a protein will have no substantive effect on protein structure or function as long as the number of fluorophores is limited,⁵⁹ and this is supported by the spectra shown in Fig. 11. By comparison to the spectra of clinical grade Trastuzumab, the conjugate species gave profiles with near identical lineshapes, suggesting little to no change in the protein's tertiary structure as a result of FITC-labelling. These conjugates would be expected to bind to Her-2 overexpressing cells and would be interesting moieties to immobilise on APTES@SPION.

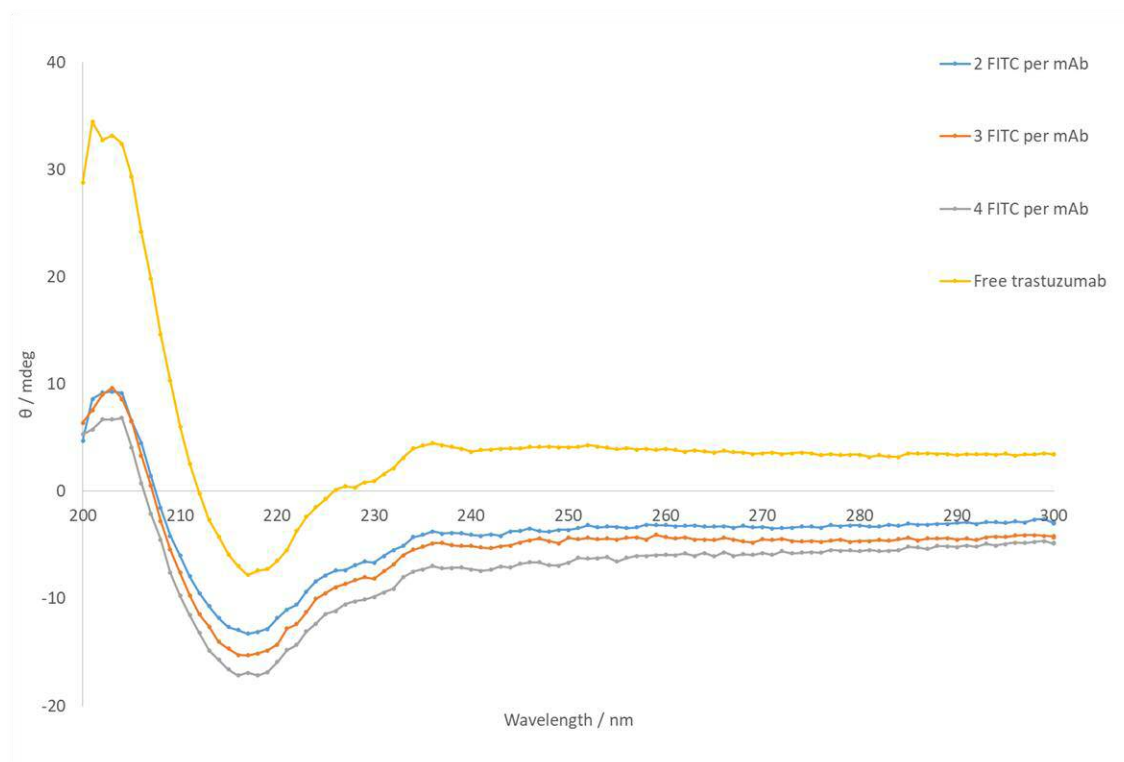


Figure 11. CD spectra of trastuzumab and FITC-conjugate species with differing values of F/P. The line shapes of the conjugate species are similar to that of the free antibody,

4.3.2 Immobilisation of FITC-Trastuzumab on APTES@SPION and the synthesis of FITC-APTES@SPION as a control species

The immobilisation of FITC-Trastuzumab onto APTES@SPION was achieved via the reductive amination method discussed in Chapter 3. It was determined that the effect of immobilisation on protein function could be minimised by keeping the percentage of bioconjugated particles in a sample low. A compromise must however be found between the retention of function, and ensuring that a sufficient number of protein moieties are present in a sample population that a measurable degree of binding can be determined by FACS. To this end, the percentages shown in Table 3 (next page) were selected based on previous findings (see Chapter 3) and were subsequently found via FACS analysis to be suitable. In all cases, a FITC-Trastuzumab conjugate with an F/P of 4 was immobilised. Experiments to yield both theoretical immobilisation ratios were performed in triplicate and analysed independently. To act as a control species in flow cytometry experiments (i.e. to check for non-specific binding or uptake of nanoparticles to cells), FITC-APTES@SPION were synthesised (see Table 4). Aqueous dispersions of FITC-Trastuzumab-APTES@SPION and FITC-APTES@SPION were analysed to confirm their fluorescent properties (Fig. 12). Analysis showed near identical emission spectra and it was concluded that the synthesised particles were suitable for flow cytometry experiments.

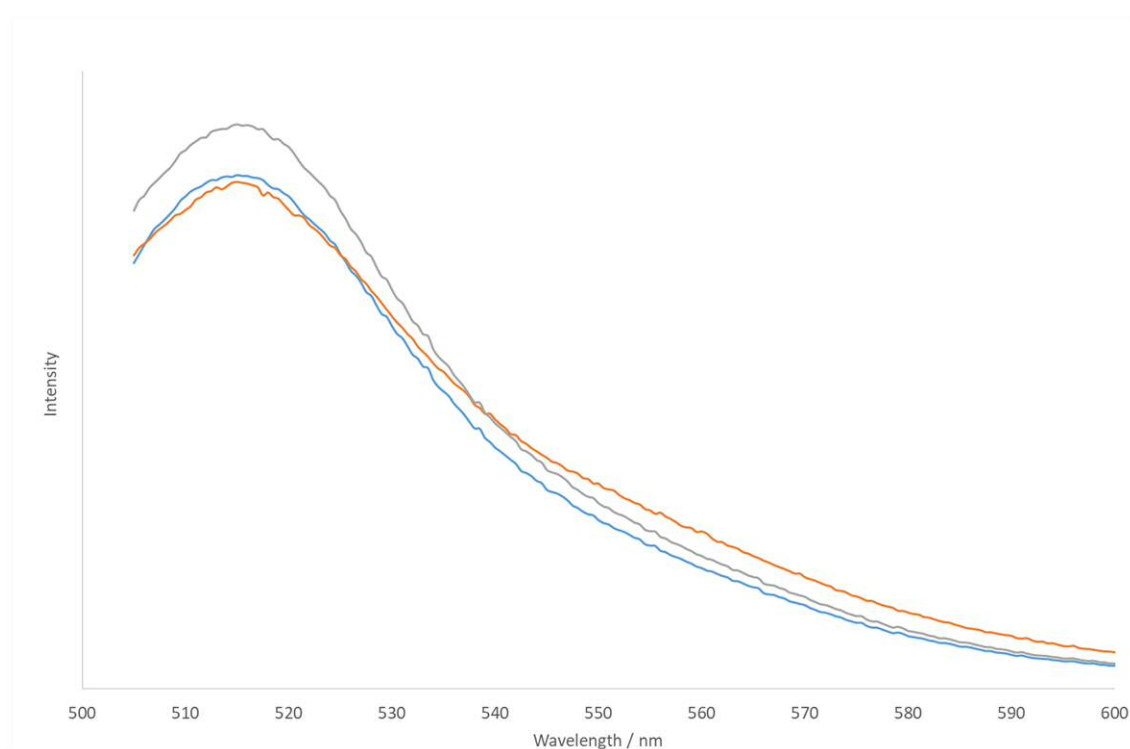


Figure 12. Emission spectra for FITC-Trastuzumab-APTES@SPION conjugates (2 % (blue) and 4 % (orange)) and FITC-APTES@SPION (grey). Wavelengths below 505 nm were not measured due to the excitation wavelength used ($\lambda_{ex} = 495$ nm).

V(APTES@SPION) / μ L (conc. /mg.mL ⁻¹)	No. of nanoparticles	V(FITC-mAb) / μ L (conc. /mg.mL ⁻¹)	No. of conjugates	Conjugate:nanoparticle ratio (% singly labelled)
200 (10)	1.98×10^{15}	3.5 (2.80)	3.96×10^{13}	1:50 (~2 %)
200 (10)	1.98×10^{15}	7.1 (2.80)	7.92×10^{13}	1:25 (~4 %)

Table 3. Volumes of nanoparticle and FITC-Trastuzumab solutions used and resulting conjugate:nanoparticle ratio.

V(APTES@SPION) / μ L (conc. /mg.mL ⁻¹)	No. of nanoparticles	V(FITC) / μ L (conc. /mg.mL ⁻¹)	No. of conjugates	FITC:nanoparticle ratio
200 (10)	1.98×10^{15}	2.6 (1.0)	4.02×10^{15}	2:1

Table 4. Volumes of nanoparticle and FITC solutions used and resulting FITC:nanoparticle ratio. The FITC-mAb conjugate has $M_w \sim 150$ kDa.

4.3.3 Flow cytometry and *in vitro* validation

To detect the binding of FITC-Trastuzumab-APTES@SPION to Her-2 overexpressing BT-474 cells, a near confluent cell culture was trypsinised to facilitate removal, exposed to the nuclear stain DAPI (to allow assessment of cell viability and a measure of nanoparticle toxicity) and diluted to a concentration of approximately 5×10^5 cells.mL⁻¹; each cell has an average of 7×10^5 Her-2 receptors, equivalent to 3.5×10^{11} receptors.mL⁻¹. To this sample was added an excess of FITC-Trastuzumab-APTES@SPION: 500 μ L of 10 mg.mL⁻¹ nanoparticle solution per 1 mL of cell media, equivalent to approximately 4.95×10^{15} nanoparticles of which 9.90×10^{13} or 1.98×10^{14} are calculated to bear a FITC-Trastuzumab moiety, depending on the initial reaction stoichiometry. There is therefore an excess of 282 or 565 antibodies per receptor.

Determination of 'population identities'

Flow cytometers measure a user-defined number of 'events' per experiment. An 'event' can be loosely defined as any object passing the laser which gives detectable values for Front (FSC) and Side (SSC) scatter.⁶⁰ Typically these are cells, but nanoparticle aggregates, cell aggregates and debris can all register as an 'event'. Initial experiments were performed on a dispersion of nanoparticles with no cells, and on a dispersion of cells with no nanoparticles to determine FSC and SSC ranges which would allow the unequivocal identification of cells (nanoparticle-bound or otherwise) from free nanoparticles and debris.

Fig. 13a shows a two-parameter histogram for a dispersion of antibody-labelled SPION. Nanoparticles, nanoparticle aggregates and small debris have low FSC intensity; the intensity of FSC indicates the diameter of an 'event' with larger species giving greater FSC intensity, but entities smaller than the wavelength of light being used (e.g. nanoparticles) have little effect on FSC and may not register as an event.⁶⁴

Fig. 13b shows histograms for BT-474 cells prior to incubation. The two-parameter dot-plot on the left shows that cells, cell debris and cell aggregates can have a range of values for FSC and SSC. The gated sub-population of events labelled 'P1' has values of FSC and SSC known to roughly signify single, healthy BT-474 cells and eliminates nanoparticles and debris. This population was refined into the smaller sub-population P2 by the exclusion of anomalous species based on the height and width (FSC-H and FSC-W) of the FSC signal. P2 was refined further into P3 by using the height and width (SSC-H and SSC-W) of the SSC signal. Thus, the events populating the group P3 can be determined to be individual, healthy cells only. By

comparison to Fig. 13a, it can be observed that single cells and nanoparticle species in a mixed sample will appear as different regions on a two-parameter histogram.

Fig. 13c is a histogram of fluorescence intensity (FITC-A) against number of events (count) obtained when events in P3 are excited with 495 nm light and emission at 520 nm is measured. The population of single cells in gate P3 all have low fluorescence intensity, falling into a pre-determined region for FITC-negative events.

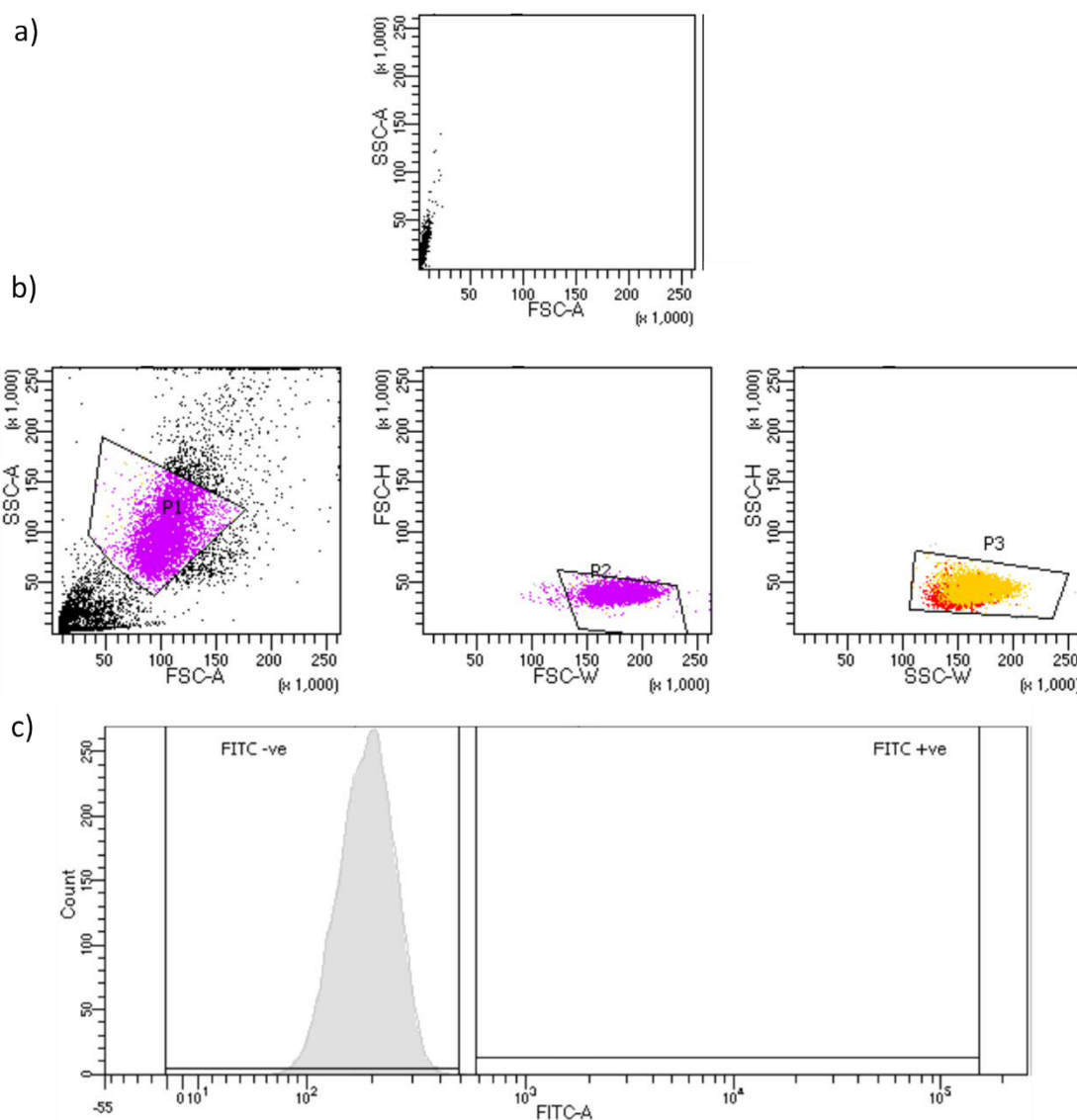


Figure 13a. FSC vs. SSC for antibody-labelled SPION in aqueous solution. FSC is low, indicating sizes approaching the limit of detection.

b. FACS analysis for BT-474 cells in solution. Gate P1 is known to approximate single, healthy cells. P2 and P3 refine this group. P3 is tested for FITC emission ($\lambda_{ex} = 495$ nm).

c. The fluorescence intensity of the population within P3 is low ($\sim 2 \times 10^2$ relative units), hence is not FITC emissive. FITC-A refers to emission intensity, count refers to number of events (here, single, healthy cells).

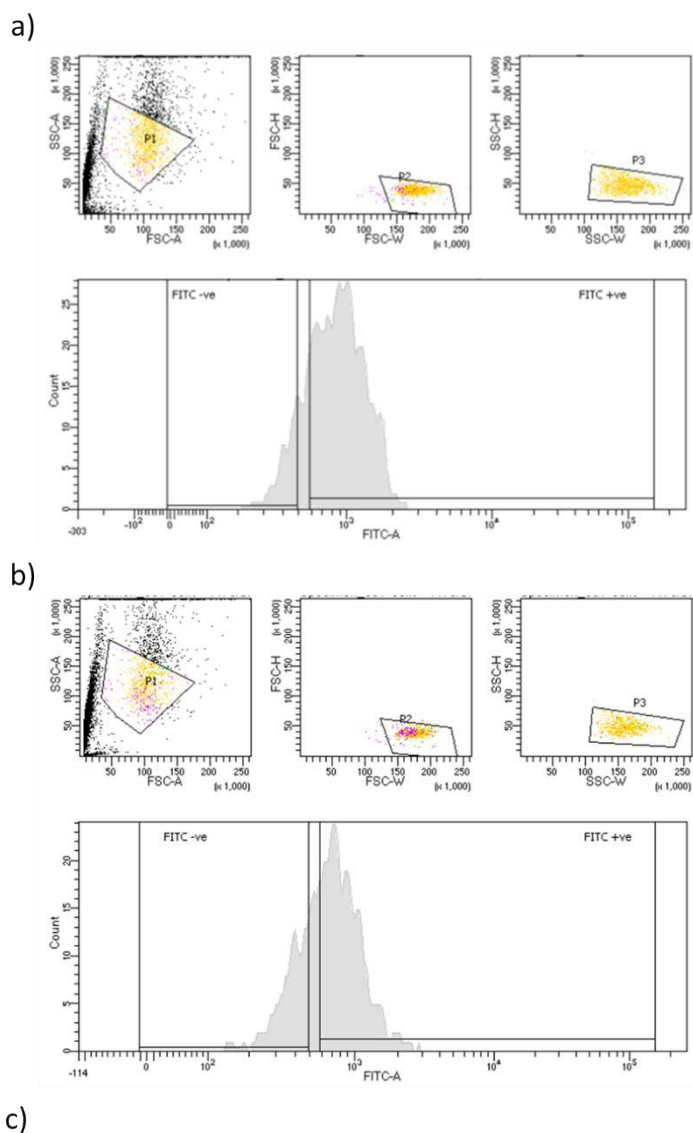
Incubation of BT-474 cells with antibody-bearing SPION

Nanoparticles with theoretical mAb percentage loadings of 2 % and 4 % were incubated together with BT-474 cells with regular mixing for 30 mins at 37 °C, after which the media was analysed by flow cytometry. Initial results for both loadings were similar but the higher percentage coating samples were more prone to precipitation and to blocking the cytometer uptake and were not studied further.

Following incubation with trastuzumab-bearing SPION, FACS analysis of the same culture of BT-474 cells studied in Fig. 13b and Fig. 13c using the same gates to define event sub-populations gave much greater fluorescence intensity upon excitation at 495 nm. Fig. 14a shows how the measured number of 10,000 events was divided into sub-populations P1, P2 and P3 based on light scattering so that the events in sub-population P3 are known to be single, healthy cells. When excited with 495 nm light, the cells show fluorescence intensity at 520 nm ten times that observed in the single parameter histogram Fig. 14c, and the intensity is sufficient to deem them 'FITC positive'. From no FITC positive events prior to incubation, 77.2 % of the events in Gate P3 were definitively FITC emissive, indicating binding of the nanoparticles to the BT-474 cells.

To confirm the strength of the binding, an aliquot of the experimental mixture was diluted by half with appropriate media. The cell media was vortexed vigorously and re-analysed using the same gating procedure (Fig. 14b). It would be expected that few FITC positive events would remain following this harsh treatment if weak, non-specific binding (i.e. adsorption) was occurring. Post-dilution, the percentage of FITC positive events recorded dropped to 60.7 %, indicating some loss of binding. The binding of nanoparticles to cells is of significant strength, with most losses following dilution and vortexing likely due to the slow binding time of antibodies giving incomplete formation of the antigen-antibody interactions (see Fig. 14c).⁶⁵

Control experiments were performed where BT-474 cells were incubated with FITC-APTES@SPION. Resulting FACS analysis (not shown) showed a sub-population P3 that was known to contain single, healthy cells but which had no fluorescence intensity arising due to the presence of FITC. No binding was observed when nanoparticles did *not* carry an antibody moiety, allowing the conclusion that the strong binding inferred from Fig. 14 is antibody mediated.



Population	No. of events		%Parent	
	Pre-dilution	Post-dilution	Pre-dilution	Post-dilution
All events	10000	10000	-	-
P1 (approx. single cells)	936	721	9.4	7.2
P2 (refined cells)	908	702	97.0	97.4
P3 (refined cells, $\lambda_{ex} = 495 \text{ nm}$)	893	700	98.3	99.7
FITC negative	125	191	14.0	27.3
FITC positive	689	425	77.2	60.7

Figure 14a. FACS analysis of BT-474 cells incubated with trastuzumab bearing SPION. Emission intensity of P3 was $\sim 1 \times 10^3$ relative units (FITC positive).

b. FACS analysis performed post-dilution and vortexing to remove weakly/non-specifically bound species. Emission intensity remained high ($\sim 7 \times 10^2$ relative units).

c. Table showing the numbers of events per subpopulation. The majority of FITC positive events are retaining following dilution and vortexing.

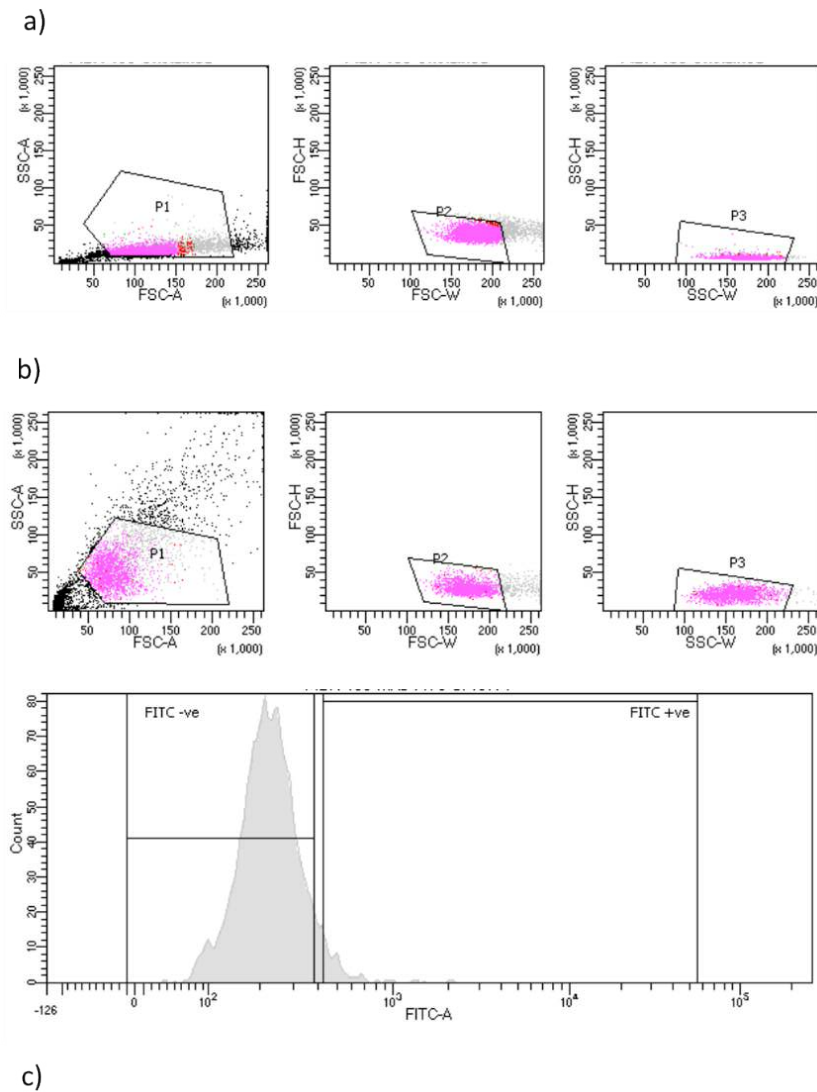
Incubation of MDA-MB-468 cells with antibody-bearing SPION

MDA-MB-468 cells (not Her-2 overexpressing, 'negative') were incubated with FITC-Trastuzumab-APTES@SPION to investigate the antibody's specificity for the Her-2 receptor upon immobilisation; limited binding was observed due to the presence of some Her-2 receptors (Fig. 15).

Fig. 15a shows the identification of FSC and SSC parameters for individual healthy cells from the negative cell line; the negative cells have different scatter characteristics to the positive cell line shown in Fig. 13b, requiring different gates to be applied to achieve sub-population identification (P1, P2 and P3).

Following incubation with the antibody-coated SPION, the presence of the nanoparticles can be seen by the increased side scatter and the changes in the nature of the cells in response to the change in the environment (Fig. 15b). The first two-parameter histogram shows the approximate region (within population P1) where single, healthy cells would be expected. The second and third show the refinement of this population to eliminate cell aggregates and cell debris. The single, healthy cells of P3 were excited at 495 nm, yielding the histogram of fluorescence intensity (FITC-A) versus count. Some events had intensity sufficient to register as 'FITC positive'.

The number of FITC positive events within the cell population increases from 0 % prior to incubation with nanoparticles (not shown) to 5.4 % (Fig. 15c). MDA-MB-468 does have some Her-2 receptors (it is referred to as 'negative' because Her-2 is not 'over-expressed' as in BT-474),⁶⁶ so some binding and fluorescence is to be expected but will be limited as the antibody should not bind to other surface receptors present. The difference to the percentage of positive events observed in the case of BT-474 cells is sufficient to conclude that immobilised Trastuzumab largely retains specificity to the Her-2 receptor and does not bind efficiently to other receptors.



Population	No. of events	%Parent
All events	10000	-
P1 (approx. single cells)	2552	25.5
P2 (refined cells)	2040	79.9
P3 (refined cells, $\lambda_{ex} = 495 \text{ nm}$)	2010	98.5
FITC negative	1880	93.5
FITC positive	108	5.4

Figure 15a. FACS analysis of MDA-MB-468 cells prior to incubation with trastuzumab bearing SPION. Different gates are required to the positive cell line discussed previously.

b. FACS analysis post-incubation, showing gates for population identification. The majority of events have low emission intensity, and are therefore 'FITC negative'.

c. Table of populations expressed in post incubation FACS plots above. Note the small percentage of FITC positive events (5.4 %) in comparison to that observed for BT-474 cells previously (77.2 %).

Effects of incubation with nanoparticles on cell viability

Experiments were performed to determine the effect of incubation with the antibody-bearing nanoparticles on cell viability. Populations of BT-474 and MDA-MB-468 cells were cultured, exposed to a small quantity of DAPI dye and their cell viabilities assessed using FACS. Both cell lines were split into two centrifuge tubes each and to one of the tubes for each line was added antibody-bearing nanoparticles. The tubes were then incubated at 37 °C for 30 mins and their cell viability measured again (see Table 5 below).

The initial viability of BT-474 cells was 96.8 %; this was reduced to 86.9 % by incubation alone, and to 84.8 % by incubation with the SPION sample. The initial viability of the MDA-MB-474 was 98.5 %, dropping to 98.1 % following incubation alone, and 97.2 % following incubation with the particles. Incubation with the particles has limited effect on cell viability, showing that despite the harmful chemicals used to achieve immobilisation, repeated washing of the particles is efficient at removing these toxins, alleviating any concern that transfer to *in vivo* studies could involve accidental poisoning of the subject. Removal from ideal culture conditions in the incubator has a greater effect on cell viability than the presence of the nanoparticles.

Summary of FACS analysis

Flow cytometry confirmed the ability of FITC-labelled trastuzumab immobilised via reductive amination on APTES@SPION to bind strongly to the Her-2 surface receptor specifically with no significant effect on cell viability. Within populations of individual, living, healthy cells, the Her-2 overexpressing cell line BT-474 showed significantly greater binding to the antibody-directed nanoparticles than observed for the ‘negative’ cell line due to the greater number of Her-2 receptors present. Where binding was observed, the complexes formed were not easily disrupted by dilution or by vigorous agitation of the sample. Where nanoparticles did not carry the antibody, no binding was observed. The antibody-bearing nanoparticle species were deemed suitable for *in vivo* experimentation.

	BT-474 / no. of events (%Parent)			MDA-MB-468 / no. of events (%Parent)		
	Pre-incubation	Post-incubation	Post-incubation with nanoparticles	Pre-incubation	Post-incubation	Post-incubation with nanoparticles
All events	10000 (-)	10000 (-)	10000 (-)	10000 (-)	10000 (-)	10000 (-)
P1 (approx. single cells)	8394 (83.9)	8694 (86.8)	2441 (24.4)	7296 (73)	7113 (71.1)	2428 (24.3)
P2 (refined cells)	7946 (94.7)	8234 (94.8)	2253 (92.3)	6040 (82.8)	5829 (81.9)	1901 (78.3)
P3 (refined cells, $\lambda_{\text{ex}} = 495$ nm)	6433 (81.0)	6603 (80.2)	2083 (92.5)	6017 (99.6)	5811 (99.7)	1883 (99.1)
FITC positive	27 (0.4)	21 (0.3)	1732 (83.1)	0 (0)	0 (0)	108 (5.7)
Live	6227 (96.8)	5739 (86.9)	1767 (84.8)	5925 (98.5)	5698 (98.1)	1831 (97.2)

Table 5. Table of FACS data relating how cell viability changes with incubation with particles. Note the case of BT-474 cells where there is greater loss in viability as a result of incubation, and the high number of cells which are live and FITC positive.

4.3.4 Fluorescence microscopy

In addition to flow cytometry, the binding of FITC-trastuzumab-APTES@SPION to BT-474 cells was visualised qualitatively by fluorescence microscopy using three fluorescence channels ('blue', $\lambda_{\text{ex}} = 355 \text{ nm}$, $\lambda_{\text{em}} = 433 \text{ nm}$; 'green', $\lambda_{\text{ex}} = 480 \text{ nm}$, $\lambda_{\text{em}} = 517 \text{ nm}$; 'red', $\lambda_{\text{ex}} = 556 \text{ nm}$, $\lambda_{\text{em}} = 615 \text{ nm}$). Excitation with the different wavelengths of light following incubation with DAPI and the nanoparticle agent and subsequent fixing of the cells allows the cells to be shown to have blue fluorescence (due to DAPI), green fluorescence (due to the FITC of the nanoparticle agent) but no red fluorescence, excluding the possibility that autofluorescence is occurring.

In the top set of images in Fig. 16 below, three cells can be observed with black aggregates that show some green fluorescence. In the bottom set, two cells are visible on the right, while a piece of cell debris is expressing blue fluorescence on the left. This would not give a false positive in FACS analysis as it would have different front and side scatter characteristics from whole cells, and is likely an artefact of the fixing process.

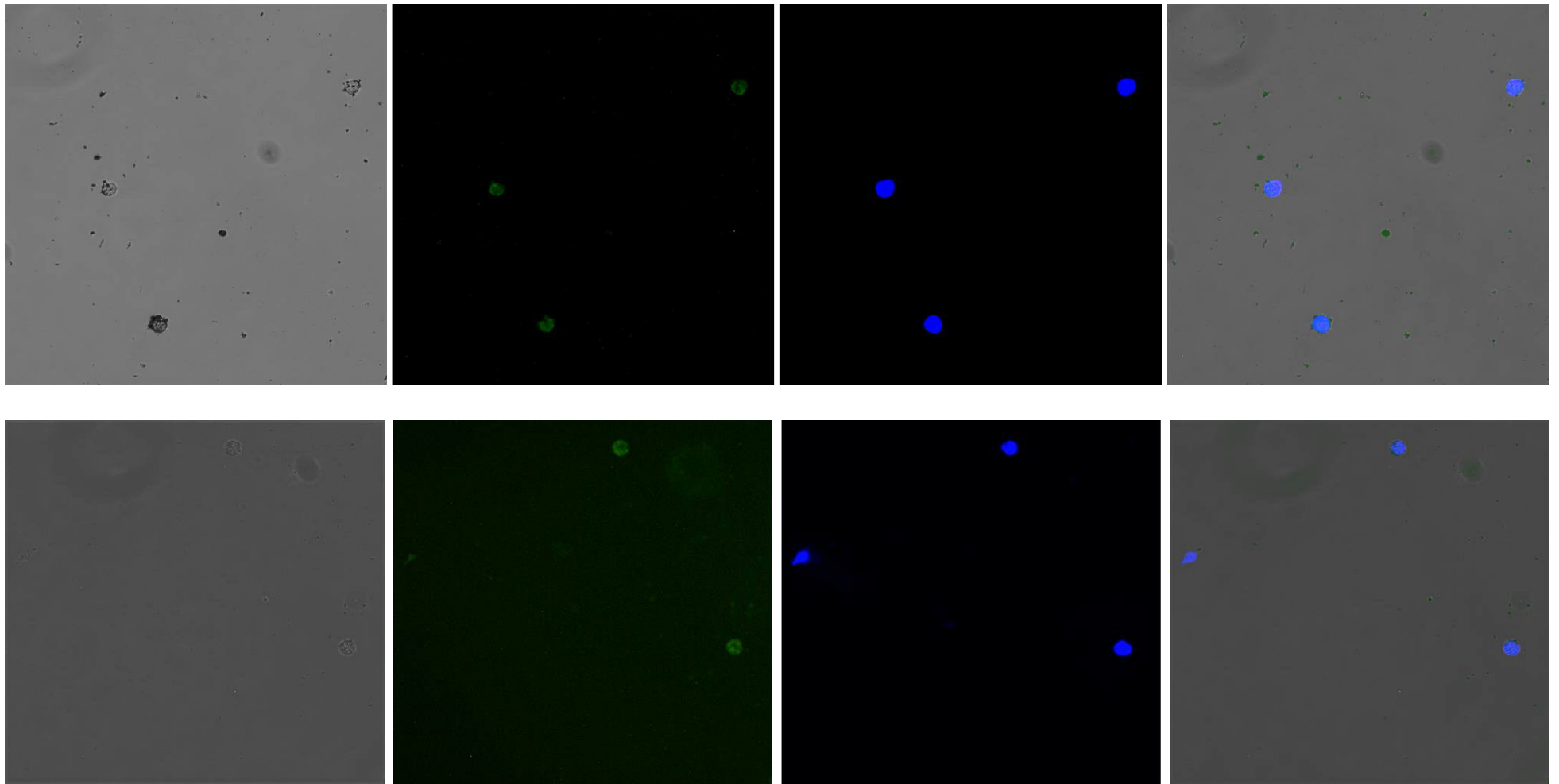


Figure 16. Fluorescence microscopy images of BT-474 cells binding Trastuzumab-bearing SPION illuminated with different light sources. From left to right: white light, green fluorescence channel, all available fluorescence wavelengths, blue fluorescence channel.

4.3.5 Synthesis of ^{89}Zr -radiolabelled FITC-Trastuzumab-APTES@SPION

An ^{89}Y foil target was subjected to proton bombardment within a cyclotron by a radioengineer from PETIC, University Hospital of Wales, Cardiff. The impure reaction mixture containing ^{89}Zr and waste products was transferred to a hot cell and purified by use of SOPs based on the method described by Walther *et al.*²⁹ A sample of the product ^{89}Zr oxalate solution was neutralised prior to addition to the iron salt-containing SPION-precursor solution lest it affect pH adversely and change the properties of the reaction.

Only a small proportion of the final radiolabelled particles (approximately 2 %) would be conjugated to antibodies in order to retain *in vivo* function and maximise solubility. It was important that as much radioactivity as possible should be incorporated into the nanoparticles to compensate for this and for losses going through the synthesis. For the *in vivo* experiments described below, a volume of ^{89}Zr oxalate with activity of 802 MBq was used, approximately twenty times that which had been used in initial experiments which had shown high labelling efficiency. This was calculated to be equivalent to 0.54 nmol or 3.27×10^{14} atoms using the equation:

$$\frac{N}{n} = \frac{A}{\lambda}$$

where N is the number of radioactive atoms, n is the number of moles of radioisotopes, N_A is Avogadro's number, λ is the radioactive decay constant and $t_{1/2}$ is the half-life of ^{89}Zr in seconds (282600 s). Based on previous APTES@SPION preparations on this scale and on the average physical dimensions discussed in Chapter 3, it was estimated that a final yield of labelled particles would be approximately 50 mg, equivalent to 4.94×10^{16} nanoparticles. Taking the number of ^{89}Zr atoms present at the start of the experiment, the theoretical maximum radiolabelling yield would be:

$$\frac{4.94 \times 10^{16} \text{ nanoparticles}}{3.27 \times 10^{14} \text{ atoms}} = 151 \text{ atoms per nanoparticle}$$

The initial co-precipitation of uncoated SPION occurred without incident, but of the 802 MBq introduced into the system 406 MBq of ^{89}Zr was not incorporated into the SPION and was contained in the washings from the reaction (see Table 6). This was not anticipated as preliminary investigations had shown the incorporation of approximately 90 % of the radioactivity at this stage of the reaction.

The radiolabelled particles were coated with APTES and left to dry in air in the hot cell overnight. On the following morning, it was observed that drying was not complete; an additional cycle of dispersal in water, precipitation with MeCN, repeated washing with fresh water and further drying was required to achieve the radiolabelled APTES@SPION as a fine black powder that could be manipulated remotely. This resulted in some loss of product. The final mass of ^{89}Zr -APTES@SPION (15.8 mg, 1.56×10^{16} nanoparticles) was measured to have activity of 108.4 MBq (Equivalent to 4.42×10^{13} ^{89}Zr atoms; specific activity = 6.86 GBq.g⁻¹). Using the same approach as described above for the theoretical case:

This is equivalent to 1 in 353 of the synthesised nanoparticles being radiolabelled with one atom of ^{89}Zr . This quantity is small but should be considered as an initial proof of concept; increased labelling efficiency may result from future experiments to optimise reaction times and conditions. The current experiment suffers from the need to perform the nanoparticle synthesis on a scale small enough that gigabecquerels of radioactivity is not needed to achieve a useful degree of labelling, but large enough that quantities can be accurately weighed and manipulated.

Experimental step	Sub-division of materiel	Activity / MBq
i) Initial reaction mixture	N/A	802
ii) Post-precipitation	Washed uncoated SPION	396
	Washings	406
iii) Post-coating	Wet APTES@SPION	319
	Washings	66.2
iv) Final drying	Labelled APTES@SPION	108.4
	Losses through manipulation	210.6 (estimated)

Table 6. Distribution of activity throughout synthesis of ^{89}Zr -APTES@SPION.

The dried radiolabelled nanoparticles were dispersed in sterile saline (10 mg.mL⁻¹) prior to bioconjugation to FITC-Trastuzumab. The fluorescent species was used for consistency with the *in vitro* studies described above and to offer the possibility of dissection and fluorescence microscopy should the *in vivo* biodistribution be favourable.

The radiolabelled particle dispersion was split, with the equivalent of 10 mg (66 MBq) being the subject of bioconjugation experiments and the remainder (5.8 mg, 42 MBq) not receiving bioconjugation to act as a control species. Bioconjugation proceeded via reductive amination with the experimental stoichiometry shown in Table 7. No significant experimental losses of radioactivity were noted during this step of the reaction.

V(APTES@SPION) /μL (conc. /mg.mL-1)	1000 (10)
No. of nanoparticles	9.88×10^{15}
V(FITC-mAb)/μL (conc. /mg.mL-1)	40.0 (1.1)
No. of conjugates	1.77×10^{14}
Conjugate:nanoparticle ratio (% singly labelled)	1:56 (~2 %)
Initial activity / MBq	65.8
Final activity / MBq	61.2

Table 7. Volumes of nanoparticles and FITC-Trastuzumab solutions used in preparation of ⁸⁹Zr-radiolabelled FITC-Trastuzumab-APTES@SPION. Approximate M_w (FITC-mAb) = 150 kDa.

Both the antibody-bearing and non-antibody-bearing nanoparticles were suspended in sterile pH 7.2 buffer overnight with mixing, then allowed to stand without agitation for 30 mins. In both cases the stabilities of the dispersions were much poorer than had been observed with ‘cold’ analogous experiments, suggesting a higher drive to aggregate. The presence of aggregates that could not be dispersed satisfactorily at higher concentrations required dilution which significantly reduced the amount of radioactivity that could be used *in vivo*. Much of the 61.2 MBq discussed in Table 7 persisted as a black solid that would not disperse at high concentrations under the conditions used.

Following dilution of a poorly dispersed sample until aggregates were not visible, supernatants were collected and confirmed to have retained some radioactivity (0.3 MBq.mL⁻¹). It was noted that the weakly radioactive dispersions may not be sufficient to observe contrast in the tumour, but the experiment was continued to the animal model phase as the mice already bore the xenograft tumours and the radioactivity present would at least be suitable to characterise the biodistribution of the particles and to assess their toxicity if any.

4.3.6 *In vivo* biodistribution of radiolabelled SPION

Experimental design and approach

Twelve female nude mice were housed at the School of Medicine, Cardiff University under conditions meeting institutional guidelines for live animal experiments. The mice were all determined to be of similar age and weight and the group was divided randomly into two cohorts of six mice. BT-474 and MDA-MB-468 cells were cultured on Matrigel matrix and a volume (100 μ L) containing $\sim 5 \times 10^6$ cells of a given cell-line was injected subcutaneously into the right flank region of each mouse. The Matrigel was observed to set with no immediate ill-effects on the mice. The tumours were allowed to develop with regular checking on the health and welfare of the mice for 30 days. The two types of tumours expressed different growth rates such that the MDA-MB-468 tumours were well developed and externally visible after 30 days and were in danger of becoming necrotic (at which point euthanasia would be performed); in contrast the BT-474 tumours, while palpable, were smaller and were not externally visible.

Three of each group were to be administered with antibody-bearing nanoparticles and three were to be administered radiolabelled APTES@SPION with no degree of antibody conjugation (Table 8). For accurate comparisons between the cohorts, all of the mice would have to be administered particles from the same production. Because of this, the experiment proceeded despite the small size of the BT-474 tumours in an attempt to avoid the need to sacrifice the mice bearing MDA-MB-468 tumours.

Cohort 1 No. of Mice = 3 Tumour type = BT-474 Administered species = mAb-conjugated ^{89}Zr -APTES@SPION	Cohort 2 No. of Mice = 3 Tumour type = BT-474 Administered species = ^{89}Zr -APTES@SPION
Cohort 3 No. of Mice = 3 Tumour type = MDA-MB-468 Administered species = mAb-conjugated ^{89}Zr -APTES@SPION	Cohort 4 No. of Mice = 3 Tumour type = MDA-MB-468 Administered species = ^{89}Zr -APTES@SPION

Table 8. Schematic of experimental groups. Specific binding of the radiolabelled nanoparticles to tumour tissue would only be expected in Cohort 1.

Drug formulation volumes administered to small animals must be small to prevent harm; 200 μL is typically a safe maximum single-injection volume. The formulation must be clear from visible aggregates which can cause fatal blood vessel blockages. To satisfy these conditions, the supernatant solutions containing the bioconjugated and non-bioconjugated radiolabelled particles were diluted until they were observed to be clear from aggregates, at which point an activity of 0.03 MBq of radioactivity per 100 μL of solution was measured. The tumour bearing mice were separated into their cohorts and 200 μL (0.06 MBq) of the appropriate nanoparticle suspension was administered by injection into the tail vein. For both antibody-bearing and non-bearing radiolabelled APTES@SPION, 0.06 MBq can be converted to an equivalent number of ^{89}Zr atoms:

—
—

—————

This number is equivalent to the number of radiolabelled nanoparticles administered to each mouse. Due to the immobilisation stoichiometry, 2 % of this number would be calculated to bear an antibody i.e. 4.90×10^8 nanoparticles or 8.13×10^{-16} moles of antibody-directed radiolabelled nanoparticles were administered to each mouse of Cohorts 1 and 2. An average mouse has a blood volume of 1.5 mL, hence particle concentration can be calculated to be:

—————

PET scanners are sensitive enough that contrast can be observed with sub-picomolar contrast agent concentrations,^{67,68} but a recent meta-analysis suggests that over 99 % of all nanoparticles will be prevented from reaching the target tumour due to physical and biological barriers.⁶⁹ Unfortunately the experiments performed had antibody-directed nanoparticle concentrations approaching or below the limit of detection, and contrast in tumours deriving from the antibody-conjugated particles would not be expected. In addition, as only 2 % of the radiolabelled particles bear an antibody, background noise would be high compared to any ‘antibody-directed signal’. The mice were anaesthetised prior to scanning; their heart rates and core body temperatures were monitored throughout to ensure welfare. PET scanning was carried out over seven days post-injection (Figs. 17-20). At no point was a significant signal corresponding to nanoparticle agents determined in the tumour of any mouse, regardless of tumour type or the presence of antibody-bearing nanoparticles.

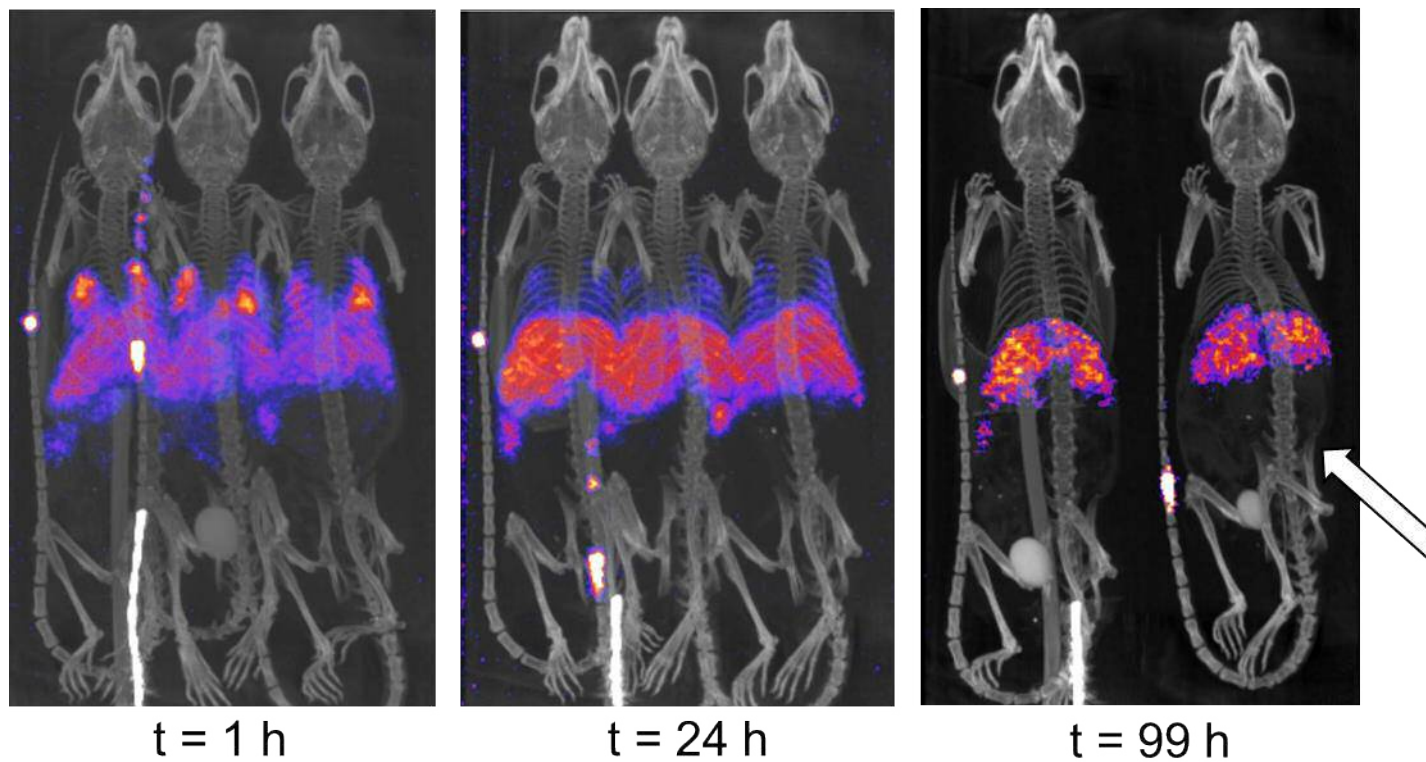


Figure 17. Serial PET-CT imaging of Cohort 1: nude mice bearing Her-2 positive (BT-474) tumours administered with ^{89}Zr -labelled Trastuzumab-bearing SPION. Radioactivity rapidly accumulates in the liver. Approximate tumour location for each mouse indicated by arrow.

(Note: following the 23 h scan, one mouse succumbed to hypothermia due to the low temperature in the scanner.)

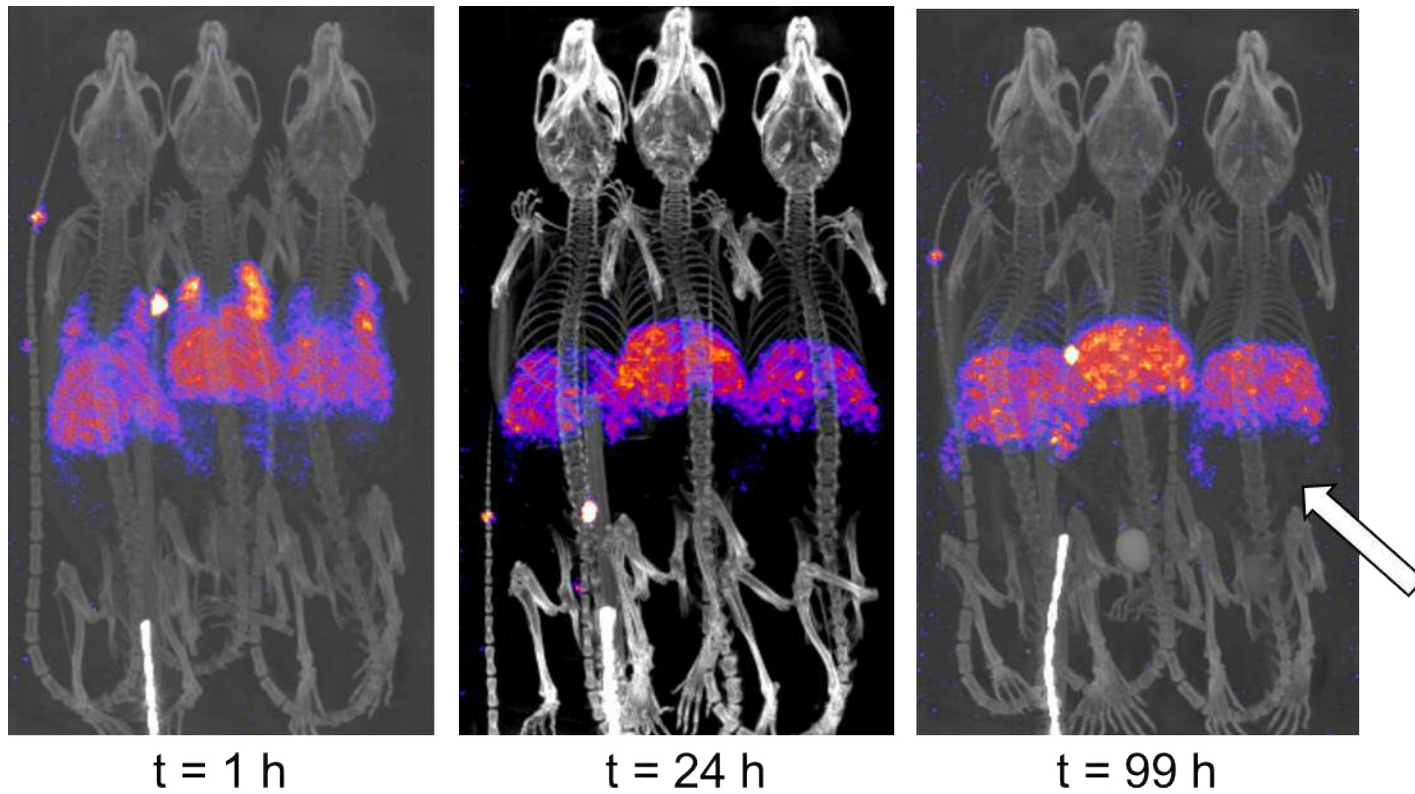


Figure 18. Serial PET-CT imaging of Cohort 3: nude mice bearing Her-2 negative (MDA-MB-468) tumours administered with ^{89}Zr -labelled Trastuzumab-bearing SPION. Radioactivity rapidly accumulates in the liver. Approximate tumour location for each mouse indicated by arrow.

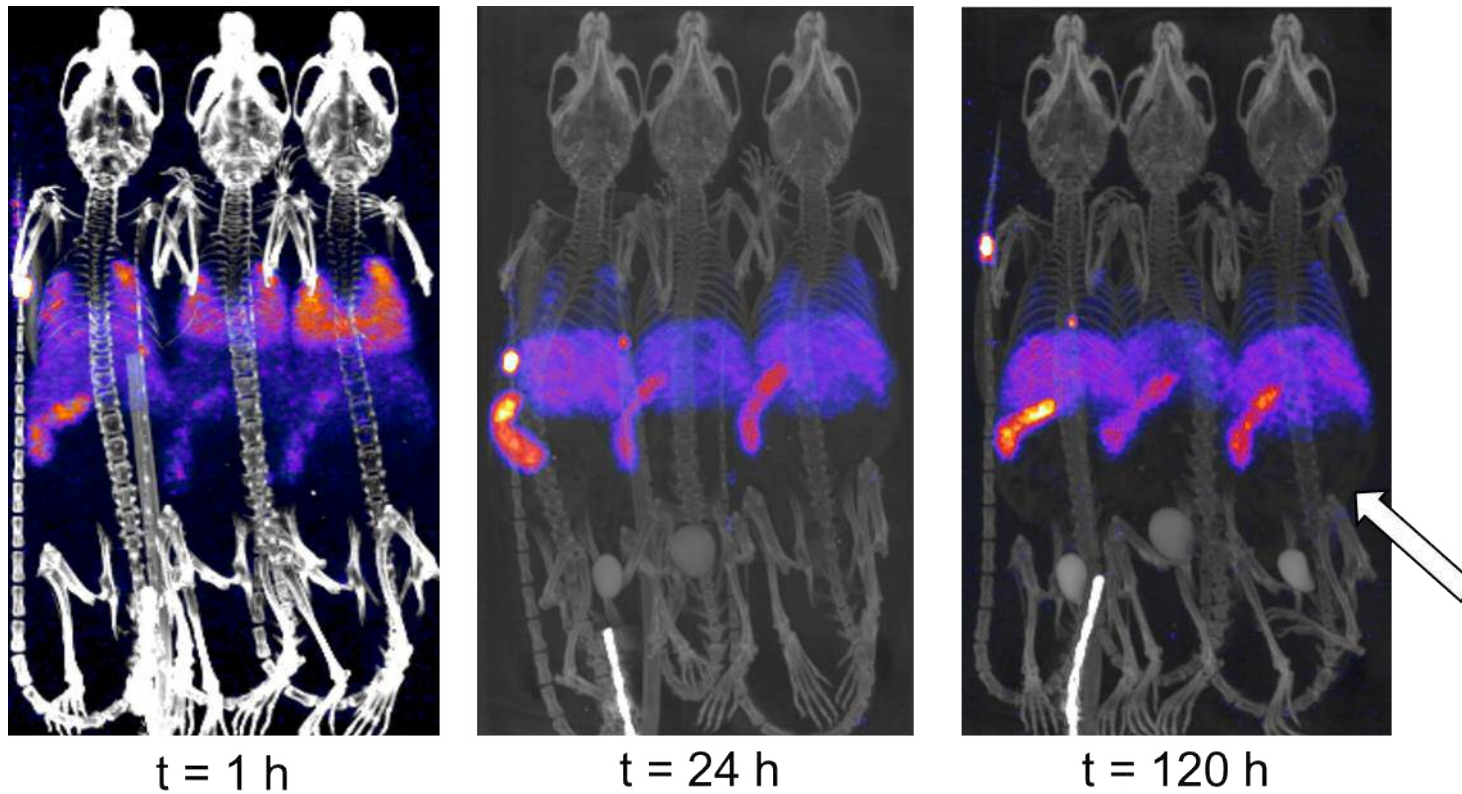


Figure 19. Serial PET-CT imaging of Cohort 2: nude mice bearing Her-2 positive (BT-474) tumours administered with ^{89}Zr -labelled SPION with no degree of bioconjugation. The degree of localisation in the spleen is higher than for antibody functionalised SPION. Approximate tumour location for each mouse indicated by arrow.

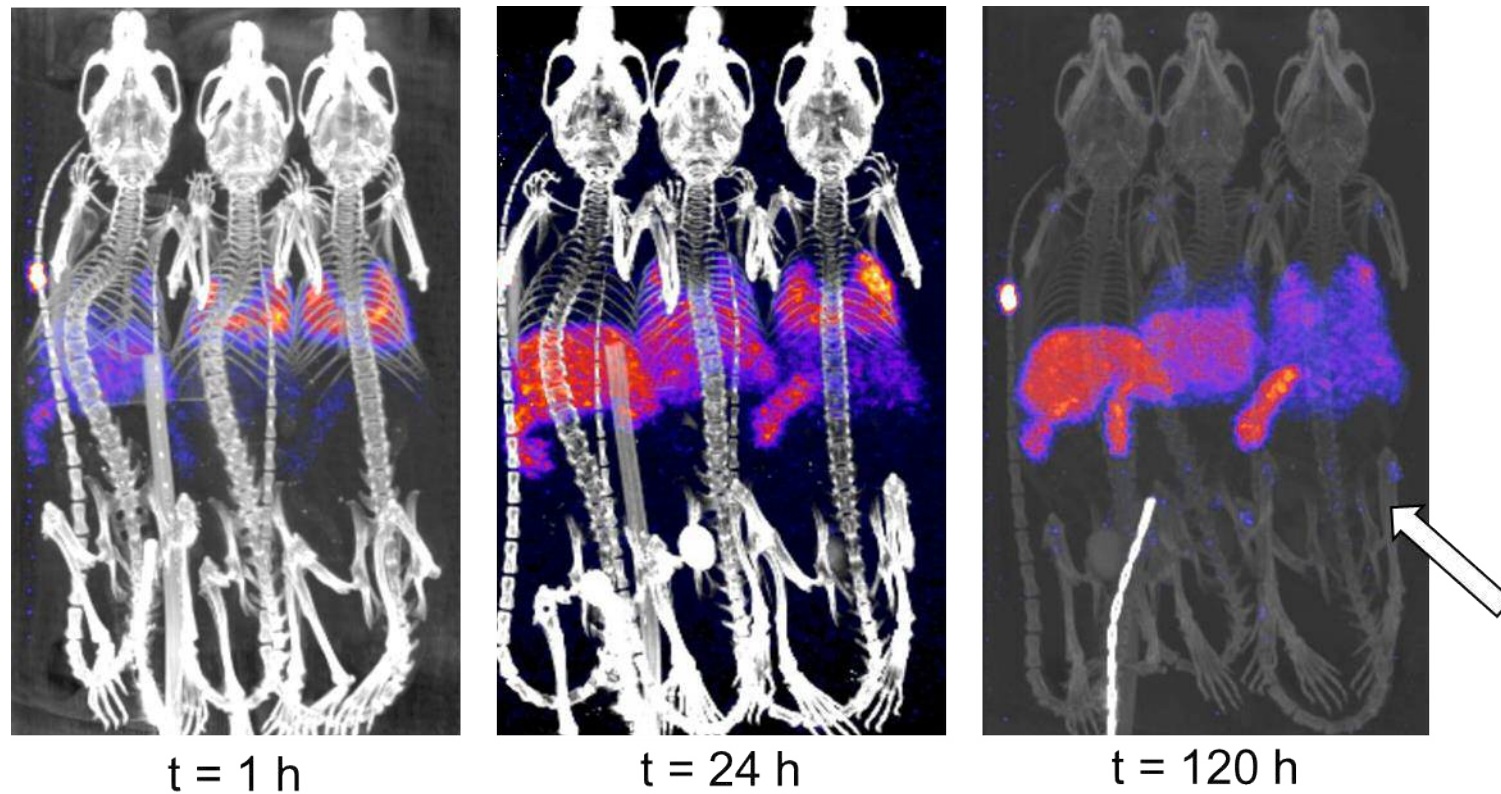


Figure 20. Serial PET-CT imaging of Cohort 4: nude mice bearing Her-2 negative (MDA-MB-468) tumours administered with ^{89}Zr -labelled SPION with no degree of bioconjugation. The degree of localisation in the spleen is higher than for antibody functionalised SPION. Approximate tumour location for each mouse indicated by arrow.

Region of interest analysis

Post-scan analysis was carried out by defining key organs as three-dimensional regions of interest (ROI) and determining the percentage of radioactivity in the region relative to the total radioactivity present in the mouse. Nine ROI were determined for the analysis of the radioactivity distribution: the mouse as a whole, the tail (the site of injection), the skeleton, the lungs, the kidneys, the bladder, the liver, the spleen and the tumour itself. By defining these regions in each mouse at each scan time, how activity distribution changes over time (i.e. the effects of metabolism or blood circulation) can be quantified.

Administration of antibody-directed, radiolabelled SPION

The results of ROI analysis for the surviving mice of Cohort 1 (BT-474 tumour, antibody-bearing nanoparticles) are shown in Fig. 21. Upon administration, particles initially localised in the lungs before rapid uptake into the liver, where the majority of the radioactivity remained throughout the scanning period. Although some radiation was observed in the kidneys, no radiation was observed in the bladder, precluding excretion via the renal system. Radiation in the tail is an unavoidable artefact of injection via the tail vein.

Levels of radioactivity in the tumour given in Fig. 21 below are likely to be noise arising from signal gain during analysis. The values are greater than if all of the antibody-directed particles that were administered *and* which avoided uptake into the liver or other organs were bound to the tumour cells within an hour of administration. In the first scan (see Fig. 21), 0.03 % (18 Bq) of the total activity at that time (approximately 60,000 Bq) is measured to be in the tumour. Of the 60,000 Bq, only 2 % would be expected to be in a particle bearing an antibody (1200 Bq), and as is discussed elsewhere, it would be estimated that only 1 % of these particles would avoid uptake by the liver and other organs (equivalent to 12 Bq).⁶⁹ It is known that antibody-antigen interactions are strong but are typically slow to form, and it would not be expected for all possible particles to bind to the tumour immediately upon administration. Because the measured value is larger than would be plausible or possible, it may be concluded that it is likely inaccurate and not significant.

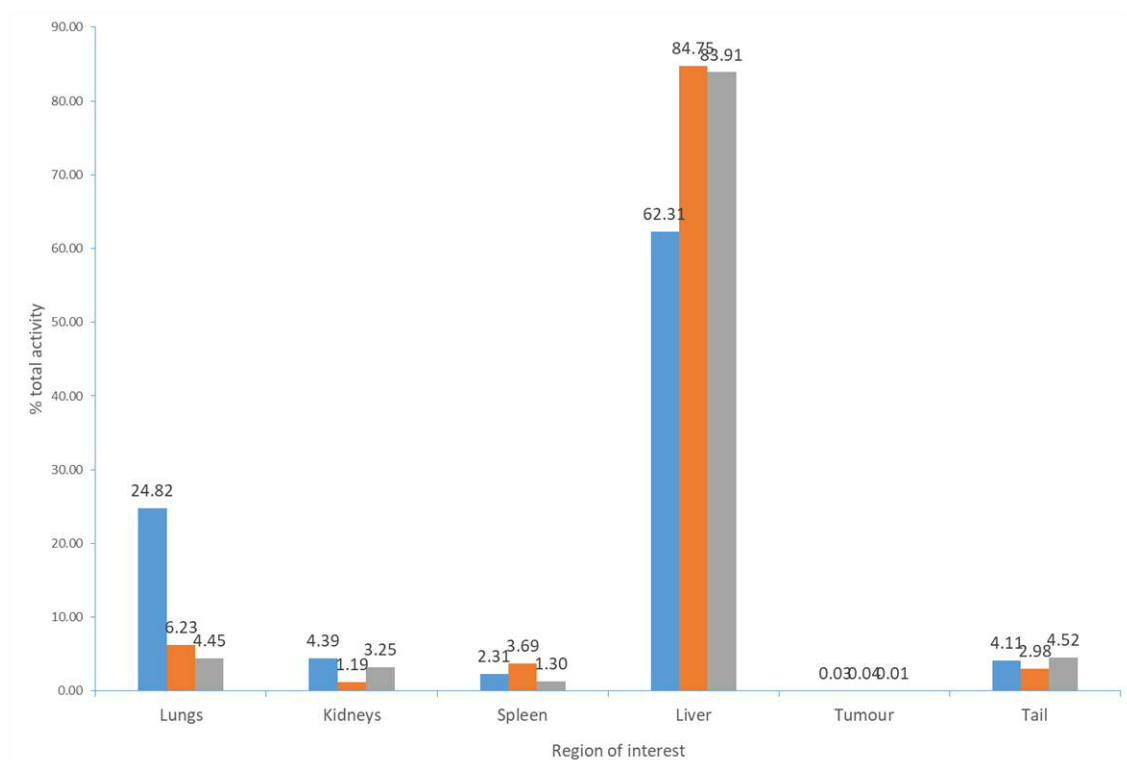


Figure 21. Average percentages of total activities for selected ROI for Cohort 1 mice ($n = 2$) at different scan times (blue = Scan 1, orange = Scan 2, grey = Scan 3).

ROI analysis of the Her-2 negative MDA-MB-468 tumours of Cohort 3 (Fig. 22) showed similar tumour activity levels to those observed in Fig. 21, confirming that the measurement of radioactivity in the BT-474 tumours is likely an artefact of the analytical approach taken (i.e. system error or signal gain) and is not indicative of the specific binding of an antibody-directed nanoparticle.

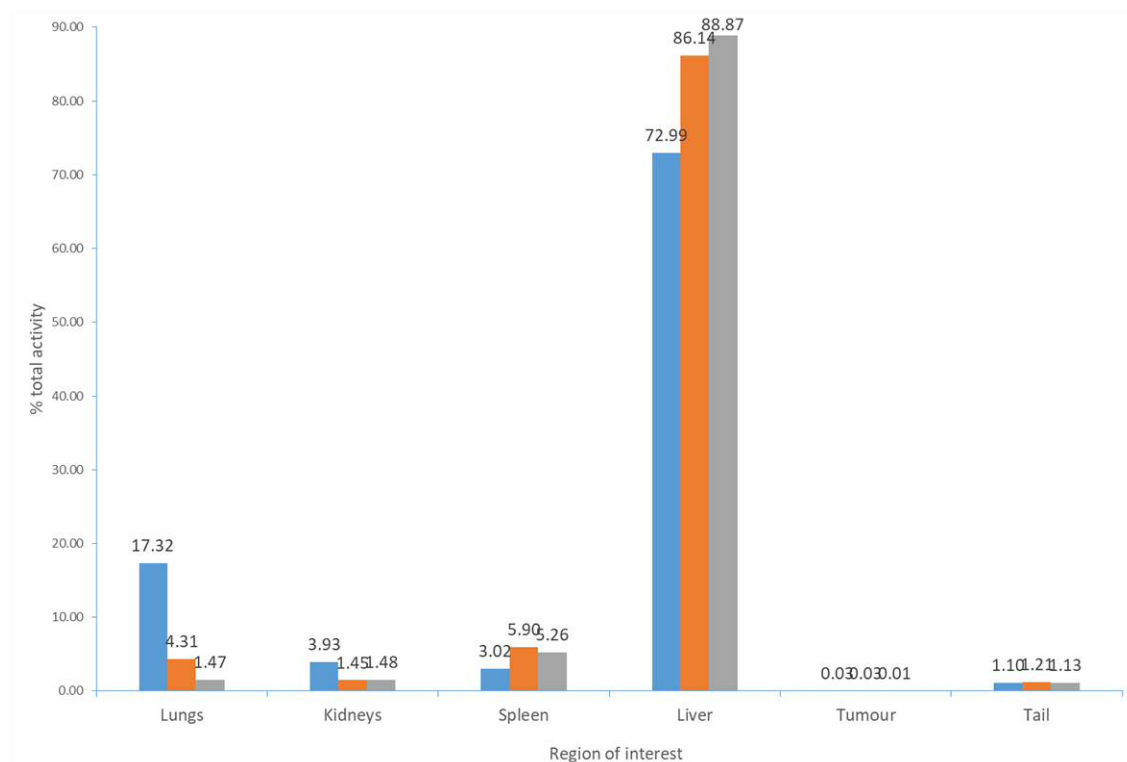


Figure 22. Average percentages of total activities for selected ROI for Cohort 3 mice ($n = 3$) at different scan times (blue = Scan 1, orange = Scan 2, grey = Scan 3).

Administration of radiolabelled SPION with no antibody-conjugation

Although only a small proportion of the particles described above bore an antibody, the methodology used for bioconjugation does have an effect on the nanoparticles' biodistribution: when ^{89}Zr -labelled APTES@SPION are administered, their biodistribution was nearly identical within the mice of Cohorts 2 and 4, but was different to that of the antibody bearing particles in Cohorts 1 and 3 (see Figs. 23 and 24).

The non-bioconjugated particles persist in the lungs to a greater extent throughout the experiment, with the effect being most noticeable in the first scan. Approximately 50 % of the radioactivity was in the lungs one hour after administration, whereas 17-24 % was present in the lungs for the antibody-labelled SPION at the same time. The percentage of the activity present in the spleen increased throughout the experiment to between 12 and 17 % for non-bioconjugated particles but remained much lower (≤ 6 %) and relatively constant throughout for the functionalised particles. Less radioactivity was observed in the liver when the particles were not functionalised (a maximum of ~ 70 %) compared to the functionalised species (85-89 %).

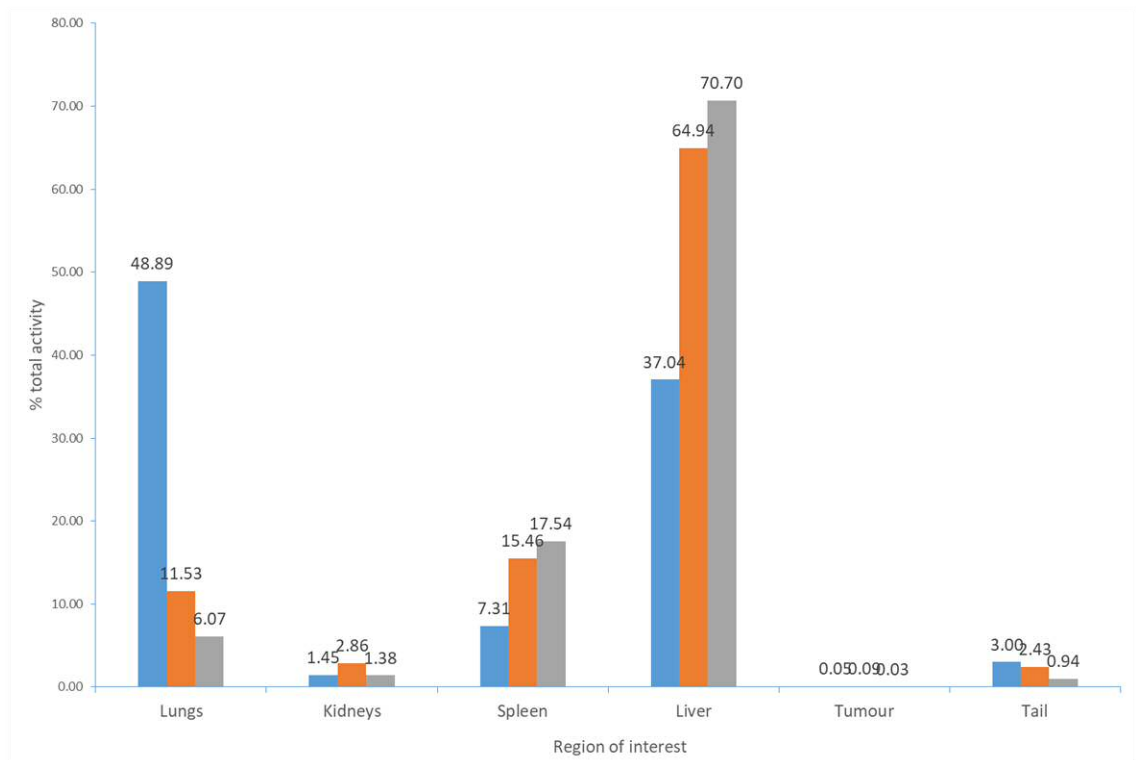


Figure 23. Average percentages of total activities for selected ROI for Cohort 2 mice ($n = 3$) at different scan times (blue = Scan 1, orange = Scan 2, grey = Scan 3).

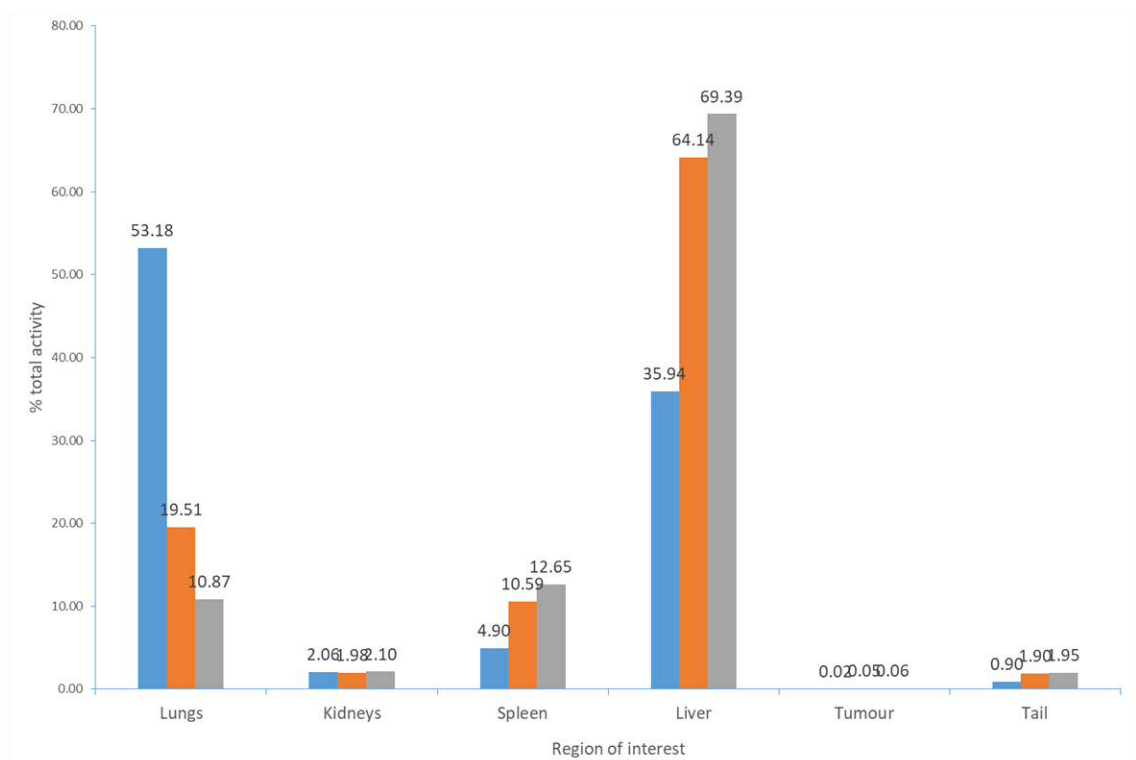


Figure 24. Average percentages of total activities for selected ROI for Cohort 4 mice ($n = 3$) at different scan times (blue = Scan 1, orange = Scan 2, grey = Scan 3).

Although only two per cent of nanoparticles in the ‘antibody-containing’ cohorts bear biomolecules, the effect of the immobilisation process on other parameters results in them being almost twice as likely (62-73 % vs. 36-37 %) to have been sequestered into the liver in less than one hour post-injection. The particles that were exposed to bioconjugation conditions were observed *ex vivo* to be more prone to aggregation than non-bioconjugated particles (most likely due to changes in their protonation state or surface charge) and this ROI data would suggest that *in vivo* this may result in an increased rate of detection by the immune system and sequestration into the liver.

It is therefore likely that the differences in biodistribution described above are not directly related to the presence of antibody molecules on just two per cent of the nanoparticles (as the effect would be disproportionate) but arise indirectly due to the effect of the immobilisation methodology on the bulk physical parameters of the nanoparticles. Further research would be required to clarify the effect of the immobilisation method on the particles in general, and to identify the major factors that result in the different *in vivo* behaviour and which could inform future experiment design.

The lack of significant signal in the tumours of any mice suggests that passive sequestration of any radiolabelled nanoparticles through porous blood vessels (the enhanced permeability and retention (EPR) effect) did not occur to an appreciable degree.⁷⁰

Analysis of ROI data trends: protein adsorption, immune responses and RES uptake

Mice urinate near constantly.⁷¹ This, and the small amount of radioactivity present at any time in the kidneys of any mouse studied is sufficient to conclude that renal excretion is not a major elimination pathway. As it is known that sub-10 nm particles are removed by this pathway,⁷² the particles must exist as aggregate species *in vivo*.

While *in vitro* experiments allowed the confirmation of the specificity of SPION-immobilised trastuzumab, this was insufficient to predict *in vivo* behaviour. Nanoparticles aggregate to minimise energy due to their high surface area:volume ratio. This can also be achieved by the non-specific adsorption of proteins *in vivo* to give a ‘protein corona’.⁷³ The size of the particles affects the amount and identities of the species in the protein corona, and the protein corona affects numerous physical quantities (e.g. surface charge, hydrophobicity, size and shape) *in vivo*, which affects biodistribution.^{73,74} Increased hydrophobicity results in an increased immune response to nanoparticles.^{75,76} Positively charged nanoparticles have shown a preference to bind ‘opsonins’, proteins that enhance the uptake of the nanoparticles by elements of the reticuloendothelial system (RES) which are part of the innate immune

response e.g. macrophages. Dispersed APTES@SPION will have positive surface charges and will likely bind opsonins; particles that are aggregating together become more hydrophobic. In either case, the nanoparticles administered to the mice will trigger an immune response. When comparing the different biodistribution patterns of particles that have or have not undergone bioconjugation conditions, it would seem that the process changes their aggregation behaviour, which ultimately affects how the nanoparticles are cleared in a manner which may not be related solely to the presence of the mAbs.

The mice used in the current experiment are athymic but retain their innate immune response to foreign bodies. Particles are engulfed by macrophage cells in the blood, liver or spleen and are sequestered in the latter two organs to undergo degradation as part of the body's attempt to protect itself.^{72,77,78} Although RES sequestration may be reduced by different coating species, it is a common and persistent problem in nanoparticle research in general;⁷⁷ a recent meta-analysis calculated that on average less than one per cent of administered particles are delivered to a target tumour due to RES uptake.⁶⁹ It was calculated that 4.90×10^8 antibody-directed nanoparticles were injected into the mice of Cohorts 1 and 3, of which an estimate of one per cent (4.90×10^6 nanoparticles) might be expected to have been delivered to the tumours: a femtomolar 'available concentration' that is too low to be detected and which may have been indistinguishable from background noise even had the equipment used been more sensitive. For one of the mice of Cohort 2 at the time of Scan 3 (120 h, see Fig. 19), contrast can be observed in the tail corresponding to 1.4 % of the total activity present (0.02 MBq maximum). This is equivalent to 1.1×10^8 nanoparticles, approximately twenty times that of the number of antibody-directed nanoparticles that may reach the tumours of Cohort 1; however, this lower number is currently below detection. It may be hoped that future experiments with different methodologies to the one described above would improve the solubility of the protein-bearing nanoparticles or would increase the percentage of particles bearing a mAb, thus increasing the absolute concentration of antibody-bearing radiolabelled nanoparticles to within the limits of detection.

The immediate value of the experiment above is in showing the lack of toxicity of the agent at the concentration used, which leaves the opportunity for future development. The approach described does not yet offer a viable alternative to more 'traditional' immunoPET agents, but future work may address improving the solubility of the antibody-bearing nanoparticles to obtain higher *in vivo* concentrations.

4.4 Conclusion

The monoclonal antibody trastuzumab was fluorescently labelled and immobilised onto APTES@SPION via reductive amination of the sugar side chains. *In vitro* incubation of the antibody-bearing nanoparticles with Her-2 overexpressing cells was analysed by cytometry and observed to bind specifically, confirming the retention of antibody specificity following immobilisation.

Water dispersible ^{89}Zr -labelled SPION were synthesised on as small a scale as possible and using as much radioactive material as practicable to generate a species intended for administration to tumour-bearing mice. Of the twelve mice studied, eleven survived to the end of the PET-CT scanning window with the sole mortality due to hypothermia. The radiolabelled nanoparticles were not toxic in the quantity administered, which had been a concern due to difficulties observed in their solubilisation. Over the experimental timeframe, the radiolabelled nanoparticles were rapidly cleared from the bloodstream and sequestered into the liver and spleen, as has been reported as a common *in vivo* excretion route for nanoparticles. Several clinically approved SPION MRI agents have been used for the direct imaging of tumours of the liver and spleen,^{79,80} so in principle the ^{89}Zr -labelled APTES@SPION synthesised as part of the current work could function as a bimodal PET/MRI agent in an analogous way.

There are multiple ways to improve the methodology described. Reducing the rate of RES uptake of particles is crucial to ensuring that antibody-bearing SPION have a long enough blood clearance time to allow the opportunity to bind to tumour cells. This would require experiments to study the nature of the protein corona of the nanoparticles. Improvements to the method of APTES coating are also called for to improve their colloidal stability (unexpectedly poor dispersal resulted in the loss of most of the radioactive particles prior to administration). This would be hoped to allow a greater degree of bioconjugation to occur without increasing the drive to aggregate. A greater number of nanoparticles bearing an antibody moiety would increase the likelihood of successful tumour-labelling events.

The methodology used to radiolabel the particles is not easily modified to increase the degree of radiolabel inclusion while retaining the essence of the approach. To achieve 'one isotope to one nanoparticle labelling' would require either reaction on an exceptionally small scale which would be beset by difficulties in terms of manipulations and reproducibility, or the use of large quantities of ^{89}Zr which would by necessity require a different methodology (for example using automated steps to limit operator exposure). An alternative approach may be

required; the pre-forming of monodisperse oleic acid coated SPION was described in Chapter 2 and is known to be highly reproducible. Several methods for the removal of the organic coating from this species and its replacement to give hydrophilic surfaces with bioconjugation-ready functionalities have been reported,⁸¹⁻⁸³ and it has been observed that radioarsenic labelling of such particles can be achieved by gentle heating (37 °C) in air for two hours.²⁶ The use of OA@SPION as starting materials would in theory result in reduced polydispersity and increased colloidal stability in the hydrophilic product species. Reducing the scale of the radiolabelling step would be less susceptible to variable results as the particles are pre-formed and can be accurately handled on a small scale prior to the introduction of radiation. Radiolabelling efficiency could be increased due to the smaller iron oxide cores having a greater surface area:volume ratio and the particles having a reduced drive to aggregate. Experiments to validate this approach to radiolabelling prior to bioconjugation would be of great interest.

4.5 References

- 1 R. Nahta and F. J. Esteva, *Cancer Lett.*, 2006, **232**, 123–138.
- 2 J. Mendelsohn and J. Baselga, *Oncogene*, 2000, **19**, 6550–6565.
- 3 C. A. Hudis, *N. Engl. J. Med.*, 2007, **357**, 39–51.
- 4 N. Patani and K. Mokbel, *Surg. Oncol.*, 2010, **19**, e11–e21.
- 5 S. Zhang, W.-C. Huang, P. Li, H. Guo, S.-B. Poh, S. W. Brady, Y. Xiong, L.-M. Tseng, S.-H. Li, Z. Ding, A. A. Sahin, F. J. Esteva, G. N. Hortobagyi and D. Yu, *Nat. Med.*, 2011, **17**, 461–469.
- 6 B. D. Wright and S. E. Lapi, *J. Nucl. Med.*, 2013, **54**, 1171–1174.
- 7 M. N. Lub-de Hooge, J. G. W. Kosterink, P. J. Perik, H. Nijhuis, L. Tran, J. Bart, A. J. H. Suurmeijer, S. de Jong, P. L. Jager and E. G. E. de Vries, *Br. J. Pharmacol.*, 2004, **143**, 99–106.
- 8 P. J. Perik, M. N. Lub-De Hooge, J. A. Gietema, W. T. A. van der Graaf, M. A. de Korte, S. Jonkman, J. G. W. Kosterink, D. J. van Veldhuisen, D. T. Sleijfer, P. L. Jager and E. G. E. de Vries, *J. Clin. Oncol.*, 2006, **24**, 2276–2282.
- 9 S. Palm, R. M. Enmon, C. Matei, K. S. Kolbert, S. Xu, P. B. Zanzonico, R. L. Finn, J. A. Koutcher, S. M. Larson and G. Sgouros, *J. Nucl. Med.*, 2003, **44**, 1148–1155.
- 10 W.-J. Chen, C.-L. Yen, S.-T. Lo, K.-T. Chen and J.-M. Lo, *Appl. Radiat. Isot.*, 2008, **66**, 340–345.
- 11 J. N. Tinianow, H. S. Gill, A. Ogasawara, J. E. Flores, A. N. Vanderbilt, E. Luis, R. Vandlen, M. Darwish, J. R. Junutula, S.-P. Williams and J. Marik, *Nucl. Med. Biol.*, 2010, **37**, 289–297.
- 12 M. Moreau, O. Raguin, J.-M. Vrigneaud, B. Collin, C. Bernhard, X. Tizon, F. Boschetti, O. Duchamp, F. Brunotte and F. Denat, *Bioconjug. Chem.*, 2012, **23**, 1181–1188.
- 13 S. Sasada, H. Kurihara, T. Kinoshita, M. Yoshida, N. Honda, T. Shimoi, A. Shimomura, M. Yunokawa, K. Yonemori, C. Shimizu, A. Hamada, Y. Kanayama, Y. Watanabe, Y. Fujiwara and K. Tamura, *Ann. Oncol.*, 2017, **28**, 2028–2029.
- 14 K. Tamura, H. Kurihara, K. Yonemori, H. Tsuda, J. Suzuki, Y. Kono, N. Honda, M. Kodaira, H. Yamamoto, M. Yunokawa, C. Shimizu, K. Hasegawa, Y. Kanayama, S. Nozaki, T. Kinoshita, Y. Wada, S. Tazawa, K. Takahashi, Y. Watanabe and Y. Fujiwara, *J. Nucl. Med. Off. Publ. Soc. Nucl. Med.*, 2013, **54**, 1869–1875.
- 15 R. F. Meredith, J. Torgue, M. T. Azure, S. Shen, S. Saddekni, E. Banaga, R. Carlise, P. Bunch, D. Yoder and R. Alvarez, *Cancer Biother. Radiopharm.*, 2014, **29**, 12–17.
- 16 S. Rasaneh, H. Rajabi, M. H. Babaei, F. J. Daha and M. Salouti, *Nucl. Med. Biol.*, 2009, **36**, 363–369.
- 17 L. Fiandra, S. Mazzucchelli, C. De Palma, M. Colombo, R. Allevi, S. Sommaruga, E. Clementi, M. Bellini, D. Prospero and F. Corsi, *ACS Nano*, 2013, **7**, 6092–6102.
- 18 E. Occhipinti, P. Verderio, A. Natalello, E. Galbiati, M. Colombo, S. Mazzucchelli, A. Salvadè, P. Tortora, S. M. Doglia and D. Prospero, *Nanoscale*, 2011, **3**, 387–390.
- 19 H. Kulhari, D. Pooja, S. V. K. Rompicharla, R. Sistla and D. J. Adams, *Med. Res. Rev.*, 2015, **35**, 849–876.
- 20 H. Zolata, H. Afarideh and F. Abbasi-Davani, *J. Radioanal. Nucl. Chem.*, 2014, **301**, 451–460.
- 21 H. Zolata, F. Abbasi Davani and H. Afarideh, *Nucl. Med. Biol.*, 2015, **42**, 164–170.
- 22 H. Zolata, H. Afarideh and F. A. Davani, *Cancer Biother. Radiopharm.*, 2016, **31**, 324–329.
- 23 M. A. Deri, B. M. Zeglis, L. C. Francesconi and J. S. Lewis, *Nucl. Med. Biol.*, 2013, **40**, 3–14.
- 24 Y. W. S. Jauw, M. der H. van Oordt, C. Willemien, O. S. Hoekstra, N. H. Hendrikse, D. J. Vugts, J. M. Zijlstra, M. C. Huisman, V. Dongen and G. A. M. S, *Front. Pharmacol.*, 7, 131.
- 25 G. Fischer, U. Seibold, R. Schirmacher, B. Wängler and C. Wängler, *Molecules*, 2013, **18**, 6469–6490.

- 26 F. Chen, P. A. Ellison, C. M. Lewis, H. Hong, Y. Zhang, S. Shi, R. Hernandez, M. E. Meyerand, T. E. Barnhart and W. Cai, *Angew. Chem. Int. Ed.*, 2013, **52**, 13319–13323.
- 27 R. Chakravarty, H. F. Valdovinos, F. Chen, C. M. Lewis, P. A. Ellison, H. Luo, M. E. Meyerand, R. J. Nickles and W. Cai, *Adv. Mater.*, 2014, **26**, 5119–5123.
- 28 F. Chen, S. Goel, H. F. Valdovinos, H. Luo, R. Hernandez, T. E. Barnhart and W. Cai, *ACS Nano*, 2015, **9**, 7950–7959.
- 29 M. Walther, P. Gebhardt, P. Grosse-Gehling, L. Würbach, I. Irmeler, S. Preusche, M. Khalid, T. Opfermann, T. Kamradt, J. Steinbach and H.-P. Saluz, *Appl. Radiat. Isot.*, 2011, **69**, 852–857.
- 30 B. M. Zeglis, J. L. Houghton, M. J. Evans, N. Viola-Villegas and J. S. Lewis, *Inorg. Chem.*, 2013, **53**, 1880–1899.
- 31 'Ionising radiation - radiation protection', <http://www.hse.gov.uk/radiation/ionising/protection.htm>, (accessed 12 September 2017).
- 32 K. Wilson and J. Walker, Eds., *Principles and Techniques of Biochemistry and Molecular Biology*, Cambridge University Press, Cambridge, UK : New York, 7th edition., 2010.
- 33 D. L. Holliday and V. Speirs, *Breast Cancer Res.*, 2011, **13**, 215.
- 34 'BT-474 ATCC ® HTB-20™ Homo sapiens mammary gland'; https://www.lgcstandards-atcc.org/Products/All/HTB-20.aspx?geo_country=gb, (accessed 4 September 2017).
- 35 B. Chazotte, *Cold Spring Harb. Protoc.*, 2011, doi: 10.1101/pdb.prot5556..
- 36 'NC-200™ Automated Cell Counter', <https://chemometec.com/cell-counters/cell-counter-nc-200-nucleocounter/>, (accessed 4 September 2017).
- 37 'Counting cells using a hemocytometer', <http://www.abcam.com/protocols/counting-cells-using-a-hemocytometer>, (accessed 4 September 2017).
- 38 'DAPI Solution (1 mg/mL) - Thermo Fisher Scientific', <https://www.thermofisher.com/order/catalog/product/62248>, (accessed 4 September 2017).
- 39 M. de Jong and T. Maina, *J. Nucl. Med.*, 2010, **51**, 501–504.
- 40 E. A. Sausville and A. M. Burger, *Cancer Res.*, 2006, **66**, 3351–3354.
- 41 R. A. Morgan, *Mol. Ther.*, 2012, **20**, 882–884.
- 42 M. Cariati, R. Marlow and G. Dontu, in *Cancer Cell Culture*, Humana Press, 2011, pp. 471–482.
- 43 D. Siolas and G. J. Hannon, *Cancer Res.*, 2013, **73**, 5315–5319.
- 44 D. Voet, J. G. Voet and C. W. Pratt, *Fundamentals of Biochemistry: Life at the Molecular Level*, Wiley, Hoboken, NJ, 2nd edition., 2012.
- 44 'Athymic Nude Mouse', <http://www.criver.com/products-services/basic-research/find-a-model/athymic-nude-mouse?loc=GB>, (accessed 4 September 2017).
- 46 G. Benton, H. K. Kleinman, J. George and I. Arnautova, *Int. J. Cancer*, 2011, **128**, 1751–1757.
- 47 S. Festing and R. Wilkinson, *EMBO Rep.*, 2007, **8**, 526–530.
- 48 J. W. Engle, H. Hong, Y. Zhang, H. F. Valdovinos, D. V. Myklejord, T. E. Barnhart, C. P. Theuer, R. J. Nickles and W. Cai, *Mol. Pharm.*, 2012, **9**, 1441–1448.
- 49 J.-H. Lee, Y.-M. Huh, Y. Jun, J. Seo, J. Jang, H.-T. Song, S. Kim, E.-J. Cho, H.-G. Yoon, J.-S. Suh and J. Cheon, *Nat. Med.*, 2007, **13**, 95–99.
- 50 B. Riemann, K. P. Schäfers, O. Schober and M. Schäfers, *Q. J. Nucl. Med. Mol. Imaging Off. Publ. Ital. Assoc. Nucl. Med. AIMN Int. Assoc. Radiopharmacol. LAR Sect. Soc. Of*, 2008, **52**, 215–221.
- 51 M. L. James and S. S. Gambhir, *Physiol. Rev.*, 2012, **92**, 897–965.
- 51 C. Kuntner and D. B. Stout, *Front. Phys.*, doi:10.3389/fphy.2014.00012.
- 53 N. Long and W.-T. Wong, *The Chemistry of Molecular Imaging*, Wiley-Blackwell, Hoboken, NJ, 1st edition., 2015.
- 54 J. R. Lakowicz, *Principles of Fluorescence Spectroscopy*, Springer, New York, 3rd edition., 2010.

- 55 A. Periasamy, Ed., *Methods in Cellular Imaging*, OUP USA, Oxford ; New York, 2001.
- 56 G. T. Hermanson, *Bioconjugate Techniques*, Academic Press, London ; Waltham, MA, 3rd edition., 2013.
- 56 'Fluorescein isothiocyanate isomer I',
<http://www.sigmaaldrich.com/catalog/product/sigma/f7250>, (accessed 30 August 2017).
- 58 N. Chekina, D. Horák, P. Jendelová, M. Trchová, M. J. Beneš, M. Hrubý, V. Herynek, K. Turnovcová and E. Syková, *J. Mater. Chem.*, 2011, **21**, 7630–7639.
- 59 S. Vira, E. Mekhedov, G. Humphrey and P. S. Blank, *Anal. Biochem.*, 2010, **402**, 146–150.
- 60 H. M. Shapiro, *Practical Flow Cytometry*, Wiley-Blackwell, New York, 4th edition., 2003.
- 61 M. G. Ormerod, *Flow Cytometry - a Basic Introduction*, Redhill, 2008.
- 61 'What is flow cytometry (FACS analysis)?', <http://www.antibodies-online.com/resources/17/1247/what-is-flow-cytometry-facs-analysis/>, (accessed 13 September 2017).
- 62 'ISS Data Tables, Lifetime Data of Selected Fluorophores',
http://www.iss.com/resources/reference/data_tables/LifetimeDataFluorophores.html, (accessed 30 August 2017).
- 64 J. P. Nolan and S. A. Stoner, *Cytom. Part J. Int. Soc. Anal. Cytol.*, 2013, **83**, 301–305.
- 63 K. Andersson, H. Björkelund and M. Malmqvist, *Nat. Preced.*, doi:10.1038/npre.2010.5218.1.
- 66 J. Xu, A. F. Chambers, A. B. Tuck and D. I. Rodenhiser, *Cancer Genet.*, 2008, **181**, 1–7.
- 67 P. H. Elsinga, *Trends on the Role of PET in Drug Development*, World Scientific, Singapore, 2012.
- 68 M. Ito, S. J. Hong and J. S. Lee, *Biomed. Eng. Lett.*, 2011, **1**, 70–81.
- 69 S. Wilhelm, A. J. Tavares, Q. Dai, S. Ohta, J. Audet, H. F. Dvorak and W. C. W. Chan, *Nat. Rev. Mater.*, 2016, **1**, 1–12.
- 70 U. Prabhakar, H. Maeda, R. K. Jain, E. M. Sevick-Muraca, W. Zamboni, O. C. Farokhzad, S. T. Barry, A. Gabizon, P. Grodzinski and D. C. Blakey, *Cancer Res.*, 2013, **73**, 2412–2417.
- 71 L. C. Drickamer, *J. Chem. Ecol.*, 1995, **21**, 1481–1493.
- 72 A. K. Gupta and M. Gupta, *Biomaterials*, 2005, **26**, 3995–4021.
- 73 P. Aggarwal, J. B. Hall, C. B. McLeland, M. A. Dobrovolskaia and S. E. McNeil, *Adv. Drug Deliv. Rev.*, 2009, **61**, 428–437.
- 74 M. Mahmoudi, I. Lynch, M. R. Ejtehadi, M. P. Monopoli, F. B. Bombelli and S. Laurent, *Chem. Rev.*, 2011, **111**, 5610–5637.
- 75 S.-Y. Seong and P. Matzinger, *Nat. Rev. Immunol.*, 2004, **4**, 469–478.
- 76 D. F. Moyano, M. Goldsmith, D. J. Solfiell, D. Landesman-Milo, O. R. Miranda, D. Peer and V. M. Rotello, *J. Am. Chem. Soc.*, 2012, **134**, 3965–3967.
- 77 R. F. Minchin and D. J. Martin, *Endocrinology*, 2010, **151**, 474–481.
- 78 A. M. Lutz, D. Weishaupt, E. Persohn, K. Goepfert, J. Froehlich, B. Sasse, J. Gottschalk, B. Marincek and A. H. Kaim, *Radiology*, 2005, **234**, 765–775.
- 79 P. Reimer and T. Balzer, *Eur. Radiol.*, 2003, **13**, 1266–1276.
- 80 S. Laurent, D. Forge, M. Port, A. Roch, C. Robic, L. Vander Elst and R. N. Muller, *Chem. Rev.*, 2008, **108**, 2064–2110.
- 81 T. Zhang, J. Ge, Y. Hu and Y. Yin, *Nano Lett.*, 2007, **7**, 3203–3207.
- 82 Y. I. Park, E. Kim, C.-H. Huang, K. S. Park, C. M. Castro, H. Lee and R. Weissleder, *Bioconjug. Chem.*, 2017, **28**, 33–37.
- 83 Y.-T. Kuo, C.-Y. Chen, G.-C. Liu and Y.-M. Wang, *PLOS ONE*, 2016, **11**, e0148695.

Chapter 5: The design and synthesis of Cu-ATSM-like complexes for use as haptens in custom antibody production

5.1 Introduction

As part of the initial proposal for this project, we determined to prepare a series of metal complexes analogous to the hypoxia-targeting contrast agent ^{64}Cu -ATSM. These complexes would be used as haptens conjugated to carrier proteins and used to generate antibodies in sheep. It was hoped that from the antibodies produced in this manner some could be identified that could function as catalysts for the reduction by which ^{64}Cu -ATSM selectively images hypoxia. Such an antibody would have been raised against a metal complex that showed a distorted geometry such that it could function as a model for the *transition state* of this process. A more thorough discussion of the different aspects and theory behind this proposition is given below. Difficulties in the synthesis of the target molecules prevented the production of chemical species that were of sufficient purity to be used in a bioconjugation context. Due to a corporate restructuring of sponsors, the opportunity to use the molecules *in vivo* did not arise (antibody generation *in vivo* is expensive). However, the materials prepared were successfully analysed *in vitro* for antibacterial and anthelmintic activity.

5.1.1 Angiogenesis and hypoxia (reduced oxygen content) in cancer

Solid cancerous tumours arise as a result of a number of genetic mechanisms that share a common result on the cellular level: rapid, excessive cell division where apoptosis is down regulated. Cancer cells require blood vessels for the delivery of nutrients and oxygen and to remove waste. These processes are necessary for continued growth and thus the development of new blood vessels (angiogenesis) is crucial. Studies have shown that cancer models stop dividing and become necrotic or apoptotic when deprived of the opportunity for angiogenesis.¹ It has also been shown that the levels of angiogenic factors in tissue are indicative of the tumour's 'aggressiveness' and are therefore of prognostic value. Cancer cells show the ability to penetrate the blood vessels that supply them and may travel to distant sites within the body, lodge and proliferate to give metastases.¹ Any form of cancer becoming metastatic has a dramatic and negative effect on the prognosis of the patient; of all deaths attributed to cancer, 90% are due to metastases rather than the primary tumour.²

Angiogenesis is triggered by cells requiring nutrients or oxygen and is controlled by the interplay of activator or inhibitor molecules.¹ In the case of cancer, up-regulation of activators and down-regulation of inhibitors synergistically promote development of vasculature to support the solid tumour. The exact nature of how angiogenesis has been

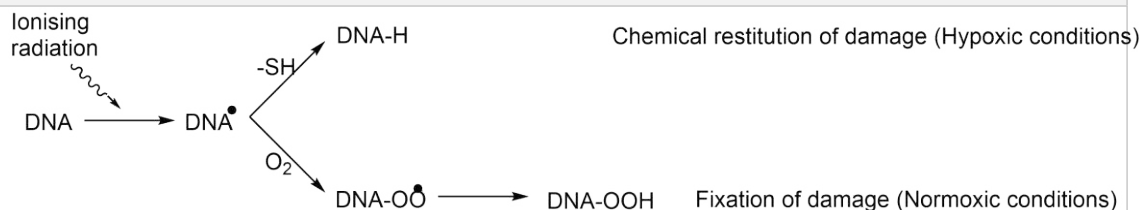
triggered may be referred to as the 'angiogenic phenotype'. The onset of cellular hypoxia (a decrease in the concentration of dissolved oxygen, pO_2) due to insufficient blood supply can trigger angiogenesis.^{1,3}

Hypoxia is therefore part of a mechanism of cancer development: increased cell division reduces oxygen concentration within daughter cells, resulting in an increased demand for new blood vessels. As the tumour grows the daughter cells become distant from the blood vessels; the distance between vessels can exceed the diffusion distances of oxygen in the perivascular space (70-180 μL).⁴ This decreases the amount of oxygen that can be supplied to the cells, adding to the demand for new vasculature. New blood vessels allow for further cell division but architectural faults caused by the speed of their formation exacerbate hypoxia by making the vessels porous and inefficient.^{1,3} Hypoxia has been shown to drive many intra-cellular and extra-cellular changes that ultimately lead to intravasation and metastasis, the mechanisms of which have been extensively reviewed.^{2,5-8}

In addition to its proliferative effects, hypoxia also shows protective effects for the tumour by limiting the efficacy of radio- and chemo-therapies (Fig. 1). In the case of radiotherapy the presence of oxygen allows the damage to DNA caused by ionising radiation to be made permanent. Molecular oxygen has a high affinity for the radical formed by radiation. Binding leads to a peroxy radical that can be protonated, essentially trapping the damage, a process known as the 'oxygen enhancement effect'.⁹ In hypoxic cells, the peroxy radical formation is prevented. Rather, endogenous thiols donate protons that return DNA to its undamaged form such that hypoxic cells can be referred to as 'radiation resistant' or 'desensitised'.¹⁰ For chemotherapy, several mechanisms for resistance exist (see Fig. 1).¹⁰

Due to its contribution to the growth and spread of tumours and the resistance to therapies to which it contributes, the state of hypoxia in a solid mass is of great diagnostic and prognostic value. Early attempts to use the level of oxygen in a tissue diagnostically were focussed on direct, invasive methods. The polarographic O_2 electrode (Eppendorf electrode) is a 17 μm gold micro-electrode mounted on a needle that is advanced through a tissue; the current measured is proportional to the oxygen tension present.^{10,11} Although effective, this technique is limited to superficial tumours and so research has tended to focus on indirect identification of hypoxic tissues throughout the body using molecular imaging.

Mechanism of radiotherapy resistance imbued by hypoxia



Mechanisms of chemotherapy resistance imbued by hypoxia

- Increased distance from blood vessels limit exposure to agents
- Cellular proliferation decreases as a function of distance from blood vessel, limiting effect of proliferation-limiting agents.
- Hypoxia selects for loss of p53 and reduced sensitivity to p53-mediated apoptosis, which is a target mechanism for some agents.
- Some agents' methods of action is similar to that of radiation, and so similar desensitisation mechanisms as discussed above apply.
- Hypoxia upregulates several genes involved in drug resistance e.g. the multi-drug resistance gene MDR1, upregulating efflux of drugs.

Figure 1. Hypoxic tumour resistance to radiotherapy arises from the loss of the oxygen enhancement effect 'fixing' DNA damage (top). Several mechanisms of hypoxic tumour resistance to chemotherapy exist (bottom). Adapted from Brown¹⁰ and Bertout et al.⁵

5.1.2 ⁶⁴Cu-ATSM – a hypoxia selective PET imaging agent

Although other modes of molecular imaging have been used to study hypoxia, in practice most interest is centred on the use of PET as the tracers used can directly report pO₂ levels and do not rely on hypoxia-related cell phenotypes.⁴ The majority of research is focussed on two tracers, ¹⁸F and ⁶⁴Cu via the ¹⁸F-labelled nitroimidazoles and ^{60/62/64}Cu-labelled bis(thiosemicarbazones) (BTSC) compared in Fig. 2.⁴

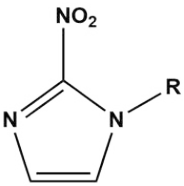
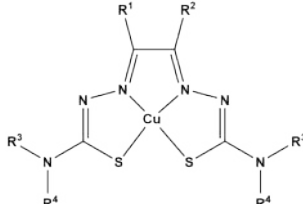
<p>Properties required of an ideal hypoxia-imaging probe</p>	<ul style="list-style-type: none"> • Agent retained in regions of low pO_2, but not normoxic or necrotic cells. • Mechanism of retention should be understood and general for multiple cell/tumour types. • Lipophilic enough to cross cell membranes but sufficiently hydrophilic to prevent membrane sequestration. • Pharmacokinetic behaviour should be dependent solely on pO_2 i.e. independent of blood flow, pH etc. • Metabolically stable except in the case of hypoxic surroundings. • Kinetics allow for imaging on a practicable timescale. • Repeatable to allow for observation of hypoxia and recovery to normoxia.
<p>Nitroimidazole analogues</p>	<p>bis(thiosemicarbazone) analogues</p>
<div style="text-align: center;">  </div> <ul style="list-style-type: none"> • Enters cells by passive diffusion. • Reduced in cells to nitro-radical anion. • In normoxic cells, species is re-oxidised and diffuses out. • In hypoxic cells, further reduction occurs, trapping the species at rates inversely proportional to pO_2. • Reduction requires active reductases, thus accumulation only occurs in viable cells. • R-groups typically contain ^{18}F, $t_{1/2} = 109.8$ min. 	<div style="text-align: center;">  </div> <ul style="list-style-type: none"> • Enters cells by passive diffusion. • Reduced in cells by endogenous thiols or redox-active proteins. • In hypoxic cells, the reduced form is unable to diffuse back out and persists; protonation is followed by metal dissociation and sequestration by proteins in the cell. • Multiple isotopes have been investigated; different imaging modes, timescales and therapeutic effects are possible. • R-groups can be changed independently to adapt characteristics.

Figure 2. Ideal characteristics for a hypoxia-selective PET imaging probe (top) and brief profiles of the mechanisms of the two main agent families being investigated today (bottom).⁴

While nitroimidazole species are numerous, one of the most commonly studied has considerable disadvantages. ^{18}F -FMISO shows slow pharmacokinetics and slow clearance from normoxic tissues. Physicians must wait approximately 2 hours for ^{18}F -FMISO to clear normoxic tissues, during which time the radioactivity will have decayed significantly. Modest

tumour-to-background ratios (> 1.2) limit the contrast observed. Other nitroimidazole species designed to improve upon ^{18}F -FMISO are not currently widely available.⁴

Cu-ATSM is a square-planar BTSC complex that overcomes many of the limitations of the nitroimidazoles. Localisation within hypoxic tissue occurs within an hour of administration with high tumour-to-background ratios ($\gg 2.0$).¹² A range of positron emitting copper isotopes have been used of which ^{64}Cu is the most common. With a 12.7 h radioactive half-life (several times that of ^{18}F), repeat scanning of the patient can occur over a longer period of time (approximately 48 h). The longer half-life also allows for distribution of the isotope to facilities without direct production capabilities.¹² The complexation of the isotope by the ligand occurs rapidly and with a minimum of manipulation and purification, an advantage over the often harsh, multistep syntheses of organic agents such as the fluorinated nitroimidazoles.¹³

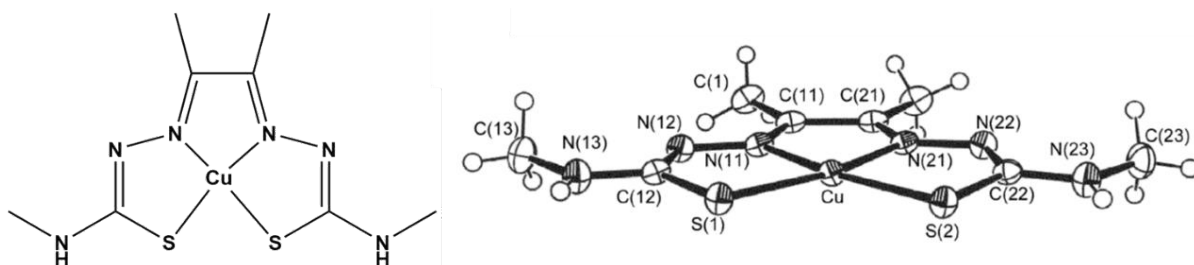


Figure 3. Diagram of Cu-ATSM (left) showing the electronic nature of tetradentate coordination, and an ORTEP representation of crystalline Cu-ATSM (right) demonstrating square planar geometry, taken from Blower *et al.*¹⁴

Cu-ATSM was first noted as displaying hypoxia-selectivity in 1997.¹⁵ In 1998, Dearling *et al.* carried out a systematic study which showed that manipulating the ligand framework of BTSC complexes could change the observed selectivity for hypoxic cells and correlated this to the reduction potential of the metal atom.¹⁶ Later *in vitro* and *in vivo* studies further characterised different aspects of Cu-ATSM's pharmacokinetic behaviour, an excellent introduction to which is available.¹² In 2006 *in vivo* studies confirmed that ^{64}Cu -ATSM could function as a hypoxia-targeting PET agent in most tumour types.¹⁷ Human clinical trials using Cu-ATSM for the imaging of different cancer types have been carried out since 2000^{18–20} and novel uses of Cu-ATSM for imaging and treatment continue today.²¹

Several copper bis(thiosemicarbazones) including Cu-ATSM and Cu-GTSM (see below) have been shown to also have antibacterial properties against pathogenic bacteria such as *Neisseria gonorrhoeae*,^{22,23} *Mycobacterium tuberculosis*²⁴ and *Staphylococcus aureus*.²⁵ The ability of lipophilic BTSC compounds to transport copper ions across cell membranes into bacterial

cell cytoplasm leads to inhibition of cellular processes and/or increased redox stress (depending on the bacterium) that ultimately renders the species toxic; copper BTSC complexes may be of great interest in the development of the next generation of antibiotics.²²

5.1.3 The mechanism of Cu-ATSM's hypoxia selectivity

A diagram of the proposed biphasic mechanism of Cu-ATSM's *in vivo* hypoxia selectivity is shown in Fig. 4. This mechanism has been the subject of much research and debate worldwide.¹² The observed tendency for Cu-ATSM to label hypoxic tissues is generally agreed to be dependent largely on the $\text{Cu}^{2+}/\text{Cu}^{1+}$ redox potential and lipophilicity of the complex.^{14,16,26} Research into 'tuning' these properties in novel species to optimise hypoxia selectivity is ongoing.²⁷

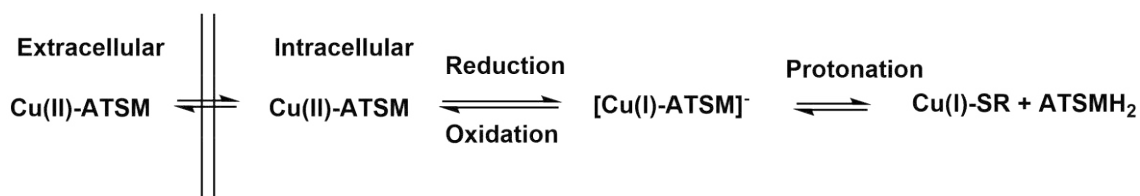


Figure 4. *Bioreductive trapping of Cu-ATSM is dependent on the ability of the complex to enter the cell (lipophilicity), and how readily the metal can dissociate from the ligand. Cytosolic thiols replace the ATSM. Adapted from Dearling and Packard.²⁸*

The neutral, lipophilic complex Cu-ATSM can diffuse across cell membranes. Once inside the cytoplasm, thiol groups on endogenous redox-active proteins can react with the oxidising metal centre (forming disulphide bonds as part of a common mechanism of protecting cellular function), resulting in a reduction of the metal from the +II oxidation state to the +I oxidation state.²⁸⁻³⁴

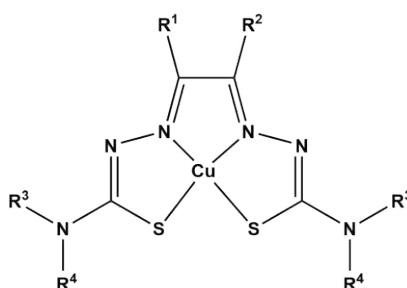
The charged complex $[\text{Cu}^{1+}\text{-ATSM}]^-$ is less lipophilic and is unable to diffuse out of the cell. In normoxic cells oxygen content is sufficient to reoxidise the metal centre and allow egress of the complex, but in hypoxic cells the equilibrium of the redox is shifted and the reduced form persists. Cu^{1+} is a $3d^{10}$ metal centre and has a ligand field stabilisation energy (LFSE) of zero. It is a soft acid with a preference for soft donors, hence sulphur donors are bound more strongly by Cu^{1+} than by Cu^{2+} which is an intermediate/hard acid with a preference for intermediate/hard donors e.g. N, O.³⁵

Although BTSC complexes bind strongly to Cu^{2+} ($K_D \sim 10^{-17} \text{ M}^{-1}$) and Cu^{1+} ($K_D \sim 10^{-13} \text{ M}^{-1}$), reduction followed by ligand distortion would allow ligand donor groups to be replaced by S-donors (*via* dissociative ligand substitution) from competing cytosolic thiols that may be

present in millimolar quantities and which can function as a thermodynamic sink for Cu^{1+} ($K_D \sim 10^{-39} \text{ M}^{-1}$).³⁶ The reducing environment within a hypoxic cell aids this acid-catalysed dissociation; N-donors will be replaced by the preferred S-donors, and the ligand-based S-groups can be protonated and out-competed by the endogenous donors. Upon dissociation, the metal will be sequestered by the cell's endogenous proteins, irreversibly trapping the radionuclide.²⁸

The study of the *in vivo* behaviour of analogues of Cu-ATSM allowed this mechanistic understanding to be arrived at. Although some lipophilicity (the affinity for a molecule for a lipophilic (i.e. non-polar) environment, often quantified as the partition coefficient K_{ow} measured by extraction of the species into octanol from water) is necessary for complexes of this family to enter cells (i.e. the molecules must have $\log_{10}K_{ow} > 0$), it has been found that structural changes that result in moderate lipophilicity differences show little correlation to hypoxia selectivity.^{16,26}

Changing the redox potential of the metal centre has a marked effect on hypoxia selectivity (Table 1).^{12,14,16,26} Cu-BTSC complexes that are 'hypoxia-selective' (i.e. which preferentially accumulate in hypoxic tissues as observed from radiotracer studies) have more negative redox potentials than their analogues which show no selectivity or which are normoxia-selective.



Complex	R ¹	R ²	R ³	R ⁴	$E_{1/2} \text{ Cu}^{2+}/+$ V vs. Ag/AgCl	Backbone C- C bond length (Å)	Selectivity in CHO320 cells
Cu-GTSM	H	H	CH ₃	H	-0.43	1.452(3)	Normoxia
Cu-PTS	CH ₃	H	H	H	-0.50	1.470(4)	Insignificant
Cu-ATSM	CH ₃	CH ₃	CH ₃	H	-0.59	1.479(3)	Hypoxia
Cu-DTS	C ₂ H ₅	C ₂ H ₅	CH ₃	H	-0.59	1.480(6)	Hypoxia

Table 1. Data for selected BTSC complexes. Note how as C-C bond lengths increase, redox potential decreases and hypoxia is selected for. Adapted from Blower *et al.*¹⁴ and Vavere and Lewis.¹²

Having a more negative redox potential indicates that the Cu^{2+} centre is less readily reduced (and Cu^{1+} is more readily oxidised) when bound as Cu-ATSM ($E_{1/2} = -0.59$ V vs Ag/AgCl) than for Cu^{2+} coordinated in Cu-GTSM ($E_{1/2} = -0.43$ V vs Ag/AgCl).¹² Hypoxic cells must have a greater reduction from normal oxygen levels in order to reduce Cu^{2+} , to prevent reoxidation of Cu^{1+} and to facilitate radioisotope dissociation and sequestration when ^{64}Cu -ATSM is administered. For complexes with less negative redox potentials, Cu^{2+} can be reduced at oxygen levels that are lower than normal but which are not indicative of truly chronic hypoxia, allowing sequestration to occur in cells that are not cancerous; the complex is not 'hypoxia-selective'.

The redox potential may be reduced by introducing electron donating backbone constituents that have a two-fold effect (structural changes away from the co-ordination sphere have little effect on selectivity).¹⁴ First, increased electron donation stabilises the higher oxidation state. More importantly, steric clash between the groups leads to a lengthening of the backbone C-C bond.¹⁴ This results in the sulphur arms moving inward, allowing the ligand to coordinate in a manner closer to an ideal square-planar geometry. In the work by Blower *et al.* the average N-Cu-S angle increases from 84.24 to 85.16 °, while the average S-Cu-S angle decreases from 109.75 to 108.99 °.¹⁴ Both angles are closer in value to the bond angles measured in Ni-ATSM, showing an improved 'metal-ligand fit' along with reduced reduction potential and enhanced hypoxia-selectivity as a result of backbone alkylation. This is also reflected in the planarity of the complexes as expressed by torsion angles: the angles are lowest in the almost planar Ni-ATSM, increase for Cu-ATSM (reflecting the poorer fit of the larger metal ion forcing a geometric distortion), and increase again when the alkyl groups are not present in Cu-GTSM, as the shorter backbone results in a smaller ligand cavity and worse fit.¹⁴

Cu^{2+} (intermediate/hard acid, d^9) typically coordinates in a Jahn-Teller distorted octahedral geometry, while Cu^{1+} (soft acid, d^{10}) prefers tetrahedral coordination, most commonly with soft sulphur donors. The release of Cu^{1+} that is necessary for hypoxia-selective contrast is blocked by several energetic barriers: the initial one-electron reduction of Cu^{2+} is disfavoured as it results in the loss of the Jahn-Teller stabilisation energy, the coordination sphere (N_2S_2) is not the preferred donor set of Cu^{1+} , and the ligand must twist to change to the preferred coordination geometry of Cu^{1+} . Backbone alkylation improves the metal-ligand fit for Cu^{2+} by limiting strain within the molecule that can contribute to a distortion towards tetrahedral geometry, promoting planarity and increasing the energy barrier to reduction.

To conclude, reductive ^{64}Cu -ATSM dissociation in hypoxic cells results in tracer accumulation. The ability of the cell to reduce the metal ion and the maintenance of the lower oxidation state is crucial to the selectivity of the agent. Once reduced, a distortion of the square planar ligand system can result in dissociation. A protein binding ^{64}Cu -ATSM in a way that induces tetrahedral distortion increases strain and would increase the likelihood of the radioisotope dissociating by reducing the energetic barrier that must be overcome ('the entatic effect'). If such a protein could be directed to internalise in cancer cells, the selectivity for ^{64}Cu -ATSM to dissociate and label cancer cells would be enhanced.

5.1.4 The use of haptens in polyclonal antibody development

The generation of antibodies within a living creature is the result of the immune system recognising a foreign entity. Any species identified as 'non-self' is defined as an antigen. If an immune response such as antibody production is elicited, the antigen is an immunogen.³⁷ To generate an immune response a species must have a recognisable epitope and be physically large enough to initiate lymphocyte activation. Small molecules and ions with molecular weights less than approximately 1000 are not large enough to elicit an immune response, but if the molecule in question can be attached to a 'carrier protein', the size of the protein will stimulate an immune response and the bound molecule will serve as the recognised epitope.³⁸ In this case the small molecule is referred to as a 'hapten'. The most common carrier proteins used today are Bovine Serum Albumin (BSA) and Keyhole Limpet Hemocyanin (KLH). KLH is extremely immunogenic due to its non-mammal origin, extremely large molecular weight and complex structure. With several hundred lysine groups per molecule to allow hapten conjugation KLH is the most widely used carrier protein.³⁷

Antibodies raised in an animal will be polyclonal. Released by different B cell lines within the body, they will identify different epitopes of an immunogen. In the context of a hapten-carrier conjugate, a population of polyclonal antibodies will contain immunoglobulins that recognise the hapten when it is in different states or will bind the hapten in different ways.

5.1.5 Enzymes, catalytic antibodies and the proposed use of M-BTSC complexes as haptens

Enzymes catalyse biological processes by offering a binding site that has geometric and electronic complementarity to a substrate molecule. This binding site is largely preformed but is changed upon binding according to the 'induced fit' model of enzyme catalysis. However this is insufficient to explain the large rate enhancements seen in enzymatically catalysed reactions. It is known that enzymes bind the transition state of a process with

greater affinity than the product or substrate molecules.³⁹ Transition states cannot be isolated, but computational studies and an understanding of the likely mechanism can allow researchers to hypothesise the nature of the transition state for a given process, allowing stable mimics of the transition state to be synthesised. Using such analogues as haptens has allowed researchers to generate antibodies that stabilise the transition state of a chemical process and which function as catalysts by straining the substrate, reducing the energetic barrier that must be overcome.⁴⁰ The first catalytic antibodies were reported in the 1986 independently by the Schultz and Lerner groups (Fig. 5).^{41,42} Early work focussed on the use of ‘abzymes’ for small molecule transformations in industrial contexts but more recently diverse applications of this technology have been investigated, including the treatment of addiction, Alzheimer’s disease and the degradation of chemical warfare agents.⁴³

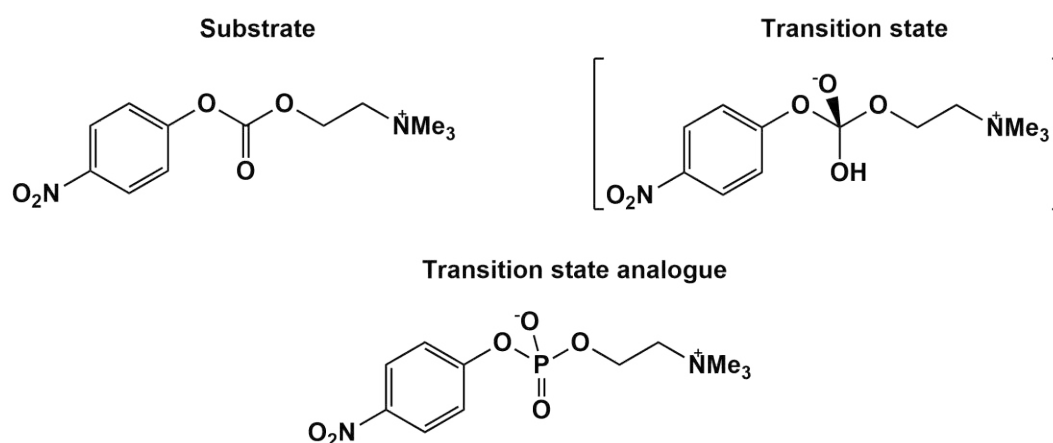


Figure 5. One of the first catalytic antibodies catalysed the hydrolysis of a carbonate group. The monoanionic tetrahedral transition state is mimicked by the stable phosphonate group of the analogue.⁴¹

It was postulated that antibodies could be raised that would catalyse the reduction of Cu-ATSM. As has been described, the sensitivity of the hypoxia-targeting function of ⁶⁴Cu-ATSM is dependent on the ability of the complex to undergo a twist from square-planar to tetrahedral following reduction of the metal. It has been reported that deviations in planarity reported in the crystal structure of Cu-BTSC complexes are a result of external packing forces and not inherent in the structures of the ligands themselves, which energetically would favour the square planar geometry when coordinating a metal.¹⁴ However, the nature of the metal may contribute to deviations from ideal geometry. A study of bond angles in Cu-BTSC complexes showed that the cavity presented in these ligands is too small to ideally accommodate the Cu²⁺ ion; N-Cu-N bond angles are typically 80 ° (compared to an ideal value of 90 °), and the sulphur donors are pushed out to approximately 120 °. The

coordination of the smaller Ni^{2+} (d^8) ion by the ATSM ligand show angles at the metal centre closer to 90° , more closely approximating ideal square planar coordination (see Fig. 6).¹⁴ Moving to a larger ion, Zn-ATSM shows a distorted square pyramidal crystal structure in the solid state.⁴⁴ As a d^{10} centre, no ligand field stabilisation energy (LFSE) is gained by coordination of the metal to offset the increased energy resulting from ligand strain. It can be assumed that in the solution phase, the Zn analogue of Cu-ATSM tends to twist away from square planar to minimise the strain. Other studies have shown that the larger Cd^{2+} can be accommodated by similar ligands opening further to give a distorted octahedral geometry with solvent molecules in apical positions.⁴⁵

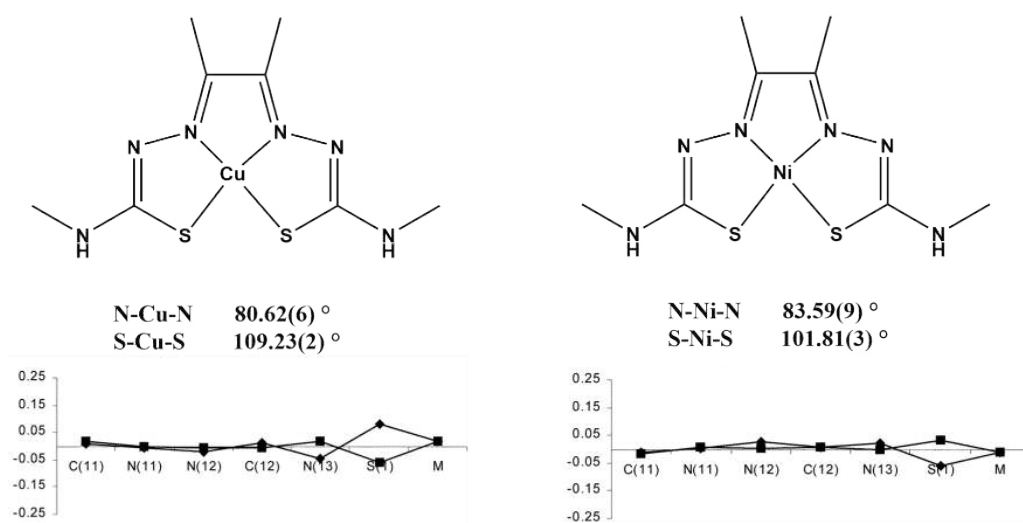


Figure 6. *Cu-ATSM and Ni-ATSM share a tetradentate coordination sphere, but the nickel complex shows bond angles in closer agreement with ideal square planar geometry. Analysis of displacement of ligands atoms from a plane defined by the metal show a more planar complex for Ni^{2+} . Adapted from Blower et al.¹⁴*

Bifunctional chelators based on Cu-ATSM are known.⁴⁶ Introduction of functional groups away from the coordination sphere does not significantly affect the coordination or redox potential of the copper centre. Asymmetric ligands displaying carboxylate and amine groups for conjugation have been studied.⁴⁷ In the current work, three ligands (Fig. 7) were synthesised and characterised, along with their complexes with Cu^{2+} , Ni^{2+} , Zn^{2+} and Cd^{2+} . $\mathbf{H}_2\mathbf{L}^1$ and $\mathbf{H}_2\mathbf{L}^2$ are based respectively on 2, 3-butandione and glyoxal backbones and have 2-carbon linker arms terminating in ethyl ester protected carboxylic acids. The loss of the backbone methyl groups from $\mathbf{H}_2\mathbf{L}^1$ would theoretically result in shorter C-C backbone bonds in $\mathbf{H}_2\mathbf{L}^2$.¹⁴ This would in effect make the ligand cavity smaller and would force greater deviation from planarity when coordinating a metal centre. $\mathbf{H}_2\mathbf{L}^3$ is an analogue for $\mathbf{H}_2\mathbf{L}^1$ where the terminal groups are t-Butoxycarbonyl protected amine groups. Deprotection of

these species would give functionalities which could be used to achieve bioconjugation to a carrier protein. The deprotected forms of the three ligands and their complexes would coordinate differently to a carrier protein due to the different functionalities and so would present different recognisable epitopes for antibody generation. The relatively short linker arms were chosen to force the complex close to the bulky carrier protein, increasing steric effects that could distort the ligand cavity.

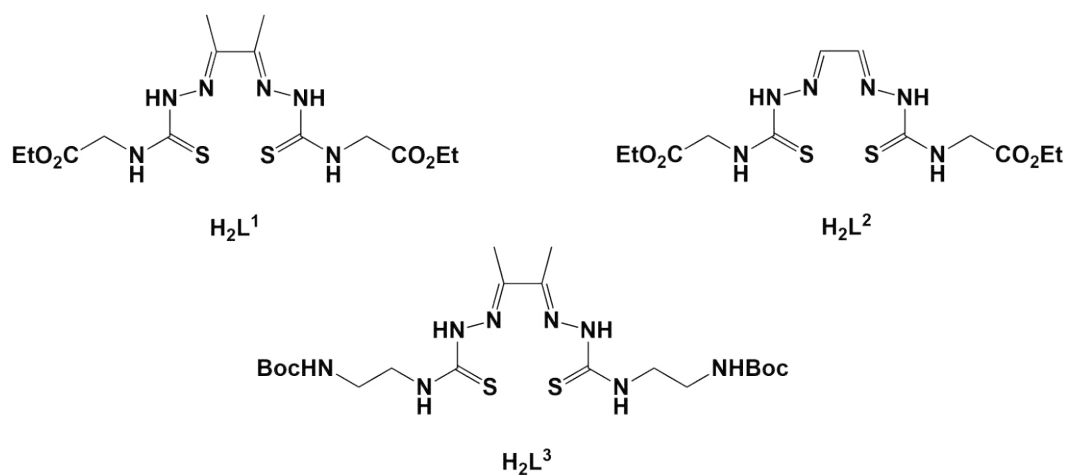


Figure 7. Structures of ligands H₂L¹⁻³. Transition metal complexes were synthesised and are discussed below.

5.1.6 Aims and objectives

Three ligands and their metal complexes were designed for use as haptens for antibody generation in sheep. Ligands were designed to be similar to known BTSC ligands (e.g. ATSMH₂ and GTSMH₂) but which could be bioconjugated to proteins via two groups. The use of different metals with different ionic sizes and coordination preferences was intended to maximise the potential for identifying an antibody that would bind Cu-ATSM in a geometry approaching tetrahedral and act as a catalyst for demetallation. The target antibody was then to be used along with a relevant clinically approved therapeutic monoclonal antibody (mAb) to create a bispecific antibody capable of first internalising in cancerous cells and then catalysing the reduction of ⁶⁴Cu-ATSM, enhancing the *in vivo* selectivity of the copper species for cancer cells based on their hypoxic environment *and* on their phenotype.

Additionally, it was considered that several of the BTSC complexes synthesised for use as haptens may have antibacterial or anthelmintic activity. Experiments were performed to identify whether such complexes satisfied unmet clinical needs.

Unfortunately, deprotection conditions to give forms of the complexes and ligands suitable for bioconjugation could not be identified. Example procedures that were unsuccessful are given in Additional Experimental Section III. For all conditions trialled an uncharacterisable mixture of multiple species resulted. Future work on this project could focus on developing conditions that deprotect the complexes and ligands without significant decomposition. Other ligands designed and synthesised as part of this work are also discussed in Additional Experimental Section III. They are not included here because in all cases, the syntheses resulted in an impure sample that due to their limited solubility and stability under harsh conditions could not be purified or characterised satisfactorily.

5.2 Experimental

5.2.1 Materials and Methods

All reactions were performed with the use of vacuum line and Schlenk techniques. Reagents were commercial grade and were used without further purification. All reagents and solvents were purchased from Alfa Aesar or Sigma Aldrich. ^1H and $^{13}\text{C}\{-^1\text{H}\}$ NMR spectra were recorded on an NMR-FT Bruker 400 MHz or Joel Eclipse 300 MHz spectrometer and recorded in CDCl_3 , CD_3OD or $d^6\text{-DMSO}$. ^1H and $^{13}\text{C}\{-^1\text{H}\}$ NMR chemical shifts (δ) were determined relative to internal TMS and are given in ppm. Coupling constants J are given in hertz (Hz). Low- and high-resolution mass spectra were obtained using a Waters LCT Premier XE instrument and are reported as m/z (relative intensity). IR spectra are recorded as solid samples on a Shimadzu IRAffinity-1 FTIR spectrometer. UV-Vis studies were performed on a Jasco V-570 spectrophotometer as MeCN solutions (5×10^{-5} M). Microanalyses were performed by London Metropolitan University, UK. X-ray crystallography was performed by the UK National Crystallography Service.⁴⁸ Anti-parasitic assays were kindly performed by K. Whatley, Parasitology and Epidemiology Group, Aberystwyth University, UK. Antibacterial MIC determination experiments were performed by Sion Edwards and Prof. D.W. Williams School of Biosciences, Cardiff University, UK and were carried out on a BMG LabTech FLUOstar Omega plate reader.

5.2.2 Synthesis and analytical techniques

Ethyl-2-(hydrazinecarbothioamido)acetate (1)

Ethyl isothiocyanatoacetate (3 mL, 24.2 mmol) was dissolved in EtOH (60 mL) at 0 °C. Hydrazine hydrate (1.22 mL, 25 mmol) in cold EtOH (20 mL) was added dropwise over 30 mins with stirring. The mixture was stirred for a further 30 mins, allowed to reach room temperature, stirred for 30 mins, then cooled to 0 °C once again. The precipitate was collected by filtration, washed with cold EtOH (20 mL) and dried to give the product as a white solid (3.56 g, 20.1 mmol, 83%). ^1H NMR (400 MHz, CDCl_3) $\delta_{\text{H}} = 7.82$ (1H, br s, NH), 7.14 (1H, br s, NH), 4.38 (2H, d, $^3J_{\text{HH}} = 5.2$ Hz, CH_2NH), 4.18 (2H, q, $^3J_{\text{HH}} = 7.2$ Hz, CH_2CH_3), 3.79 (2H, br s, NH_2), 1.24 (3H, t, $^3J_{\text{HH}} = 7.2$ Hz, CH_2CH_3) ppm. ^{13}C NMR (75 MHz, CDCl_3) $\delta_{\text{C}} = 183.1$ (CS), 169.8 (CO), 61.7 (CH_2CH_3), 45.8 (CH_2NH), 14.3 (CH_2CH_3) ppm. HR-MS (EI+) found m/z 177.0571, calculated m/z 177.0572 for $[\text{C}_5\text{H}_{11}\text{N}_3\text{O}_2\text{S}]^+$. IR (ATP) $\nu = 3341$ (NH), 3311 (NH), 3264 (NH), 1743 (CO), 1079 (CS) cm^{-1} .

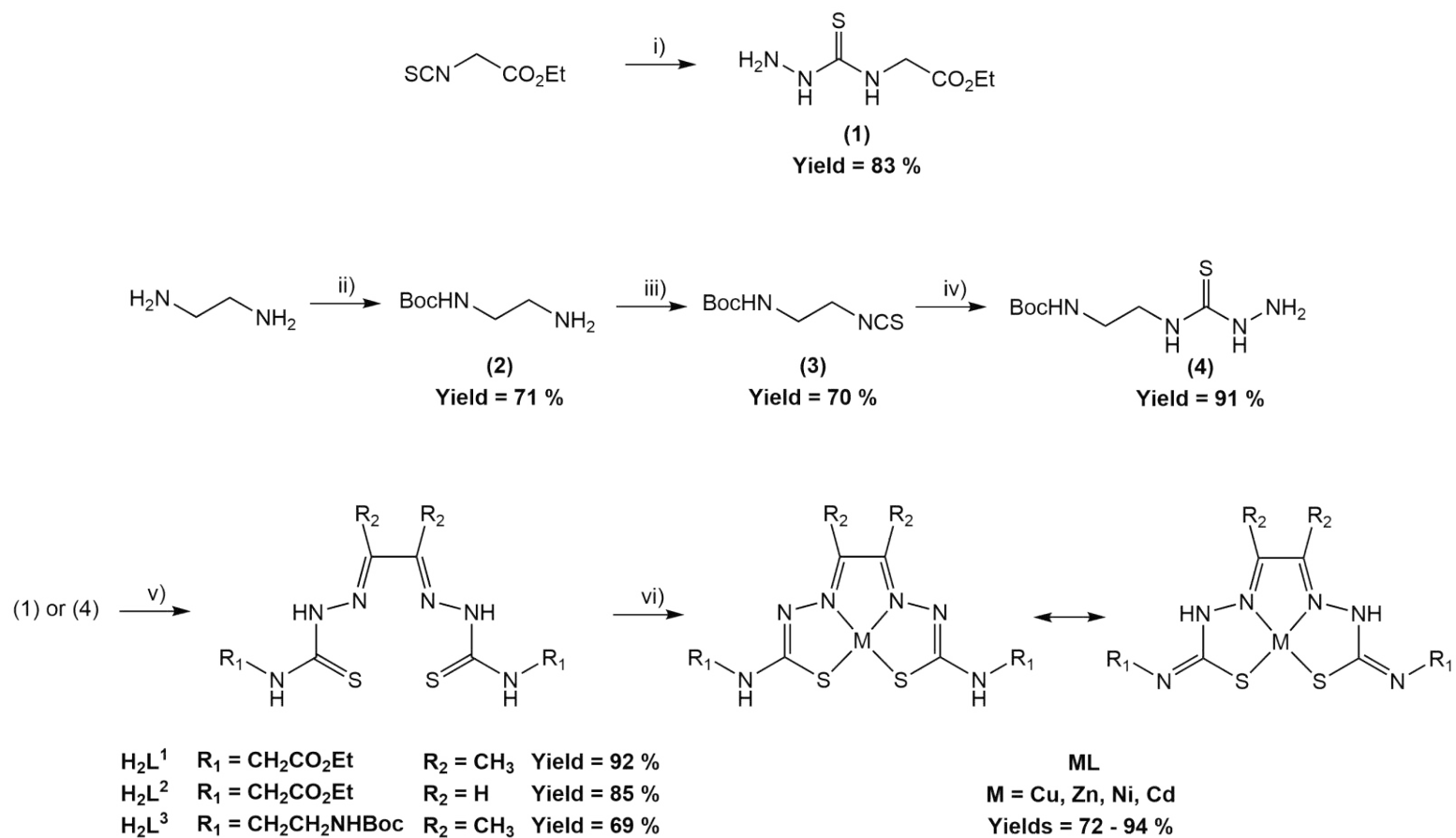


Figure 8. Synthetic schemes for ligand and complexes described in this report. i) $N_2H_4 \cdot H_2O$, EtOH, 0 °C, 1 h. ii) Boc_2O , DCM, 0 °C, 0.5 h, RT, overnight. iii) CS_2 , NEt_3 , TsCl, THF, RT, overnight. iv) $N_2H_4 \cdot H_2O$, EtOH, 0 °C, 1 h. v) 2, 3-butandione or glyoxal, EtOH, reflux, 4 h or overnight. vi) $M(OAc)_2 \cdot xH_2O$, EtOH, reflux, 4 h.

Ligand H₂L¹

Ethyl-2-(hydrazinecarbothioamido)acetate (**1**) (1.062 g, 6.00 mmol) and 2,3-butanedione (0.263 mL, 3.00 mmol) in EtOH (20 mL) were heated at reflux with H₂SO₄ (1 drop) for 4 h. The mixture was allowed to cool to room temperature, the precipitate collected by filtration, washed with cold EtOH (10 mL) and dried *in vacuo* to give the product as a white solid (1.12 g, 2.76 mmol, 92 %). ¹H NMR (400 MHz, d⁶-DMSO) δ_H = 10.60 (2H, s, 2 × NH), 8.69 (2H, t, ³J_{HH} = 5.9 Hz, 2 × NHCH₂), 4.33 (4H, d, ³J_{HH} = 5.9 Hz, 2 × NHCH₂), 4.16 (4H, q, ³J_{HH} = 7.1 Hz, 2 × CH₂CH₃), 2.26 (6H, s, 2 × CCH₃), 1.22 (6H, t, ³J_{HH} = 7.1 Hz, 2 × CH₂CH₃) ppm. ¹³C NMR (75 MHz, d⁶-DMSO) δ_C = 179.5 (CS), 169.9 (CO), 149.1 (CCH₃), 61.1 (CH₂CH₃), 46.1 (CH₂NH), 14.7 (CH₂CH₃), 12.4 (CCH₃) ppm. HR-MS (ES+) found m/z 427.1183, calculated m/z 427.1198 for [C₁₄H₂₄N₆O₄S₂ + Na]⁺. IR (ATP) ν = 3335 (NH), 3190 (NH), 2997 (CH), 1730 (CO), 1487, 1200 (CS) cm⁻¹.

Ligand H₂L²

Prepared similarly from ethyl-2-(hydrazinecarbothioamido)acetate (**1**) (1.062 g, 6.00 mmol) and glyoxal (6.33 mL, 40 % aqueous solution, 3.00 mmol) in EtOH (20 mL) to give the product as a pale yellow solid (0.96 g, 2.55 mmol, 85 %). ¹H NMR (400 MHz, d⁶-DMSO) δ_H = 8.88 (2H, t, ³J_{HH} = 5.9 Hz, 2 × NHCH₂), 7.86 (2H, s, 2 × NCH), 4.32 (4H, d, ³J_{HH} = 5.9 Hz, 2 × NHCH₂), 4.18 (4H, q, ³J_{HH} = 7.1 Hz, 2 × CH₂CH₃), 1.27 (6H, t, ³J_{HH} = 7.09 Hz, 2 × CH₂CH₃) ppm. ¹³C NMR (75 MHz, d⁶-DMSO) δ_C = 178.6 (CS), 169.8 (CO), 141.2 (NCH), 61.0 (CH₂CH₃), 45.7 (CH₂NH), 14.7 (CH₂CH₃) ppm. HR-MS (ES+) found m/z 399.0869, calculated m/z 399.0885 for [C₁₂H₂₀N₆O₄S₂ + Na]⁺. IR (ATP) ν = 3285 (NH), 3250 (NH), 2988 (CH), 1740 (CO), 1479, 1200 (CS) cm⁻¹.

Complex CuL¹

Ligand H₂L¹ (0.500 g, 1.24 mmol) and Cu(OAc)₂·H₂O (0.247 g, 1.24 mmol) were heated at reflux in EtOH (20 mL) for 4 h. The solution turned dark purple over the 4 h. The solvent was removed *in vacuo*, the crude product dissolved in CH₂Cl₂ (15 mL) and washed with water (2 × 25 mL) and brine (25 mL). The organic phase was collected, dried over Na₂SO₄ and filtered. The solvent was then removed *in vacuo* to give the product as a dark purple solid (0.416 g, 0.89 mmol, 72 %). Elemental analysis: Calcd. (%) for C₁₄H₂₂N₆O₄S₂Cu: C, 36.08, H, 4.76, N, 18.03; Found: C, 35.93, H, 4.85, N, 17.95. HR-MS (ES+) found m/z 466.0522, calculated m/z 466.0518 for [C₁₄H₂₃N₆O₄S₂⁶³Cu]⁺. IR (ATP) ν = 3390 (NH), 3321 (NH), 2972 (CH), 1738 (CO), 1445, 1215 (CS) cm⁻¹. UV-Vis (MeCN): λ_{max} (ε / L mol⁻¹ cm⁻¹) 522(2610) 473(4868), 346(8981), 306(18732), 250(10265) nm.

Complex ZnL¹

Prepared similarly from ligand H₂L¹ (0.150 g, 0.37 mmol) and Zn(OAc)₂·2H₂O (0.107 g, 0.37 mmol) in EtOH (20 mL). A precipitate formed, which was filtered and washed with EtOH (10 mL) to give the product as a bright yellow solid (0.147 g, 0.31 mmol, 85 %). ¹H NMR (400 MHz, d⁶-DMSO) δ_H = 7.69 (2H, br s, NH), 4.14 (4H, q, ³J_{HH} = 7.2 Hz, 2 × CH₂CH₃), 3.98 (4H, br s, 2 × NHCH₂), 2.20 (6H, s, 2 × CCH₃), 1.24 (6H, t, ³J_{HH} = 7.2 Hz, 2 × CH₂CH₃) ppm. ¹³C NMR (75 MHz, d⁶-DMSO) δ_C = 170.7 (CO), 147.1 (CN), 60.5 (CH₂CH₃), 44.2 (CH₂NH), 14.7 (CH₂CH₃), 14.2 (CCH₃) ppm. Elemental analysis: Calcd. (%) for C₁₄H₂₂N₆O₄S₂Zn: C, 35.94, H, 4.74, N, 17.96; Found: C, 35.81, H, 4.73, N, 17.82. HR-MS (ES+) found m/z 467.0521, calculated m/z 467.0514 for [C₁₄H₂₃N₆O₄S₂⁶⁴Zn]⁺. IR (ATP) ν = 3399 (NH), 3316 (NH), 2968 (CH), 1783 (CO), 1543, 1198 (CS) cm⁻¹. UV-Vis (MeCN): λ_{max} (ε / L mol⁻¹ cm⁻¹) 424(9950), 305(12600), 258(11000) nm.

Complex NiL¹

Prepared similarly from ligand H₂L¹ (0.250 g, 0.62 mmol) and Ni(OAc)₂·4H₂O (0.154 g, 0.62 mmol) in EtOH (10 mL). A precipitate formed, which was filtered and washed with EtOH (10 mL) to give the product as a brown solid (0.234 g, 0.51 mmol, 82 %). ¹H NMR (400 MHz, d⁶-DMSO) δ_H = 8.17 (2H, br s, 2 × NH), 4.11 (4H, br, 2 × CH₂CH₃), 4.04 (4H, br s, 2 × NHCH₂), 1.88 (6H, br s, 2 × CCH₃), 1.20 (6H, br, 2 × CH₂CH₃) ppm. ¹³C NMR (75 MHz, CDCl₃) δ_C = 169.2 (CO), 158.0 (CN), 61.7 (CH₂CH₃), 40.0 (CH₂), 14.2 (CH₂CH₃), 14.0 (CCH₃) ppm. Elemental analysis: Calcd. (%) for C₁₄H₂₂N₆O₄S₂Ni: C, 36.46, H, 4.81, N, 18.22; Found: C, 36.53, H, 4.93, N, 18.17. HR-MS (ES+) found m/z 461.0585, calculated m/z 461.0576 for [C₁₄H₂₃N₆O₄S₂⁵⁸Ni]⁺. IR (ATP) ν = 3377 (NH), 3333 (NH), 2968 (CH), 1724 (CO), 1497, 1198 (CS) cm⁻¹. UV-Vis (MeCN): λ_{max} (ε / L mol⁻¹ cm⁻¹) 392(12118), 330(6556), 255(27184) nm.

Complex CdL¹

Prepared similarly from ligand H₂L¹ (0.500 g, 1.24 mmol) and Cd(OAc)₂·2H₂O (0.330 g, 1.24 mmol) in EtOH (10 mL). A precipitate formed, which was filtered and washed with EtOH (10 mL) to give the product as a bright yellow solid (0.581 g, 1.13 mmol, 91 %). ¹H NMR (400 MHz, d⁶-DMSO) δ_H = 7.60 (2H, br s, 2 × NHCH₂), 4.75 (4H, q, ³J_{HH} = 7.1 Hz, 2 × CH₂CH₃), 3.91 (4H, m, 2 × NHCH₂), 2.16 (6H, s, 2 × CCH₃), 1.18 (6H, t, ³J_{HH} = 7.1 Hz, 2 × CH₂CH₃) ppm. ¹³C NMR (75 MHz, d⁶-DMSO) δ_C = 170.0 (CO), 144.8 (CN), 61.3 (CH₂CH₃), 40.5 (CH₂NH), 15.3 (CH₂CH₃), 14.3 (CCH₃) ppm. Elemental analysis: Calcd. (%) for C₁₄H₂₂N₆O₄S₂Cd: C, 32.66, H, 4.31, N, 16.32; Found: C, 32.76, H, 4.26, N, 16.25. HR-

MS (ES+) found m/z 517.0250, calculated m/z 517.0256 for $[\text{C}_{14}\text{H}_{23}\text{N}_6\text{O}_4\text{S}_2^{114}\text{Cd}]^+$. IR (ATP) $\nu = 3404$ (NH), 2968 (CH), 1736 (CO), 1201 (CS) cm^{-1} . UV-Vis (MeCN): λ_{max} ($\epsilon / \text{L mol}^{-1} \text{cm}^{-1}$) 410(8760), 298(9400), 263(7680), 206(26360) nm.

Complex CuL²

Prepared similarly to CuL¹ from ligand H₂L² (0.200 g, 0.53 mmol) and Cu(OAc)₂·H₂O (0.107 g, 0.53 mmol) in EtOH (20 mL) yielding the product as a dark red solid (0.169 g, 0.39 mmol, 73 %). Elemental analysis: Calcd. (%) for C₁₂H₁₈N₆O₄S₂Cu: C, 32.77, H, 4.13, N, 19.11; Found: C, 32.84, H, 4.08, N, 19.04. HR-MS (ES+) found m/z 438.0200, calculated m/z 438.0205 for $[\text{C}_{12}\text{H}_{19}\text{N}_6\text{O}_4\text{S}_2^{63}\text{Cu}]^+$. IR (ATP) $\nu = 3316$ (NH), 2972 (CH), 1734 (CO), 1215 (CS) cm^{-1} . UV-Vis (MeCN): λ_{max} ($\epsilon / \text{L mol}^{-1} \text{cm}^{-1}$) 544(4164), 503(6650), 359(11550), 312(20300) nm.

Complex ZnL²

Prepared similarly to ZnL¹ from ligand H₂L² (0.200 g, 0.53 mmol) and Zn(OAc)₂·2H₂O (0.117 g, 0.53 mmol) in EtOH (10 mL) yielding the product as a bright yellow solid (0.200 g, 0.46 mmol, 86 %). ¹H NMR (400 MHz, d⁶-DMSO) $\delta_{\text{H}} = 7.90$ (2H, br s, 2 × NH), 7.60 (2H, s, 2 × NCH), 4.14 (4H, q, ³J_{HH} = 7.1 Hz, 2 × NHCH₂), 4.04 (4H, m, 2 × CH₂CH₃), 1.25 (6H, t, ³J_{HH} = 7.1 Hz, 2 × CH₂CH₃) ppm. ¹³C NMR (75 MHz, d⁶-DMSO) $\delta_{\text{C}} = 169.4$ (CO), 137.1 (CHN), 61.7 (CH₂CH₃), 14.3 (CH₂CH₃) ppm. Elemental analysis: Calcd. (%) for C₁₂H₁₈N₆O₄S₂Zn: C, 32.91, H, 4.14, N, 19.19; Found: C, 32.95, H, 4.30, N, 18.99. HR-MS (ES+) found m/z 439.0207, calculated m/z 439.0201 for $[\text{C}_{12}\text{H}_{19}\text{N}_6\text{O}_4\text{S}_2^{64}\text{Zn}]^+$. IR (ATP) $\nu = 3352$ (NH), 2968 (CH), 1738 (CO), 1215 (CS) cm^{-1} . UV-Vis (MeCN): λ_{max} ($\epsilon / \text{L mol}^{-1} \text{cm}^{-1}$) 445(22100), 424(20479), 318(10480), 262(6250) nm.

Complex NiL²

Prepared similarly to NiL¹ from ligand H₂L² (0.100 g, 0.27 mmol) and Ni(OAc)₂·4H₂O (0.067 g, 0.27 mmol) in EtOH (10 mL) yielding the product as brown solid (0.104 g, 0.24, 89 %). ¹H NMR (400 MHz, CDCl₃) $\delta_{\text{H}} = 8.42$ (2H, br s, 2 × NHCH₂), 6.98 (2H, br s, 2 × NCH), 4.12 (4H, m, 2 × CH₂CH₃), 3.93 (4H, d, ³J_{HH} = 5.8 Hz, 2 × NHCH₂), 1.19 (6H, t, ³J_{HH} = 7.1 Hz, 2 × CH₂CH₃) ppm. ¹³C NMR (75 MHz, d⁶-DMSO) $\delta_{\text{C}} = 179.0$ (CN), 169.6 (CO), 146.2 (CNH), 61.2 (CH₂CH₃), 47.2 (CH₂NH), 14.6 (CH₂CH₃) ppm. Elemental analysis: Calcd. (%) for C₁₂H₁₈N₆O₄S₂Ni: C, 33.28, H, 4.19, N, 19.40; Found: C, 33.15, H, 4.10, N, 19.27. HR-MS (ES+) found m/z 433.0264, calculated m/z 433.0263 for $[\text{C}_{12}\text{H}_{19}\text{N}_6\text{O}_4\text{S}_2^{58}\text{Ni}]^+$. IR (ATP) $\nu = 3339$ (NH), 3304 (NH), 2972 (CH), 1738 (CO), 1570,

1215 (CS) cm^{-1} . UV-Vis (MeCN): λ_{max} ($\epsilon / \text{L mol}^{-1} \text{cm}^{-1}$) 414(10240), 334(4860), 257(22240) nm.

Complex CdL²

Prepared similarly to CdL¹ from ligand H₂L² (0.100 g, 0.27 mmol) and Cd(OAc)₂·2H₂O (0.072 g, 0.27 mmol) in EtOH (10 mL) yielding the product as a bright yellow solid (0.122 g, 0.25 mmol, 93 %). ¹H NMR (400 MHz, d⁶-DMSO) δ_{H} = 7.65 (2H, br s, 2 × NHCH₂), 7.48 (2H, br s, 2 × NCH), 4.02 (4H, m, 2 × CH₂CH₃), 3.88 (4H, br s, 2 × NHCH₂), 1.12 (6H, t, ³J_{HH} = 7.1 Hz, 2 × CH₂CH₃) ppm. ¹³C NMR (75 MHz, d⁶-DMSO) δ_{C} = 170.6 (CO), 138.0 (CSN), 137.8 (CHN), 60.7 (CH₂CH₃), 40.9 (CH₂NH), 14.7 (CH₂CH₃) ppm. Elemental analysis: Calcd. (%) for C₁₂H₁₈N₆O₄S₂Cd: C, 29.60, H, 3.73, N, 17.26; Found: C, 29.78, H, 3.68, N, 17.11. HR-MS (ES+) found m/z 488.9937, calculated m/z 488.9943 for [C₁₂H₁₉N₆O₄S₂¹¹⁴Cd]⁺. IR (ATP) ν = 3416 (NH), 3325 (NH), 2972 (CH), 1738 (CO), 1540, 1200 (CS) cm^{-1} . UV-Vis (MeCN): λ_{max} ($\epsilon / \text{L mol}^{-1} \text{cm}^{-1}$) 441(13178), 416(14166), 310(10545), 272(9976) nm.

N-Boc-ethylenediamine (2)

Prepared by modification of literature methods.⁴⁹ Ethylenediamine (24 mL, 36.8 mmol) was dissolved in dry DCM (150 mL) and cooled to 0 °C. Boc₂O (8.0 g, 36.8 mmol) was dissolved in dry DCM (50 mL) and added dropwise over 30 mins. The reaction mixture was allowed to come to room temperature and stirred overnight. A white suspension was seen to form. The reaction mixture was diluted with DCM (50 mL), washed with H₂O (5 × 40 mL), and the organic layer dried over Na₂SO₄. The solvent was removed *in vacuo* to give the product as a colourless oil (4.2 g, 26.2 mmol, 71 %) that was used without further purification. ¹H NMR (400 MHz, CDCl₃) δ_{H} = 4.94 (1H, br, NHBoc), 3.10 (2H, dd, NH₂CH₂), 2.73 (2H, t, ³J_{HH} = 6.03 Hz, CH₂), 1.38 (9H, s, C(CH₃)₃) ppm. HR-MS (APCI+) found m/z 161.1291, calculated m/z 161.1290 for [C₇H₁₇N₂O₂]⁺.

N-Boc-2-Isothiocyanatoethylamine (3)

Prepared by modification of literature methods.⁵⁰ N-Boc-ethylenediamine (2) (4 g, 25 mmol) was dissolved in dry THF (50 mL) and cooled to 0 °C. Carbon disulfide (1.5 mL/, 25 mmol) and NEt₃ (12.2 mL, 87.7 mmol) were added, and the ice was removed to allow the reaction mixture to be stirred for 1 h at room temperature. The reaction mixture was cooled back to 0 °C, and tosyl chloride (7.16 g, 37.6 mmol) was added. The solution was stirred at room temperature for 3 h, DCM (50 mL) was added, and the solution stirred overnight. The reaction was washed with 10 % citric acid solution (5 × 20 mL), H₂O (3 × 20 mL), and the

organic fraction was dried over anhydrous Na_2SO_4 . The solvent was removed *in vacuo* to give the product as an off-white solid (3.54 g, 17.5 mmol, 70 %) that was used without further purification. ^1H NMR (400 MHz, CDCl_3) $\delta_{\text{H}} = 4.90$ (1H, br, $\text{NH}(\text{Boc})$), 3.58 (2H, b, NH_2CH_2), 3.31 (2H, br, CH_2), 1.39 (9H, s, $\text{C}(\text{CH}_3)_3$) ppm. ^{13}C NMR (100 MHz, d^6 -DMSO) $\delta_{\text{C}} = 130.3$ (CO), 127.1 (CS), 80.2 ($\text{C}(\text{CH}_3)_3$), 45.5 (CH_2NCS), 40.6 (CH_2NH), 28.4 ($\text{C}(\text{CH}_3)_3$) ppm. HR-MS (APCI+) found m/z 202.0773, calculated m/z 202.0776 for $[\text{C}_8\text{H}_{14}\text{N}_2\text{O}_2\text{S}]^+$. IR (ATP) $\nu = 3343$ (NH), 2097 (NCS), 1688 (CO) cm^{-1}

N-Boc-2-thiocarbohydrazidoethylamine (4)

N-Boc-2-Isothiocyanatoethylamine (3) (3 g, 14.8 mmol) was dissolved in EtOH (20 mL) and cooled to 0 °C. Hydrazine hydrate (0.8 mL, 16.4 mmol) was dissolved in cold EtOH (20 mL) and added dropwise over 30 min. The reaction mixture was stirred for 30 min, allowed to come to room temperature, stirred for another 30 min, then cooled and the solvent removed *in vacuo* to give a colourless oil, which was triturated with CHCl_3 to give the product as an off-white solid (3.16 g, 13.5 mmol, 91 %). ^1H NMR (400 MHz, CDCl_3) $\delta_{\text{H}} = 7.76$ (1H, br, NH), 7.30 (1H, br, NH), 4.93 (1H, br, $\text{NH}(\text{Boc})$), 3.70 (2H, m, CH_2), 3.33 (2H, m, CH_2), 1.37 (9H, s, $\text{C}(\text{CH}_3)_3$) ppm. ^{13}C NMR (100 MHz, CDCl_3) $\delta_{\text{C}} = 182.5$ (CS), 156.6 (CO), 79.6 ($\text{C}(\text{CH}_3)_3$), 44.3 (CH_2), 40.2 (CH_2), 28.6 ($\text{C}(\text{CH}_3)_3$) ppm. HR-MS (APCI+) found m/z 235.1219, calculated m/z 235.1229 for $[\text{C}_8\text{H}_{19}\text{N}_4\text{O}_2\text{S}]^+$. IR (ATP) $\nu = 3298$ (NH), 2972 (NH), 2934 (NH), 1686 (CO), 1533, 1161 (CS) cm^{-1} .

Ligand H₂L³

N-Boc-2-thiocarbohydrazidoethylamine (4) (2.24 g, 9.57 mmol) was suspended in EtOH (20 mL), and 2, 3-butanedione (0.41 mL, 4.668 mmol) added dropwise over 10 min before the reaction mixture was heated at reflux for 24 h. The precipitate formed was collected by filtration, washed with cold EtOH, and dried *in vacuo* to give the product as a yellow solid (1.67 g, 3.22 mmol, 69 %). ^1H NMR (400 MHz, d^6 -DMSO) $\delta_{\text{H}} = 10.45$ (2H, s, $2 \times \text{NH}$), 8.52 (2H, t, $^3J_{\text{HH}} = 6.0$ Hz, $2 \times \text{NHCH}_2$), 7.12 (2H, t, $^3J_{\text{HH}} = 4.0$ Hz, $2 \times \text{NH}(\text{Boc})$), 3.65 (4H, m, $2 \times \text{CH}_2$), 3.25 (4H, m, $2 \times \text{CH}_2\text{NH}(\text{Boc})$), 2.30 (6H, s, $2 \times \text{CH}_3$), 1.43 (18H, s, $2 \times \text{C}(\text{CH}_3)_3$). ^{13}C NMR (75 MHz, d^6 -DMSO) $\delta_{\text{C}} = 178.6$ (CS), 156.7 (CO), 148.7 (CN), 78.4 ($\text{C}(\text{CH}_3)_3$), 45.0 (CH_2), 28.8 ($\text{C}(\text{CH}_3)_3$), 12.3 (CH_3) ppm. HR-MS (EI+) found m/z 518.2454, calculated m/z 518.2457 for $[\text{C}_{20}\text{H}_{38}\text{N}_8\text{O}_4\text{S}_2]^+$. IR (ATP) $\nu = 3377$ (NH), 3316 (NH), 2968 (CH), 1738 (CO), 1667 (CN), 1200 (CS) cm^{-1} .

Complex CuL³

Ligand H₂L³ (0.100 g, 0.19 mmol) and Cu(OAc)₂·H₂O (0.040 g, 0.20 mmol) were heated at reflux in EtOH (20 mL) for 4 h. The solution turned dark purple over the 4 h. The solvent was removed *in vacuo*, the crude product dissolved in CH₂Cl₂ (15 mL) and washed with water (2 × 25 mL) and brine (25 mL). The organic phase was collected, dried over Na₂SO₄ and filtered. The solvent was then removed *in vacuo* to give the product as a dark red solid (0.080 g, 0.14 mmol, 73 %). Elemental analysis: Calcd. (%) for C₂₀H₃₆N₈O₄S₂Cu: C, 41.40, H, 6.25, N, 19.31; Found: C, 58.48, H, 6.06, N, 18.19. HR-MS (ES+) found m/z 578.1516, calculated m/z 578.1524 for [C₂₀H₃₅N₈O₄S₂⁶³Cu]⁻. IR (ATP) ν = 3310 (NH), 2972 (CH), 1740 (CO), 1364, 1215 (CS) cm⁻¹. UV-Vis (MeCN): λ_{\max} (ϵ / L mol⁻¹ cm⁻¹) 472(6135), 354 (10738), 308(21767) nm.

Complex ZnL³

Prepared similarly from ligand H₂L³ (0.100 g, 0.19 mmol) and Zn(OAc)₂·2H₂O (0.043 g, 0.20 mmol) in EtOH (20 mL) to give the product as a bright yellow solid (0.088 g, 0.152 mmol, 80 %). ¹H NMR (400 MHz, d⁶-DMSO) δ_{H} = 7.23 (2H, br, 2 × NH), 6.89 (2H, t, ³J_{HH} = 6.6 Hz, 2 × NHCH₂), 3.11 (4H, q, ³J_{HH} = 6.6 Hz, 2 × CH₂), 2.21 (6H, s, 2 × CH₃), 1.88 (4H, br, 2 × CH₂), 1.38 (18H, s, 2 × C(CH₃)₃) ppm. ¹³C NMR (75 MHz, d⁶-DMSO) δ_{C} = 155.6 (CS), 145.0 (CO), 77.6 (C(CH₃)₃), 28.2 (C(CH₃)₃), 13.9 (CH₃) ppm. Elemental analysis: Calcd. (%) for C₂₀H₃₆N₈O₄S₂Zn: C, 41.27, H, 6.23, N, 19.25; Found: C, 41.43, H, 6.36, N, 19.11. HR-MS (ES+) found m/z 581.1699, calculated m/z 581.1666 for [C₂₀H₃₇N₈O₄S₂⁶⁴Zn]⁺. IR (ATP) ν = 3298 (NH), 3228 (NH), 2972 (CH), 1740 (CO), 1504, 1215 (CS) cm⁻¹. UV-Vis (MeCN): λ_{\max} (ϵ / L mol⁻¹ cm⁻¹) 418(9040), 316(10241) 273(20742) nm.

Complex NiL³

Prepared similarly from ligand (0.100 g, 0.19 mmol) and Ni(OAc)₂·4H₂O (0.050 g, 0.20 mmol) in EtOH (20 mL) to give the product as a brown solid (0.090g, 0.156 mmol, 83 %). ¹H NMR (400 MHz, d⁶-DMSO) δ_{H} = 7.82 (2H, br, 2 × NH), 6.91 (2H, br, 2 × NH), 3.28 (4H, br, 2 × CH₂), 3.10 (4H, br, 2 × CH₂), 2.01 (6H, s, 2 × CH₃), 1.44 (18H, s, 2 × C(CH₃)₃) ppm. ¹³C NMR (75 MHz, d⁶-DMSO) δ_{C} = 156.1 (CS), 155.8 (CO), 78.3 (C(CH₃)₃), 28.8 (C(CH₃)₃) ppm. Elemental analysis: Calcd. (%) for C₂₀H₃₆N₈O₄S₂Ni: C, 41.75, H, 6.31, N, 19.48; Found: C, 43.78, H, 5.82, N, 19.35. HR-MS (ES-) found m/z 573.1577, calculated m/z 573.1582 for [C₂₀H₃₅N₈O₄S₂⁵⁸Ni]⁻. IR (ATP) ν = 3298 (NH), 2972 (CH), 1740 (CO), 1215 (CS) cm⁻¹. UV-Vis (MeCN): λ_{\max} (ϵ / L mol⁻¹ cm⁻¹) 396(14893), 328(8599), 257(33833) nm.

Complex CdL³

Prepared similarly from ligand H₂L³ (0.100 g, 0.19 mmol) and Cd(OAc)₂·2H₂O (0.053 g, 0.20 mmol) in EtOH (20 mL) to give the product as a bright yellow solid (0.112 g, 0.177 mmol, 94 %). ¹H NMR (400 MHz, d⁶-DMSO) δ_H = 7.19 (2H, br, 2 × NH), 6.90 (2H, t, ³J_{HH} = 4 Hz, 2 × NH), 3.13 (4H, dt, ³J_{HH} = 8, 4 Hz, 2 × CH₂), 2.24 (6H, s, 2 × CH₃), 1.39 (18H, s, 2 × C(CH₃)₃) ppm. ¹³C NMR (75 MHz, d⁶-DMSO) δ_C = 156.1 (CO), 147.8 (CN) 78.2 (C(CH₃)₃), 42.8 (CH₂), 28.8 (C(CH₃)₃), 15.2 (CH₃) ppm. Elemental analysis: Calcd. (%) for C₂₀H₃₆N₈O₄S₂Cd: C, 38.19, H, 5.77, N, 17.81; Found: C, 38.29, H, 5.86, N, 17.76. HR-MS (ES⁺) found m/z 631.1403, calculated m/z 631.1407 for [C₂₀H₃₇N₈O₄S₂¹¹⁴Cd]⁺. IR (ATP) ν = 3304 (NH), 2968 (CH), 1734 (CO), 1518, 1324 (CS) cm⁻¹. UV-Vis (MeCN): λ_{max} (ε / L mol⁻¹ cm⁻¹) 412(7800), 300(7440), 266(5840) nm.

Electrochemistry

Cyclic voltammograms were measured using a Princeton Applied Research PARSTAT 2273 using Electrochemistry Powersuite V.2.58 software and a cell with a MW2013 Pt working electrode, a MW4130 Pt wire auxiliary electrode and a Au pseudo-reference electrode. Scans were measured at 50, 100, 250 and 500 mV/s. Measurements were carried out on solutions of CuL¹, CuL² and CuL³ in anhydrous, degassed DCM containing NBu₄PF₆ as a support electrolyte, and referenced against an internal ferrocene/ferrocene⁺ redox couple. The Cu²⁺/Cu⁺ and Cu²⁺/Cu³⁺ potentials are reported as the mid-point between the reduction and oxidation current peaks.

Crystallography

Suitable crystals of ZnL¹ and CdL¹ were selected for analysis by the UK National Crystallography Service and measured following a standard method on a Rigaku AFC12 goniometer equipped with an enhanced sensitivity (HG) Saturn724+ detector mounted at the window of a FR-E+ SuperBright molybdenum rotating anode generator with VHF Varimax optics (100m) focus at 100 K. Cell determination and data collection were carried out using CrystalClear-SM Expert 2.0 r11. Data reduction, cell refinement, and absorption correction were carried out using CrystalClear-SM Expert 2.1 r29. Structures were solved using SUPERFLIP⁵¹ and refined using SHELXL-2013.⁵²

Determination of Antibacterial Minimum Inhibitory Concentrations (MIC)

Stock cultures of strains of *Staphylococcus aureus* (NCIMB 9518), *Pseudomonas aeruginosa* (ATCC 15692) and *Escherichia coli* (NCTC 12923) were maintained on MicrobankTM plastic beads at

-80 °C. Working cultures were maintained at 4 °C on tryptone soy agar culture media (TSA, Sigma Aldrich). For each organism, a single colony was transferred to Mueller Hinton Broth (MHB, Sigma Aldrich) (10 mL) and incubated at 37 °C for 14 h. Cultures were then diluted to 1×10^8 CFU.mL⁻¹ through use of spectroscopic analysis (Ultraspec 2000, Pharmacia Biotech) and comparison to MacFarland standard 0.5, and then serially diluted to 1×10^6 CFU.mL⁻¹.

Ligands H₂L¹⁻³ and complexes CuL¹⁻³ were dissolved in DMSO to give stock solutions (10 mg.mL⁻¹). These stock solutions were serially diluted with DMSO before addition to MHB broth (100 µL) in a well of a 96-well plate. To the compound-containing broth (100 µL) was added a broth-bacteria inoculum (100 µL, 1×10^6 CFU.mL⁻¹) to give final compound concentrations ranging from 25 µg.mL⁻¹ to 0.78 µg.mL⁻¹ for MIC testing. Each concentration was prepared in triplicate for each chemical species and bacterium. Positive controls of the appropriate organism (1×10^6 CFU.mL⁻¹) in broth containing 1 % v/v DMSO were prepared in triplicate, as were negative controls (broth containing 1 % v/v DMSO). The plates were incubated for 24 h at 37 °C before bacterial growth in each well was assessed by absorption at 600 nm. The lowest concentration resulting in an 80 % reduction in A₆₀₀ relative to the positive control is the MIC for the compound against the organism being studied.

Determination of Antiparasitic potential

Samples of H₂L¹, H₂L², H₂L³ and their complexes with Cu, Zn, Ni and Cd were assessed for anti-parasitic capability against *Schistosoma mansoni* by use of the automated, high through-put Roboworm drug-discovery platform, Parasitology and Epidemiology Group, Aberystwyth University, Wales, UK. Schistosomula populations were incubated for 72 hr at 37 °C under 5 % CO₂ enriched atmosphere with a given compound (10 µM). Compounds were dissolved in DMSO prior to addition. Following incubation, larva phenotype and motility were assessed by bright field imaging analysis and scored where compounds were considered a hit with a score value of -0.15 for phenotype and -0.35 for motility.⁵³ Auranofin and praziquantel were used as positive controls; DMSO was used as a negative control.

5.3 Results and discussion

5.3.1 Preparation and characterisation of complexes

The synthesis of the bis(thiosemicarbazone) ligands H_2L^1 , H_2L^2 and H_2L^3 proceeded using typical methodologies for this class of ligand.⁵⁴⁻⁵⁶ The intermediates **1** and **3** were synthesised by the modification of literature methods.^{50,57} The complexation reactions utilised the acetate salts of the metal to be coordinated with EtOH as a solvent. The basic nature of the acetate anion aids in the deprotonation of the ligand and the formation of the neutral complex. In the case of copper, other salts have been studied previously but have resulted in charged complexes.^{44,45} In all cases, metalation was rapid and gave strongly coloured dispersions from which solid products could be isolated and purified for analysis.

The complexes of H_2L^1 , H_2L^2 and H_2L^3 were observed to be insoluble in water, ethanol, diethyl ether and hexane and displayed sparing solubility in chloroform, dichloromethane, ethyl acetate, methanol, acetonitrile, DMF and DMSO. The ligands and intermediates were characterised using 1H and ^{13}C -NMR spectroscopies, HR-MS and FT-IR spectroscopy. The complexes were characterised by 1H and ^{13}C -NMR spectroscopies, HR-MS, elemental analysis, FT-IR spectroscopy, UV-Vis studies and where suitable cyclic voltammetry.

5.3.2 NMR Spectroscopy

The 1H NMR spectra of H_2L^1 , H_2L^2 and H_2L^3 show several common features. Geminal coupling between alkyl groups present allowed for the unequivocal identification of peaks with little to no discrepancy when considering integration values. When measured in d^6 -DMSO all three ligands gave spectra containing peaks for all proton environments present in the molecule but when measured in protic solvents (e.g. MeOD), one or more NH environments were not observed due to the deuterium exchange. The only exception is in the case of H_2L^2 where an expected NH peak between 10-11 ppm was not observed. This may be due to transient deprotonation of the ligand by water impurities in the sample. The identification of all three ligands was aided by use of ^{13}C NMR. Peaks for all carbon environments present in each of the molecules could be observed.

The coordination of metals by the three novel ligands required an initial deprotonation. The loss of two secondary amine protons allowed for the donation of electron density to a metal ion using an N_2S_2 coordination sphere. A lack of NH peaks above ~ 10 ppm in the 1H NMR spectra of the complexes is therefore indicative of complexation. An upfield shift of the remaining secondary amine proximal to the coordination sphere arises due to the presence of two resonance formula for the complexes (see Fig. 8); for H_2L^1 forming ZnL^1 , NiL^1 and

CdL¹, a shift from 10.60 ppm to 7.69, 8.17 and 7.60 ppm respectively is observed. Similar shifts are observed between H₂L², H₂L³ and their respective complexes. The values of the chemical shifts of environments not directly involved with metal coordination show little change between ligand and complex. The ¹H NMR spectra of the nickel complexes are typically broadened implying that these complexes exist in equilibrium between the expected square planar geometries and octahedral geometries formed by the coordination of solvent molecules. Such complexes would be high spin and paramagnetic, giving rise to the observed broadening.⁶⁰

Some environments in the complexes, namely C=S and C=N, can be difficult to observe using ¹³C NMR spectroscopy due to the lack of a hydrogen resulting in a poor signal. HMBC-NMR spectroscopy was used to elucidate coupling behaviour and on occasion yielded an additional peak for the imine carbon arising from 2, 3-butandione. When observed this imine peak was seen to be upshifted 2-4 ppm in the case of zinc and cadmium complexes, but downshifted 5-9 ppm for nickel complexes, reflecting the considerable back donation of electron density from nickel into the π -system.⁶¹

5.3.3 IR Spectroscopy

The carbonyl groups present in all ligands and complexes gave the strongest bands visible in the IR spectra, occurring between 1700-1750 cm⁻¹ (similarly to as reported by Waghorn *et al.* for the glyoxal-based analogue of H₂L³ species with a strong carbonyl group absorbance at 1697 cm⁻¹)⁶². Bands between 3200-3400 cm⁻¹ (NH stretching modes) can be observed, along with CH stretches occurring between 2900-3000 cm⁻¹. Related compounds in the literature show similar values e.g. NH stretches at 3315 cm⁻¹ and 3355 cm⁻¹ for Ni-GTSM and Cu-GTSM.⁶⁰

Bands for the imine stretches in these molecules would be expected between 1640-1690 cm⁻¹ for the free ligands with lower values for the complexes as electron density is donated from the bonds to the metal centre, weakening them; from the literature, the ligand H₂GTSM has an imine stretch at 1560 cm⁻¹ versus 1555 cm⁻¹ and 1540 cm⁻¹ for its Ni²⁺ and Cu²⁺ complexes respectively, reflecting the higher effective nuclear charge of the copper ion.⁶⁰ The IR spectra of H₂L³ shows such a band at 1667 cm⁻¹ but in all other cases the high number of bands in this region prevent the unambiguous identification of the desired absorption.

Strong absorptions observed in all spectra between 1190-1220 cm⁻¹ can with reasonable confidence be assigned to the thiocarbonyl groups, which typically give strong absorptions between 1050-1200 cm⁻¹ as observed for the precursors **(1)** (1079 cm⁻¹) and **(4)** (1161 cm⁻¹).

5.3.4 UV-Vis Spectroscopy

Solutions of the complexes studied showed intense colour; copper complexes appeared dark red, zinc complexes appeared orange or yellow, nickel complexes appeared green or greenish-brown, while cadmium complexes gave canary yellow solutions. According to the literature, all of the bands present may be described as ligand centred one electron $\pi \rightarrow \pi^*$ transitions. Absorption occurs with the movement of electrons from the sulfur atoms to the carbon backbone of the ligand.⁶³ The exact transitions and their contribution to given bands in the electronic spectra of Cu-ATSM and Zn-ATSM have been defined.^{55,63} Given the similarities between these reference spectra and those of the complexes described here, and that computational studies are beyond the focus of this report, the exact nature of these transitions will not be discussed in detail. Figures 9-12 show the electronic spectra of the complexes grouped by metal.

The electronic spectra of the copper complexes CuL¹⁻³ (Fig. 9) show considerable similarity to that observed for Cu-ATSM and are all generally alike.⁵⁵ The low energy bands observed at 473, 495 and 472 nm respectively for the three complexes represent HOMO \rightarrow LUMO transitions with shoulder peaks at 522, 544 and 529 nm most likely arising from conformational changes in the coordination of the ligand; such bands occur at 476 nm and 525 nm for Cu-ATSM. The intense peaks observed at 306, 312 and 308 nm with shoulder peaks at 346, 359 and 354 nm occur at very similar wavelengths to similar features in the spectra of Cu-ATSM (314 nm and 355 nm) and it can be concluded that these peaks are composed from the same or similar transitions as previously described.⁵⁵ The lowest energy peaks seen in the spectra of the copper complexes all occur at longer wavelengths than for the analogous transitions seen for the other metal complexes, while other peaks occur at comparable wavelengths. The HOMO \rightarrow LUMO transition requires less energy for the Cu²⁺ complexes due to the d⁹ configuration of the metal. Orbital mixing would result in an unpaired electron occupying the HOMO, and excitation to the LUMO would not require the energetically unfavourable separation of spin coupled electrons.

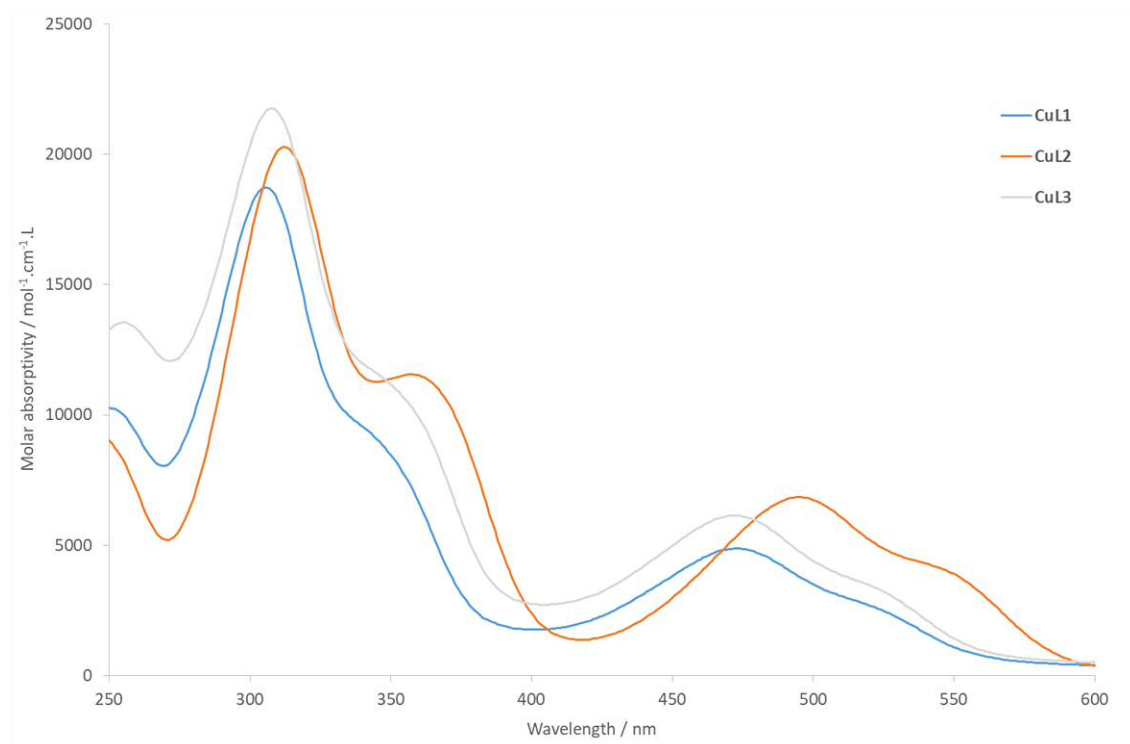


Figure 9. UV-Vis spectra of the copper complexes CuL^{1-3} , measured as $5 \times 10^{-5} \text{ M MeCN}$ solutions.

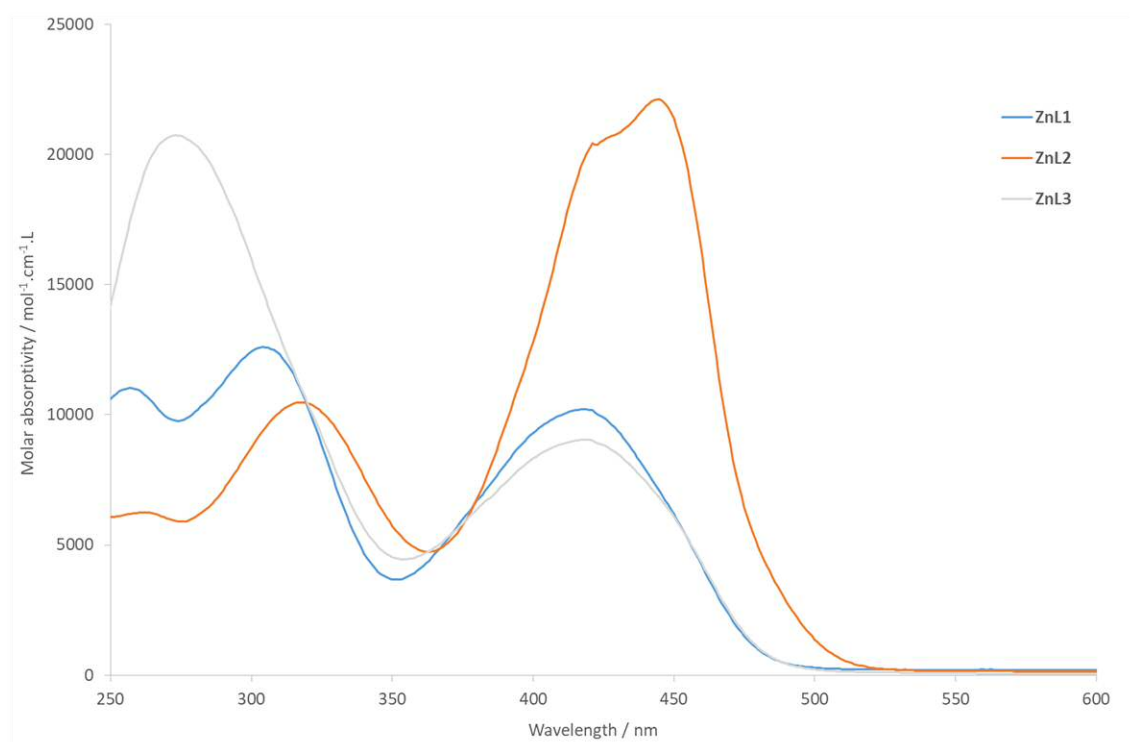


Figure 10. UV-Vis spectra of the zinc complexes ZnL^{1-3} , measured as $5 \times 10^{-5} \text{ M MeCN}$ solutions.

The zinc complexes (Fig. 10) all show similar spectroscopic features and the spectra of ZnL¹ and ZnL³ are comparable to that observed for Zn-ATSM, where peaks at 405 and 305 nm are assigned to HOMO→LUMO and HOMO-1→LUMO transitions respectively.⁶³ These assignments would be consistent with the peaks observed in the spectra above. The spectrum of ZnL² shows the interesting feature that the HOMO→LUMO band at 445 nm showing a shoulder peak at 424 nm is considerably more intense than the peak seen at 318 nm. The ratio of these peaks are shown in Table 2. As such high ratios between the two peaks are not seen for the zinc complexes of H₂L¹ and H₂L³, it may be concluded that the lack of alkyl groups on the ligand backbone and the coordination of a d¹⁰ ion is the origin of this effect. A preference by the metal for tetrahedral geometry combined with a shortened C-C bond in the ligand would result in a distortion towards tetrahedral geometry.¹⁴ This is in agreement with the electrochemical observation that CuL² is easier to reduce than CuL¹ and CuL³ (see below), implying that the ligand more readily assumes a twist away from planarity as observed for Cu-GTSM.¹⁴ The ligand's propensity to distort away from a plane is overcome by Cu²⁺ and Ni²⁺ having an energetic drive to form square planar complexes. When the complex binds Zn²⁺ and is more tetrahedral-like in geometry different orbital mixing occurs, giving a different absorption profile to that observed for Zn-ATSM, ZnL¹ and ZnL³. The lineshape is more similar to that observed for the cadmium complexes (Fig. 11)

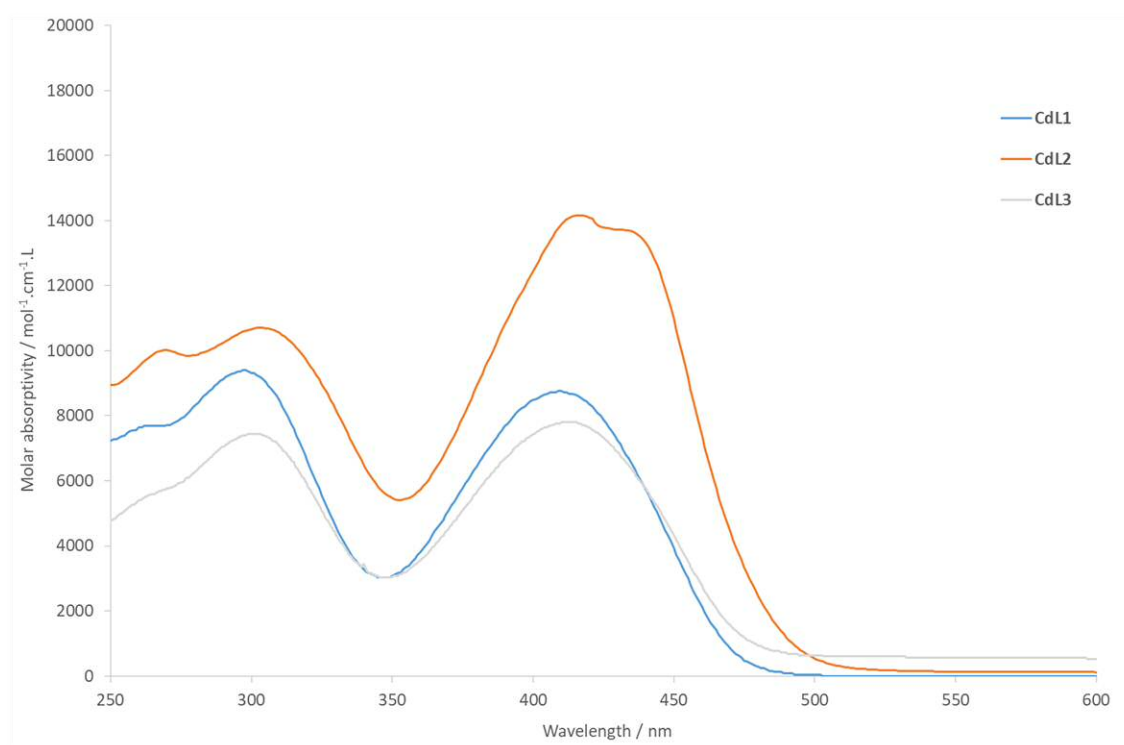


Figure 11. UV-Vis spectra of cadmium complexes CdL¹⁻³, measured as 5×10^{-5} M MeCN solutions.

The cadmium complexes (Fig. 11) show $\epsilon_{\text{HOMO} \rightarrow \text{LUMO}} : \epsilon_{\text{HOMO-1} \rightarrow \text{LUMO}}$ ratios of 0.93 or greater (see Table 2) within spectra that are broadly similar. This reflects that for all ligands discussed here the large cadmium cation exists in a non-square planar geometry. From analogous compounds in the literature and the experimentally observed crystal structure for CdL^1 (see below) the complexes will be in a distorted octahedral geometry in the solid state, where the ligand will coordinate in an approximate plane (with significant distortions) about the equatorial positions with other complexes coordinating in the apical positions via sulphur atoms. In the solution phase, the apical positions may be occupied by solvent molecules with less steric bulk, and the ligand will distort further away from a planar geometry towards a more tetrahedral-like form, yielding spectra lineshapes closer to that observed for ZnL^2 . As the peaks observed occur from ligand based electronic transitions, it can be assumed that the identity of these transitions is analogous to those described above.

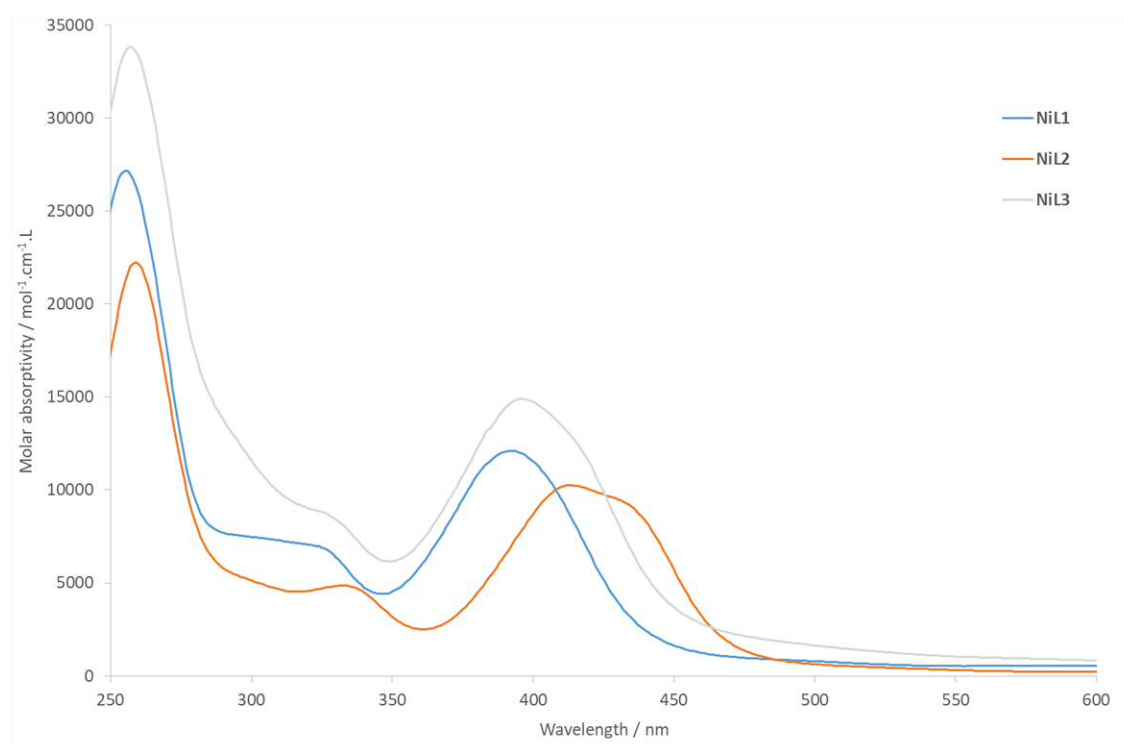


Figure 12. UV-Vis spectra of nickel complexes NiL^{1-3} , measured as $5 \times 10^{-5} \text{ M}$ MeCN solutions.

The nickel complexes all yield similar spectra (see Fig. 12). By reference to analogous compounds such as Ni-ATSM ,¹⁴ it is likely that these complexes are square planar with little deviation from planarity. The features within the spectra ($\text{HOMO} \rightarrow \text{LUMO}$ transitions at 392, 414 and 396 nm for NiL^{1-3} , $\text{HOMO-x} \rightarrow \text{LUMO}$ transitions at approximately 255, 257 and 257 nm with shoulder peaks at 330, 334 and 328 nm) are broadly similar to those

observed for the copper complexes. The peaks observed for NiL² occur at marginally longer wavelengths, indicating a lower HOMO→LUMO gap than for the alkylated analogues. Backbone alkylation has previously been calculated to raise the energy of the LUMO of similar molecules.¹⁴

	$\epsilon_{\text{HOMO}\rightarrow\text{LUMO}}$		$\epsilon_{\text{HOMO}\rightarrow\text{LUMO}}$		$\epsilon_{\text{HOMO}\rightarrow\text{LUMO}}$
	$\epsilon_{\text{HOMO-1}\rightarrow\text{LUMO}}$		$\epsilon_{\text{HOMO-1}\rightarrow\text{LUMO}}$		$\epsilon_{\text{HOMO-1}\rightarrow\text{LUMO}}$
CuL¹	0.26	CuL²	0.33	CuL³	0.28
ZnL¹	0.79	ZnL²	2.11	ZnL³	0.44
NiL¹	0.45	NiL²	0.46	NiL³	0.44
CdL¹	0.93	CdL²	1.34	CdL³	1.05

Table 2. Ratios of $\epsilon_{\text{HOMO}\rightarrow\text{LUMO}}:\epsilon_{\text{HOMO-1}\rightarrow\text{LUMO}}$ for metal complexes of ligands H₂L¹⁻³. Note that the highest ratios are generally observed for complexes with the highest likelihood of forming non-square planar geometries (ZnL² and the cadmium complexes).

The d-d transitions that would be expected for these complexes were not observed in the spectra measured. These transitions have relatively low values of ϵ : $\sim 10 \text{ mol}^{-1}\cdot\text{cm}^{-1}\cdot\text{L}$ for the ‘Spin’ and ‘LaPorte’ forbidden Ni complexes up to several hundred for the ‘Spin’ allowed and ‘LaPorte’ partially allowed Cu complexes, and can be difficult to observe in dilute solutions. Unfortunately, the limited solubility of these complexes prevented the study of more concentrated samples.

5.3.5 Cyclic voltammetry

The complexes CuL^1 , CuL^2 and CuL^3 were studied using cyclic voltammetry to ascertain the effect of the ligand framework on the copper centre's redox potential. Reduction and oxidation potentials for these complexes referenced against an internal Fc/Fc^+ standard are shown in Fig. 13. The limited solubility of the complexes necessitated the use of non-aqueous conditions with a supporting electrolyte ($\text{N}^i\text{Bu}_4\text{PF}_6$) and an internal Fc/Fc^+ reference.

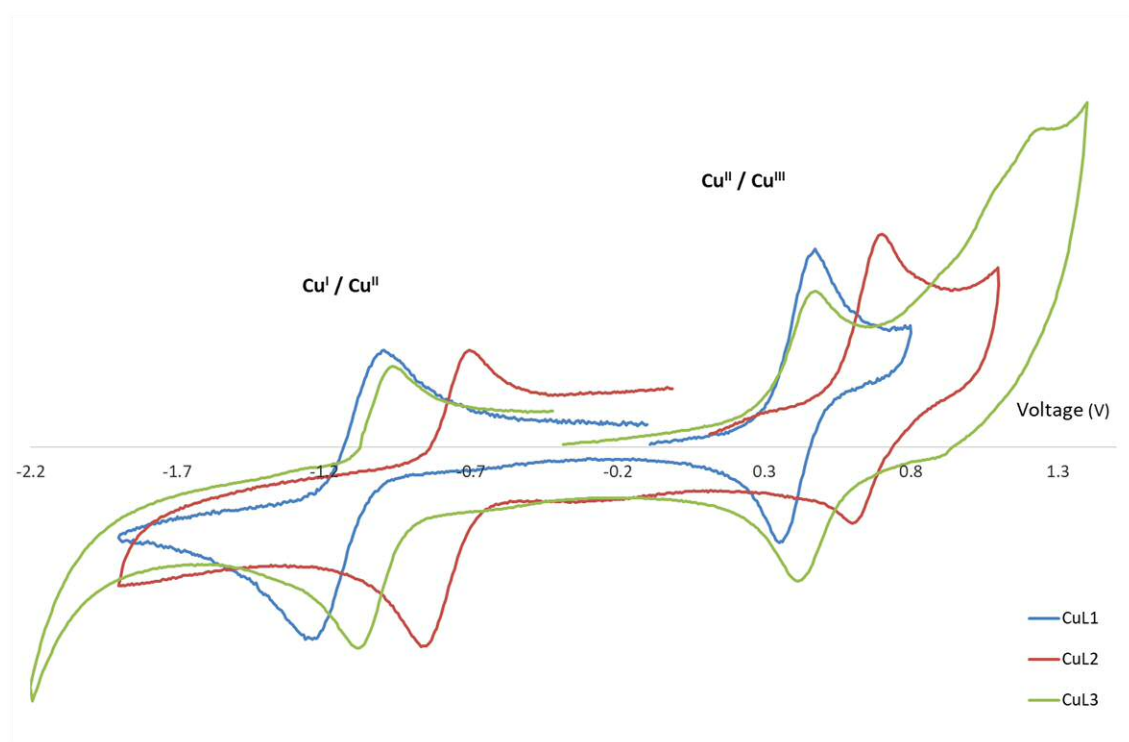


Figure 13. Cyclic voltammograms of CuL^{1-3} at 250 mV/s scan rate, showing reduction (left) and oxidation (right) processes, later referenced against Fc/Fc^+ .

All three complexes showed two quasi-reversible one electron redox couples; the electrochemical properties are shown in Table 3. In all cases the anodic and cathodic peak separations varied with scan rate with values typically close to those observed for the standard. However, the anodic and cathodic peak currents were generally similar with a ratio that approximated that observed for the standard, and a plot of the square root of the scan rate versus anodic peak current showed a close-to-linear relationship (Fig. 14). Analysis of cyclic voltammograms of Cu-ATSM and related species reached similar conclusions.^{26,55} The quasi-reversible character of the reduction peaks arises from the need of the ligand to twist and change geometries about the metal centre as the oxidation state (and therefore coordination preferences) of the metal changes. For the oxidation processes, decomposition of the complexes may be occurring.⁶⁴

Complex	$E_{1/2}$ $\text{Cu}^{2+}/\text{Cu}^+$ (V)	ΔE (V)	i_a/i_c	$E_{1/2}$ $\text{Cu}^{3+}/\text{Cu}^{2+}$	ΔE (V)	i_a/i_c
CuL¹	-1.12	0.203	0.87	0.43	0.090	1.01
CuL²	-0.81	0.118	0.89	0.64	0.094	1.45
CuL³	-1.10	0.137	0.83	0.41	0.056	1.07
Cu-ATSM	-0.99	-	-	0.32	-	-
Cu-GTSM	-0.83	-	-	-	-	-

Table 3. Electrochemical properties of complexes CuL^{1-3} measured at 100 mV/s scan rate and referenced against a Fc/Fc⁺ internal reference. Calculated values for Cu-ATSM and Cu-GTSM based on studies against Ag/AgCl are included for comparison.⁵⁰

The selectivity of a BTSC complex for hypoxic tissue is related to the reduction potential of the $\text{Cu}^{2+}/\text{Cu}^+$ couple.¹² Reduction being less favoured enhances the selectivity of the complex for tissues with severe hypoxia. In the absence of biological studies it can be predicted that the complexes CuL^1 and CuL^3 , having lower reduction potentials than Cu-ATSM, would display a similar or greater selectivity for hypoxic cells. As the effect of modifications away from the ligand backbone have been shown to be slight in related molecules, deprotected analogues of these species would likely show similar reduction potentials.¹⁴ CuL^2 has a reduction potential similar to Cu-GTSM and would probably select for normoxic tissue.

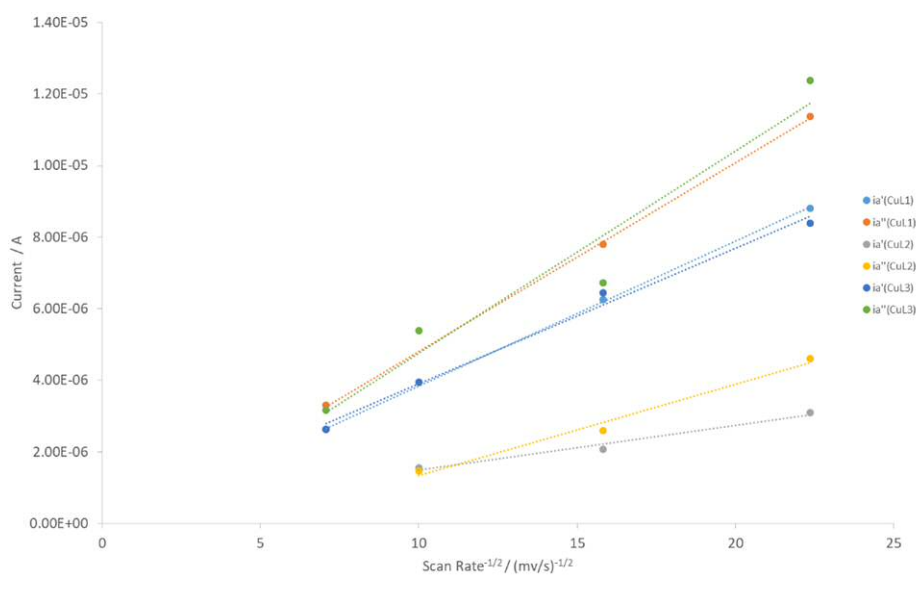


Figure 14. Plot of scan rate^{-1/2} versus anodic peak currents for CuL^{1-3} . Deviations from a linear relationship and variance of peak separation with scan rate confirm that the processes are quasi-reversible.

5.3.6 Crystallography

Suitable crystals for structural determination of ZnL^1 (Fig. 15) were obtained by the slow evaporation of a MeOH solution. Data collection parameters are given in Appendix III. The structure shows that in the solid state two molecules of ZnL^1 exist as a dimer. Each Zn centre receives electron donation from four donor atoms from one ligand, with a sulphur atom from the neighbouring ligand occupying the fifth coordination site to give a distorted square pyramidal coordination geometry where the metal lies slightly above the plane of the ligand. DFT and crystallographic studies of the similar species Zn-ATSM have shown a similar dimeric configuration, and it can be predicted from experimental observations that the presence of a fifth donor atom (e.g. from solvent molecules) is likely in solution.⁶³

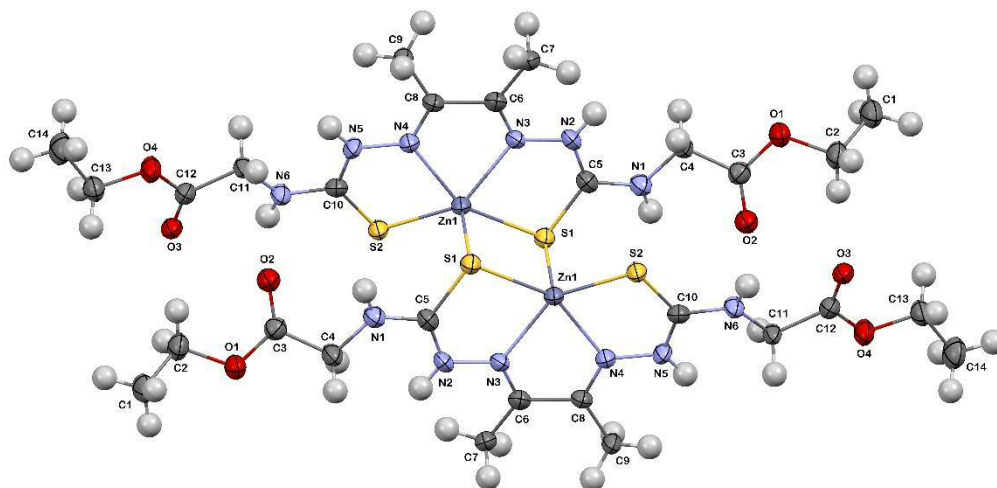


Figure 15. X-Ray crystal structure of ZnL^1 with ellipsoids at 50 % occupancy. The Zn centre lies slightly out of the plane of the square pyramidal geometry. The coordination sphere has Zn-S bonds longer than Zn-N bonds where $d(\text{Zn-S}^1)$, $d(\text{Zn-S}^2)$, $d(\text{Zn-N}^3)$, $d(\text{Zn-N}^4)$ and $d(\text{Zn-S}^{1i})$ are 2.4197(18) Å, 2.3384(15) Å, 2.119(4) Å, 2.115(5) Å and 2.504(2) Å respectively. The bond angles ($\text{S}^2\text{-Zn-S}^1$) and ($\text{S}^{2i}\text{-Zn}^i\text{-S}^{1i}$) are 114.73(6) ° and 108.65(5) ° respectively, with ($\text{N}^4\text{-Zn-N}^3$) being 74.95(17) °.

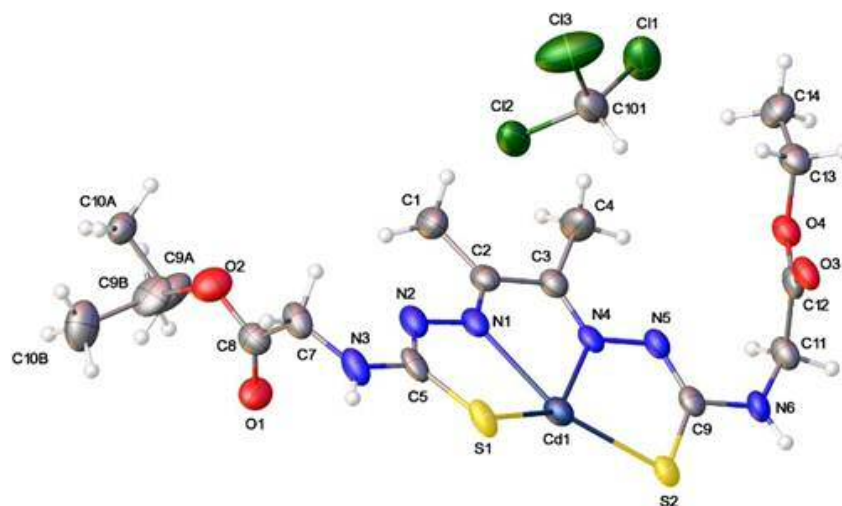


Figure 16. X-Ray crystal structure of CdL^1 with ellipsoids at 50 % occupancy. In the asymmetric part of the unit cell, Cd-S bonds are longer than Cd-N bonds; $d(\text{Cd}-\text{S}^1)$, $d(\text{Cd}-\text{S}^2)$, $d(\text{Cd}-\text{N}^1)$, $d(\text{Cd}-\text{N}^4)$ are 2.5029(12) Å, 2.5239(12) Å, 2.326(4) Å and 2.327(3) Å respectively. Here the bond angles ($\text{S}^1-\text{Cd}^1-\text{S}^2$) and ($\text{N}^4-\text{Cd}^1-\text{N}^1$) are 138.58(4) ° and 69.59(12) ° respectively, due to the greater ionic size of Cd^{2+} (compared to Zn^{2+} in ZnL^1).

Suitable crystals for structural determination of CdL^1 (Fig. 16) were obtained by the slow diffusion of Et_2O into a solution of the complex in CHCl_3 . CdL^1 shows a polymeric structure in the solid state, with sulfur atoms bridging six-coordinate cadmium centres in a distorted octahedral geometry, where the ligand defines the equatorial plane (Fig. 17).

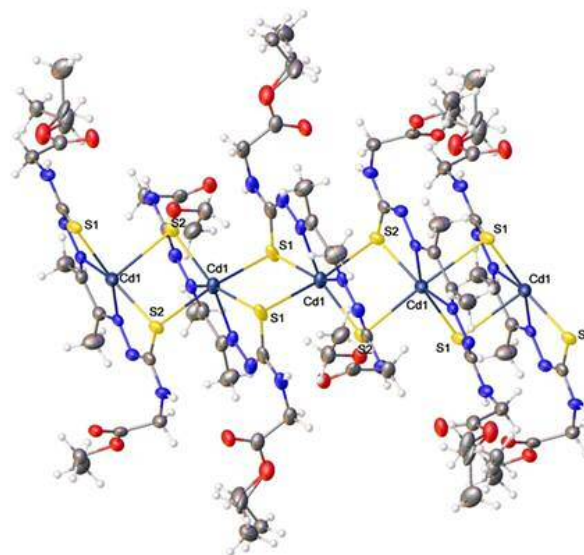


Figure 17. Polymeric structure of CdL^1 . The structure may be described as ‘distorted octahedral’ as the elongated apical bonds ($d(\text{Cd}^1-\text{S}^2) = 2.8706(12)$ Å, $d(\text{Cd}^1-\text{S}^1) = 2.9574(12)$ Å) exist at approximately 90 ° to the plane defined by the ligand, but the bond angles within the plane are not equivalent ($\text{N}^1-\text{Cd}^1-\text{N}^4 = 69.59(12)$ °, $\text{N}^1-\text{Cd}^1-\text{S}^1 = 76.08(9)$ °, $\text{N}^4-\text{Cd}^1-\text{S}^1 = 143.77(9)$ °, $\text{N}^1-\text{Cd}^1-\text{S}^2 = 145.30(9)$ °) and out-of-plane twisting is observed.

Apical positions are filled by sulfur atoms from neighbouring molecules to form an ‘off-set’ polymer chain. In the plane of the ligand bond lengths and angles are typical of this class of complex (Table 4), with the apical bonds showing a lengthening away from true octahedral geometry due to the electron density of the bridging sulfurs being donated mainly to the cadmium centre in the equatorial plane. Bond angles within the equatorial plane deviate from 90 ° as a result of strain imposed by bond lengths within the ligand backbone when coordinating the large Cd²⁺ ion (0.92 Å). The S(2)’-Cd(1)-S(1)’ angle of 170.68(4) ° that gives the ‘off-set’ nature likely arises as a result of compromise between satisfying electronic and steric demands. Cadmium complexes of thiosemicarbazones have previously been shown to assume a number of coordination geometries and to form similar polymeric structures.^{65–68}

Cd(1)-N(1)	2.326(4)	N(1)-Cd(1)-N(4)	69.59(12)
Cd(1)-N(4)	2.327(3)	N(1)-Cd(1)-S(1)	76.08(9)
Cd(1)-S(1)	2.5029(12)	N(4)-Cd(1)-S(1)	143.77(9)
Cd(1)-S(2)	2.5239(12)	N(1)-Cd(1)-S(2)	145.30(9)
Cd(1)-S(2)'	2.8706(12)	N(4)-Cd(1)-S(2)	76.14(9)
Cd(1)-S(1)''	2.9574(12)	S(1)-Cd(1)-S(2)	138.58(4)
		N(1)-Cd(1)-S(2)'	89.57(9)
		N(4)-Cd(1)-S(2)'	100.34(9)
		S(1)-Cd(1)-S(2)'	90.57(4)
		S(2)-Cd(1)-S(2)'	91.17(3)
		N(1)-Cd(1)-S(1)''	81.27(9)
		N(4)-Cd(1)-S(1)''	74.36(9)
		S(1)-Cd(1)-S(1)''	89.56(3)
		S(2)-Cd(1)-S(1)''	94.90(4)
		S(2)''-Cd(1)-S(1)''	170.68(4)

Table 4. Selected bond lengths (Å) and bond angles (°) for CdL^I.

5.3.7 Stability under deprotection conditions

In the forms presented here the complexes ML^{1-3} would be of limited use in the context of imaging disease states. Their poor solubility in aqueous conditions may inhibit their applicability for *in vivo* studies as small molecule drugs and the presence of protecting groups prevents their use as haptens in bioconjugate species. Unfortunately, deprotection conditions for these molecules that did not degrade the ligand could not be determined despite the successful deprotection of similar molecules being reported in the literature.^{47,62,69} The use of strong basic conditions (e.g. 6 equivalents of NaOH in THF) to deprotect H_2L^1 , H_2L^2 and their respective complexes gave inconclusive results. Basic hydrolysis of the ligand may be occurring as result of nucleophilic attack at the imine groups. Although TFA has been used to remove the Boc groups from the terminal amines of molecules similar to H_2L^3 and its complexes, all efforts in the current case were unsuccessful. This may indicate that such experiments require the use of anhydrous conditions and purified, dried reagents (although TFA is typically used without further purification) to prevent hydrolysis. It may be considered that the ethyl ester protecting group used for H_2L^1 and H_2L^2 is unsuitable for the synthesis of bis(thiosemicarbazones) due to the associated deprotection conditions. Other protecting groups for carboxylic acids do not present particular attractive alternatives; the inclusion of terminal acid groups may require alternative routes of synthesis that avoid the need for protecting groups.⁷⁰ Further experiments are therefore required to allow the use of analogous products to the complexes described in this report in bioconjugate systems.

5.3.8 Anti-bacterial MIC assessments

The effects of incubation with different concentrations ($0.78 - 25 \mu\text{g.mL}^{-1}$) of the ligands H_2L^{1-3} and the copper complexes CuL^{1-3} on three bacterial strains (*E. coli*, *S. aureus* and *P. aeruginosa*) were measured by observing changes in a population's absorbance at 600 nm relative to a control population to determine a Minimum Inhibitory Concentration (MIC).⁷¹ The MIC is the lowest agent concentration required to inhibit measurable bacterial growth following overnight incubation. Higher concentrations were unavailable due to the limited solubilities of the species. For a species to be a hit, an 80 % or greater decrease in A_{600} relative to the positive control in two or more of the triplicate experiments must be observed.

In a 2014 study, Cu-GTSM was found to have antibacterial properties against only *S. aureus* from a panel of 50 Gram-positive and Gram-negative bacteria including *E. coli* and *P. aeruginosa*; bactericidal properties of Cu-GTSM, Cu-PTSM and Cu-ATSM against *S. aureus* were related to the redox potential of the metal centre (Cu-GTSM most active, Cu-ATSM inactive) (see Table 5).²⁵

	$E_{1/2}$ / V	CLogP	MIC ₉₀ / μ M		$E_{1/2}$ / V	CLogP	MIC ₈₀ / μ M
Cu-GTSM	-0.83	0.07	0.30	CuL ²	-0.81	1.05	3.57
Cu-PTSM	-0.91	0.48	1.25	CuL ¹	-1.12	2.47	Inactive
Cu-ATSM	-0.99	0.89	Inactive	CuL ³	-1.10	3.95	Inactive

Table 5. Redox potentials, calculated Log P values and MICs for copper complexes discussed. Redox potentials for literature compounds against Fc/Fc^+ calculated from experimental values elsewhere.¹² CLogP calculated for the metal complexes using the commercial software package ChemBioDraw Ultra 13.0. MIC values for literature compounds against *S. aureus* quoted from Haeili et al.²⁵

Although the three complexes were all lipophilic, neutral species able to diffuse passively into bacteria, Cu-GTSM had the highest redox potential and was most rapidly reduced in the cell, resulting in metal dissociation, the rapid overwhelming of the bacteria's protective metabolic pathways and copper poisoning. The complexes with lower redox potentials may also be more susceptible to efflux prior to copper release.²² The ligands themselves did not display antibacterial properties against *S. aureus*.²⁵

Experimentally, the only compound with sufficiently bacteriostatic effects to qualify as a hit was CuL² against *S. aureus* (Table 6). No other compounds at any concentrations reduced any bacterial population enough to be a hit. CuL² serves as a Cu-GTSM analogue, CuL¹ and CuL³ as Cu-ATSM analogues with no effect at any concentration used (not shown).

While Cu-ATSM is more hydrophobic than Cu-GTSM (CLogP = 0.89 and 0.07 respectively), CuL² (CLogP = 1.05) is more hydrophobic than Cu-ATSM, indicating that lipophilicity is not the major contributing factor to the antibacterial properties of the glyoxal-based species. The redox potentials of CuL² ($E_{1/2}$ = -0.81 V) and Cu-GTSM ($E_{1/2}$ = -0.83 V) are nearly identical, but comparing the experimentally derived MIC₈₀ of 1.56 μ g.mL⁻¹ or 3.6 μ M to the MIC₉₀ of Cu-GTSM against wild-type *S. aureus* (0.3 μ M) shows that increasing lipophilicity approximately eleven-fold increases the MIC approximately twelve-fold. Although it must be considered that the bacterial strains used here and in the literature were different, it appears that the more lipophilic species may be subject to retention while passively crossing the phospholipid membrane,⁷² introducing a rate determining step that slows the delivery of the metal and that allows *S. aureus* to counteract copper toxicity. Further experimentation to determine the Minimum Bactericidal Concentration of CuL² would be of interest, but it can be concluded that Cu-GTSM remains a better option for development as a novel antibiotic.

	Conc / $\mu\text{g.mL}^{-1}$	25	12.5	6.25	3.13	1.56	0.78	Positive control
CuL²	A_{600} /nm	0.055	0.032	0.031	0.031	0.032	0.240	0.239
	(% positive control)	(23.0 %)	(13.4 %)	(13.0 %)	(13.0 %)	(13.4 %)	(100 %)	
	A_{600} /nm	0.054	0.031	0.030	0.031	0.281	0.215	0.221
	(% positive control)	(24.4 %)	(14.0 %)	(13.6 %)	(14.0 %)	(127 %)	(97.3 %)	
	A_{600} /nm	0.046	0.035	0.031	0.031	0.030	0.184	0.250
(% positive control)	(18.4 %)	(14.0 %)	(12.4 %)	(12.4 %)	(12.0 %)	(73.6 %)		
Result	HIT	HIT	HIT	HIT	HIT- MIC	No hit		
H₂L²	A_{600} /nm	0.246	0.216	0.193	0.216	0.236	0.178	0.201
	(% positive control)	(122 %)	(107 %)	(96.0 %)	(107 %)	(117 %)	(88.6 %)	
	A_{600} /nm	0.285	0.238	0.032	0.158	0.280	0.235	0.228
	(% positive control)	(125 %)	(104 %)	(14.0 %)	(69.3 %)	(123 %)	(103 %)	
	A_{600} /nm	0.277	0.214	0.224	0.251	0.271	0.227	0.258
(% positive control)	(107 %)	(82.9 %)	(86.8 %)	(97.3 %)	(105 %)	(88.0 %)		
Result	No hit	No hit	No hit	No hit	No hit	No hit	No hit	

Table 6. MIC determination for CuL² and H₂L² against *S. aureus*.. Bacteriostatic effects were observed for CuL² at concentrations of 25 to 1.56 $\mu\text{g.mL}^{-1}$. The MIC is 1.56 $\mu\text{g.mL}^{-1}$.

5.3.9 Anti-parasitic assessments

The effect of incubation of the ligands H_2L^{1-3} and their respective complexes with Cu, Zn, Ni and Cd on the larval stage of *Schistosoma mansoni* was assessed by an automated, high throughput optical assay similar to that described in described in Paveley *et al.*⁵³ This parasitic flatworm is one of several related species that cause Schistosomiasis, a ‘neglected tropical disease’ which kills over 200,000 people per year and for which there is currently only one chemotherapeutic agent (praziquantel).^{73,74} However, praziquantel has limited effect on the immature worm and resistance can be developed, highlighting the need for a diversification in clinical management options.⁷⁵

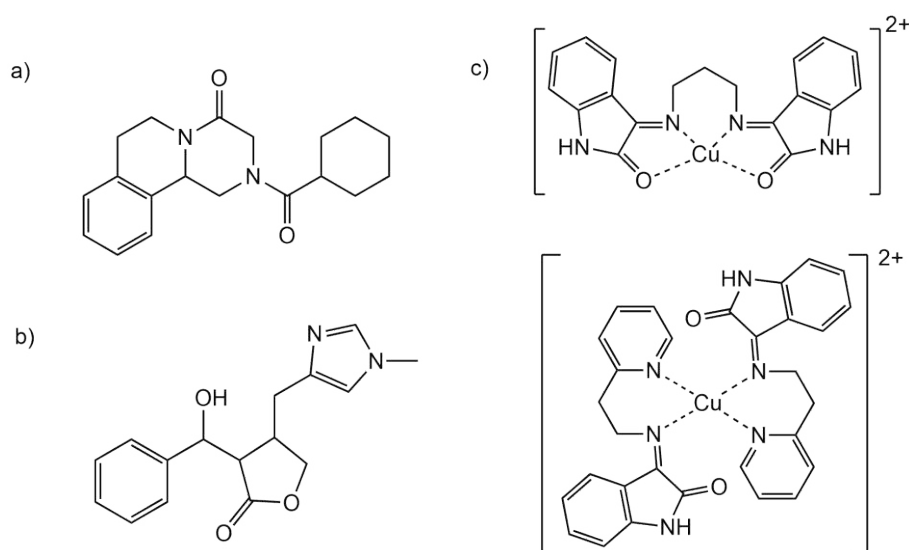


Figure 18. Chemical agents with anthelmintic properties **a.** Praziquantel. **b.** EPI, an imidazole alkaloid derived from a Brazilian plant.⁷⁶ **c.** Copper oxindolimine complexes (note the similarity between the top complex and the BTSC complexes described herein.)⁷⁷

In the 1950's, copper oleate was reported as having potential as a barrier ointment for rice farmers due to its' demonstrated toxicity against the infective phase of *S. japonicum*.⁷⁸ More recently, the alkaloid epiisopiloturine (EPI) derived from the Brazilian 'jaborandi' plant has been shown to have anthelmintic activity (against all life cycle phases of *S. mansoni*)⁷⁶ which is enhanced by coordination to copper but reduced by coordination to zinc; the authors of the research hypothesise that coordination to copper aids in alkaloid delivery into the worm, whereupon the metal is released and causes oxidative stress that is synergistic to the effects of the ligand.⁷⁵ In addition, oxindolimine complexes of copper (which are structurally similar to BTSC complexes) have shown significantly greater antischistosomal activity than zinc and vanadyl analogues.⁷⁷ While the study of organometallic agents against *S. mansoni* is in its' infancy,⁷⁹ the to-date unexplored copper bis(thiosemicarbazones) (e.g. CuL^1 , CuL^2 and CuL^3)

could offer effective new routes of Schistosomiasis therapy, especially since *in vivo* schistosomal granulomas display a hypoxic tissue microenvironment for which BTSCs would be expected to show selectivity.⁸⁰

The results of the high-throughput automated assay are shown in Figs. 19, 20 and Table 7. Compounds that were found to give an average phenotype score below -0.15 *and* an average motility score below -0.35 were considered a hit. Of the compounds studied, four registered as consistent hits: CuL¹, CuL², CdL¹ and CdL³. Automated analysis gave H₂L² and CuL³ as inconsistent hits, but direct observation concluded that the discrepancy was an artefact of the experiment and that both compounds were likely hits. CdL² (not shown) displayed considerably more toxicity than other non-hit compounds (consistent hits on motility and a near hit on phenotype in Scan 1), but was insufficiently effective to be deemed a hit.

Auranofin has been shown to be 100 % lethal to schistosomula at 10 µM following 24 hours incubation as a result of enzyme inhibition and increased oxidative stress.⁷³ By comparison of the observed phenotype and motility scores, in both scans CuL¹ and CuL² showed similar levels of toxicity as auranofin against the schistosomes (see Table 7) suggesting that similarly to as observed in antibacterial studies,²² the copper complexes are taken into the worm, where the metal can be released with a resulting toxic effect on metabolic processes. This is likely due to the metal being redox active and able to form reactive oxygen species (ROS);⁸¹ redox inactive zinc and nickel analogues were non-hits. The exact nature of how free copper disrupts metabolism or otherwise kills schistosomulae requires further investigation. There is insufficient data to assess the relationship of toxicity to the redox potential or lipophilicity of the compounds. All of the copper complexes studied satisfy Lipinski's 'Rule of Five', a useful although imperfect set of criteria often used in drug discovery by which the likelihood of absorption and permeation *in vivo* is predicted.^{82,83}

Although auranofin is clinically approved for the treatment of rheumatoid arthritis and has a known toxicity profile which would reduce development costs relative to a new species,⁸⁴ on the scale needed to replace praziquantel for combatting schistosomiasis in the developing world its unit cost as a gold containing compound would probably render it economically unviable. Cu-ATSM or novel BTSC complexes as described here may offer an alternative.

The cadmium-containing hit compounds CdL¹ and CdL³ were not significantly or consistently more toxic than auranofin or the copper hits. Cadmium has previously been shown to have anthelmintic properties against a parasite in fish,⁸⁵ but as the metal is extremely toxic to humans the barriers to development of a cadmium-based antischistosomiasis drug would be considerable.

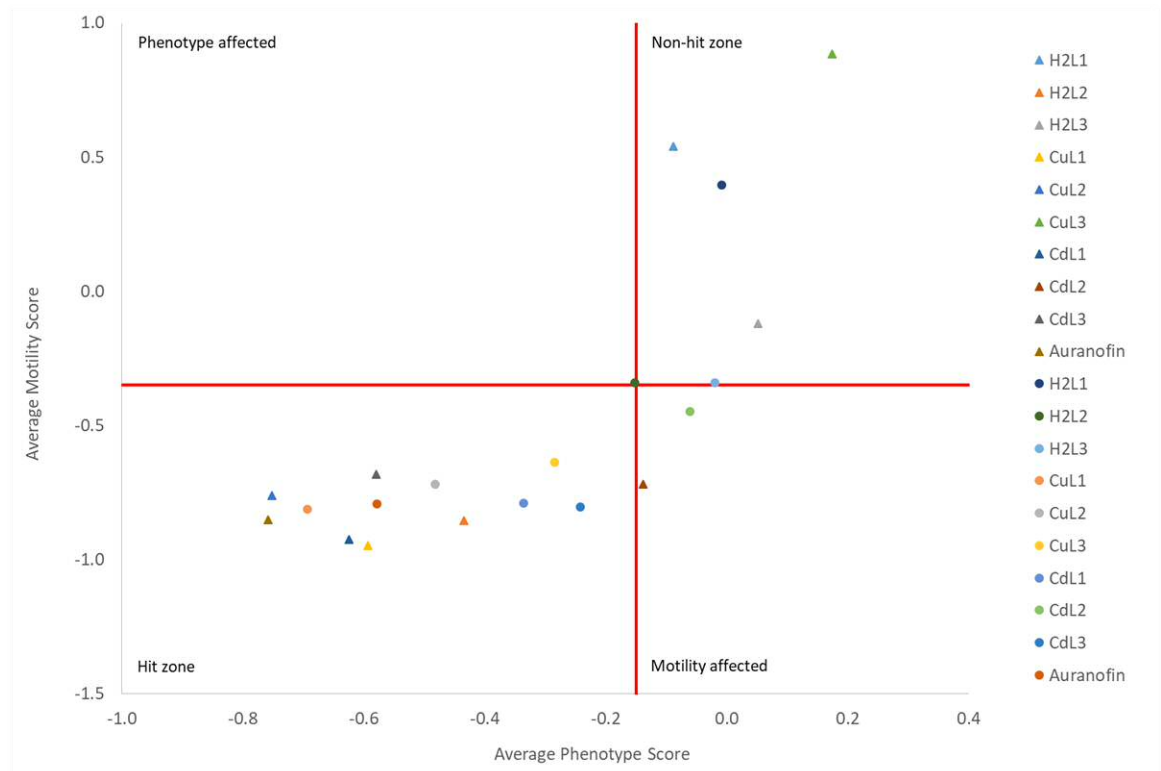


Figure 19. Graphical representation of anthelmintic properties of selected compounds. Results from Scan 1 denoted by triangle, Scan 2 by circles.

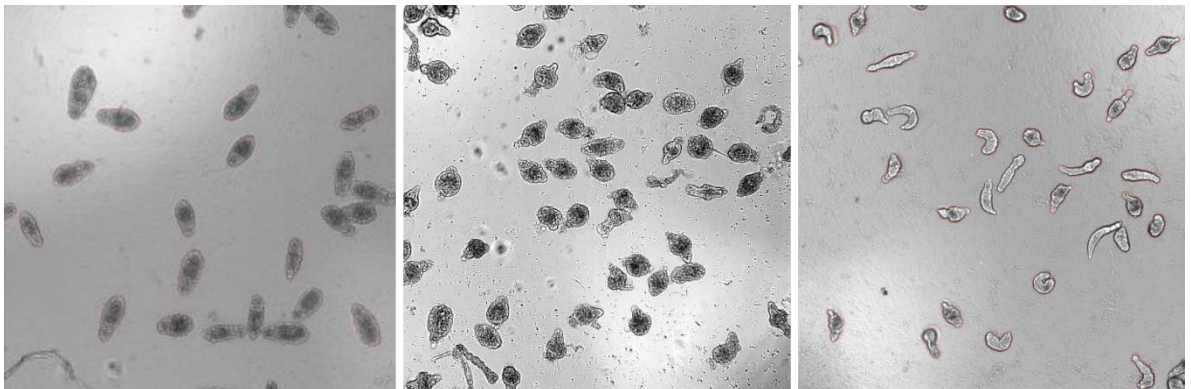


Figure 20. *Schistosomula* treated with CuL¹ (left), Praziquantel (centre) and DMSO i.e. healthy (right).

Screen No.	Compound (10 μ M)	Average Phenotype Score (# larva seg)	Average Motility Score (# larva seg)	Hit Status
1	H ₂ L ¹	-0.08876 (61)	0.54063 (80)	Non-hit
	H ₂ L ²	-0.43538 (27)	-0.85493 (38)	Hit
	H ₂ L ³	0.05112 (41)	-0.12105 (53)	Non-hit
	CuL ¹	-0.59315 (45)	-0.94621 (52)	Hit
	CuL ²	-0.75162 (33)	-0.76071 (37)	Hit
	CuL ³	0.1737 (32)	0.88356 (33)	Non-hit
	CdL ¹	-0.62528 (63)	-0.92407 (61)	Hit
	CdL ²	-0.13805 (56)	-0.71746 (81)	Non-hit
	CdL ³	-0.57992 (66)	-0.68172 (90)	Hit
	Auranofin	-0.759	-0.852	Hit (Positive control)
	DMSO	-0.029	-0.000	Non-hit Negative control
2	H ₂ L ¹	-0.00833 (78)	0.39619 (77)	Non-hit
	H ₂ L ²	-0.15182 (49)	-0.33941 (63)	Non-hit
	H ₂ L ³	-0.02032 (59)	-0.33941 (63)	Non-hit
	CuL ¹	-0.69323 (54)	-0.81174 (65)	Hit
	CuL ²	-0.4822 (32)	-0.71841 (49)	Hit
	CuL ³	-0.28459 (51)	-0.63766 (69)	Hit
	CdL ¹	-0.33541 (57)	-0.78952 (71)	Hit
	CdL ²	-0.06167 (83)	-0.44709 (90)	Non-hit
	CdL ³	-0.2418 (61)	-0.80255 (78)	Hit
	Auranofin	-0.578	-0.793	Hit (Positive control)
	DMSO	-0.034	0.000	Non-hit Negative control

Table 7. Selected results from anthelmintic screening. Scores reaching relevant hit-boundariess shown in bold; a compound must reach both to be considered a hit.

5.4 Conclusion

The synthesis of three novel bis(thiosemicarbazone) ligands, H_2L^{1-3} and their complexes with copper, zinc, nickel and cadmium are reported. The metal complexes are spectroscopically and electrochemically similar to literature compounds. Depending on the metal used, different coordination geometries may be inferred based on the characterisation given; CuL^{1-3} exist as square planar complexes about Cu^{2+} , but reduction of the metal induces a twist in the ligand to give a tetrahedral geometry. ZnL^1 and ZnL^3 exist as approximately square planar complexes in solution; ZnL^1 is seen to form dimers in the solid state where the metal centre is in a square pyramidal geometry. From the electronic spectrum, ZnL^2 appears to assume a different geometry, most likely tetrahedral, as both metal and ligand would be energetically most satisfied in this case. As is typical for a d^8 metal the nickel complexes NiL^{1-3} are square planar in nature. Cadmium complexes CdL^{1-3} appear square planar based on the study of electronic spectra but reference to crystal structures reported here and in the literature reveal a distorted octahedral geometry where apical positions are filled by coordinated solvent molecules in solution or by polymers in the solid state. From the electronic spectra it is likely that the nickel complexes show too great a tendency to assume a square planar geometry to serve as a transition state analogue for Cu-ATSM demetallation. Further work using the other metal complexes described here would be speculative as what epitopes the complexes would present upon bioconjugation is unknown.

The ligands reported here represent a proof of concept for the generation of bis(thiosemicarbazone) haptens. Although the optimisation of synthetic routes to include particular functionalities is required, preferably avoiding the use of protecting groups, observed similarities to Cu-ATSM, Cu-GTSM,^{14,26} Zn-ATSM⁶³ and Ni-ATSM¹⁴ suggest that the complexes discussed above may show similar behaviour *in vivo* and therefore warrant further investigation.

CuL^2 registered as a hit compound against *S. aureus* with a MIC_{80} of 3.57 μM . Additional research may yield elucidation of the exact nature of the 'delivery system' provided by copper bis(thiosemicarbazones) against some bacteria i.e. how lipophilicity and redox potential interplay in the determination of antibacterial activity. CuL^1 , CuL^2 , CdL^1 and CdL^3 all registered as hit compounds in an assay to determine toxicity against parasitic worm larvae (*S. mansoni*), with the copper species showing similar results to a known lethal agent (auranofin). Copper bis(thiosemicarbazones) may warrant investigation as potential novel agents in the struggle against a neglected tropical disease.

5.5 References

- 1 N. Nishida, H. Yano, T. Nishida, T. Kamura and M. Kojiro, *Vasc. Health Risk Manag.*, 2006, **2**, 213–219.
- 2 D. M. Gilkes, G. L. Semenza and D. Wirtz, *Nat. Rev. Cancer*, 2014, **14**, 430–439.
- 3 U. Prabhakar, H. Maeda, R. K. Jain, E. M. Sevick-Muraca, W. Zamboni, O. C. Farokhzad, S. T. Barry, A. Gabizon, P. Grodzinski and D. C. Blakey, *Cancer Res.*, 2013, **73**, 2412–2417.
- 4 I. N. Fleming, R. Manavaki, P. J. Blower, C. West, K. J. Williams, A. L. Harris, J. Domarkas, S. Lord, C. Baldry and F. J. Gilbert, *Br. J. Cancer*, 2015, **112**, 238–250.
- 5 J. A. Bertout, S. A. Patel and M. C. Simon, *Nat. Rev. Cancer*, 2008, **8**, 967–975.
- 6 T. L. Whiteside, *Oncogene*, 2008, **27**, 5904–5912.
- 7 E. C. Finger and A. J. Giaccia, *Cancer Metastasis Rev.*, 2010, **29**, 285–293.
- 8 G. L. Semenza, *Trends Mol. Med.*, 2012, **18**, 534–543.
- 9 B. J. Moeller, R. A. Richardson and M. W. Dewhirst, *Cancer Metastasis Rev.*, 2007, **26**, 241–248.
- 10 J. M. Brown, *Methods Enzymol.*, 2007, **435**, 297–321.
- 11 D. R. Collingridge, W. K. Young, B. Vojnovic, P. Wardman, E. M. Lynch, S. A. Hill and D. J. Chaplin, *Radiat. Res.*, 1997, **147**, 329–334.
- 12 A. L. Vāvere and J. S. Lewis, *Dalton Trans.*, 2007, 4893–4902.
- 13 B. M. Zeglis, J. L. Houghton, M. J. Evans, N. Viola-Villegas and J. S. Lewis, *Inorg. Chem.*, 2014, **53**, 1880–1899.
- 14 P. J. Blower, T. C. Castle, A. R. Cowley, J. R. Dilworth, P. S. Donnelly, E. Labisbal, F. E. Sowrey, S. J. Teat and M. J. Went, *Dalton Trans.*, 2003, 4416–4425.
- 15 Y. Fujibayashi, H. Taniuchi, Y. Yonekura, H. Ohtani, J. Konishi and A. Yokoyama, *J. Nucl. Med. Off. Publ. Soc. Nucl. Med.*, 1997, **38**, 1155–1160.
- 16 J. L. J. Dearling and P. J. Blower, *Chem. Commun.*, 1998, 2531–2532.
- 17 H. Yuan, T. Schroeder, J. E. Bowsher, L. W. Hedlund, T. Wong and M. W. Dewhirst, *J. Nucl. Med.*, 2006, **47**, 989–998.
- 18 N. Takahashi, Y. Fujibayashi, Y. Yonekura, M. J. Welch, A. Waki, T. Tsuchida, N. Sadato, K. Sugimoto and H. Itoh, *Ann. Nucl. Med.*, 2000, **14**, 323–328.
- 19 N. Takahashi, Y. Fujibayashi, Y. Yonekura, M. J. Welch, A. Waki, T. Tsuchida, N. Sadato, K. Sugimoto, A. Nakano, J. D. Lee and H. Itoh, *Ann. Nucl. Med.*, 2001, **15**, 293–296.
- 20 K. Tateishi, U. Tateishi, M. Sato, S. Yamanaka, H. Kanno, H. Murata, T. Inoue and N. Kawahara, *AJNR Am. J. Neuroradiol.*, 2013, **34**, 92–99.
- 21 S. Y. Park, W. J. Kang, A. Cho, J. R. Chae, Y. L. Cho, J. Y. Kim, J. W. Lee and K. Y. Chung, *PLOS ONE*, 2015, **10**, e0131083.
- 22 K. Y. Djoko, M. M. Goytia, P. S. Donnelly, M. A. Schembri, W. M. Shafer and A. G. McEwan, *Antimicrob. Agents Chemother.*, 2015, **59**, 6444–6453.
- 23 K. Y. Djoko, B. M. Paterson, P. S. Donnelly and A. G. McEwan, *Metallomics*, 2014, **6**, 854–863.
- 24 A. Speer, T. B. Shrestha, S. H. Bossmann, R. J. Basaraba, G. J. Harber, S. M. Michalek, M. Niederweis, O. Kutsch and F. Wolschendorf, *Antimicrob. Agents Chemother.*, 2013, **57**, 1089–1091.
- 25 M. Haeili, C. Moore, C. J. C. Davis, J. B. Cochran, S. Shah, T. B. Shrestha, Y. Zhang, S. H. Bossmann, W. H. Benjamin, O. Kutsch and F. Wolschendorf, *Antimicrob. Agents Chemother.*, 2014, **58**, 3727–3736.
- 26 J. L. Dearling, J. S. Lewis, G. E. Mullen, M. J. Welch and P. J. Blower, *JBIC J. Biol. Inorg. Chem.*, 2002, **7**, 249–259.
- 27 O. C. Brown, J. B. Torres, K. B. Holt, P. J. Blower and M. J. Went, *Dalton Trans.*, 2017, DOI:10.1039/C7DT02008B.
- 28 J. L. J. Dearling and A. B. Packard, *Nucl. Med. Biol.*, 2010, **37**, 237–243.
- 29 D. Schilter, *Nat. Rev. Chem.*, 2017, **1**, s41570-016-0013-016.
- 30 N. Haugaard, *Ann. N. Y. Acad. Sci.*, 2000, **899**, 148–158.

- 31 R. Requejo, T. R. Hurd, N. J. Costa and M. P. Murphy, *Febs J.*, 2010, **277**, 1465–1480.
- 32 C. E. Paulsen and K. S. Carroll, *Chem. Rev.*, 2013, **113**, 4633–4679.
- 33 R. C. Smith, V. D. Reed and W. E. Hill, *Phosphorus Sulfur Silicon Relat. Elem.*, 1994, **90**, 147–154.
- 34 D. H. Petering, *Bioinorg. Chem.*, 1972, **1**, 273–288.
- 35 R. W. Hay, *Bio-Inorganic Chemistry*, Halsted Pr, Chichester, 1984.
- 36 K. Y. Djoko, P. S. Donnelly and A. G. McEwan, *Metallomics*, 2014, **6**, 2250–2259.
- 37 'Antibody Production (Immunogen Preparation)', <https://www.thermofisher.com/uk/en/home/life-science/protein-biology/protein-biology-learning-center/protein-biology-resource-library/pierce-protein-methods/antibody-production-immunogen-preparation.html> (accessed 21/12/2016)
- 38 R. Lemus and M. Karol, in *Allergy Methods and Protocols*, eds. M. Jones and P. Lympany, Humana Press, 2008, pp. 167–182.
- 39 D. Voet, J. G. Voet and C. W. Pratt, *Fundamentals of Biochemistry: Life at the Molecular Level*, Wiley, Hoboken, NJ, 2nd edition., 2012.
- 40 D. Hilvert, in *Catalytic Antibodies*, ed. E. Keinan, Wiley-VCH Verlag GmbH & Co. KGaA, 2004, pp. 30–71.
- 41 S. J. Pollack, J. W. Jacobs and P. G. Schultz, *Science*, 1986, **234**, 1570–1573.
- 42 A. Tramontano, K. D. Janda and R. A. Lerner, *Science*, 1986, **234**, 1566–1570.
- 43 S. Padiolleau-Lefèvre, R. B. Naya, M. A. Shahsavarian, A. Friboulet and B. Avalle, *Biotechnol. Lett.*, 2014, **36**, 1369–1379.
- 44 A. R. Cowley, J. R. Dilworth, P. S. Donnelly, E. Labisbal and A. Sousa, *J. Am. Chem. Soc.*, 2002, **124**, 5270–5271.
- 45 E. López-Torres, M. A. Mendiola, J. Rodríguez-Procopio, M. T. Sevilla, E. Colacio, J. Ma Moreno and I. Sobrados, *Inorganica Chim. Acta*, 2001, **323**, 130–138.
- 46 B. M. Paterson and P. S. Donnelly, *Chem. Soc. Rev.*, 2011, **40**, 3005–3018.
- 47 B. M. Paterson, J. A. Karas, D. B. Scanlon, J. M. White and P. S. Donnelly, *Inorg. Chem.*, 2010, **49**, 1884–1893.
- 48 S. J. Coles and P. A. Gale, *Chem. Sci.*, 2012, **3**, 683–689.
- 49 L. A. Howell, R. Gulam, A. Mueller, M. A. O'Connell and M. Searcey, *Bioorg. Med. Chem. Lett.*, 2010, **20**, 6956–6959.
- 50 R. Wong and S. J. Dolman, *J. Org. Chem.*, 2007, **72**, 3969–3971.
- 51 G. C. Lukáš Palatinus, *J. Appl. Crystallogr.*, 2007, **40**, 786–790.
- 52 G. M. Sheldrick, *Acta Crystallogr. A*, 2008, **64**, 112–122.
- 53 R. A. Paveley, N. R. Mansour, I. Hallyburton, L. S. Bleicher, A. E. Benn, I. Mikic, A. Guidi, I. H. Gilbert, A. L. Hopkins and Q. D. Bickle, *PLoS Negl. Trop. Dis.*, 2012, **6**, e1762.
- 54 M. Christlieb and J. R. Dilworth, *Chem. – Eur. J.*, 2006, **12**, 6194–6206.
- 55 J. P. Holland, F. I. Aigbirhio, H. M. Betts, P. D. Bonnitcha, P. Burke, M. Christlieb, G. C. Churchill, A. R. Cowley, J. R. Dilworth, P. S. Donnelly, J. C. Green, J. M. Peach, S. R. Vasudevan and J. E. Warren, *Inorg. Chem.*, 2007, **46**, 465–485.
- 56 R. Hueting, M. Christlieb, J. R. Dilworth, E. G. Garayoa, V. Gouverneur, M. W. Jones, V. Maes, R. Schibli, X. Sun and D. A. Tourwé, *Dalton Trans.*, 2010, **39**, 3620–3632.
- 57 V. A. Vaillancourt, S. D. Larsen, S. P. Tanis, J. E. Burr, M. A. Connell, M. M. Cudahy, B. R. Evans, P. V. Fisher, P. D. May, M. D. Meglasson, D. D. Robinson, F. C. Stevens, J. A. Tucker, T. J. Vidmar and J. H. Yu, *J. Med. Chem.*, 2001, **44**, 1231–1248.
- 58 L. Alsop, A. R. Cowley, J. R. Dilworth, P. S. Donnelly, J. M. Peach and J. T. Rider, *Inorganica Chim. Acta*, 2005, **358**, 2770–2780.
- 59 E. Franco, E. López-Torres, Ma. Mendiola and Mt. Sevilla, *Polyhedron*, 2000, **19**, 441–451.
- 60 H. Beraldo, L. P. Boyd and D. X. West, *Transit. Met. Chem.*, 1998, **23**, 67–71.
- 61 D. X. West, J. S. Ives, G. A. Bain, A. E. Liberta, J. Valdés-Martínez, K. H. Ebert and S. Hernández-Ortega, *Polyhedron*, 1997, **16**, 1895–1905.
- 62 P. A. Waghorn, M. W. Jones, M. B. M. Theobald, R. L. Arrowsmith, S. I. Pascu, S. W. Botchway, S. Faulkner and J. R. Dilworth, *Chem. Sci.*, 2013, **4**, 1430–1441.

- 63 M. Christlieb, J. P. Holland and J. R. Dilworth, *Inorganica Chim. Acta*, 2010, **363**, 1133–1139.
- 64 L. E. Warren, S. M. Horner and W. E. Hatfield, *J. Am. Chem. Soc.*, 1972, **94**, 6392–6396.
- 65 T. S. Lobana, R. Sharma, G. Bawa and S. Khanna, *Coord. Chem. Rev.*, 2009, **253**, 977–1055.
- 66 W. C. Ahmed Jasim M Al-Karawi, *Dalton Trans. Camb. Engl. 2003*, 2009, 564–70.
- 67 D. G. Calatayud, E. López-Torres and M. Antonia Mendiola, *Polyhedron*, 2008, **27**, 2277–2284.
- 68 D. G. Calatayud, E. Lopez-Torres and M. Antonia Mendiola, *Polyhedron*, 2013, **54**, 39–46.
- 69 P. D. Bonnitcho, S. R. Bayly, M. B. M. Theobald, H. M. Betts, J. S. Lewis and J. R. Dilworth, *J. Inorg. Biochem.*, 2010, **104**, 126–135.
- 70 WO2010066010 A1, 2010.
- 71 J. M. Andrews, *J. Antimicrob. Chemother.*, 2001, **48 Suppl 1**, 5–16.
- 72 A. Avdeef, *Absorption and Drug Development: Solubility, Permeability, and Charge State*, Wiley-Blackwell, Hoboken, N.J, 2nd edition., 2012.
- 73 E. Peak, I. W. Chalmers and K. F. Hoffmann, *PLoS Negl. Trop. Dis.*, 2010, **4**, e759.
- 74 J. Utzinger, G. Raso, S. Brooker, D. D. Savigny, M. Tanner, N. Ørnbjerg, B. H. Singer and E. K. N'goran, *Parasitology*, 2009, **136**, 1859–1874.
- 75 M. C. Portes, J. De Moraes, L. M. Costa Veras, J. R. Leite, A. C. Mafud, Y. P. Mascarenhas, A. E. Virgino Luz, F. C. Dalmatti Alves De Lima, R. R. Do Nascimento, H. M. Petrilli, P. L. Silva Pinto, G. Althoff and A. M. Da Costa Ferreira, *J. Coord. Chem.*, 2016, **69**, 1663–1683.
- 76 L. M. Veras, M. A. Guimaraes, Y. D. Campelo, M. M. Vieira, C. Nascimento, D. F. Lima, L. Vasconcelos, E. Nakano, S. S. Kuckelhaus, M. C. Batista and J. R. L. and J. Moraes, *Curr. Med. Chem.*, 2012, **19**, 2051–2058.
- 77 J. de Moraes, B. S. Dario, R. A. A. Couto, P. L. S. Pinto and A. M. da C. Ferreira, *Antimicrob. Agents Chemother.*, 2015, **59**, 6648–6652.
- 78 G. W. Hunter, E. H. Kaufman and C. Pan, *Exp. Parasitol.*, 1952, **1**, 168–175.
- 79 J. Hess, J. Keiser and G. Gasser, *Future Med. Chem.*, 2015, **7**, 821–830.
- 80 A. P. Araújo, T. F. Frezza, S. M. Allegretti and S. Giorgio, *Exp. Mol. Pathol.*, 2010, **89**, 327–333.
- 81 M. Valko and H. M. and M. T. D. Cronin, *Curr. Med. Chem.*, 2005, **12**, 1161–1208.
- 82 C. A. Lipinski, F. Lombardo, B. W. Dominy and P. J. Feeney, *Adv. Drug Deliv. Rev.*, 2001, **46**, 3–26.
- 83 L. Z. Benet, C. M. Hosey, O. Ursu and T. I. Oprea, *Adv. Drug Deliv. Rev.*, 2016, **101**, 89–98.
- 84 C. Roder and M. J. Thomson, *Drugs RD*, 2015, **15**, 13–20.
- 85 M. Pietrock, D. J. Marcogliese and J. D. McLaughlin, *Chemosphere*, 2002, **47**, 29–33.

Chapter 6: Concluding remarks

Introduction

The research presented in Chapters 2, 3 and 4 of this thesis represent an investigation into the possibility of taking a relatively simple approach to iron oxide nanoparticle synthesis and developing from it a novel immunoPET agent that could help meet unmet clinical need in the developed world. Chapter 5 related the synthesis of novel bis(thiosemicarbazone) complexes intended for use in antibody production but which were shown to have antibacterial and antiparasitic properties against a neglected tropical disease. This final discussion gives a brief overview and critical analysis of the work reported above.

ImmunoPET agents from SPION

The importance of immunoPET imaging and the considerations that go into agent design were discussed in Chapter 1. Zirconium-89 is currently the favourite isotope for use in immunoPET agents due to its' long half-life but there is a need for improved methods of using this isotope that avoid the side-effects reported with coordination via DFO.^{1,2} The method reported in Chapters 2 and 4 where ⁸⁹Zr is incorporated into SPION forming via co-precipitation is novel in this regard. Initial experiments utilising smaller quantities of radioactive material proceeded with higher radiolabelling efficiency than later, larger scale approaches, an issue that will require further study if this approach were to be repeated.

Although APTES@SPION could be synthesised 'hot' with the use of remote manipulators, refinement of the experimental methodology, even automation, would be preferable to scaling the reaction up or down from that reported here. It is likely that an alternative synthetic approach is required to significantly improve upon the *in vivo* results shown in Chapter 4.

Bioconjugation of glycoproteins (both antibodies and enzymes) to APTES@SPION by reductive amination is an efficient and cost-effective method of immobilising biomolecules of interest onto particles that may be used as MRI contrast agents or which may be made to incorporate other functionalities with relative ease. Low solubility of some bioconjugate products under certain conditions were observed; while aqueous solubility is a requirement for *in vivo* use, it may be less necessary for *in vitro* purposes. A magnetically recoverable dispersion of enzyme- or antibody-bearing particles synthesised as described may find purpose outside of the body e.g. *in vitro* assays,³⁻⁵ environmental clean-up and water

remediation⁶⁻¹⁴ or biofuel and chemical feedstock production¹⁵⁻¹⁹. The potential applications of SPION are restricted only by imagination.

The conclusion to be drawn from the above is that Chapter 4 records first steps into a complex field of research where multiple disciplines intersect. Although biocompatible, radiolabelled particles could be synthesised and bioconjugated antibodies on the surface of such nanoparticles retained their activity, *in vivo* studies showed that the antibody-bearing, radiolabelled particles were *not* 'greater than the sum of their parts', and that the successful implementation of immunoPET-active SPION remains to be reported.

Bis(thiosemicarbazones) in the imaging and treatment of disease

Chapter 5 presents a record of the syntheses of a number of novel metal bis(thiosemicarbazone) complexes that were initially intended for use as haptens in antibody production to develop improved methods of hypoxia imaging. This was not achieved. However, it could be argued that the identification of CuL² as having antibacterial activity against *S. aureus* and CuL¹ and CuL² having anthelmintic activity against *S. mansoni* is of greater importance. Antibiotic resistant bacterial drug strains (e.g. MRSA) have become global epidemics,²⁰ and schistosomiasis is a chronic and debilitating disease afflicting populations across the developing world, with relatively little effort being expended upon research into novel treatments.²¹ Research into the use of copper BTSC complexes in developing novel disease treatments could be of great significance in the coming years.

References

- 1 M. A. Deri, B. M. Zeglis, L. C. Francesconi and J. S. Lewis, *Nucl. Med. Biol.*, 2013, **40**, 3–14.
- 2 O. C. Boerman and W. J. G. Oyen, *J. Nucl. Med.*, 2011, **52**, 1171–1172.
- 3 C. Burtea, S. Laurent, I. Mahieu, L. Larbanoix, A. Roch, M. Port, O. Rousseaux, S. Ballet, O. Murariu, G. Toubeau, C. Corot, L. Vander Elst and R. N. Muller, *Contrast Media Mol. Imaging*, 2011, **6**, 236–250.
- 4 S. Tong, B. Ren, Z. Zheng, H. Shen and G. Bao, *ACS Nano*, 2013, **7**, 5142–5150.
- 5 C. Burtea, S. Laurent, A. Roch, L. V. Elst and R. N. Muller, *J. Inorg. Biochem.*, 2005, **99**, 1135–1144.
- 6 J. Theron, J. A. Walker and T. E. Cloete, *Crit. Rev. Microbiol.*, 2008, **34**, 43–69.
- 7 C. Okoli, M. Boutonnet, S. Järås and G. Rajarao-Kuttuva, *J. Nanoparticle Res.*, 2012, **14**, 1194.
- 8 R. Lakshmanan, C. Okoli, M. Boutonnet, S. Järås and G. K. Rajarao, *Bioresour. Technol.*, 2013, **129**, 612–615.
- 9 E. Vélez, G. E. Campillo, G. Morales, C. Hincapié, J. Osorio, O. Arnache, J. I. Uribe and F. Jaramillo, *J. Phys. Conf. Ser.*, 2016, **687**, 012050.
- 10 R. Lakshmanan and G. Kuttuva Rajarao, *Bioresour. Technol.*, 2014, **153**, 333–339.
- 11 M. r. Lasheen, I. Y. El-Sherif, D. Y. Sabry, S. t. El-Wakeel and M. f. El-Shahat, *Desalination Water Treat.*, 2016, **57**, 17421–17429.
- 12 Y. C. Sharma, V. Srivastava, V. K. Singh, S. N. Kaul and C. H. Weng, *Environ. Technol.*, 2009, **30**, 583–609.
- 13 T. Burks, A. Uheida, M. Saleemi, M. Eita, M. S. Toprak and M. Muhammed, *Sep. Sci. Technol.*, 2013, **48**, 1243–1251.
- 14 J. Xu, T. Tang, K. Zhang, S. Ai and H. Du, *Process Biochem.*, 2011, **46**, 1160–1165.
- 15 G. de Gonzalo, D. I. Colpa, M. H. M. Habib and M. W. Fraaije, *J. Biotechnol.*, 2016, **236**, 110–119.
- 16 M. Ahmad, J. N. Roberts, E. M. Hardiman, R. Singh, L. D. Eltis and T. D. H. Bugg, *Biochemistry (Mosc.)*, 2011, **50**, 5096–5107.
- 17 P. D. Sainsbury, E. M. Hardiman, M. Ahmad, H. Otani, N. Seghezzi, L. D. Eltis and T. D. H. Bugg, *ACS Chem. Biol.*, 2013, **8**, 2151–2156.
- 18 R. Datta, A. Kelkar, D. Baraniya, A. Molaei, A. Moulick, R. S. Meena and P. Formanek, *Sustainability*, 2017, **9**, 1163.
- 19 J. Hu, B. Yuan, Y. Zhang and M. Guo, *RSC Adv.*, 2015, **5**, 99439–99447.
- 20 S. Stefani, D. R. Chung, J. A. Lindsay, A. W. Friedrich, A. M. Kearns, H. Westh and F. M. MacKenzie, *Int. J. Antimicrob. Agents*, 2012, **39**, 273–282.
- 21 J. Utzinger, G. Raso, S. Brooker, D. D. Savigny, M. Tanner, N. Ørnbjerg, B. H. Singer, E. K. N'goran, *Parasitology*, 2009, **136**, 1859–1874.
- 22 M. Fang, V. Ström, R. T. Olsson, L. Belova and K. V. Rao, *Appl. Phys. Lett.*, 2011, **99**, 222501.
- 23 V. Ström, R. T. Olsson and K. V. Rao, *J. Mater. Chem.*, 2010, **20**, 4168–4175.
- 24 D. Liu, A. M. Pourrahimi, L. K. H. Pallon, R. L. Andersson, M. S. Hedenqvist, U. W. Gedde and R. T. Olsson, *RSC Adv.*, 2015, **5**, 48094–48103.

Additional Experimental Section I: Selected attempted methods of synthesising APTES@SPION

1.1 Introduction

A crucial part of the work described in Chapter 2 was the development of reproducible methods of synthesising biocompatible SPION that could be characterised fully and serve as a foundation for subsequent bioconjugation. As has been shown, APTES@SPION were synthesised in the chemistry laboratory and were dispersible in aqueous media; their analogues produced in the radioisotope laboratory had near identical characteristics when analysed. SPION produced in this manner could be radiolabelled with high efficiency and retain their aqueous solubility. The use of APTES as a coating agent was desirable for the stability with which the coating is attached to the iron oxide surface and for the amine functionality which was predicted to be crucial for future functionalisation. Before the approach described above was developed, other approaches were attempted which resulted in particles which had little or no solubility in aqueous conditions and which were deemed unsuitable for further analysis. Two such methods are described below and are typical of many synthetic approaches reported in the literature.

An attempt to improve the Massart co-precipitation methodology by use of a ‘rapid mixing’ reactor is also described. It was hoped that the use of such an approach would reduce variation in several parameters that have been reported to affect nanoparticle size and monodispersity (such as rate of reactant addition, reaction time, degree of mixing) by reducing researcher intervention to the rapid squeezing of two syringes. Unfortunately, inconsistencies in qualitative behaviours, quantitative measurements and low yields showed this approach to be unsuitable for further development.

1.2 Experimental

1.2.1 Methods and materials

Reactions were performed with the use of vacuum line and Schlenk techniques where appropriate. Reagents were commercial grade and were used without further purification. All reagents and solvents were purchased from Alfa Aesar or Sigma Aldrich, except APTES which was purchased from TCI Chemicals. FeCl₂·4H₂O and APTES were stored under inert atmospheres. The aluminium mixing head described was made by the Workshops department, School of Chemistry, Cardiff University.

1.2.2 Synthesis and analytical techniques

Uncoated SPION via the Massart method

Water (50 mL) was added to a two-neck round bottom flask (250 mL), the system was sealed and degassed under nitrogen for 30 min. FeCl₃·6H₂O (2.322 g, 8.6 mmol) and FeCl₂·4H₂O (0.854 g, 4.3 mmol) was added carefully under a blanket of nitrogen and the solution mixed to homogenise. 1 M NaOH (40 mL) was added in a rapid single addition with vigorous stirring and the reaction mixture seen to turn black immediately. The reaction mixture was stirred at room temperature for 10 min. The black precipitate was collected by use a permanent magnet and washed with EtOH (3 × 10 mL) and MeOH (3 × 10 mL) then dried *in vacuo* to give the *title compound* (1.13 g). IR (ATP) $\nu = 631$ (Fe-O-Fe stretch), 590 (Fe-O-Fe stretch), 431 cm⁻¹.

NB. If subsequent coating was required, the final drying was omitted.

Method 1: Heating in EtOH

Uncoated SPION (0.25 g) and APTES (100 μ L, 4.29 mmol) were heated to reflux in degassed EtOH (25 mL) for 2h, collected with a permanent magnet and washed with fresh EtOH (3 × 10 mL) then dried *in vacuo*. The resulting black particles could not be fully dispersed in aqueous media.

Method 2: Heating in toluene

Uncoated SPION (0.1 g) and APTES (10 μ L, 0.43 mmol) were heated to reflux in degassed toluene (25 mL) under nitrogen overnight, collected with a permanent magnet and washed with fresh MeOH (3 × 10 mL) then dried *in vacuo*. The resulting black particles could not be fully dispersed in aqueous media except at pH 1.

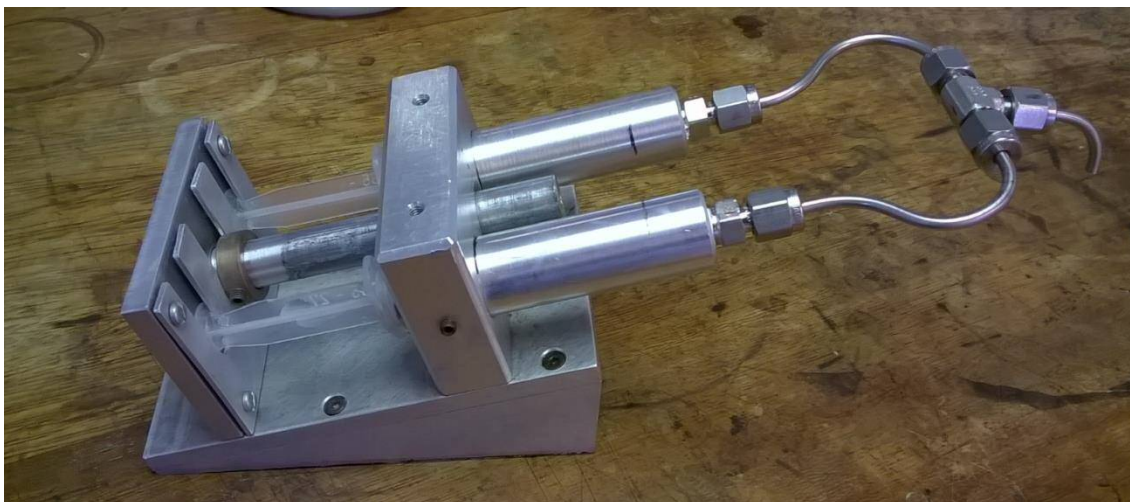


Figure 1. Custom built mixing head reactor cell for SPION synthesis. Note the two syringes (left) for iron salt solution and base, and the T-joint (right) where mixing occurs.

Based on the methods developed by Olsson et al.^{31,32,34} Water (20 mL) was degassed thoroughly using the freeze-pump-thaw method. A stock solution of iron salts was made using $\text{FeCl}_3 \cdot 6\text{H}_2\text{O}$ (360 mg, 1.33 mmol) and $\text{FeCl}_2 \cdot 4\text{H}_2\text{O}$ (133 mg, 0.69 mmol) in degassed H_2O (10 mL). 4M NH_3 was prepared from the dilution of 35 % NH_3 (2.2 mL) with degassed H_2O . 1 mL of each of the above solutions was transferred into one of the two syringes on the stop flow reactor, and rapid mixing was achieved by injection of the two syringes, such that the black solution produced was collected in an Eppendorf tube. The reaction mixture was sonicated at room temperature for 5 min. The black precipitate of uncoated SPION was collected by centrifugation (13200 rpm, 5 min) and was washed with fresh H_2O (3×2 mL). The washed particles were suspended and sonicated for 3 min in a stock solution (3 mL) made by mixing H_2O (2.8 mL) isopropyl alcohol (12.6 mL) and 35 % NH_3 (0.32 mL). APTES (90 μL) was added and the reaction mixture mixed with use of an inverting carousel mixer. The particles were collected by centrifugation (13200 rpm, 5 min), washed with fresh EtOH (3×2 mL) and allowed to dry in air to give *APTES@SPION* as a black solid (8-12 mg). Yields from this approach varied significantly and DLS analysis of 1 mg.mL⁻¹ solutions in 1 M acetic acid showed large hydrodynamic sizes (300-500 nm) with little agreement between samples.

Additional Experimental Section II – Novel naphthalimide species synthesised for use as fluorescent dyes

1.1 Introduction

In addition to the use of the commercial dye FITC as a fluorescent marker described in Chapter 4, it was proposed that the development of a number of novel fluorophores might be an interesting addition to the work described above. Previous research has shown that 1, 8-naphthalic anhydride reacts with the amine groups of APTES@SPION, forming naphthalimide groups on the particle surface which could be seen to fluoresce despite their proximity to the strongly quenching iron oxide core. This observation prompted us to investigate the usefulness of naphthalimide fluorophores in the field of SPION research.

1.2 Naphthalimide fluorophores in bioconjugate chemistry

1, 8- naphthalimide derivatives have several properties that make them of great interest to researchers looking for novel fluorophore species for bioconjugate purposes. Beginning from commercially available species such as 4-Chloro-1,8-naphthalic anhydride, stepwise reactions allow for the synthesis of the imide and the functionalisation of the ring system. These reactions can typically occur on a large scale and with excellent yields. The ease of their synthesis has contributed to the large number of naphthalimide species reported in the scientific literature and their use in such varied fields as cellular imaging (marketed as ‘Lucifer yellow’ derivatives¹), drug discovery, DNA binding², as small molecule probes³, as dyes and pigments⁴ and as metal sensors⁵. In addition, the ease of their synthesis can allow for the ‘fine-tuning’ of the molecule’s properties including solubility, lipophilicity and their photophysical characteristics.⁶

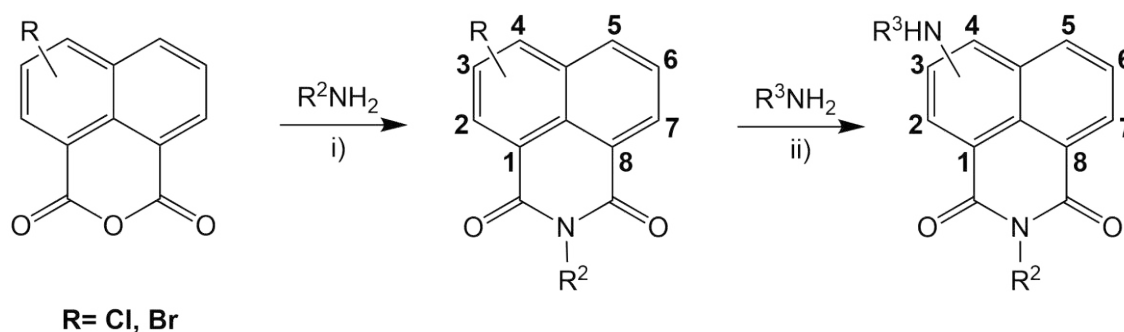


Figure 1. General synthesis and numbering scheme for naphthalimides. i) EtOH, reflux, 24 h. ii) DMSO, 90 °C, 3-5 days.

Naphthalimide species having an electron donating group at the 4-position show highly efficient fluorescence in the yellow-green region of the visible spectrum.⁴ The inclusion of an amino group increases the charge transfer character of the excited state and increases the Stokes shift observed for such a naphthalimide.⁶ This allows for greater distinction between the fluorescence of the probe and any autofluorescence that would be observed in a biological context.⁶ However, Lucifer yellow probes used for cell imaging bear two sulphonate groups to increase aqueous solubility to approximately 1.5 %, ¹ and so researchers must be conscious of inherently limited aqueous solubility when designing novel naphthalimides.

Within the context of fluorescently labelling either a SPION or synthesizing a fluorescent bioconjugate based on such nanoparticles one must be aware of the risk of ‘quenching’. As has been discussed in Chapter 4, fluorescence quenching occurs when the interaction between a fluorophore and its local environment results in a diminishing of the intensity of emitted light. The iron oxide core of the SPION is a very efficient quenching agent although as quenching is often distance dependent the presence of a coating agent can partially compensate for this. APTES@SPION solutions absorb most strongly at the blue end of the visible spectrum. Naphthalimides, having typically lower absorbance maxima than FITC (between 400-450 nm versus 495 nm) but displaying much larger bathochromic shifts (emitting at 530-550 nm versus 519 nm for FITC) are more able to overcome quenching by the core.

Given their inexpensive starting materials, facile syntheses and desirable photophysical characteristics, naphthalimides make excellent candidates for novel fluorophores for use in bioconjugation.

1.3 Experimental

1.3.1 Materials and Methods

All reactions were performed with the use of vacuum line and Schlenk techniques where appropriate. Reagents were commercial grade and were used without further purification. All reagents and solvents were purchased from Alfa Aesar or Sigma Aldrich. ^1H and $^{13}\text{C}\{-^1\text{H}\}$ NMR spectra were recorded on an NMR-FT Bruker 400 MHz or Joel Eclipse 300 MHz spectrometer and recorded in CDCl_3 or $\text{d}^6\text{-DMSO}$. ^1H and $^{13}\text{C}\{-^1\text{H}\}$ NMR chemical shifts (δ) were determined relative to internal TMS and are given in ppm. Coupling constants J are given in hertz (Hz). Low- and high-resolution mass spectra were obtained using a Waters LCT Premier XE instrument and are reported as m/z (relative intensity). IR spectra are recorded as solid samples on a Shimadzu IRAffinity-1 FTIR spectrometer. UV-Vis studies were performed on a Jasco V-570 spectrophotometer as solutions (5×10^{-5} M) in CHCl_3 or H_2O . Photophysical data was obtained on a JobinYvon-Horiba Fluorolog spectrometer fitted with a JY-TBX picoseconds photodetection module as CHCl_3 , H_2O or DMSO solutions. Emission spectra were uncorrected and excitation spectra were instrument corrected. The pulsed source was a Nano-LED configured for 355 nm output operating at 1 MHz. Luminescence lifetime profiles were obtained using the JobinYvon-Horiba FluoroHub single photon counting module and the data fitted using DAS6 deconvolution software.

1.3.2 Synthesis and analytical techniques

Naphthalimide-APTES@SPION (1)

APTES@SPION synthesised as described in Chapter 2 (0.100 g) and naphthalic anhydride (0.35 g, 0.18 mmol) were heated to 70°C in DMF (10 mL) for 5 h. The black solid was collected with a permanent magnet and washed with acetone (3×5 mL), then dried *in vacuo* to give the *title compound* as a sparingly soluble black solid (0.070 g). IR (ATP) $\nu = 2924$ (CH), 1698 (amide CO), 1625, 1654 (NH), 1589, 1016 (CN), 780, 545 cm^{-1} . UV-vis (H_2O): $\lambda_{\text{max}} = 345$ nm. Emission (H_2O): $\lambda_{\text{em}} = 400$ nm.

4-Chloro-(N-(3-triethoxysilyl(propyl))-1, 8-naphthalimide (2)

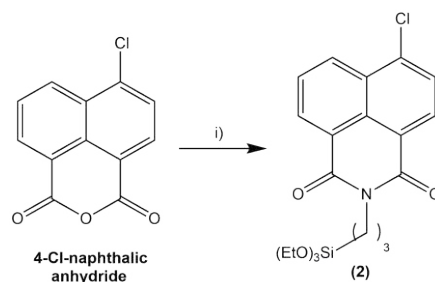


Figure 2. Synthetic scheme for naphthalimide (2). i) 2 eq. APTES, EtOH, reflux, 24h

APTES (1 mL, 4.3 mmol) and 4-Chloronaphthalic anhydride (0.498 g, 2.15 mmol) were heated to reflux in EtOH (10 mL) for 24 h. The pale white suspension becomes a bright orange solution within 1 h. Upon cooling to room temperature, a precipitate formed, was collected by filtration and washed with cold EtOH (3 × 5 mL) to give the *title compound* as a yellow solid (0.622 g, 1.43 mmol, 66.5 %). $^1\text{H NMR}$ (400 MHz, CDCl_3) δ_{H} = 8.53 (1H, d, $^3J_{\text{HH}}$ = 6.50 Hz, CH), 8.45 (1H, d, $^3J_{\text{HH}}$ = 8.48 Hz, CH), 8.36 (1H, d, $^3J_{\text{HH}}$ = 7.89 MHz, CH), 7.76-7.68 (2H, m, 2 × CH), 4.07 (2H, t, $^3J_{\text{HH}}$ = 7.66 MHz, CH_2N), 3.74 (6H, q, $^3J_{\text{HH}}$ = 6.99 MHz, 3 × CH_2CH_3) 1.82-1.71 (2H, m, $\text{CH}_2\text{CH}_2\text{CH}_2$), 1.13 (9H, t, $^3J_{\text{HH}}$ = 6.96 MHz, 3 × CH_2CH_3) ppm. $^{13}\text{C NMR}$ (300 MHz, CDCl_3) δ_{C} = 164.1 (C=O), 139.4 (CCl), 132.1 (CH), 131.5 (CH), 131.0 (CH), 128.3 (CH), 127.8 (CH), 58.9 (CH_2O), 43.4 (CH_2N), 21.9 ($\text{CH}_2\text{CH}_2\text{Si}$), 18.7 (CH_3), 8.4 (CH_2Si) ppm. LR-MS (APCI) found m/z 458.06, calculated m/z 458.12 for $[\text{C}_{21}\text{H}_{26}\text{NO}_5\text{SiCl}+\text{Na}]^+$. IR (ATP) ν = 2968 (CH), 2880 (CH), 1701, 1662 (amide CO), 1587, 1572, 1379, 1342, 1244, 1076 (SiO) cm^{-1} . UV-vis (CHCl_3): λ_{max} ($\epsilon / \text{L mol}^{-1} \text{cm}^{-1}$) = 343(9700), 358(8220) nm. Emission (CHCl_3) λ_{em} = 506 nm (9.12 ns, $\chi^2 = 0.97$)

Attempted synthesis of 4-((2-(2-(2-aminoethoxy)ethoxy)ethyl)amino)-(N-(3-triethoxysilyl(propyl))-1, 8-naphthalimide (3)

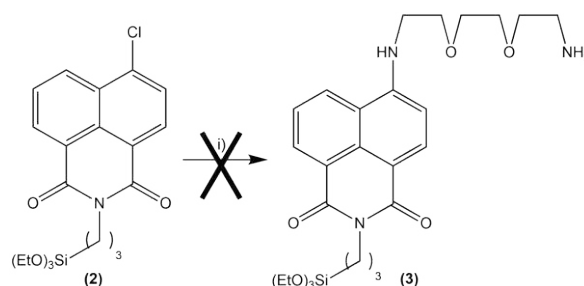


Figure 3. Synthetic scheme for naphthalimide (3). i) 10 eq. 2,2'-ethylenedioxybisethylamine, DMSO, 8 C, 5 days. The presence of hydrolysable ethoxy groups prevented the isolation of the target species.

2, 2'-ethylenedioxybisethylamine (0.34 mL, 2.3 mmol) was added to dry DMSO (2 mL) under N₂. Naphthalimide (**2**) (0.100 g, 0.23 mmol) in DMSO (2 mL) was added, and the reaction mixture stirred at 80 °C for 5 days. The orange solution was allowed to cool to room temperature, and added to H₂O (50 mL). The solution was neutralised by addition of 2 M HCl. The coloured compound was extracted into DCM (3 × 10 mL). The organic fraction was washed with H₂O (3 × 10 mL), brine (3 × 10 mL), and dried over MgSO₄. The drying agent was removed by filtration, and the solvent removed *in vacuo* to give a brown oil that contained multiple species that could not be characterised satisfactorily.

4-Chloro-(N-(propyl))-1, 8-naphthalimide (**4**)

Propylamine (0.15 mL, 1.82 mmol) and 4-Chloronaphthalic anhydride (0.212 g, 0.91 mmol) were heated to reflux in EtOH (10 mL) for 24 h. The pale white suspension becomes a bright yellow solution within 1 h. Upon cooling to room temperature, a precipitate formed, was collected by filtration and washed with cold EtOH (3 × 5 mL) to give the *title compound* as a yellow solid (0.200 g, 0.73 mmol, 81 %). ¹H NMR (400 MHz, CDCl₃) δ_H = 8.60 (1H, d, ³J_{HH} = 7.11 Hz, CH), 8.54 (1H, d, ³J_{HH} = 8.14 Hz, CH), 8.44 (1H, d, ³J_{HH} = 7.92 Hz, CH), 7.83-7.73 (2H, m, 2 × CH), 4.08 (2H, t, ³J_{HH} = 7.58 Hz, CH₂N), 1.75-1.64 (2H, m, CH₂CH₃), 0.95 (3H, t, ³J_{HH} = 7.42 Hz, CH₃) ppm. ¹³C NMR (400 MHz, CDCl₃) δ_C = 164.0 (CO), 139.4 (CH), 132.4 (CH), 131.6 (CH), 131.0 (CH), 129.7 (CH), 129.5 (CH), 128.3 (CH), 127.8 (CH), 123.5 (CH), 122.1 (CH), 42.5 (CH₂), 21.8 (CH₂), 12.0 (CH₃) ppm. LR-MS (EI+) found m/z 273.03, calculated m/z 273.06 for [C₁₅H₁₂NO₂Cl]⁺. IR (ATP) ν = 3065 (CH), 2949 (CH), 2873 (CH), 1695, 1653 (amide CO), 1585, 1348 cm⁻¹. UV-vis (CHCl₃): λ_{max} (ε / L mol⁻¹ cm⁻¹) = 342(14060), 358(11880) nm. Emission (CHCl₃) λ_{em} = 501 nm (9.30 ns, χ² = 0.92)

4-((2-(2-(2-aminoethoxy)ethoxy)ethyl)amino)-(N-(propyl))-1,8-naphthalimide (**5**)

2, 2'-ethylenedioxybisethylamine (0.54 mL, 3.7 mmol) was added to DMSO (2 mL) under N₂. Naphthalimide (**4**) (0.100 g, 0.37 mmol) in DMSO (2 mL) was added, and the reaction mixture stirred at 80 °C for 5 days. The orange solution was allowed to cool to room temperature, and added to H₂O (50 mL). The solution was neutralised by addition of 2 M HCl. The coloured compound was extracted into DCM (3 × 10 mL). The organic fraction was washed with H₂O (3 × 10 mL), brine (3 × 10 mL), and dried over MgSO₄. The drying agent was removed by filtration, and the solvent removed *in vacuo* to give the *title compound* as a bright yellow solid (0.121 g, 0.31 mmol, 85 %). ¹H NMR (400 MHz, CDCl₃) δ_H = 8.52 (1H, d, ³J_{HH} = 8.00 Hz, CH), 8.39 (1H, d, ³J_{HH} = 8.37 Hz, CH), 8.14 (1H, d, ³J_{HH} = 8.05 Hz, CH), 7.58-7.53 (1H, m, CH(CH)₂), 6.64 (1H, d, ³J_{HH} = 8.44 Hz, CH(CN)), 5.95-5.91 (1H, m, NH), 4.08-4.03 (2H, m, CH₂N), 3.83 (2H, t, ³J_{HH} = 5.24 Hz, CH₂O), 3.69-3.60 (4H, m, 2 × CH₂O),

3.55-3.50 (2H, m, CH_2NH_2), 3.48 (2H, m, CH_2), 2.83 (2H, t, $^3J_{\text{HH}} = 5.20$ Hz, CH_2N), 1.73-1.63 (2H, m, CH_2CH_3), 0.94 (3H, t, $^3J_{\text{HH}} = 7.43$ Hz, CH_3) ppm. ^{13}C NMR (400 MHz, CDCl_3) $\delta_{\text{C}} = 165.2$ (CO), 164.7 (CN), 134.8 (CH), 131.6 (CH), 126.9 (CH), 125.1 (CH), 70.8 (CH_2O), 70.6 (CH_2O), 69.1 (CH_2O), 42.1 (CH_2N), 42.0 (CH_2N), 41.4 (CH_2N), 21.8 (CH_2CH_3), 12.0 (CH_3) ppm. LR-MS (ES+) found m/z 386.19, calculated m/z 386.21 for $[\text{C}_{21}\text{H}_{28}\text{N}_3\text{O}_4]^+$. IR (ATP) $\nu = 3529$ (NH), 3354 (NH), 2874 (CH), 1680, 1643 (amide CO), 1585, 1342, 1066 cm^{-1} . UV-vis (CHCl_3): λ_{max} ($\epsilon / \text{L mol}^{-1} \text{cm}^{-1}$) = 424 (9760), 278(13100), 261(15560) nm. Emission (CHCl_3) $\lambda_{\text{em}} = 510$ nm (8.73 ns, $\chi^2 = 1.07$)

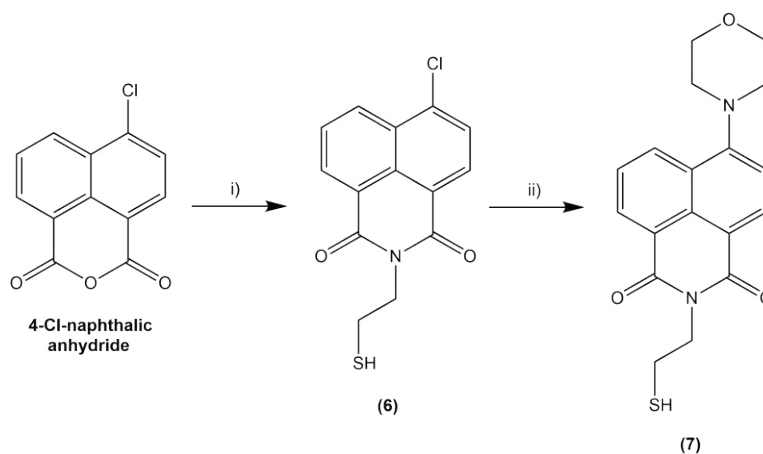


Figure 4. Synthetic scheme for naphthalimides **(6)** and **(7)**. i) 2 eq. 2-aminoethanethiol hydrochloride, 4 eq. NEt_3 , EtOH, reflux, 24. ii) 4 eq. morpholine, DMSO, 95 °C, 72 h.

4-Chloro-(N-(2-mercaptoethyl))-1,8-naphthalimide (6)

4-Chloronaphthalic anhydride (0.200 g, 0.86 mmol) and NEt_3 (0.24 mL, 1.7 mmol) were added to a solution of 2-aminoethanethiol hydrochloride (0.195 g, 1.70 mmol) in EtOH (20 mL) under N_2 . The reaction mixture was heated to reflux overnight, then allowed to cool to room temperature. A precipitate was collected on a filter, washed with cold EtOH (3×10 mL) and dried *in vacuo* to give the *title compound* as a yellow solid (0.195 g, 0.67 mmol, 78 %). ^1H NMR (400 MHz, CDCl_3) $\delta_{\text{H}} = 8.59$ -8.52 (2H, m, $2 \times \text{CH}$), 8.41 (1H, d, $^3J_{\text{HH}} = 7.90$, CH), 7.81-7.74 (2H, m, $2 \times \text{CH}$), 4.49 (2H, t, $^3J_{\text{HH}} = 7.27$ Hz, CH_2N), 3.09-3.02 (2H, m, CH_2SH) ppm. ^{13}C NMR (400 MHz, CDCl_3) $\delta_{\text{C}} = 163.9$ (CO), 131.7 (CH), 128.3 (CH), 127.9 (CH), 121.9 (CH), 45.1 (CH_2N), 36.0 (CH_2SH) ppm. LR-MS (EI+) found m/z 258.03, calculated m/z 258.03 for $[\text{C}_{14}\text{H}_9\text{NO}_2\text{Cl}]^+$ ($[\text{M-SH}]^+$). IR (ATP) $\nu = 3067$ (CH), 2949, 2926, 1697 (amide CO), 1657 (amide CO), 1589, 1570, 1338, 1232 cm^{-1} . UV-vis (CHCl_3): λ_{max} ($\epsilon / \text{L mol}^{-1} \text{cm}^{-1}$) = 359(11940), 344(14200), 327(10000) nm. Emission (DMSO) $\lambda_{\text{em}} = 519$ nm (2.64 ns, $\chi^2 = 0.93$)

4-morpholinyl-(N-(2-mercaptoethyl))-1, 8-naphthalimide (7)

Naphthalimide (**6**) (0.060 g, 0.21 mmol) and morpholine (72 μ L, 0.825 mmol) were dissolved in DMSO (3 mL) under N_2 . The reaction mixture was heated at 95 $^{\circ}$ C for 3 days, and then allowed to cool to room temperature. The reaction mixture was added to H_2O (30 mL) and neutralised with 2 M HCl. The organic content was extracted into DCM (3×10 mL), washed with H_2O (3×10 mL) and brine (3×10 mL), then dried over $MgSO_4$. The drying agent was removed by filtration and the solvent removed *in vacuo* to give the *title compound* as a bright yellow solid (0.020 g, 0.06 mmol, 28 %). 1H NMR (400 MHz, $CDCl_3$) δ_H = 8.50 (1H, d, $^3J_{HH}$ = 7.303 Hz, CH), 8.45 (1H, d, $^3J_{HH}$ = 8.243 Hz, CH), 8.35 (1H, d, $^3J_{HH}$ = 8.353 Hz, CH), 7.63 (1H, m, 7.66-7.60 Hz, $CH(CH)_2$), 7.16 (1H, d, $^3J_{HH}$ = 7.95 Hz, CH), 4.49 (2H, t, $^3J_{HH}$ = 7.07 Hz, $CH_2N(CO)_2$), 3.99-3.91 (4H, m, $2 \times CH_2O$), 3.24-3.14 (4H, m, $2 \times CH_2N$), 3.05 (2H, t, $^3J_{HH}$ = 7.21 Hz, CH_2SH) ppm. ^{13}C NMR (125 MHz, $CDCl_3$) δ_C = 164.3 (CO), 155.7 (CN), 132.7 (CH), 131.3 (CH), 130.2 (CH), 126.2 (CH), 125.9 (CH), 123.2 (CH), 117.0 (CH), 115.0 (CH), 67.0 (CH_2O), 53.5 ($CH_2N(CH_2)_2$), 39.5 ($CH_2N(CO)_2$), 35.7 (CH_2SH) ppm. LR-MS (ES+) found m/z 381.31, calculated m/z 381.07 for $[C_{18}H_{18}N_2O_3S+K]^+$. IR (ATP) ν = 2959 (CH), 2847 (CH), 1697 (amide CO), 1657 (amide CO), 1585, 1570, 1379, 1231 cm^{-1} . UV-vis ($CHCl_3$): λ_{max} ($\epsilon / L mol^{-1} cm^{-1}$) = 387(11160), 334(4020), 319(2880) nm. Emission ($CHCl_3$) λ_{em} = 501 nm (4.52 ns, $\chi^2 = 0.92$)

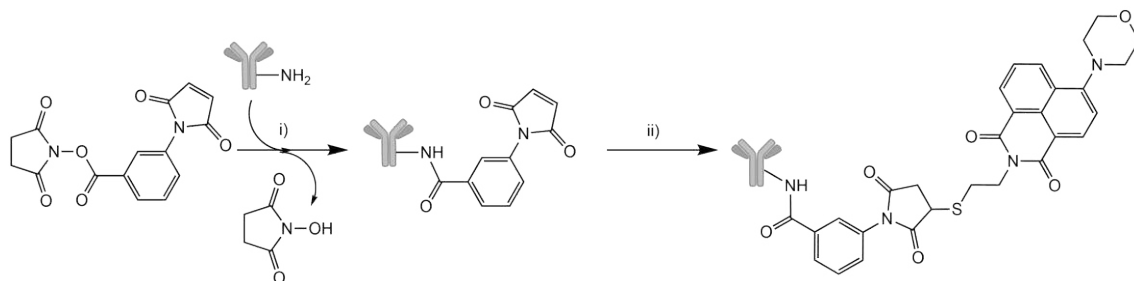


Figure 5. Simplified scheme for attempted labelling of trastuzumab with naphthalimide (**7**). i) 10 eq. MBS, pH 7.4 buffer. ii) 100 eq. naphthalimide probe (**12**), pH 7.4 buffer. F/P ratio for the antibody species is unknown.

Attempt to label trastuzumab with naphthalimide (7) (MBS mediated method)

Trastuzumab was dissolved in 0.1 M sodium phosphate, 0.15 M NaCl, pH 7.2 (0.5 mL, 10 mg.mL $^{-1}$). The crosslinker MBS (16.5 mg) was dissolved in DMSO (100 μ L), and 5 μ L was added to the antibody solution achieving an 80-fold excess. The microemulsion observed is typical of the use of MBS. The reaction mixture was mixed at room temperature for 1 h. The solution was applied to a PD-10 column equilibrated with 0.1 M sodium phosphate, 0.15 M NaCl, pH 7.2, and 0.5 mL fractions eluted using the same buffer. The concentration of the

protein was measured by monitoring absorbance at 280 nm, and the two most concentrated fractions were added together. The naphthalimide probe (**12**) was dissolved in DMSO at a concentration of 0.02 mg.mL⁻¹ and an appropriate volume added to the antibody solution to achieve a 100-fold excess over the protein. The mixture was mixed at room temperature overnight, before purification on a PD-10 column using 0.1 M sodium phosphate, 0.15 M NaCl, pH 7.4. By monitoring the absorbance at 280 nm, the most concentrated fraction was determined and analysed by UV-vis and fluorescence analysis. Emission (H₂O) λ_{em} = 540 nm.

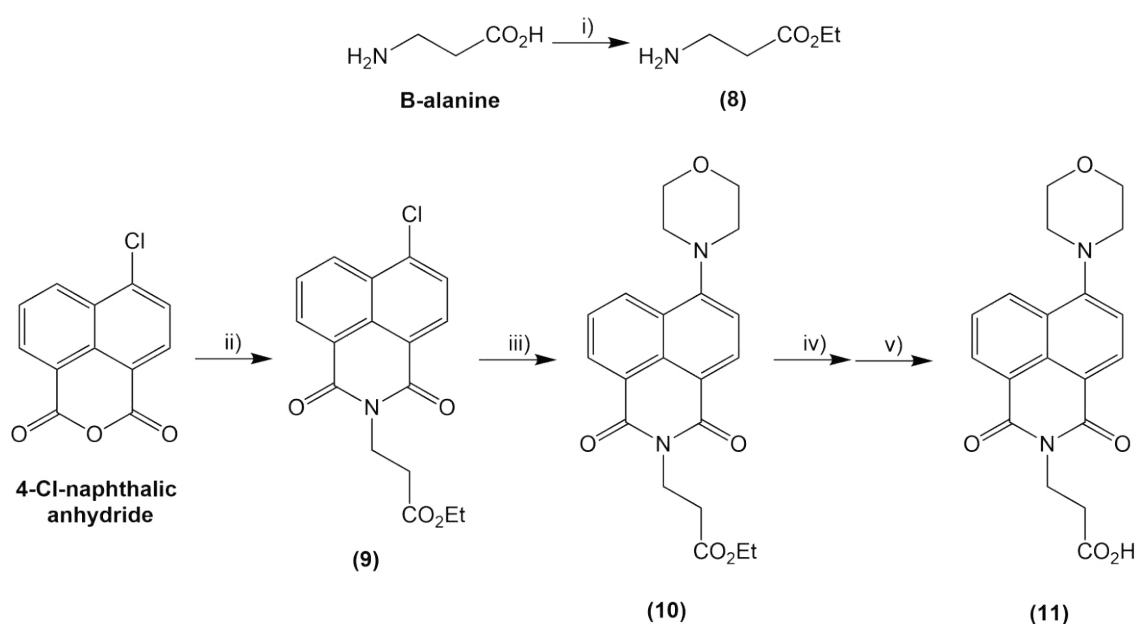


Figure 6. Synthetic scheme for naphthalimides (**9**), (**10**) and (**11**). i) EtOH, SOCl₂, RT, 2 h. ii) 2 eq. (**13**), EtOH, NEt₃, reflux, 24 h. iii) 4 eq. morpholine, DMSO, 90 °C, 72 h. iv) NaOH, acetone, RT, 24 h. v) 2 M HCl, H₂O, RT, 10 min.

*β -alanine ethyl ester (**8**)*

β -alanine (1.016 g, 11.4 mmol) was suspended in cold EtOH (50 mL). SOCl₂ (10 mL) was added dropwise with stirring. The reaction mixture was observed to become clear, and was allowed to come to room temperature, then stirred for 2 h. The solvent was removed under reduced pressure, and the beige solid recrystallised from hot EtOH. The solid was collected by filtration, washed with cold Et₂O (3 × 5 mL) and dried *in vacuo* to give the *title compound* as a white solid (0.901 g, 7.68 mmol, 67 %). ¹H NMR (400 MHz, CDCl₃) δ_H = 8.11 (2H, br s, NH₂), 4.10 (2H, q, ³J_{HH} = 7.38 Hz, CH₂CH₃), 3.30 (2H, t, ³J_{HH} = 6.83 Hz, CH₂NH₂), 2.86 (2H, t, ³J_{HH} = 6.83 Hz, CH₂CO₂Et), 1.20 (3H, t, ³J_{HH} = 7.54 Hz, CH₃CH₂) ppm. ¹³C NMR (100 MHz, CDCl₃) δ_C = 171.3 (CO₂Et), 61.4 (CH₂CH₃), 35.6 (CH₂NH₂), 31.3 (CH₂CO₂),

14.4 (CH₃) ppm. HR-MS (EI+) found m/z 117.0788, calculated m/z 117.0790 for [C₅H₁₁NO₂]⁺.

4-Chloro-(N-(3-ethylpropanoate))-1, 8-naphthalimide (9)

β-alanine ethyl ester (**8**) (0.600 g, 5.16 mmol), 4-chloro-naphthalic anhydride (0.600 g, 2.58 mmol) and NEt₃ (1.08 mL, 7.74 mmol) were added to EtOH (15 mL) under N₂. The reaction mixture was heated to reflux for 24 h, and seen to turn bright orange. The reaction was cooled to room temperature, and a yellow precipitate collected by filtration. The solid was washed with cold EtOH (3 × 5 mL) and cold Et₂O (3 × 5 mL), then dried *in vacuo* to give the *title compound* as a yellow solid (0.695 g, 2.10 mmol, 81 %). ¹H NMR (400 MHz, CDCl₃) δ_H = 8.62-8.50 (2H, m, 2 × CH), 8.44 (1H, d, ³J_{HH} = 8.10 Hz, CH), 7.84-7.73 (2H, m, 2 × CH), 4.41 (2H, t, ³J_{HH} = 7.56 Hz, CH₂N), 4.08 (2H, q, ³J_{HH} = 7.13 Hz, CH₂CH₃), 2.69 (2H, t, ³J_{HH} = 7.12 Hz, CH₂CO₂), 1.16 (3H, t, ³J_{HH} = 7.00 Hz, CH₃CH₂) ppm. ¹³C NMR (100 MHz, CDCl₃) δ_C = 171.4 (CO₂Et), 163.5 (CO), 139.3 (CCl), 132.2 (CH), 131.2 (CH), 129.4 (CH), 127.8 (CH), 127.4 (CH), 122.9 (CCH), 121.5 (CCH), 60.8 (CH₂CH₃), 36.2 (CH₂N), 32.9 (CH₂CO₂), 14.2 (CH₃) ppm. HR-MS (ES+) found m/z 332.0696, calculated m/z 332.0690 for [C₁₇H₁₅NO₄Cl]⁺. IR (ATP) ν = 1714, 1699 (amide CO), 1661 (amide CO), 1587, 1573, 1502, 1342, 1259, 1201, 1014, 783 cm⁻¹. UV-vis (CHCl₃): λ_{max} (ε / L mol⁻¹ cm⁻¹) = 359(13240), 343(16200), 327(10740) nm. Emission (CHCl₃) λ_{em} = 501 nm (8.96 ns, χ² = 1.05).

4-Morpholino-(N-(3-ethylpropanoate))-1, 8-naphthalimide (10)

Naphthalimide (**9**) (0.600 g, 1.81 mmol) and morpholine (0.62 mL, 7.23 mmol) were added to DMSO (3 mL) under N₂, and the reaction mixture heated to 90 °C for 72 h. The reaction mixture was cooled and diluted with H₂O (30 mL). The solution was neutralised with 1 M HCl. The yellow precipitate was collected by filtration, washed with cold H₂O (3 × 5 mL), then dissolved in DCM (20 mL). The organic solution was washed with H₂O (3 × 10 mL), brine (3 × 10 mL), and then dried over Na₂SO₄. The solvent was removed under reduced pressure and precipitate recrystallised from hot EtOH to give the *title compound* as a yellow solid. (0.420 g, 1.10 mmol, 61 %). ¹H NMR (400 MHz, CDCl₃) δ_H = 8.54-8.50 (1H, m, CH), 8.47 (1H, d, ³J_{HH} = 9.79 Hz, CH), 8.36 (1H, d, ³J_{HH} = 9.79 Hz, CH), 7.67-7.61 (1H, m, CH), 7.17 (1H, d, ³J_{HH} = 8.16 Hz, CH), 4.42 (2H, t, ³J_{HH} = 7.34 Hz, CH₂N), 4.08 (2H, q, ³J_{HH} = 7.07 Hz, CH₂CH₃), 3.95 (4H, m, 2 × CH₂O), 3.20 (4H, m, 2 × CH₂N), 2.68 (2H, t, ³J_{HH} = 7.34 Hz, CH₂CO₂), 1.16 (3H, t, ³J_{HH} = 7.35 Hz, CH₃CH₂) ppm. ¹³C NMR (100 MHz, CDCl₃) δ_C = 171.4 (CO₂Et), 164.3 (CO), 163.8 (CO), 155.8 (CN(CH₂)₂), 132.7 (CH), 131.3 (CH), 130.2 (CH), 130.0 (CH), 126.2 (CH), 125.9 (C=C), 123.1 (C=C), 117.0 (C=C), 115.0 (C=C), 67.0 ((CH₂)₂O), 58.0 (CH₂CH₃), 53.4 ((CH₂)₂N), 36.0 (CH₂N), 32.8 (CH₂), 14.2 (CH₃) ppm.

HR-MS (ES+) found m/z 383.1590, calculated m/z 383.1607 for $[C_{21}H_{23}N_2O_5]^+$. IR (ATP) $\nu = 2970, 2818, 1718, 1687$ (amide CO), 1651 (amide CO), 1586, 1514, 1352, 1195 (CO), 1113 (CO), 1024 cm^{-1} . UV-vis ($CHCl_3$): λ_{max} ($\epsilon / L\text{ mol}^{-1}\text{ cm}^{-1}$) = 395(11400), 343(3700), 328(2160) nm. Emission ($CHCl_3$) $\lambda_{em} = 501\text{ nm}$ (8.84 ns, $\chi^2 = 0.98$).

4-Morpholino-(N-(3-propanoic acid))-1, 8-naphthalimide (11)

Naphthalimide (**10**) (0.400 g, 1.05 mmol) was dissolved in acetone (10 mL). 1 M NaOH (3 mL) was added dropwise and the solution stirred at room temperature for 24 h. The reaction mixture was placed in the freezer for 1 h. The yellow precipitate was collected by filtration and washed with cold 95:5 acetone:water ($3 \times 5\text{ mL}$). The yellow solid was dissolved in H_2O (10 mL) and washed with $CHCl_3$ ($3 \times 5\text{ mL}$). The aqueous fraction was acidified with 2 M HCl, and a yellow precipitate seen to form. This was collected by filtration, and washed with fresh H_2O ($3 \times 5\text{ mL}$) and cold EtOH ($3 \times 5\text{ mL}$). The solid was dried *in vacuo* to give the *title compound* as a yellow solid (0.257 g, 0.726 mmol, 69 %). 1H NMR (400 MHz, $CDCl_3$) $\delta_H = 8/50$ -8.43 (2H, m, $2 \times CH$), 8.39 (1H, d, $^3J_{HH} = 8.40\text{ Hz}$, CH), 7.84-7.75 (1H, m, CH), 7.34 (1H, d, $^3J_{HH} = 8.40\text{ Hz}$, CH), 4.20-4.10 (2H, m, CH_2N), 3.97-3.87 (4H, m, $2 \times CH_2O$), 3.27-3.17 (4H, m, $2 \times CH_2N$), 2.25-2.18 (2H, m, CH_2CO_2H) ppm. ^{13}C NMR (100 MHz, $CDCl_3$) $\delta_C = 173.0$ (CO_2H), 163.9 (CO), 163.4 (CO), 156.0 ($CN(CH_2)_2$), 132.7 (CH), 131.1 (CH), 129.7 (CH), 126.6 (CH), 125.8 (CH), 123.0 (C=C), 116.3 (C=C), 115.6 (C=C), 66.7 (CH_2O), 53.5 (CH_2N), 36.1 (CH_2N), 32.8 (CH_2CO_2H) ppm. HR-MS (ES+) found m/z 355.1283, calculated m/z 355.1294 for $[C_{19}H_{19}N_2O_5]^+$. IR (ATP) $\nu = 2982$ (br, CO_2H), 1734, 1687 (amide CO), 1645 (amide CO), 1576, 1510, 1358, 1177, 1098, 1029 cm^{-1} . UV-vis (H_2O): λ_{max} ($\epsilon / L\text{ mol}^{-1}\text{ cm}^{-1}$) = 395(7740), 346(3480), 331(2460) nm. Emission (H_2O) $\lambda_{em} = 506\text{ nm}$ (3.79 ns, $\chi^2 = 0.95$).

Attempt to label trastuzumab with naphthalimide (11) (EDC, sulfo-NHS mediated method)

Trastuzumab was dissolved in 0.1 M sodium phosphate, 0.15 M NaCl, pH 7.4 (0.5 mL, 10 $mg \cdot mL^{-1}$). The naphthalimide probe (**11**) was dissolved in 0.1 M sodium phosphate, 0.15 M NaCl, pH 7.4 (2.5 $mg \cdot mL^{-1}$). 100 μL of the probe solution was added to the antibody solution, yielding a 10 fold excess of dye to antibody. EDC (16 mg, 0.10 mmol) was added to 0.1 M sodium phosphate, 0.15 M NaCl, pH 7.4 (1 mL). 10 μL was taken and added to the reaction mixture and mixed, achieving a 12 fold excess over the antibody. Sulfo-NHS (10.8 mg, 5×10^{-5} mmol) was added to 0.1 M sodium phosphate, 0.15 M NaCl, pH 7.4 (0.1 mL). 10 μL was taken and added to the reaction mixture to achieve a 120 fold excess over the antibody. The reaction mixture was mixed by gentle inversion at room temperature for 2 h. Purification was achieved by use of a PD-10 size exclusion chromatography column. The column was

equilibrated with 0.1 M sodium phosphate, 0.15 M NaCl, pH 7.4, the reaction mixture applied, and fractions of 0.5 mL were collected using the same buffer as an eluent. Absorbance at 280 nm was measured to isolate the protein-containing fractions. These fractions were collected and concentrated using a 10,000 MWCO protein concentrator spin column. At antibody concentrations of 6.57 mg.mL⁻¹ as determined from A₂₈₀, the solution was colourless to the naked eye, and no absorbance was measured in the UV-vis spectrum between 300-400 nm. Labelling was not observed to occur to any appreciable degree.

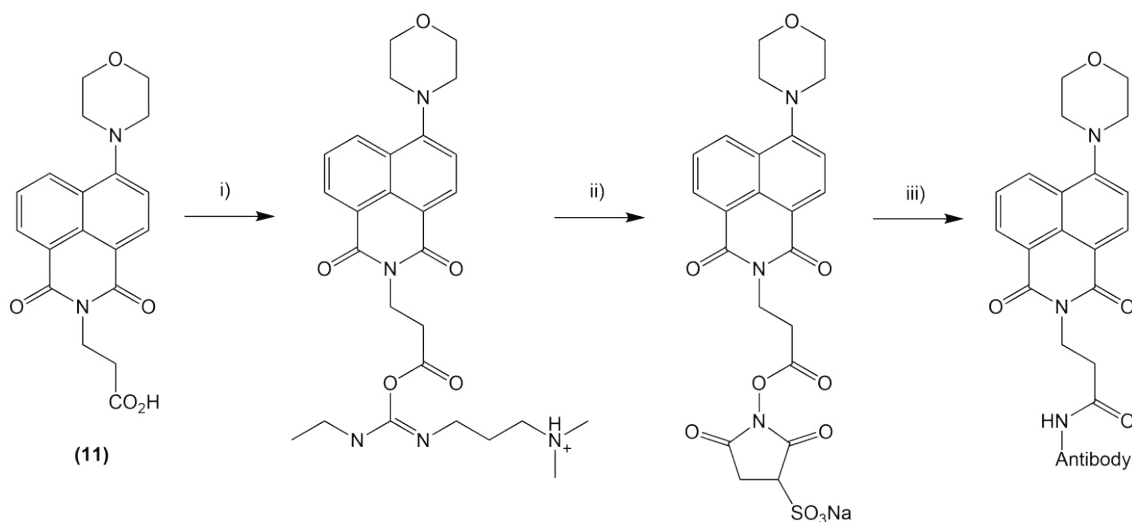


Figure 7. Simplified scheme for attempted labelling of trastuzumab with naphthalimide (11). i) 1.2 eq EDC, pH 7.4 buffer. ii) 12 eq. sulfo-NHS, pH 7.4 buffer. iii) 0.1 eq. amine bearing trastuzumab, pH 7.4 buffer. This last step was not observed to occur.

1.4 Results and discussion

1.4.1 Direct labelling of nanoparticles

Initial experiments were intended as a proof of concept that 1,8-naphthalimides could be immobilised directly onto the surface of nanoparticles and could be observed spectroscopically. Heating a suspension of APTES@SPION and 1,8-naphthalic anhydride in DMF allowed the isolation of a black solid (**1**), showing a sharp peak in the IR spectrum at 1698 cm^{-1} that could be unequivocally assigned to the naphthalimide carboxyl stretches. Concerns that this may be adsorbed 1,8-naphthalic anhydride or residual starting material were assuaged by the presence of an absorbance maxima at 345 nm in the UV-vis spectrum (Fig. 8) and by the emission maxima at 400 nm in the excitation emission spectrum (Fig. 9) which is indicative of naphthalimide formation. However, this experiment had several drawbacks not least of which was the lack of control over the degree of labelling. An approximately 1100-fold excess of the anhydride was used but the observed fluorescence was weak and the degree of labelling cannot be determined from the absorbance spectra. In addition, the final product showed reduced solubility in aqueous conditions compared to the parent nanomaterial. It is likely that quenching occurred due to fluorophore-fluorophore interaction that reduced the observed fluorescence intensity below what would be expected; saturation of the nanoparticle surface with hydrophobic fluorophores would also explain reduced aqueous solubility.

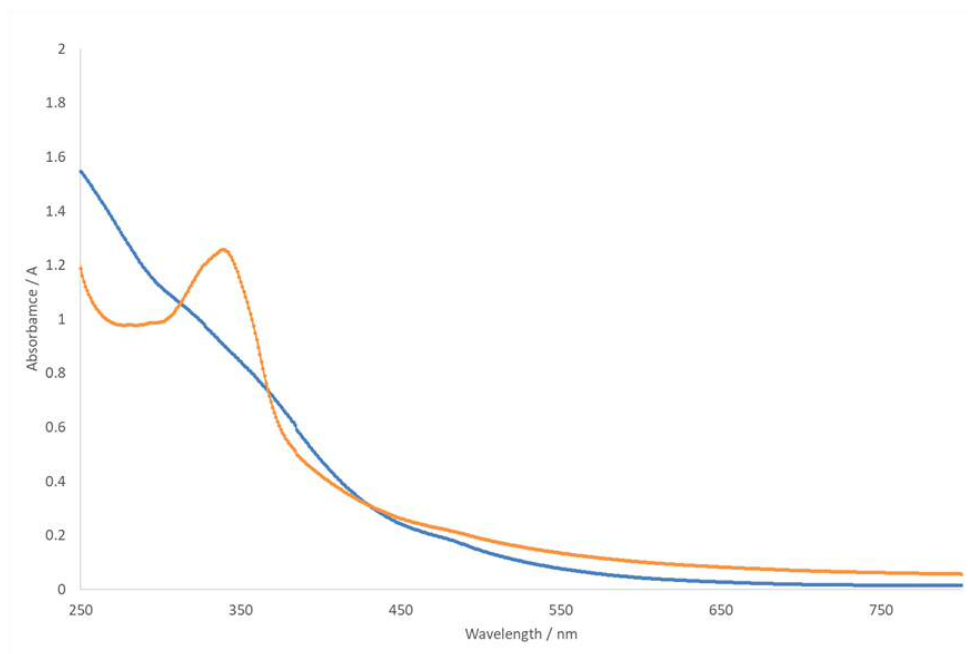


Figure 8. Absorbance spectra of naphthalimide labelled APTES@SPION (orange) and unlabelled APTES@SPION (blue).

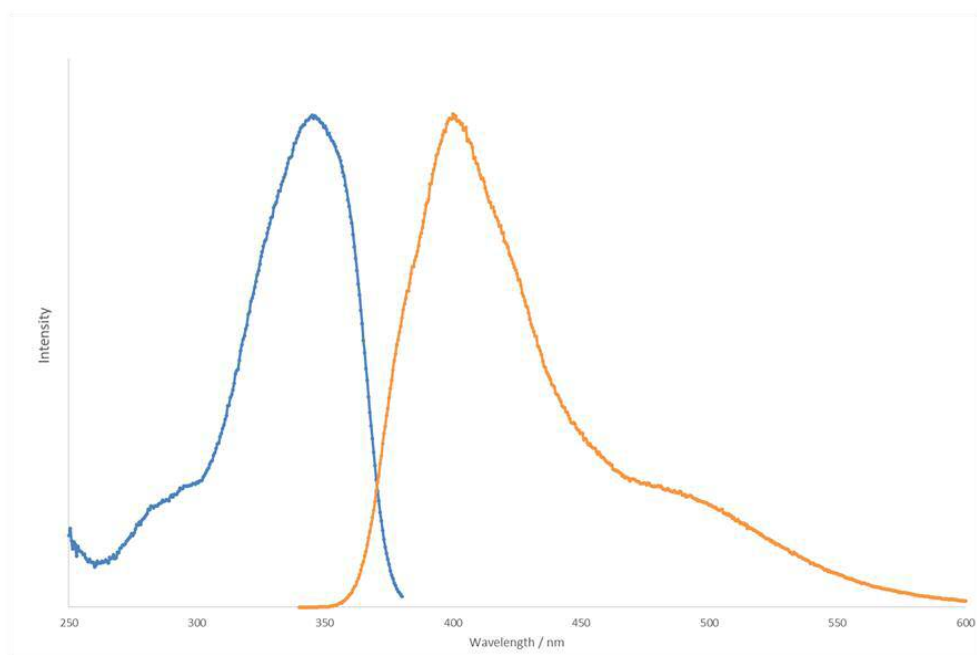


Figure 9. Excitation (blue) and emission (orange) spectra for naphthalimide-labelled APTES@SPION.

1.4.2 Naphthalimide derivatives of APTES

One method of controlling the degree of labelling of directly labelled nanoparticles would be to incorporate naphthalimide-bearing derivatives of APTES in an appropriate quantity into the coating step of the nanoparticle synthesis. For the photophysical reasons discussed in the introduction to this section, it would be desirable for such a naphthalimide to be functionalised in the 3- or 4- position. In addition to the effect this would have on the Stokes shift of the species, it could also be an opportunity to counteract the inherent hydrophobicity of the naphthalimide core by introducing a polar character to the molecule. The PEG-like species **2**, 2,2'-ethylenedioxybisethylamine would be an ideal species for this task (see Fig. 10).

The initial reaction between the anhydride and APTES occurred giving a yellow solid (**2**) in satisfactory yield. Peaks in the NMR spectrum above 7 ppm were similar to those reported in the literature for similar naphthalimide species and integrated well with respect to peaks at 4.07, 3.74, 1.82-1.71 and 1.13 ppm pertaining to the APTES-like fragment of the molecule. All other spectroscopic and spectrometric methods supported the conclusion that the reaction had occurred as expected. However, a subsequent reaction between the chloro-bearing species (**2**) and 2,2'-ethylenedioxybisethylamine gave a mixture of species that could not be satisfactorily separated by chromatographic methods.

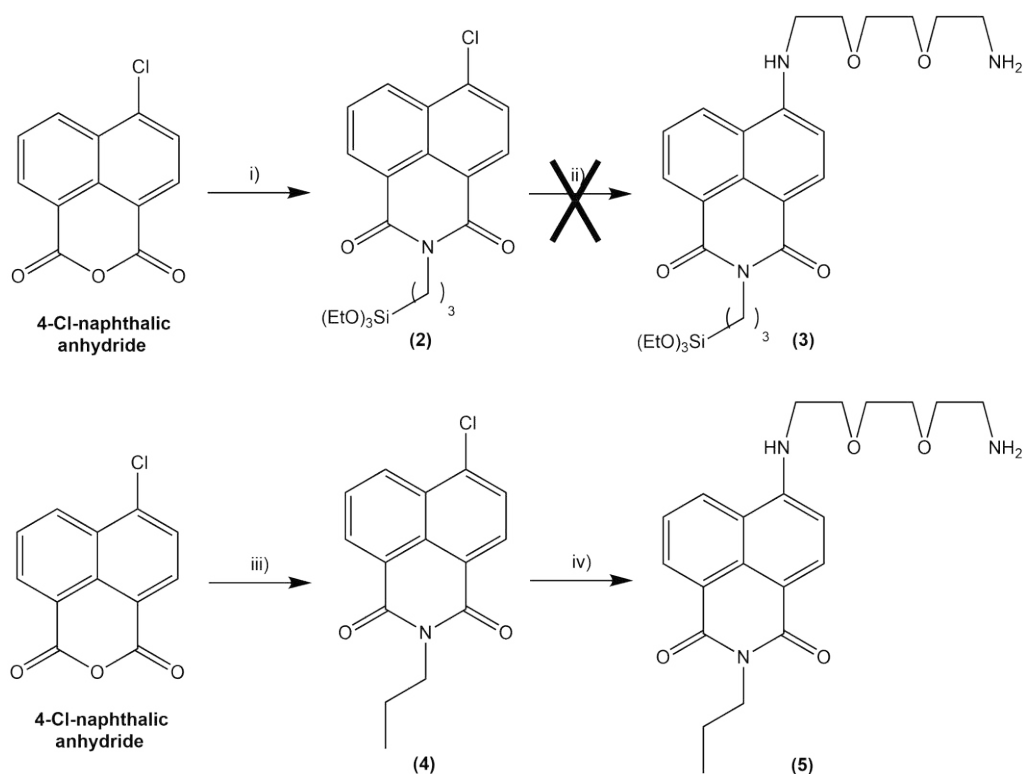


Figure 10. Synthetic schemes for naphthalimides **(2)**, **(4)** and **(5)**. The presence of hydrolysable ethoxy groups prevent the isolation of species **(3)**. i) 2 eq. APTES, EtOH, reflux, 24 h. ii) 10 eq. 2,2'-ethylenedioxybisethylamine, DMSO, 80 °C, 5 days. iii) 2 eq. Propylamine, EtOH, reflux, 24 h. iv) 10 eq. 2,2'-ethylenedioxybisethylamine, DMSO, 80 °C, 5 days.

The naphthalimide species **(4)** and **(5)** shown in Fig. 10 were synthesised in an attempt to clarify whether the failure to isolate the naphthalimide **(3)** was due to hydrolysis of the ethoxysilyl groups or due to other factors. Propylamine was chosen for its structural similarity to APTES. As the synthesis of species **(5)** occurred without issue and yielded a satisfactory quantity of the pure compound as a yellow solid, it was concluded that hydrolysis of the ethoxysilyl groups of species **(2)** occurs as a side-reaction to the functionalisation of the naphthalimide ring. Thin layer chromatography showed more than the four species that would result from partial hydrolysis (Fig. 11a below) and it may be concluded that additional side reactions also occur e.g. cross-reaction to form dimers or polymeric species.

Although dried DMSO was used in the attempt to synthesise **(3)** and every effort was taken to exclude moisture from the glassware employed, it is likely that given the long reaction time and elevated temperatures employed, the sensitivity of the ethoxysilyl groups to trace amounts of water was too great to prevent hydrolysis. Future work on this concept would focus either on alternative methods to preclude hydrolysis, to re-instate the ethoxy groups post hydrolysis, or alternatively to focus on the use of the species formed by reaction between

APTES and 1, 8-naphthalic anhydride (Fig. 11b below). Although this species would not allow for the tuning of its photophysical characteristics, it would still allow for a degree of control over the labelling of APTES@SPION.

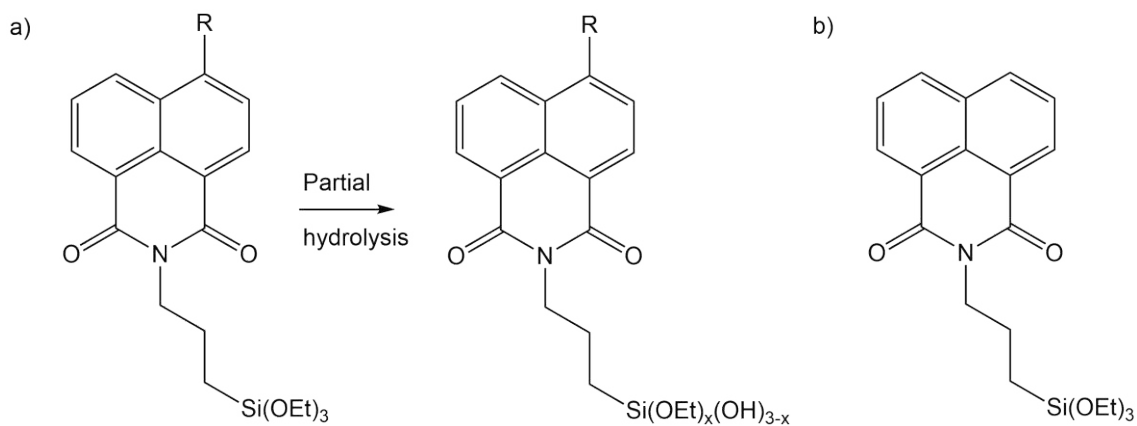


Figure 11a. Partial hydrolysis would lead to 4 potential end species; side reactions are proposed to be occurring in addition to this. **b.** Although this species will not have the Stokes shift associated with its functionalised derivatives, its use would offer better control in comparison to the direct reaction between the anhydride and the nanoparticles.

1.4.3 Naphthalimides for bioconjugation

Thiol bearing naphthalimides (6) and (7)

The labelling of antibodies with fluorescent dyes is a common and well-understood area of research, with a multitude of activated species available commercially. As seen in bioconjugation in general, the approaches most commonly employed include amine-to-thiol and amine-to-acid crosslinking and often require a suitable activating or crosslinking agent. The thiol-bearing naphthalimides **(6)** and **(7)** (see Fig. 12) were synthesised for the purpose of achieving amine-to-thiol linking with amine groups on Trastuzumab. It has been shown from the FITC-labelling described in Chapter 4 of this work that there are multiple amines present on the antibody that are able to react. The inclusion of a morpholine group was based upon the requirement for an amine group in the 4-position of the naphthalimide system (for photophysical characteristics) and the need for such a moiety to have a reasonably polar nature (to aid in solubility of the dye and of any conjugate species). A morpholine-moiety has previously been reported in a similar species by Langdon-Jones *et al.*⁷, and of the seven analogues described in that work the morpholine-bearing species was shown to have the largest Stokes shift (130 nm).

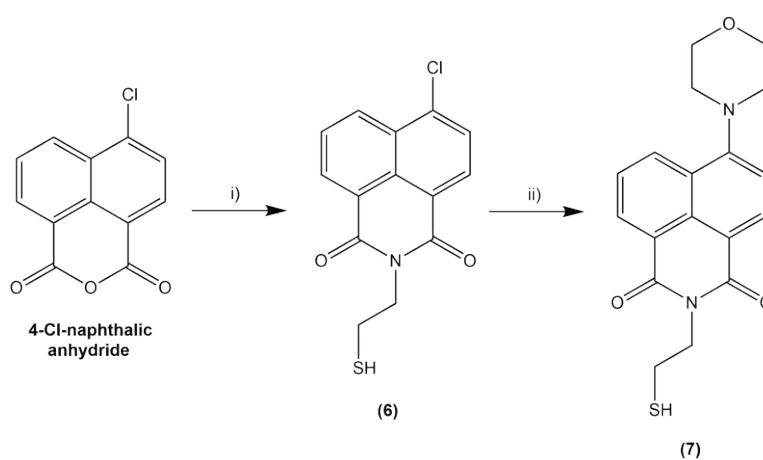


Figure 12. Synthetic scheme for naphthalimides **(6)** and **(7)**. i) 2 eq. 2-aminoethanethiol hydrochloride, 4 eq. NEt_3 , EtOH, reflux, 24. ii) 4 eq. morpholine, DMSO, 95 °C, 72 h.

The spectra below (Figs. 13 and 14) show naphthalimide **(6)** had an absorbance maxima of 344 nm and an emission maxima of 519 nm (a Stokes shift of 175 nm), while naphthalimide **(7)** had an absorbance maxima of 387 nm and an emission maxima of 501 nm (a Stokes shift of 114 nm). Species **(7)** fluoresces with a significantly increased lifetime (4.52 ns, $\chi^2 = 0.92$) compared to **(6)** (2.64 ns, $\chi^2 = 0.93$). Photophysically, both would be suitable for use in bioconjugation but the increased lifetime of **(7)** would aid in the differentiation of dye and

background autofluorescence, hence the morpholine bearing species would be the preferred candidate.

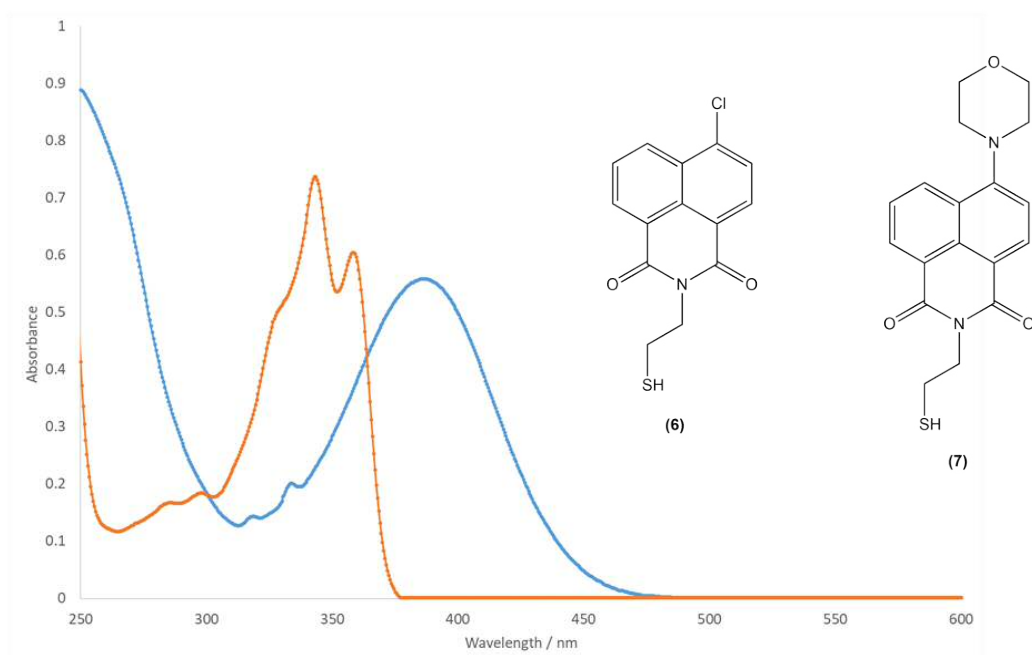


Figure 13. Absorbance spectra of thiol-bearing naphthalimides (6) (orange) and (7) (blue).

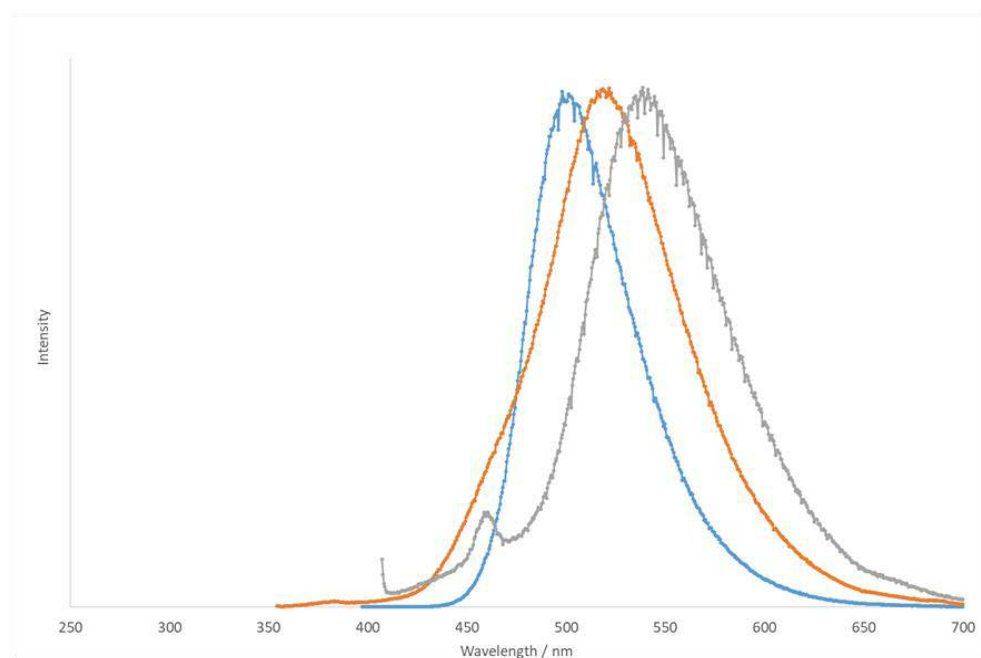


Figure 14. Emission spectra of thiol-bearing naphthalimides (6) (orange) and (7) (blue) and trastuzumab labelled with (7) (grey).

The monoclonal antibody trastuzumab has been discussed in detail in Chapters 3 and 4 of the current work, and was labelled with FITC for use in *in vitro* FACS analysis. The thiol-

bearing species (**7**) has a larger Stokes shift than FITC (114 nm compared to 25 nm respectively), and has a comparable lifetime when free (4.52 ns versus approximately 4.1 ns). Coupling of (**7**) to trastuzumab using an amine-to-thiol cross linker MBS was attempted to explore the potential of the naphthalimide in a bioconjugation context.

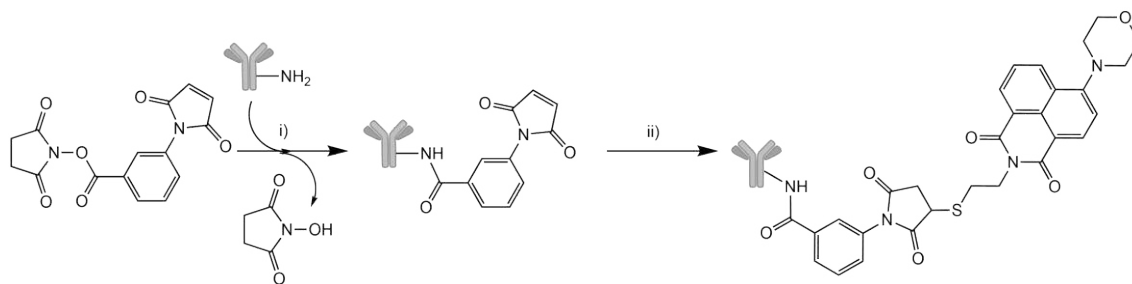


Figure 15. Simplified scheme for the attempted labelling of trastuzumab with naphthalimide (**7**). i) 10 eq. MBS, pH 7.4 buffer. ii) 100 eq. naphthalimide probe (**12**), pH 7.4 buffer. F/P ratio for the antibody species is unknown.

The MBS-mediated coupling shown in Fig. 15 was based on a procedure described by Hermanson.¹ Although not optimised for the experiment, such an approach is typically successful in labelling antibodies. Purification and concentration gave an aqueous sample that had a measurable absorbance at 280 nm, confirming the presence of the antibody, but a value for A_{350} for the fluorophore could not be measured despite an initial excess of 100 fluorophores per protein. The F/P ratio could not be determined for this species. An emission at 540 nm was measured and is shown in Fig. 14 but the solution was at that point too dilute to allow measurement of fluorescence lifetime. The increase in the emission maxima from 501 nm when free to 540 nm confirms the labelling of the antibody. The limited success of this approach suggests that a side reaction is occurring to limit fluorescent labelling e.g. degradation of the maleimide intermediate or cross-linking between monomers of the antibody. Future studies could focus on overcoming these to improve labelling efficiency.

Carboxylic acid bearing naphthalimide (11)

The sequential synthesis of (8), (9), (10) and finally deprotection was intended to yield the carboxylic acid bearing naphthalimide (11) (see Fig. 16) that would offer nearly identical photophysical characteristics to the thiol-bearing species discussed above but which could be attached to an antibody using a different and hopefully more efficient methodology. Characterisation of all species was performed by ^1H NMR, ^{13}C NMR, HR-MS and IR, confirming the nature of all species. Suitable crystals (see Fig. 17) for structure determination for (9) and (10) were obtained by the slow diffusion of ethyl acetate into an ether solution, and by slow diffusion of hexane into an ethyl acetate solution respectively. Data collection parameters are given as Appendix III.

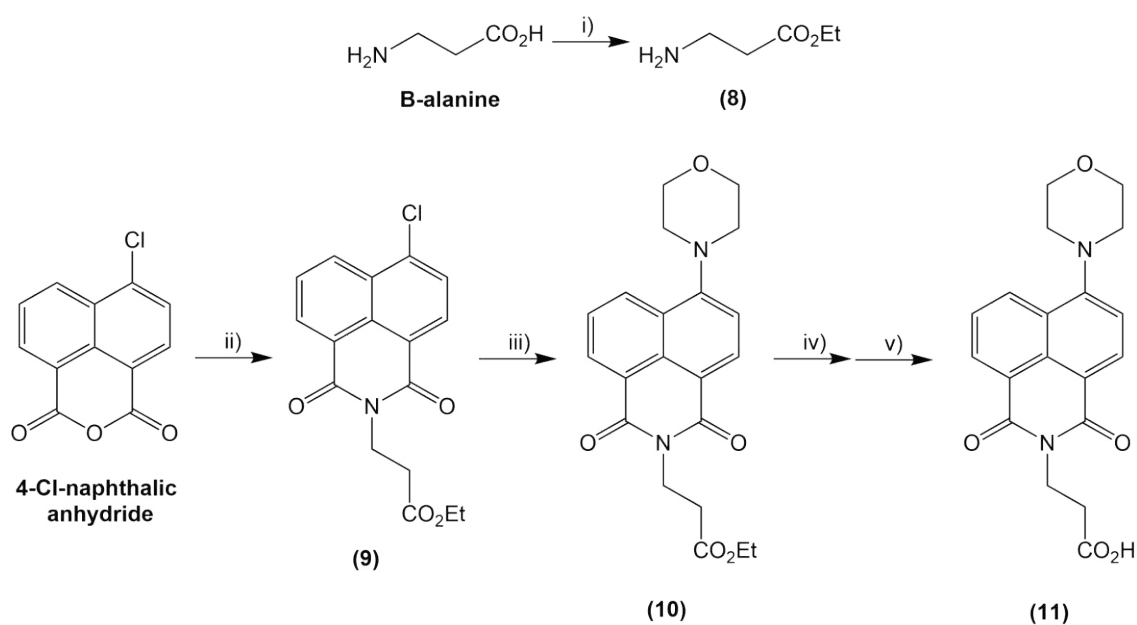


Figure 16. Synthetic scheme for naphthalimides (9), (10) and (11). i) EtOH, SOCl_2 , RT, 2 h. ii) 2 eq. (13), EtOH, NEt_3 , reflux, 24 h. iii) 4 eq. morpholine, DMSO, 90 °C, 72 h. iv) NaOH, acetone, RT, 24 h. v) 2 M HCl, H_2O , RT, 10 min.

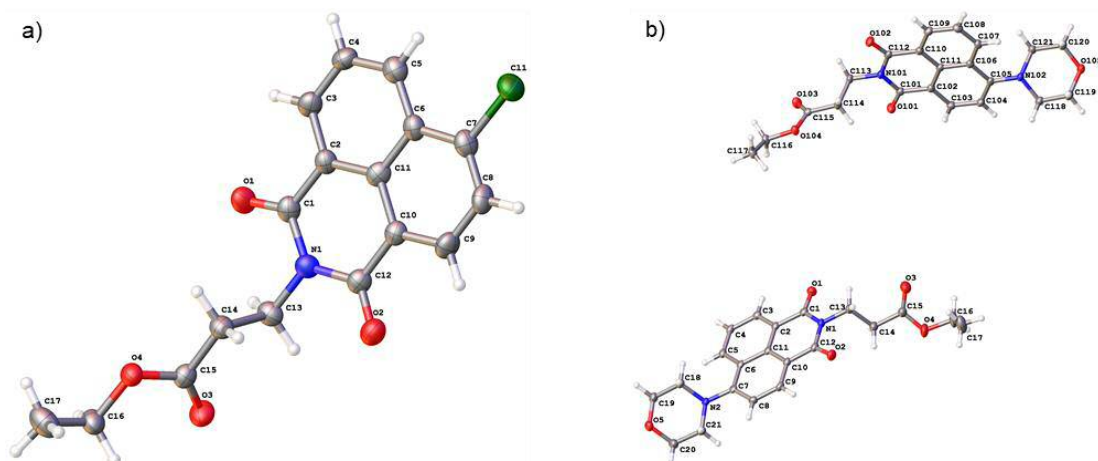


Figure 17a. X-Ray crystal structure of naphthalimide (**9**) with ellipsoids at 50 % occupancy. **b.** X-Ray crystal structure of naphthalimide (**10**) showing a dimeric arrangement with ellipsoids at 50 % occupancy.

UV-vis studies of the naphthalimides (Fig. 18) show that (**9**) has a near identical absorbance profile to its analogue species (**6**) as expected because the functional groups attached to the nitrogen of the ring are known to have little effect on the photophysical properties of the molecule as a whole.³ The ethyl ester protected species (**10**) and its deprotected acid analogue (**11**) both have absorbance maxima at 395 nm. Exciting at this wavelength gives the emission spectra shown in Fig. 19. The free acid species (**11**) has an emission maxima at 506 nm (corresponding to a Stokes shift of 111 nm) with a lifetime of 3.79 ns ($\chi^2 = 0.95$) in water, marginally shorter than that reported for the commercially available naphthalimide dye Lucifer yellow.⁸ The photophysical characteristics of this species show it to be suitable for use as a fluorophore in bioconjugation.

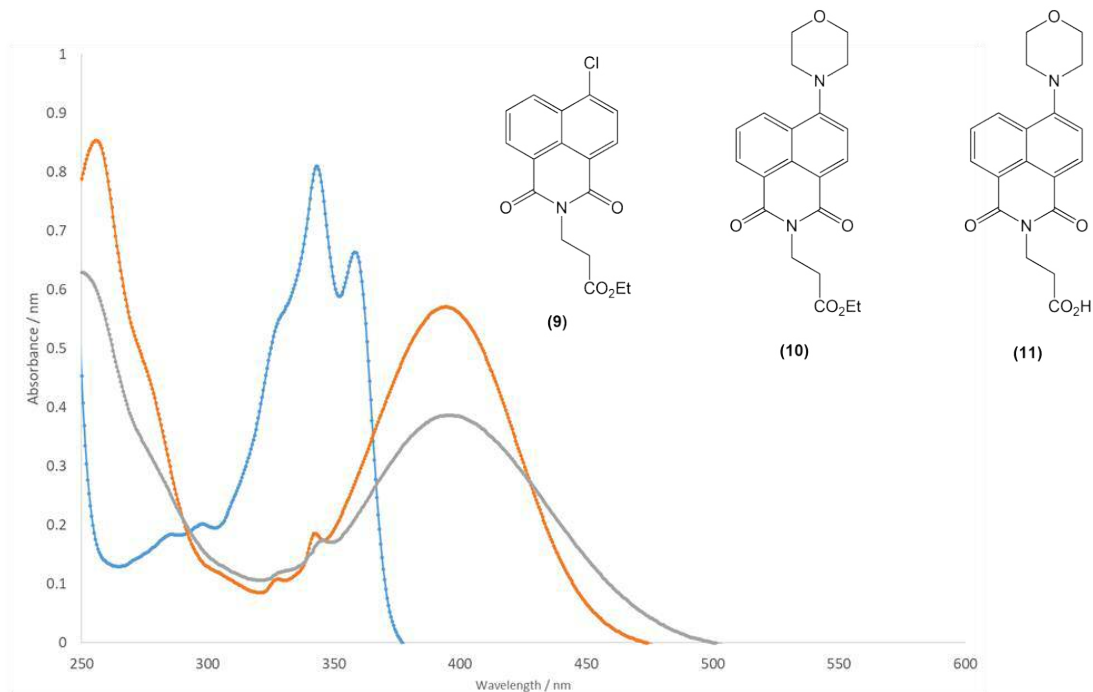


Figure 18. Absorbance spectra of naphthalimide species (9) (blue), (10) (orange) and the deprotected species (11) (grey).

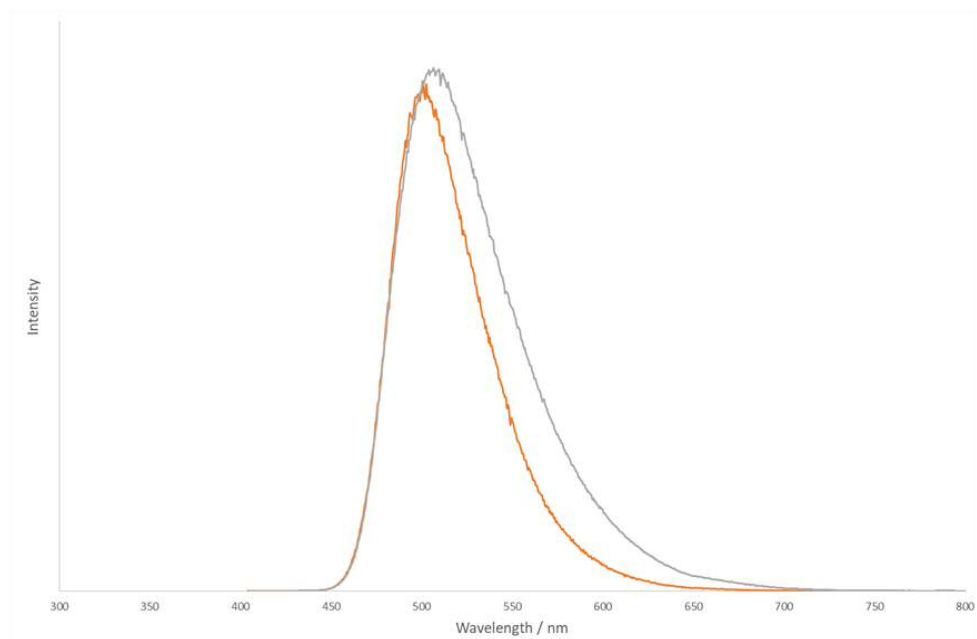


Figure 19. Emission spectra of protected naphthalimide (10) (orange) and its deprotected free acid analogue (11) (grey).

Coupling between the carboxylic acid group of naphthalimide (11) and amine groups on trastuzumab was attempted using a general approach described in Hermanson¹ for amine-acid linking by use of sulfo-NHS and EDC (see Fig. 20).

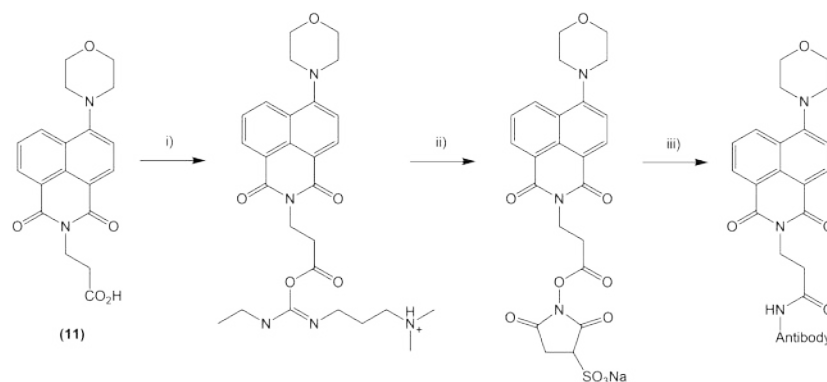


Figure 20. Simplified scheme for attempted labelling of trastuzumab with naphthalimide (11). i) 1.2 eq EDC, pH 7.4 buffer. ii) 12 eq. sulfo-NHS, pH 7.4 buffer. iii) 0.1 eq. amine bearing trastuzumab, pH 7.4 buffer. This last step was not observed to occur.

In theory, reaction between the acid and EDC and then sulfo-NHS yields a water-soluble activated ester intermediate that is reasonably stable to hydrolysis and reactive to amines. However, despite the fluorophore being in tenfold excess to the protein and the EDC and sulfo-NHS being in even greater excess as described by the protocol, isolation of the antibody following the experiment yielded a sample that had significant absorbance at 280 nm (corresponding to an antibody concentration of approximately 6.57 mg.mL⁻¹) but which did not show absorbance at 395 nm, was not seen to be coloured and did not fluoresce. Fluorescent labelling had not occurred to an observable degree. Although this may be due in part to suboptimal reaction conditions for the probe, the similarity in outcome to the experiment described for the thiol-bearing naphthalimide (7) suggests that there may be an intrinsic issue arising from the naphthalimide core used in both of these experiments. The hydrophobic naphthalimide ring system may be showing a propensity to π -stacking in aqueous solution that limits the ability of the probes to react with functional groups on protein molecules. The use of more hydrophilic alternatives (such as Lucifer yellow derivatives) may be required to introduce a naphthalimide to Trastuzumab.

1.5 Conclusion

Several novel naphthalimide species were synthesised and characterised in an effort to produce an alternative to commercial dyes for use in bioconjugation. Thiol- and acid-bearing naphthalimides were used in attempts to label the clinically used antibody Trastuzumab with limited success. The amine-to-thiol linking method described above showed the most promise; although an F/P ratio could not be determined, the conjugate did at least fluoresce. It would be interesting to determine whether changing the morpholine functionality for a more hydrophilic species would improve the outcome of similar future experiments.

1.6 References

- 1 G. T. Hermanson, *Bioconjugate Techniques*, Academic Press, London ; Waltham, MA, 3rd edition., 2013.
- 2 I. Ott, Y. Xu, J. Liu, M. Kokoschka, M. Harlos, W. S. Sheldrick and X. Qian, *Bioorg. Med. Chem.*, 2008, **16**, 7107–7116.
- 3 S. Banerjee, E. B. Veale, C. M. Phelan, S. A. Murphy, G. M. Tocci, L. J. Gillespie, D. O. Frimannsson, J. M. Kelly and T. Gunnlaugsson, *Chem. Soc. Rev.*, 2013, **42**, 1601–1618.
- 4 W. Jiang, J. Tang, Q. Qi, W. Wu, Y. Sun and D. Fu, *Dyes Pigments*, 2009, **80**, 11–16.
- 5 V. B. Bojinov and I. P. Panova, *Dyes Pigments*, 2009, **80**, 61–66.
- 6 E. E. Langdon-Jones, N. O. Symonds, S. E. Yates, A. J. Hayes, D. Lloyd, R. Williams, S. J. Coles, P. N. Horton and S. J. A. Pope, *Inorg. Chem.*, 2014, **53**, 3788–3797.
- 7 E. E. Langdon-Jones, D. Lloyd, A. J. Hayes, S. D. Wainwright, H. J. Mottram, S. J. Coles, P. N. Horton and S. J. A. Pope, *Inorg. Chem.*, 2015, **54**, 6606–6615.
- 8 'ISS Data Tables, Lifetime Data of Selected Fluorophores', http://www.iss.com/resources/reference/data_tables/LifetimeDataFluorophores.html, (accessed 30 August 2017).

Additional Experimental Section III - Small molecules arising from the study of bis(thiosemicarbazone) ligands and complexes

1.1 Introduction

In addition to the ligands and complexes described and characterised in Chapter 5, additional novel chemical species and observations arising from the current work are described below. They are not included in the main body of the report for a number of reasons, given in the relevant sections: either the work failed to achieve the desired result, did not yield a product that could be characterised sufficiently to allow conclusions to be drawn, or is of passing relevance to the main aims of the project.

1.2 Experimental

1.2.1 Materials and Methods

All reactions were performed with the use of vacuum line and Schlenk techniques. Reagents were commercial grade and were used without further purification. ^1H and $^{13}\text{C}\{-^1\text{H}\}$ NMR spectra were recorded on an NMR-FT Bruker 400 MHz or Joel Eclipse 300 MHz spectrometer and recorded in CDCl_3 , CD_3OD or $\text{d}^6\text{-DMSO}$. ^1H and $^{13}\text{C}\{-^1\text{H}\}$ NMR chemical shifts (δ) were determined relative to internal TMS and are given in ppm. Coupling constants J are given in hertz (Hz). Low- and high-resolution mass spectra were obtained using a Waters LCT Premier XE instrument and are reported as m/z (relative intensity). IR spectra are recorded as solid samples on a Shimadzu IRAffinity-1 FTIR spectrometer. UV-Vis studies were performed on a Jasco V-570 spectrophotometer as MeCN solutions (5×10^{-5} M) except where stated.

1.2.2 Synthesis and analytical techniques

Attempted deprotection of H_2L^1

H_2L^1 (0.100 g, 0.25 mmol) was suspended in THF (5 mL). NaOH (0.060 g, 1.5 mmol) was dissolved in H_2O (5 mL) and added dropwise over 10 minutes. Upon the first addition, the solution turned bright yellow, and throughout the addition the suspension is removed as the species dissolved. The reaction mixture was stirred for 10 minutes, then neutralised with the addition of 2 M HCl. The solvent was removed *in vacuo* to give a white residue that was not soluble in organic solvents. An NMR spectrum was obtained from a $\text{d}^6\text{-DMSO}$ solution of the residue, which showed a large number of environments which could not be satisfactorily identified. It was noted that the yellow colour that had been observed upon addition of base

was now dissolved in the trap of the Schlenk line, and had a strong odour of 2, 3-butandione. It was concluded that the ligand had decomposed upon addition of strong base.

Other methods were independently trialled at Mologic Ltd., with similar results.

Attempted deprotection of H_2L^3 using neat TFA

H_2L^3 (0.200 g, 0.39 mmol) was added to neat TFA (1 mL) giving a strong yellow colour and stirred for 10 min. The acid was removed *in vacuo*, MeCN (5 mL) was added, and the solution neutralised with 2 M NaOH. The reaction mixture was taken to dryness, and the yellow oily residue dissolved in d^3 -MeCN. A 1H NMR spectrum was measured which showed partial loss of the Boc groups based on peak integration, but a significant number of peaks which could not be positively identified. It was concluded that the use of neat TFA was too harsh in terms of reaction conditions, and caused decomposition.

Attempted deprotection of H_2L^3 – TFA in DCM

H_2L^3 (0.050 g, 0.10 mmol) was dissolved in dry DCM (5 mL) under a blanket of N_2 . TFA (1 mL) was dissolved in dry DCM (5 mL) and the acidic solution added dropwise. The yellow solution was seen to turn light brown, and was stirred overnight at room temperature. The solution was added dropwise to cold Et_2O (20 mL) with vigorous stirring. The solvent was removed *in vacuo* to give the *target compound* (H_2L^4) as a colourless oil (0.004 g, 0.013 mmol, 13 %). 1H NMR (400 MHz, D_2O) δ_H = 3.89 (4H, t, $^3J_{HH} = 5.81$ Hz, $2 \times CH_2NH$), 3.16 (4H, t, $^3J_{HH} = 5.62$ Hz, $2 \times CH_2NH$), 2.05 (6H, s, $2 \times CH_3$) ppm. There was insufficient material to measure a ^{13}C NMR spectrum. A representative mass spectrum was not obtainable.

Complex ZnL^4

The oil recovered from the attempted deprotection of H_2L^3 (0.004 g, 0.013 mmol) was dispersed in EtOH (5 mL), and $Zn(OAc)_2 \cdot 2H_2O$ (0.004 g, 0.018 mmol) was added. The mixture was heated to reflux for 4 hours, and seen to turn yellow. Upon cooling to room temperature, a yellow solid was seen to form. The solvent was removed *in vacuo*, and the yellow residue washed with cold H_2O (3×0.5 mL). The solid was dried *in vacuo* to give the *target compound* as a hygroscopic yellow solid (0.001 g, 0.003 mmol, 20 %). 1H NMR (400 MHz, D_2O) δ_H = 3.89 (4H, t, $^3J_{HH} = 5.81$ Hz, $2 \times CH_2NH$), 3.16 (4H, t, $^3J_{HH} = 5.62$ Hz, $2 \times CH_2NH$), 2.05 (6H, s, $2 \times CH_3$) ppm. There was insufficient material to measure a ^{13}C NMR spectrum. A representative mass spectrum was not obtainable.

N-*boc*-*diaminohexane* (5)

Diaminohexane (11.6 g, 100 mmol) was dissolved in dry DCM (400 mL) and cooled to 0 °C. Boc₂O (2.25 g, 10 mmol) was dissolved in dry DCM (50 mL) and added dropwise over 30 mins. The reaction mixture was allowed to come to room temperature and stirred overnight. A white suspension was seen to form. The reaction mixture was diluted with DCM (50 mL), washed with H₂O (5 x 40 mL), and the organic layer dried over Na₂SO₄. The solvent was removed in vacuo to give the *title compound* as a colourless oil (1.53 g, 7.08 mmol, 71 %). ¹H NMR (400 MHz, CDCl₃) δ_H = 4.56 (1H, br s, NH), 3.05 (2H, m, CH₂), 2.61 (2H, t, ³J_{HH} = 6.96 Hz, CH₂), 1.60 (2H, m, CH₂), 1.40 (2H, m, CH₂), 1.37 (9H, s, C(CH₃)₃), 1.27 (4H, m, 2 × CH₂) ppm.

N-*boc*-*2-isothiocyanatohexylamine* (6)

Compound (5) (2.85 g, 13.2 mmol) was added to THF (40 mL) in an ice bath. CS₂ (0.79 mL, 13.2 mmol) and triethylamine (5.0 mL, 37.5 mmol) were added, and the ice bath removed. The reaction mixture was stirred at room temperature for 15 min, and then reintroduced to the ice bath. Tosyl chloride (2.70 g, 15 mmol) was added in aliquots over 5 mins, and the solution stirred at room temperature for 25 min. DCM (20 mL) was added, and the organic solution washed with 10 % citric acid (3 × 10 mL), H₂O (3 × 10 mL), and brine (3 × 10 mL), and then dried over anhydrous sodium sulphate. The reaction mixture was filtered to remove the drying agent, and the solvent removed *in vacuo*. The product was dissolved in 1:4 ethyl acetate:hexane (5 mL), and flash columned on silica. The solvent was removed *in vacuo* to give the *title compound* as a yellow oil (2.55 g, 9.88 mmol, 75 %). ¹H NMR (400 MHz, CDCl₃) δ_H = 4.52 (1H, br s, NH), 3.45 (2H, t, ³J_{HH} = 6.60 Hz, CH₂), 3.04 (2H, m, CH₂), 1.63 (2H, m, CH₂), 1.41 (2H, m, CH₂), 1.39 (9H, s, C(CH₃)₃), 1.28 (4H, m, 2 × CH₂).

N-*Boc*-*2-thiocarbonylhydrazidohexylamine* (7)

Compound (6) (1.02 g, 3.95 mmol) was dissolved in EtOH (30 mL) in an ice bath. A solution of hydrazine hydrate (9.5 mL, 4.74 mmol) in EtOH (10 mL) was added dropwise over 10 min, and the reaction mixture was stirred at 0 °C for 30 min, then at room temperature for a further 30 minutes. The solvent was reduced *in vacuo* and the reaction mixture placed in a freezer overnight. A white solid was collected by filtration and washed on the pump with cold EtOH (3 × 5 mL), before being dried *in vacuo* to give the *title compound* as a white solid (0.705 g, 2.43 mmol, 62 %). ¹H NMR (400 MHz, CDCl₃) δ_H = 7.37 (1H, br s, NH), 7.14 (1H, br s, NH), 6.40 (2H, br s, NH₂), 4.47 (1H, br s, NHBoc), 3.55 (2H, dt, ³J_{HH} = 6.60 Hz, CH₂NH), 3.06 (2H, dt, ³J_{HH} = 6.66 Hz, CH₂NH), 1.57 (2H, m, CH₂), 1.42 (2H, m, CH₂), 1.38

(9H, s, C(CH₃)₃), 1.30 (4H, m, 2 × CH₂) ppm. ¹³C NMR (75 MHz, CDCl₃) δ_C = 182.7 (CS), 163.9 (CO), 80.2 (C(CH₃)₃), 44.4 (CH₂), 42.9 (CH₂), 30.4 (CH₂), 29.6 (CH₂), 28.9 (C(CH₃)₃), 26.8 (CH₂) ppm. LR-MS (ES+) found m/z 313.17, calculated m/z 313.17 for [C₁₂H₂₆N₄O₂S+Na]⁺. IR (ATP) ν = 3173 (NH), 2924 (NH), 1680 (CO), 1623, 1521, 1364, 1153 (CS) cm⁻¹.

Ligand H₂L⁵

Compound **(7)** (0.524 g, 1.81 mmol) and 2, 3-butandione (77 μL, 0.88 mmol) were dissolved in EtOH (10 mL) and heated to reflux for 24 h. The reaction was allowed to cool to room temperature, and the solvent removed *in vacuo* to give a yellow oil. DCM (10 mL) was added and the organic solution washed with H₂O (3 × 10 mL) and brine (3 × 10 mL), then dried over MgSO₄. The drying agent was removed by filtration, and the solvent removed *in vacuo* to give the *title compound* as a yellow oil (0.400 g, 0.63 mmol, 72 %). ¹H NMR (400 MHz, CDCl₃) δ_H = 8.64 (2H, br s, 2 × NH), 7.55 (2H, br s, 2 × NH), 4.48 (2H, m, 2 × NHBoc), 3.65 (4H, dt, ³J_{HH} = 6.63 Hz, 2 × CH₂NH), 3.06 (4H, m, 2 × CH₂NH), 1.94 (6H, s, 2 × CH₃), 1.64 (4H, m, 2 × CH₂), 1.42 (4H, m, 2 × CH₂) 1.38 (18H, s, 2 × C(CH₃)₃), 1.33 (8H, m, 4 × CH₂) ppm. ¹³C NMR (75 MHz, CDCl₃) δ_C = 178.1 (CS), 156.1 (CO), 145.0 (CN), 79.5 (C(CH₃)₃), 44.7 (CH₂), 40.4(CH₂), 30.1 (CH₂), 29.0 (CH₂), 28.9 (C(CH₃)₃), 26.4 (CH₂), 24.5 (CH₂), 8.6 (CH₃) ppm. LR-MS (ES-) found m/z 629.37, calculated m/z 629.37 for [C₂₈H₅₄N₈O₄S]⁻. IR (ATP) ν = 3357 (NH), 2931 (NH), 1683 (CO), 1590, 1531, 1364, 1163 (CS) cm⁻¹. Due to impurities visible in the ¹H NMR spectrum that could not satisfactorily be removed, complexes of this ligand were not synthesised.

t-Butyl (L)-2-isothiocyanatopropanoate (8)

L-alanine *t*-butyl ester hydrochloride (1 g, 5.5 mmol) was dissolved in dry DCM (10 mL). DIPEA (1.35 mL, 7.5 mmol) was added dropwise and the mixture stirred for 10 minutes at room temperature. The solution was then added dropwise to a dispersion of thiophosgene (1.3 mL, 16.5 mmol) in DCM (20 mL) in an ice bath under a blanket of N₂. Crushed NaOH (0.66 g, 16.5 mmol) was added, and the solution allowed to come to room temperature over 3 h. The reaction mixture turns black, dried *in vacuo*, and is then diluted with DCM (10 mL) to allow for transfer to a silica flash column. The eluent was 1:5 v/v DCM:Petroleum ether, increasing to pure DCM to collect the target compound. The solvent was removed *in vacuo* to give the *title compound* as a yellow oil (0.788 g, 4.20 mmol, 72%). ¹H NMR (400 MHz, CDCl₃) δ_H = 4.13 (1H, q, ³J_{HH} = 7.20 Hz, CH), 1.48 (3H, d, ³J_{HH} = 7.10 Hz, CH₃), 1.44 (9H, s, C(CH₃)₃) ppm. ¹³C NMR (75 MHz, CDCl₃) δ_C = 137.2 (CSN), 83.6 (C(CH₃)₃), 55.6 (C(CH₃)₃H), 27.8 (C(CH₃)₃), 19.5 (CH₃) ppm. LR-MS (ES-) found m/z 186.06, calculated m/z

186.06 for $[\text{C}_8\text{H}_{12}\text{NO}_2\text{S}]^-$. IR (ATP) $\nu = 2982, 2046 (\text{N}=\text{CS}), 1740 (\text{CO}), 1456, 1370, 1150 \text{ cm}^{-1}$.

t-Butyl (hydrazinecarbonothioyl)-L-alaninate (9)

Compound **(8)** (0.77 g, 4.1 mmol) was dissolved in EtOH (20 mL) in an ice bath. Hydrazine hydrate (0.21 mL, 4.32 mmol) was added to EtOH (5 mL), and added dropwise to the chilled solution over 30 min. The mixture was allowed to come to room temperature and stirred overnight. The reaction mixture was reduced *in vacuo*, chilled, and a white solid was seen to form. The solid was collected on a sinter and washed with cold EtOH ($3 \times 5 \text{ mL}$), then dried *in vacuo* to give the *title compound* as a white solid (0.321 g, 1.47 mmol, 36 %). ^1H NMR (400 MHz, CDCl_3) $\delta_{\text{H}} = 7.85 (1\text{H}, \text{s}, \text{NH}), 7.40 (1\text{H}, \text{s}, \text{NH}), 4.86 (1\text{H}, \text{q}, ^3J_{\text{HH}} = 7.30 \text{ Hz}, \text{CH}), 3.70 (2\text{H}, \text{br s}, \text{NH}_2), 1.43 (3\text{H}, \text{m}, \text{CH}_3), 1.42 (9\text{H}, \text{s}, \text{C}(\text{CH}_3)_3)$ ppm. ^{13}C NMR (75 MHz, CDCl_3) $\delta_{\text{C}} = 180.2 (\text{CS}), 172.8 (\text{CO}), 82.6 (\text{C}(\text{CH}_3)_3), 53.2 (\text{CH}), 28.4 (\text{C}(\text{CH}_3)_3), 19.2 (\text{CH}_3)$ ppm. LR-MS (ES+) found m/z 219.10, calculated m/z 219.10 for $[\text{C}_8\text{H}_{17}\text{N}_3\text{O}_2\text{S}]^+$. IR (ATP) $\nu = 2528, 1730 (\text{CO}), 1637, 1534, 1443, 1253, 1155 (\text{CS}) \text{ cm}^{-1}$.

Ligand H_2L^6

Compound **(9)** (0.321 g, 1.47 mmol) was dissolved in EtOH (15 mL). 2, 3-butandione (64 μL , 0.74 mmol) was added. The solution was seen to turn yellow, and then heated to reflux overnight. The solution was allowed to cool to room temperature, then chilled in the freezer for 2 h. A yellow solid separated from the blue-green solution. The solid was collected on a Buchner funnel, washed with cold EtOH ($3 \times 5 \text{ mL}$) and dried *in vacuo* to give the *title compound* as a yellow solid (0.250 g, 0.51 mmol, 69 %). ^1H NMR (400 MHz, CDCl_3) $\delta_{\text{H}} = 8.65 (2\text{H}, \text{s}, 2 \times \text{NH}), 8.04 (2\text{H}, \text{d}, ^3J_{\text{HH}} = 7.20 \text{ Hz}, 2 \times \text{NHCH}), 4.86 (2\text{H}, \text{q}, ^3J_{\text{HH}} = 7.10 \text{ Hz}, 2 \times \text{CH}), 2.11 (6\text{H}, \text{s}, 2 \times \text{CH}_3), 1.49 (6\text{H}, \text{d}, ^3J_{\text{HH}} = 7.10 \text{ Hz}, 2 \times \text{CH}_3), 1.44 (18\text{H}, \text{s}, 3 \times \text{C}(\text{CH}_3)_3)$ ppm. ^{13}C NMR (75 MHz, CDCl_3) $\delta_{\text{C}} = 177.2 (\text{CS}), 172.3 (\text{CO}), 146.1 (\text{CN}), 83.1 (\text{C}(\text{CH}_3)_3), 53.7 (\text{CHNH}), 28.4 (\text{C}(\text{CH}_3)_3), 19.1 (\text{CH}_3\text{CH}), 10.9 (\text{CH}_3)$ ppm. LR-MS (ES+) found m/z 511.20, calculated m/z 511.21 for $[\text{C}_{20}\text{H}_{36}\text{N}_6\text{O}_4\text{S}_2+\text{Na}]^+$. IR (ATP) $\nu = 2973 (\text{NH}), 1735 (\text{CO}), 1516, 1480, 1362, 1015 (\text{CS}) \text{ cm}^{-1}$.

Metal complexes of H_2L^6

The syntheses of metal complexes of H_2L^6 were approached analogously to the complexes described in the Chapter 5. In all cases, H_2L^6 (0.050 g, 0.2 mmol) was dispersed in EtOH (5 mL) with 1.2 molar equivalents of the relevant metal acetate hydrate. The reaction mixtures were refluxed for 4 hours, during which time colour changes were observed, indicating

complexation. However, the complexes could not be isolated or purified at the end of the reaction, hence characterisation was limited to ^1H NMR and mass spectrometry.

For CuL^6 : HR-MS (ES+) found m/z 550.1451, calculated m/z 550.1457 for $[\text{C}_{20}\text{H}_{35}\text{N}_6\text{O}_4\text{S}_2^{63}\text{Cu}]^+$.

For ZnL^6 : ^1H NMR (400 MHz, d^6 -DMSO) δ_{H} = 5.72 (2H, br s, $2 \times \text{NH}$), 4.45 (2H, br s, $2 \times \text{CH}$), 2.16 (6H, s, $2 \times \text{CH}_3$), 1.63 (6H, m, $2 \times \text{CH}_3$), 1.39 (18H, m, $2 \times \text{C}(\text{CH}_3)_3$) ppm. HR-MS (ES+) found m/z 551.1458, calculated m/z 551.1453 for $[\text{C}_{20}\text{H}_{35}\text{N}_6\text{O}_4\text{S}_2^{64}\text{Zn}]^+$.

For NiL^6 : ^1H NMR (400 MHz, d^6 -DMSO) δ_{H} = 5.56 (2H, br s, $2 \times \text{NH}$), 4.26 (2H, br s, $2 \times \text{CH}$), 1.84 (6H, s, $2 \times \text{CH}_3$), 1.54 (6H, m, $2 \times \text{CH}_3$), 1.39 (18H, m, $2 \times \text{C}(\text{CH}_3)_3$) ppm. HR-MS (ES+) found m/z 545.1516, calculated m/z 545.1515 for $[\text{C}_{20}\text{H}_{35}\text{N}_6\text{O}_4\text{S}_2^{58}\text{Ni}]^+$.

For CdL^6 : ^1H NMR (400 MHz, d^6 -DMSO) δ_{H} = 5.67 (2H, br s, $2 \times \text{NH}$), 4.41 (2H, br s, $2 \times \text{CH}$), 2.19 (6H, s, $2 \times \text{CH}_3$), 1.53 (6H, m, $2 \times \text{CH}_3$), 1.37 (18H, m, $2 \times \text{C}(\text{CH}_3)_3$) ppm. HR-MS (ES-) found m/z 631.0817, calculated m/z 631.0802 for $[\text{C}_{20}\text{H}_{34}\text{N}_6\text{O}_4\text{S}_2^{110}\text{Cd}+\text{Cl}]^-$.

Attempt to synthesise HgL^1

Ligand H_2L^1 (0.200 g, 0.5 mmol) and HgCl_2 (0.150 g, 0.55 mmol) were dissolved in EtOH (10 mL) and the reaction mixture heated to reflux. A precipitate formed, which was filtered and washed with EtOH (10 mL) to give the starting ligand as a yellow solid (0.140 g, 0.35 mmol, 70 %). Spectroscopic and mass spectrometric analysis showed that no complex had been formed.

1, 10-Phenanthroline-5, 6-dione (10)

1, 10-phenanthroline (0.81 g, 4.52 mmol) was added to H_2SO_4 (60 % v/v, 20 mL) and the colourless solution stirred at room temperature to ensure thorough mixing. KBrO_3 (0.83 g, 4.97 mmol) was added in batches over 30 min. The solution was seen to turn orange. $\text{Br}_{2(\text{g})}$ was released by the reaction but maintained in the reaction vessel throughout. The reaction was stirred overnight at room temperature. The mixture was then poured over ice and neutralised with 2M $\text{NaOH}_{(\text{aq})}$. The product was extracted by washing with DCM (3×10 mL). The organic fraction was washed with brine (3×10 mL) and dried over MgSO_4 . The solution was filtered and the solvent removed *in vacuo* to give a yellow powder, which was recrystallised from hot EtOH to give the *title compound* as a green-yellow solid (0.35 g, 1.67 mmol, 37 %). The product had identical spectroscopic properties to that recorded in the literature.¹ ^1H NMR (400 MHz, CDCl_3) δ_{H} = 9.17 (2H, d, $^3J_{\text{HH}} = 4.64$ Hz, $2 \times \text{CHN}$), 8.55

(2H, d, $^3J_{\text{HH}} = 7.86$ Hz, $2 \times \text{CH}$), 7.64 (2H, dd, $^3J_{\text{HH}} = 7.84$ Hz, $^3J_{\text{HH}} = 4.74$ Hz, $2 \times \text{CH}(\text{CH})(\text{CH})$) ppm.

Cyclised product (11)

1, 10- Phenanthroline-5, 6-dione (**10**) (0.1 g, 0.48 mmol) and ethyl-2-(hydrazinecarbothioamido)acetate (0.179 g, 1.01 mmol) were dissolved in dry EtOH (5 mL). A catalytic amount of H_2SO_4 was added. The reaction mixture was refluxed under N_2 for 4 h. Upon cooling to room temperature, a red precipitate formed. The solid was collected on a sinter and washed with cold EtOH (3×10 mL), dried *in vacuo* and recrystallised from hot EtOH to give the *title compound* as a red solid (0.083 g, 0.21 mmol, 44 %). ^1H NMR (400 MHz, d^6 -DMSO) $\delta_{\text{H}} = 10.23$ (1H, t, $^3J_{\text{HH}} = 5.73$ Hz, NH), 9.42 (1H, d, $^3J_{\text{HH}} = 8.22$ Hz, CH), 9.20 (1H, d, $^3J_{\text{HH}} = 3.20$ Hz, CH), 8.99 (1H, d, $^3J_{\text{HH}} = 4.76$ Hz, CH), 8.79 (1H, d, $^3J_{\text{HH}} = 8.10$ Hz, CH), 8.01 (1H, dd, $^3J_{\text{HH}} = 8.03, 5.09$ Hz, CH), 7.95 (1H, dd, $^3J_{\text{HH}} = 7.85, 4.78$ Hz, CH), 4.46 (2H, d, $^3J_{\text{HH}} = 5.86$ Hz, CH_2N), 4.17 (2H, q, $^3J_{\text{HH}} = 7.03$ Hz, CH_2CH_3), 3.75 (2H, q, $^3J_{\text{HH}} = 7.11$ Hz, CH_2CH_3), 1.24 (3H, t, $^3J_{\text{HH}} = 7.08$ Hz, CH_2CH_3), 1.05 (3H, t, $^3J_{\text{HH}} = 7.00$ Hz, CH_2CH_3) ppm. ^{13}C NMR (75 MHz, d^6 -DMSO) $\delta_{\text{C}} = 180.0$ (CS), 168.9 (CO), 137.6 (CH), 130.6 (CH), 128.9 (CH), 128.7 (CH), 127.0 (CH), 61.7 (CH_2O), 61.4 (CH_2O), 56.6 (CH_2N), 15.7 (CH_3), 14.7 (CH_3) ppm. LR-MS (ES+) found m/z 466.93, calculated m/z 466.1525 for $[\text{C}_{19}\text{H}_{19}\text{N}_5\text{O}_3\text{S} + \text{Na} + \text{EtOH}]^+$. IR (ATP) $\nu = 3300$ (NH), 3204 (NH), 3066 (CH), 2986 (CH), 1748 (CO), 1015 (CS) cm^{-1} . UV-vis (DMSO): λ_{max} ($\epsilon / \text{L mol}^{-1} \text{cm}^{-1}$) 439 (11440) nm.

Open chain product (12)

1, 10- Phenanthroline-5, 6-dione (**10**) (0.1 g, 0.48 mmol) and ethyl-2-(hydrazinecarbothioamido)acetate (0.179 g, 1.01 mmol) were dissolved in dry EtOH (5 mL). A catalytic amount of H_2SO_4 was added. The reaction mixture was stirred at room temperature under N_2 overnight. An orange solid was seen to form. The solid was collected on a sinter and washed with cold EtOH (3×10 mL) and dried *in vacuo* to give the *title compound* as an orange solid (0.103 g, 0.28 mmol, 58 %). ^1H NMR (400 MHz, d^6 -DMSO) $\delta_{\text{H}} = 10.15$ (1H, t, $^3J_{\text{HH}} = 5.92$ Hz, NH), 9.27 (1H, d, $^3J_{\text{HH}} = 7.88$ Hz, CH), 9.17 (1H, d, $^3J_{\text{HH}} = 4.64$ Hz, CH), 8.94 (1H, d, $^3J_{\text{HH}} = 5.97$ Hz, CH), 8.72 (1H, d, $^3J_{\text{HH}} = 8.16$ Hz, CH), 7.87 (2H, m, $2 \times \text{CH}$), 4.45 (2H, d, $^3J_{\text{HH}} = 5.90$ Hz, CH_2NH), 4.18 (2H, q, $^3J_{\text{HH}} = 7.02$ Hz, CH_2CH_3), 1.24 (3H, t, $^3J_{\text{HH}} = 7.07$ Hz, CH_2CH_3) ppm. ^{13}C NMR (75 MHz, d^6 -DMSO) $\delta_{\text{C}} = 179.6$ (CS), 168.9 (CO), 154.6 (CH), 147.4 (CH), 141.3 (CH), 138.3 (CH), 130.9 (CH), 129.0 (CH), 61.4 (CH_2O), 56.6 (CH_2N), 14.7 (CH_3) ppm. LR MS (APCI) found m/z 370.05, calculated m/z 370.10 for $[\text{C}_{17}\text{H}_{16}\text{N}_5\text{O}_3\text{S}]^+$. IR (ATP) $\nu = 3248$ (NH), 3055 (CH), 2982 (CH), 1734 (CO) cm^{-1} . UV-vis (DMSO): λ_{max} ($\epsilon / \text{L mol}^{-1} \text{cm}^{-1}$) 439 (9900) nm.

1.3 Results and discussion

1.3.1 Attempted deprotection of ligands

As has been discussed above, conditions that satisfactorily deprotected the ligands H_2L^1 , H_2L^2 and H_2L^3 could not be found. Typical efforts are described in the experimental section above. Ethyl esters such as those found in H_2L^1 and H_2L^2 are not as commonly used as protecting groups as methyl esters, but may be cleaved in a similar fashion by use of a strong mineral base in a suitable solvent.² H_2L^1 showed sparing solubility in H_2O and only dissolved in EtOH with heating. It did dissolve in THF. When an aqueous solution of NaOH was added, it was immediately apparent that decomposition was occurring; a colour change from near colourless to bright yellow was accompanied by the pungent odour of 2, 3-butanedione, indicating hydrolysis of the backbone Schiff bases. It was reasoned that H_2L^2 , due to its lack of methyl groups and their associated steric hindrance, would be more susceptible to basic hydrolysis. The metal complexes would also be susceptible due to the polarising effect of coordination. For these reasons, focus was shifted to H_2L^3 .

Boc protecting groups are deprotected by the use of strong protic acids. Initial experiments with neat TFA were unsatisfactory. After 10 minutes of being exposed to the acid, an aliquot of H_2L^3 was studied by NMR. Although the integration showed a decrease in the intensity of the Boc signal, indicating deprotection, a significant number of impurity peaks had appeared which could not be unambiguously identified. With increasing reaction time, the Boc signal continued to decrease, but the spectrum became poor. It was concluded that the use of neat TFA may be too harsh, leading to acid hydrolysis of the ligand, despite similar conditions having been reported in the literature.³

Diluting both the ligand and the acid in DCM showed promise (Fig. 1). Stirring overnight at room temperature allowed the isolation of a low quantity of a colourless oil. The only characterisation data obtainable was a 1H NMR spectrum which showed complete loss of the Boc group, limited impurities and significant differences in the chemical shifts of the CH_2 groups between this and the protected ligand. It was concluded that it was likely that deprotection had occurred, but given that no other data was available it could not be unambiguously confirmed. The decision was made to attempt an *in situ* synthesis of the Zn complex of the deprotected ligand (see below). Again, low yields suggest that the method described needs optimisation for future work to be carried out on this complex, but as a proof of principle supports the argument that deprotection occurred with a sufficient quantity of the desired ligand resulting to allow the coordination of a metal. Further study of

this species was not possible due to the reallocation of resources following our colleagues at Mologic restructuring.

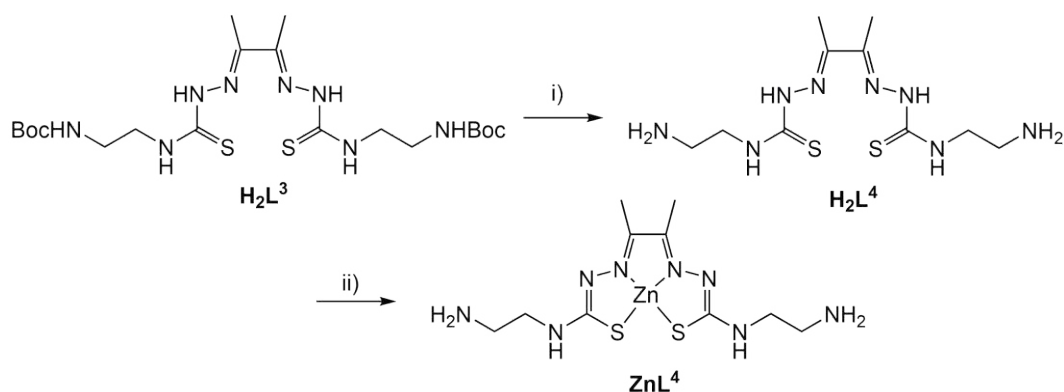


Figure 1. Deprotection of H_2L^3 and subsequent complexation. i) TFA, DCM, RT, overnight. ii) $Zn(OAc)_2 \cdot 2H_2O$, EtOH, reflux, 4 h.

1.3.2 The use of a diaminohexane-based side arm- H_2L^5

It was hypothesised that the side arms of the ligands H_2L^1 , H_2L^2 and H_2L^3 may be too short to allow bidentate coupling to a carrier protein subsequent to deprotection. As a precautionary measure, it was decided that an alternative species with a similar coordination sphere but longer side arms should be synthesised for inclusion in antibody generation. By having a longer linker arm, the coordination sphere would in theory be further away from the steric bulk of the protein and subject to less spatial pressures, offering further alternatives in terms of epitopes. The stepwise synthesis of such a ligand, here designated H_2L^5 , is described in the experimental section below. The ligand was synthesised and characterised unambiguously, but impurities present in TLC analysis and the 1H NMR spectrum could not be removed. Again, further study was not possible due to the changing nature of the project.

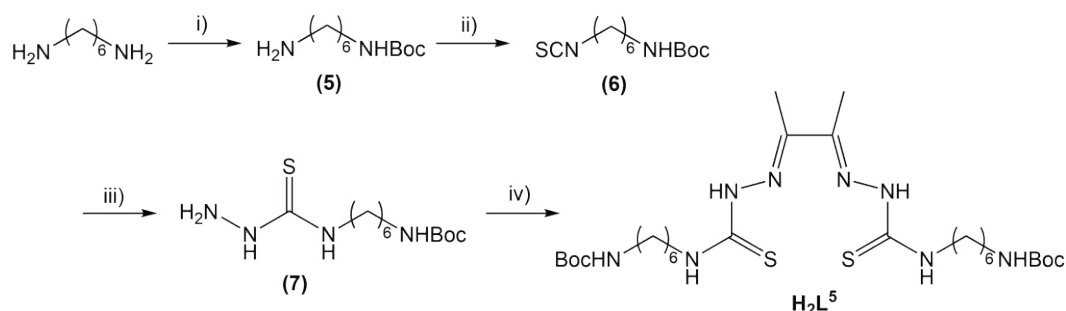


Figure 2. Synthesis of H_2L^5 . i) Boc_2O , DCM, RT, overnight. ii) CS_2 , THF, NEt_3 , $TsCl$, 30 min, RT. iii) $N_2H_4 \cdot H_2O$, EtOH, RT, 30 min. iv) 2, 3-butandione, EtOH, reflux, overnight.

1.3.3 A chiral side arm- H_2L^6 and its complexes

As a response to the need to investigate other protection methodologies, the use of t-butyl ester groups to protect the acid of an amino acid side arm was decided upon. t-butyl esters may be removed by the use of aqueous acids under relatively mild conditions, and so offered a suitable alternative to the issues encountered with the groups described above. The use of an L-alanine backbone was of interest as it would make the complex chiral, and would theoretically have an effect on the binding of the complexes to carrier proteins. The synthesis of the ligand H_2L^6 and its metal complexes are described in the experimental section. Limited spectroscopic data relating to the metal complexes was obtainable, and the species could not be isolated in a pure form, precluding them from further discussion in this report. Nevertheless, future efforts could find this ligand framework fruitful.

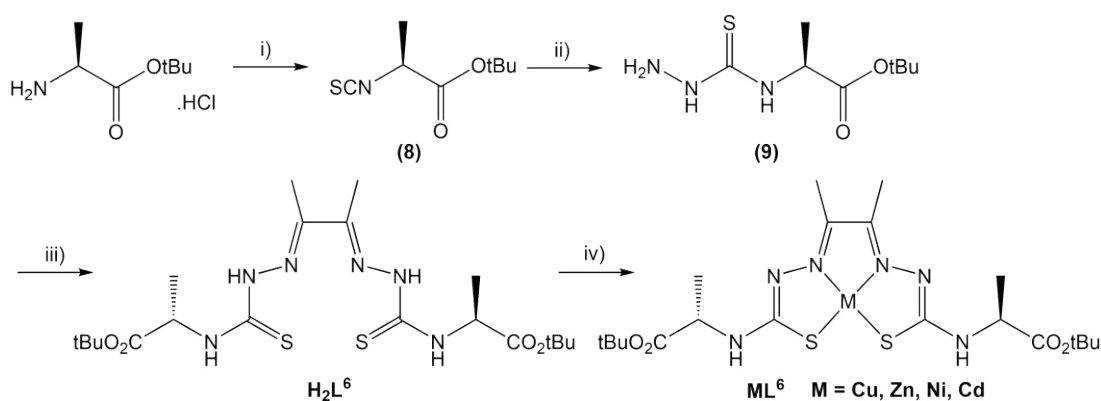


Figure 3. Synthesis of H_2L^6 and subsequent metal complexes. i) DIPEA, $CSCl_2$, NaOH, DCM, 3 h, $0^\circ C$. ii) $N_2H_4.H_2O$, EtOH, $0^\circ C$, 30 min. iii) 2, 3-butandione, EtOH, reflux, overnight. iv) Metal acetate, EtOH, reflux, 4 h.

1.3.4 Attempted synthesis of complex HgL^1

In the course of the current work, suitable crystals for single crystal X-ray diffraction were obtained for ZnL^1 and CdL^1 . If the crystal structure of the analogous Hg complex were to be obtained, it would allow an interesting crystallographic discussion of the coordination preferences of different metals going down a periodic group. This was not possible. As described below, a typical approach to the synthesis of such a complex was taken, but analysis of the yellow solid obtained showed no differences between this and the starting ligand. The coordination of Hg could not be observed spectroscopically, suggesting that this larger metal ion could not be accommodated easily by the ligand.

1.3.5 Attempted synthesis of a fluorescent bis(thiosemicarbazone), leading to an unusual cyclic structure

As part of the development of novel bis(thiosemicarbazone) ligands for antigenic purposes, it was suggested that a fluorescent derivative could be of interest in terms of tracking the pharmacological behaviour of the proposed species. A species based on a 1, 10-phenanthroline-5, 6-dione backbone would be expected to show some luminescent character due to the extensive π -system that would be observed in a 1:2 condensation project (shown in Fig. 4). As well as the proposed spectroscopic behaviour, the ligand backbone would be particularly rigid, which would have interesting effects on the coordination geometry in metal complexes which could be investigated electrochemically. Electrochemical studies of a benzil-based analogue showed a reduction potential similar to that of Cu-ATSM,⁴ but the rigid phenanthroline moiety may act to make reduction less easily achieved. Finally, the inclusion of the large, aryl moiety would give a planar, hydrophobic character to the desired compound. Monosemicarbazone ligands and complexes based on a phenanthroline moiety have previously been shown to have an apoptotic-inducing effect on drug-sensitive and drug-resistant tumour cell lines (including triple negative cell lines), possibly due to an ability to intercalate in DNA structures.⁵⁻⁸ It was hypothesised that cytotoxicity studies of the desired complexes could also be of interest from a pharmaceutical viewpoint.

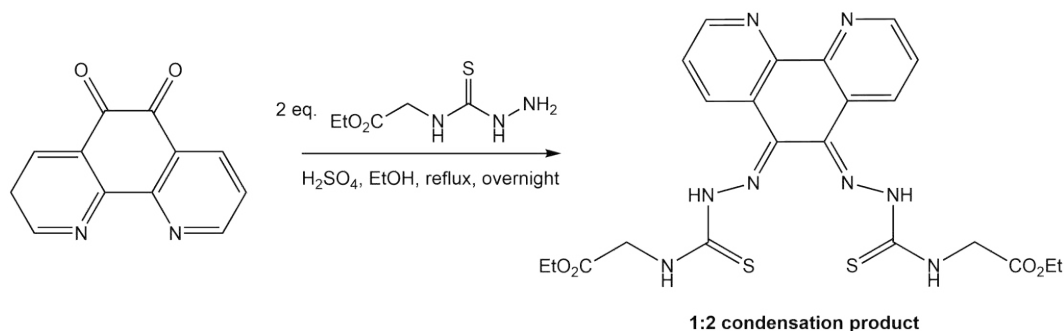


Figure 4. Proposed synthesis of a phenanthroline based bis(thiosemicarbazone). This was not achieved.

Research showed that the synthesis would be difficult. In the work reported by Calatayud *et al.*, it was noted that the synthesis of benzil-based BTSC species was complicated by the propensity for the 1:1 intermediate to cyclise to give a stable 1, 2, 4-triazine ring. The end-products of the reactions detailed in the 2007 paper were highly dependent on the reaction conditions used.⁹ The phenyl rings allow for delocalisation of electron density, and the presence of a primary amine allows for double condensations. The use of tertiary amines seems to prevent cyclising.¹⁰ It would be expected that a phenanthroline moiety would favour

the forming of a triazine, expanding the delocalised π -system and providing a rigid environment for the reaction to occur in. A stable open chain monothiosemicarbazone with a phenanthroline moiety has been reported however, and so the synthesis was approached with an eye to prevent the triazine forming instead of the BTSC.^{5,6}

A typical approach to the synthesis of the desired species was taken (see experimental section below). The conditions used were similar to those reported in Afrasiabi *et al.*⁶ 2 equivalents of the thiocarbohydrazone were heated to reflux in an acidified, protic solvent with 1 equivalent of the dione. The presence of a secondary amine was considered a potential route to the formation of a triazine, but less so than had there been a primary amine. However, as shown in the experimental section, the closed ring, triazine species **(11)** was synthesised and characterised. A proposed mechanism for the formation is shown in Fig. 5.

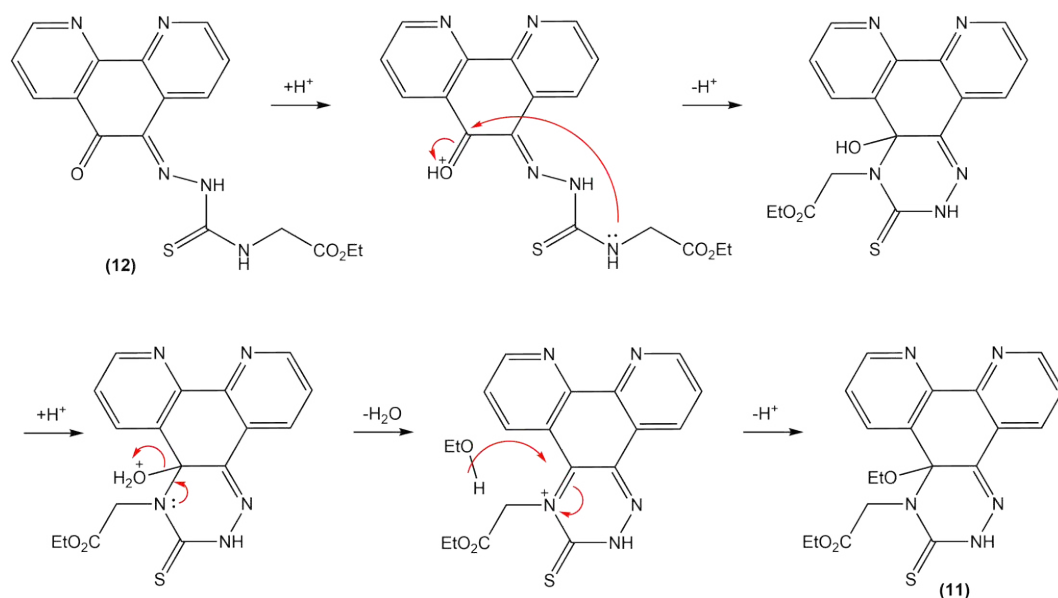


Figure 5. Proposed mechanism of triazine **(11)** formation from monothiosemicarbazone **(12)**.

Allowing longer reaction time at lower temperatures allowed the synthesis of the open chain analogue **(12)**. Both species were characterised unambiguously. Additional conditions were trialled that are not described in the experimental section, as all gave either the triazine or the monothiosemicarbazone. Results were definitive; mixtures of the two products were not observed, and the desired BTSC was not observed.

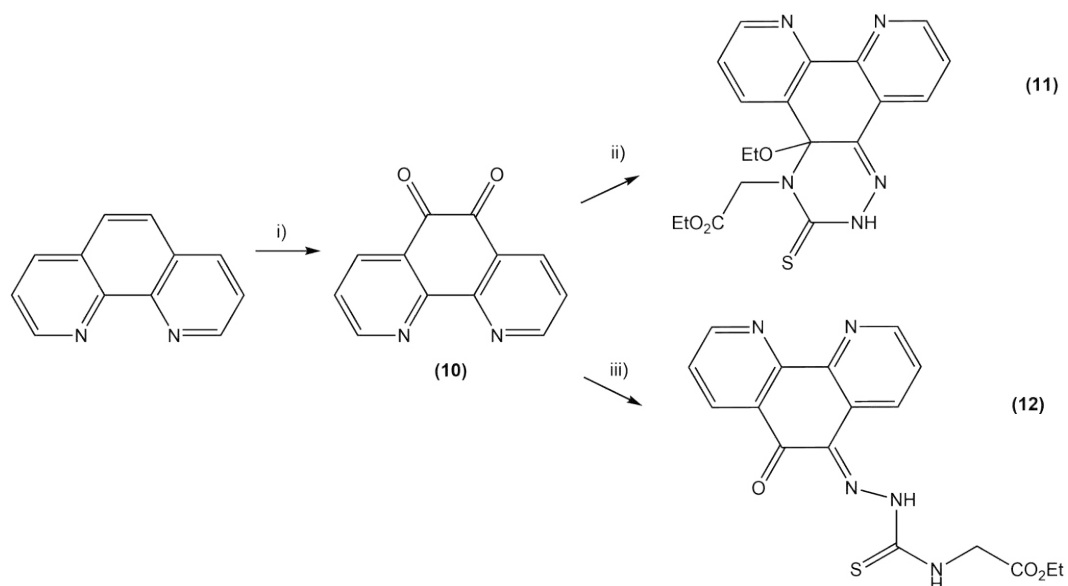


Figure 6. Synthesis of cyclised and open chain phenanthroline based species. i) $KBrO_3$, H_2SO_4 , H_2O . ii) Ethyl-2-(hydrazinecarbothioamido)acetate, EtOH, cat. H_2SO_4 , reflux, 4 h. iii) Ethyl-2-(hydrazinecarbothioamido)acetate, EtOH, cat. H_2SO_4 , RT, overnight.


It was concluded that the energetic sink provided by the open intermediate (12) forming a triazine (11) was too great to allow a second condensation with another equivalent of the thiocarbonylhydrazide. Future work on this project could develop the use of the species (12) and its metal complexes. As similar species have shown anti-tumour abilities, cytotoxicity studies could be of interest.

1.4 References

- 1 R. O. Bonello, I. R. Morgan, B. R. Yeo, L. E. J. Jones, B. M. Kariuki, I. A. Fallis and S. J. A. Pope, *J. Organomet. Chem.*, 2014, **749**, 150–156.
- 2 V. A. Vaillancourt, S. D. Larsen, S. P. Tanis, J. E. Burr, M. A. Connell, M. M. Cudahy, B. R. Evans, P. V. Fisher, P. D. May, M. D. Meglasson, D. D. Robinson, F. C. Stevens, J. A. Tucker, T. J. Vidmar and J. H. Yu, *J. Med. Chem.*, 2001, **44**, 1231–1248.
- 3 P. A. Waghorn, M. W. Jones, M. B. M. Theobald, R. L. Arrowsmith, S. I. Pascu, S. W. Botchway, S. Faulkner and J. R. Dilworth, *Chem. Sci.*, 2013, **4**, 1430–1441.
- 4 L. Alsop, A. R. Cowley, J. R. Dilworth, P. S. Donnelly, J. M. Peach and J. T. Rider, *Inorganica Chim. Acta*, 2005, **358**, 2770–2780.
- 5 S. Padhye, Z. Afrasiabi, E. Sinn, J. Fok, K. Mehta and N. Rath, *Inorg. Chem.*, 2005, **44**, 1154–1156.
- 6 Z. Afrasiabi, E. Sinn, S. Padhye, S. Dutta, S. Padhye, C. Newton, C. E. Anson and A. K. Powell, *J. Inorg. Biochem.*, 2003, **95**, 306–314.
- 7 P. Anitha, N. Chitrapriya, Y. J. Jang and P. Viswanathamurthi, *J. Photochem. Photobiol. B-Biol.*, 2013, **129**, 17–26.
- 8 Z. Afrasiabi, P. Stovall, K. Finley, A. Choudhury, C. Barnes, A. Ahmad, F. Sarkar, A. Vyas and S. Padhye, *Spectrochim. Acta Part -Mol. Biomol. Spectrosc.*, 2013, **114**, 114–119.
- 9 D. G. Calatayud, F. J. Escobar, E. López-Torres and M. A. Mendiola, *Helv. Chim. Acta*, 2007, **90**, 2201–2216.
- 10 M. Christlieb and J. R. Dilworth, *Chem. – Eur. J.*, 2006, **12**, 6194–6206.

Appendix I: PETIC Standard Operating Procedures for ⁸⁹Zr production and purification

The following pages are examples of the SOPs used within PETIC to facilitate the production, purification, safe handling and use of ⁸⁹Zr. Similar documents are referred to when using other radioisotopes. As with all laboratory research, risk assessments should be carried out fully before any experiment using radioisotopes and health and safety measures (e.g. the wearing of personal exposure monitors) must be adhered to fully.

RH 3000	PETIC School of Medicine	
Cyclotron Manual	Preparation of HC 7 for Zr-89 Separation	

Principle

This procedure describes how to prepare R & D Hot Cell 7 for Zr-89 separation **prior** to the introduction of the radioactive material into the hot cell.

Ensure that the following procedures have been completed before performing this procedure:

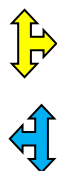
RH 3001 **Preparation for Zr-89**

Note: All glassware and plastics should be prewashed with 6M HCl (see **RH 3001**) and then deionised water before use. No metallic items should be used at any stage.

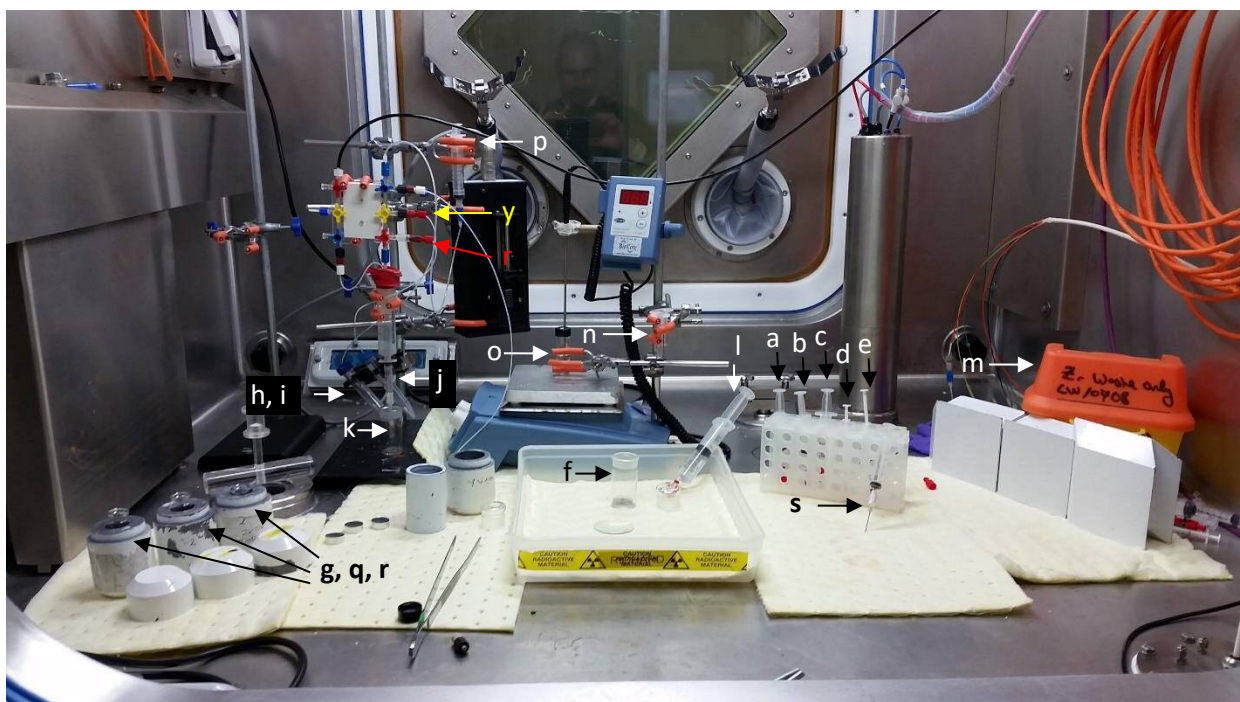
Procedure

1. Wear appropriate protective clothing (lab coat, safety glasses and gloves).
2. Check the compressed air gas supply is in the hot cell. Turn it on and test the needle valve to allow small amounts of compressed air to be released (left side manifolds outside). Turn needle valve off again and close supply.
3. Have a look at the hot cell pressures over the hot cell door. The door seal pressure should be around 1 bar and hot cell pressures should be around 300 Pa.
4. Check if there is residual activity in the hot cell by looking on the appropriate reading on the radiation monitoring node. If the residual activity is higher than 10 uS/hr contact the RPS.
5. Check the calculated residual activity of the multiple use Zr glassware and Zr waste bin. For this use Isostock as described **RS 4103**.
6. Place the absorbent mat under the delivery position for the Zr delivery lance (black circle drawn on base of hot cell) and place **Zr opening tool** (consisting of a short stiff needle attached to a 5ml syringe as in picture) in the centre of the mat (not blocking the delivery lance as well as other stuff).
7. Arrange the dispensing cassette and syringe driver as pictured below making sure that the taps on the dispensing cassette can be easily turned with the tongs from the south side of the hot cell. The taps should be in the following positions:





8. Check all connections on the dispensing cassette that they are tight. Especially the compressed air line going into the top left and the syringe driver line going into the top right of the dispensing cassette.
9. Place the hotplate in its location as shown on the picture below and check that the vial containing the temperature probe is filled with silicon oil and set the temperature probe to 110°C. Check it is working and then switch off the heater at the appropriate switch on the right side of the hot cell door using the one for the appropriate socket.
10. Place a yellow small sharp bin on the right side of the hot cell to dispose of any sharps and radioactive waste during the Zr-89 purification.
11. Transfer two white wide bore lead pots into the hot cell (labelled with Zr-89 separation, date, operator).
12. Double check that either the solid target delivery lance or access to the well counter is not blocked in any way.



13. Prepare a hydroxamate functionalised separation column in a pre-washed washed 2 ml plastic syringe (see **RH 3001**).
 - Insert 1 cm³ of prewashed glass wool into the syringe with the help of the green plastic tweezers and the syringe plunger.
 - Take the plunger out and place a red bung at the bottom end.
 - Weigh 125 mg of lyophilised hydroxamate functionalised ion exchange resin (stored in freezer in R&D QC) into the syringe (prepared as described in **RH 3003**).

- Insert the other 1 cm³ of prewashed glass wool into the syringe with the help of the green plastic tweezers
 - Take of the red bung at the bottom end and insert the syringe plunger.
14. Condition the separation column in the following order using the prewashed 50 ml syringe and made up adaptor (**RH 3001**):
- 75 ml Acetonitrile (measure with a 100 ml measuring cylinder)
 - 10 ml of 0.9% saline (use 10 ml syringe + half vigo line)
 - 2 ml of 2M metal free HCl using 2 ml syringe + half vigo line (see **RH 3001**, step 10).
15. Arrange the following items as shown above making sure that they can be manipulated by tongs with the door is shut.

Into / beside the tube rack:

- a,b,c)** 3 x 2 ml of 2 M metal free HCl in a 5 ml syringe with red cap (see **RH 3001**, step 10).
- d)** 0.1 ml of 30% H₂O₂ in a 1ml syringe with red cap
- e)** 0.5 ml of 6M HCl in a 1ml syringe with red cap (see **RH 3001**, step 5).
- l)** 12 ml of 2 M metal free HCl in a 20 ml syringe with red cap (see **RH 3001**, step 10).

In tray / on absorbent mats:

- f)** 25 ml beaker for Zr dissolution with stirrer bar for the **reaction**,
stoppers from beaker f and k, Watch glass

In holder at back of dispensing cassette:

- h)** falcon tube containing 1M Oxalic acid 3 ml (see **RH 3001**, step 9) connect to lead with tube (**r**) and insert to the bottom of the vial,
- i)** falcon tube containing deionised H₂O 15.5ml connect to lead with tube (**y**) and insert to the bottom of the vial,

Bottom of dispensing cassette with syringe + adaptor:

- j)** Pre-prepared hydroxamate functionalised resin column (from step 21)
- k)** 25 ml beaker for Y-89 waste run through,



On the right of hot cell:

- m)** Zr Waste bin (2L yellow sharps bin labelled with Isostock CW number) behind lead bricks.

On the left side of Cell

3 white lead pots and their lids with 3 crimplip vials (without lids on) labelled ZrOxF1, ZrOxF2 and ZrOxF3 crimplips for vials. Ensure the lead pots are positioned so the tongs can reach them and their lids without blocking access to the well counter.

16. Close both doors and clear low pressure alarms.
17. The hot cell is now ready for delivery of Zr-89 (**CO 3103**).

RH 3001	PETIC School of Medicine	 
Cyclotron Manual	Preparation for Zr-89 Separation - day before	

Principle

This procedure describes how to prepare the appropriate solutions and consumables a day ahead of the Zr-89 separation.


Procedure

1. Wear appropriate protective clothing (Lab coat, safety glasses and gloves).
2. Collect all the consumables needed for Zr-89 separation as listed in **RH 4001**. These are:
 - 4 x 15ml falcon tubes
 - 6 x red bungs
 - 2 x 20ml syringes
 - 3 x 5ml syringes
 - 1 x 2ml syringe
 - 2 x 1ml syringes
 - 2 x ~1cm³ glass wool
 - 2 x 1.5ml screw cap sample tube
 - 3 x disposable plastic pipette
 - 1 x plastic spoons
 - 1 x plastic tweezers
 - 3 x Weighing boats
 - 2 x 1L sharps bins with lids removed
3. The glassware should be clean and dry.
 - 2 x glass 25ml beakers with appropriate stoppers
 - 1 x Watchglass (reaction vial lid)
 - 3 x 10ml Crimptop vials
 - 1 x 100 ml measuring cylinder
4. To prepare 100ml of 6 M HCl from conc. HCl (**metal free**, glass cabinet in R&D, Zr tray), dispense 50 ml Millipore water into the lidless 1L sharps bin labelled 6M HCl acid bath and add 50ml conc HCl.
5. Dispense 0.6 ml of 6 M HCl using a disposable plastic pipette into a small screw cap vial labelled (**6 M HCl**, preparation date and initials).
6. Wash all consumables and glass ware in the 6 M HCl bath and then transfer to the second lidless 1L sharps bin and rinse 3 x with Millipore water.
7. Place all consumables into a labelled sealable plastic bag (preparation date and initials) and put it into the Zr preparation tray to be used the next day.
8. Label a falcon tube with **1 M Oxalic acid**, preparation date and initials.

- Using an acid washed falcon tube and a plastic spoon (handle) weigh out 270 mg of oxalic acid (**metal free**, glass cabinet in R&D, Zr tray).
 - Top up with Millipore water to 3 ml, close and shake well. Place into stand for Zr preparation.
9. Label two falcon tubes with **2 M HCl**, preparation date and initials. Dispense 9.2 ml Millipore water into each labelled falcon tube and add to each 1.8 ml conc HCl using a disposable plastic pipette.

Solutions of HCl

Solution	Density (grams/ml)	Concentration (moles/liter)	To make a liter of solution
36.6-38% HCl	1.18	12.0	Concentrated hydrochloric acid
6 M HCl	1.10	6.0	500 ml conc. HCl + 500 ml H ₂ O
2 M HCl	1.03	2.0	167 ml conc. HCl + 833 ml H ₂ O

RH 3002	PETIC School of Medicine	
Cyclotron Manual	Separation of Zr-89 from solid target	

Principle

This procedure describes how to separate Zr-89 from the Y-86 solid target.


Ensure that the following procedures have been completed before performing this procedure.

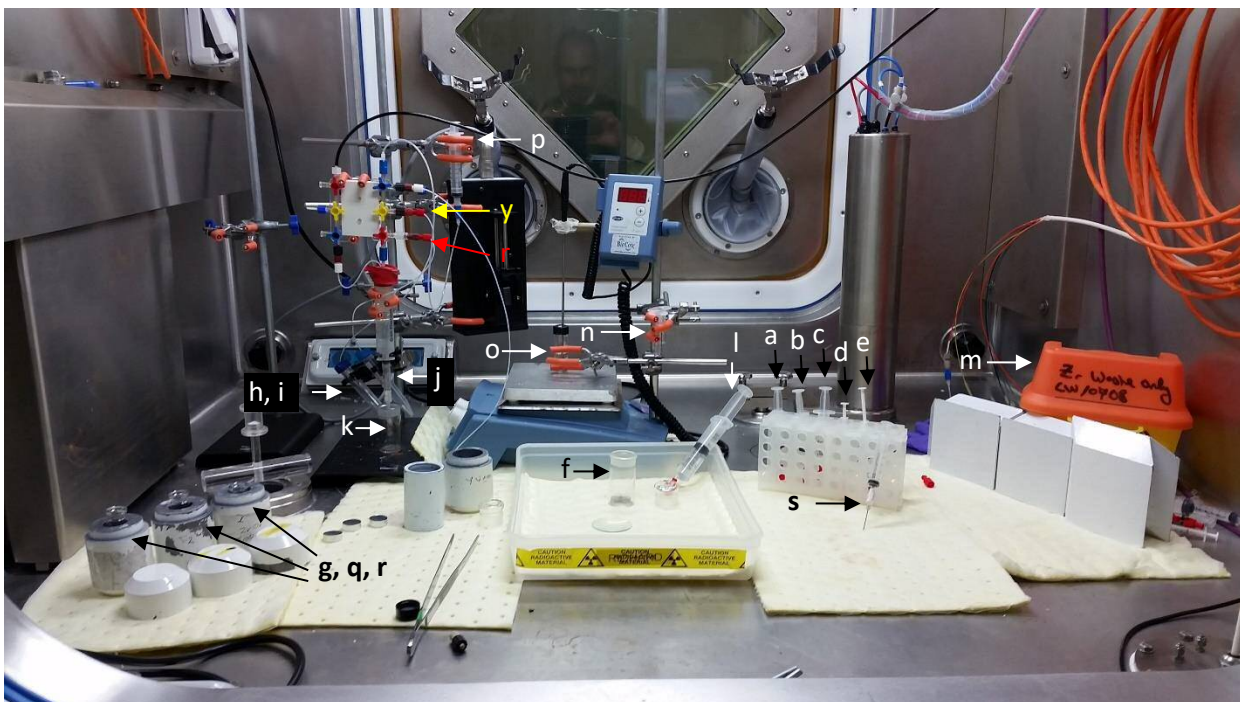
RH 3000 Preparation of Hot Cell 7 for Zr-89 Separation





RH 3001 Preparation for Zr-89 Separation day before



Note: All glassware and plastics should be prewashed with 6M HCl and then deionised water before use. The radioactivity of all waste items should be measured and logged before disposal in the Zr specific waste bin.

Procedure

1. Wear appropriate protective clothing and radiation monitoring equipment.
2. Record Activity and time of the foil target on **RH 4002**.
3. Remove the foil target from the dose calibrator and place in glass beaker (f) (see photo below) using the tongs.
4. Using tongs remove stopper from syringe (a) and place in syringe holder (n) above vial (f) and cautiously dispense **2 ml of 2M HCl syringe a** onto the foil target as slowly as possible.
5. Once the frothing has subsided remove empty syringe from holder and dispense a further **2 ml of 2M HCl syringe b** into glass beaker (f).
6. Repeat step 4 with **2 ml of 2M HCl syringe (c)**.
7. Once the frothing has subsided this should reveal a grey cloudy solution. Add **0.1 ml of H₂O₂ syringe (d)** and **0.5ml of 6M HCl from syringe (e)**.
8. Place the watch glass (tray) on glass beaker (f) and switch on the heater using the switch on the outside of the hot cell. Allow to heat up to a slow boil for 15 min.
9. Turn off the heater and allow to cool.
10. After 15 min place the plastic tubing connected to the cassette's blue tap on the right side into glass beaker (f).
11. Using tongs pull up the syringe to draw the now yellow solution into the syringe.
12. Switch the blue tap on the right side to the  position. Using tongs slowly push down on the syringe to dispense the Zr/Y solution onto the column.



13. If the flow of solution through the column stops or is slow under gravity you can apply a small amount of pressure with compressed air to increase the flow rate. If required open the compressed air on the left side of the hot cell and operate gently the needle valve. **Only use very small compressed air flows the liquid flow should always remain dropwise.**
14. Repeat steps 11-13 to fully empty the reaction vial (f).
15. Once the liquid flow has stopped dispense **12 ml of 2M HCl syringe (l)** into glass beaker (f).
16. Set the blue tap on the top right corner to the  position and then using tongs pull up the syringe to draw the new solution into the syringe.
17. Switch the top right blue tap back to the  position (and ensure the right hand red and yellow taps are also in the same orientation) and then tongs push down the syringe to dispense the 2M HCl solution onto the column in **2 ml batches** (increase the flow through the column with compressed air if required).
18. Repeat steps 16-17 until reaction vial (f) is fully empty then measure the activity of the **reaction vessel f** and record on **RH 4002**.
19. Now set the yellow tap on the right hand side to the  position and using tongs pull up the syringe to draw **4 ml of H₂O sample tube (i)** into the syringe.
20. Now switch the right hand yellow tap to the  position, then using tongs push down the syringe to dispense the water onto the column in **2 ml batches** (increase the flow through the column with compressed air if required).
21. Repeat steps 16 and 17 to dispense the remainder **of water**.

22. Once the water has all flowed through the column and the dripping has stopped remove **vial (k) (Y-89 waste fraction)** and place the stopper on it. Measure the activity and record the time. Record on **RH 4002**. Place the vial in a wide bore lead pot.
23. Place **vial (g)** under the column to collect the first Zr Oxalate fraction.
24. Now set the red tap on the bottom right corner to the  position and using tongs pull up the syringe to draw 3ml of 1.0M oxalic acid from sample tube (h) into the syringe.
25. Switch the bottom right corner red tap to the  position, then using tongs press down the syringe to dispense 0.5 ml of the oxalic acid onto the column. ZrOxF1 (increase the flow through the column with compressed air if required). **Take care not to force the liquid through too quickly.**
26. Remove the vial and place in a white lead pot and replace with a clean crimptop vial (q) and dispense a further 1ml of oxalic acid in the same way (ZrOxF2) this should contain the bulk of the activity.
27. Remove this vial and place in a white lead pot and replace with a clean crimptop vial (r) and dispense the remaining 1.5ml of oxalic acid in the same way (ZrOxF3).
28. Measure and record the activity and time on **RH 4002** of **vials g, q and r (Zr-89 Oxalate fraction)** and place the vials in lead pots for removal from the hot cell.
29. Measure and record (on RH 4002) the activity of any radioactive waste items including the column before disposal in the Zr waste bin.
30. Place the tray used vials, waste solutions and Zr waste bin in the lead safe in the corner of the R&D lab.
31. Transcribe all measured activities into isostock
32. Fill in **RH 4702** and leave the form attached to the hot cell.
33. There will be residual activity in the hotcell and on the magnetic stirrer / syringe driver. Label the cell as containing long lived radioactivity check yourself for activity and perform a contamination survey of the lab.

Appendix II: Calculations of relative enzyme activity values

1 Calculation of activities of free HRP

The observed rates of enzymatic activity are expressed in units of $A \cdot s^{-1}$ and are shown in Fig. 11. The following calculations describe the analysis performed to populate Fig. 12.

The molecular weight of the isoform of HRP used is known to be:

The concentration (c) of enzyme per well in $mg \cdot mL^{-1}$ is known from the absorbance of a stock solution at 280 nm as determined by UV-Vis spectrometry and subsequent serial dilution, and may be converted to molar concentration and thence to a number of molecules per unit volume:

As the volume of the sample is known to be 200 μL , the enzymes present may be arrived at.

For the four conditions described in Fig. 12:

For a given sample:

e.g. for $NaBH_4$ -reduced HRP:

2 Calculation of relative activities for gluteraldehyde immobilised HRP

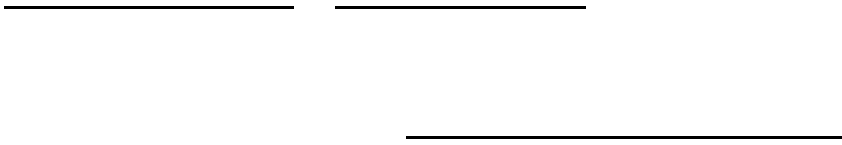
For each sample having a different initial enzyme:nanoparticle ratio, the number of nanoparticles present is determined based on the known concentration of nanoparticles in milligrams of solid per volume of stock solution ($\text{mg}\cdot\text{mL}^{-1}$) and the average mass of each nanoparticle calculated from XRD and TEM characterisation (see Fig. 13). If the average mass is taken to be 1.01×10^{-18} g per nanoparticle, then for the case where the initial enzyme:nanoparticle ratio is intended to be 3:

@

And

After the immobilisation of the enzymes, each sample was dispersed in 1 mL of an appropriate buffer, diluted 100 fold, and 20 μL of this solution transferred into each well of a 96 well plate. In the case above:

The relative activity of these enzymes may then be calculated from the observed rate in A.s^{-1} as shown in section 1 above.



3 Calculation of relative activities for reductive amination immobilised HRP

Taking the same approach as shown in section 2 above, in the case of a 17 % enzyme conjugated population:

@

and

After the immobilisation of the enzymes, each sample was dispersed in 1 mL of an appropriate buffer, diluted 1000 fold, and 20 μL of this solution transferred into each well of a 96 well plate. In the case above:

The relative activity of these enzymes may then be calculated from the observed rate in $\text{A}\cdot\text{s}^{-1}$ as shown in section 1 above.

4 Calculation of relative activities for reductive amination formed HRP-trastuzumab conjugates, free form and immobilised

The conjugate species synthesised was characterised by circular dichroism to be a 1:1 conjugate with an approximate molecular mass of 192,400 Da. The concentration (c) of a stock solution was determined spectroscopically, and an aliquot was taken and diluted 1000-fold for use in kinetic studies, thus:

Spectroscopic studies yielded an observed rate, from which an activity per enzyme relative to that of the freshly prepared and unmodified enzyme can be found:

The conjugate species was immobilised on nanoparticles analogously to the immobilisation of the enzyme. Taking the case of an approximately 2 % protein conjugated SPION population:

@

And

For the assessment of relative enzymatic activity, the particles were dispersed in 1 mL of an appropriate buffer, diluted tenfold and 20 μ L transferred to each well of 96 well plate:

The relative activity of these enzymes may then be calculated from the observed rate in $A.s^{-1}$ as shown in section 1 above.

Appendix III: Crystallographic data

1 Crystallographic data for naphthalimide (9)

Table 1. Crystal data and structure refinement details for naphthalimide (9).

Identification code	2016ncs0906r1x	
Empirical formula	C ₁₇ H ₁₄ NO ₄ Cl	
Formula weight	331.74	
Temperature	100(2) K	
Wavelength	0.71075 Å	
Crystal system	Monoclinic	
Space group	P2 ₁ /c	
Unit cell dimensions	$a = 9.4534(6)$ Å	$\alpha = 90.0^\circ$
	$b = 5.3568(3)$ Å	$\beta = 98.800(5)^\circ$
	$c = 28.9389(15)$ Å	$\gamma = 90.0^\circ$
Volume	1448.23(13) Å ³	
Z	1	
Density (calculated)	1.522 Mg / m ³	
Absorption coefficient	0.284 mm ⁻¹	
F(000)	488	
Crystal	Plate; yellow	
Crystal size	0.10 × 0.07 × 0.02 mm ³	
θ range for data collection	2.180 – 27.485°	
Index ranges	-12 ≤ h ≤ 11, -6 ≤ k ≤ 5, -37 ≤ l ≤ 37	
Reflections collected	12815	
Independent reflections	3306 [$R_{int} = 0.0445$]	
Completeness to $\theta = 27.5^\circ$	100 %	
Absorption correction	Semi-empirical from equivalents	
Max. and min. transmission	1.000 and 0.813	
Refinement method	Full-matrix least-squares on F^2	
Data / restraints / parameters	3306 / 0 / 209	
Goodness-of-fit on F^2	1.008	
Final R indices [$F^2 > 2\sigma(F^2)$]	$R1 = 0.1245$, $wR2 = 0.3077$	
R indices (all data)	$R1 = 0.1472$, $wR2 = 0.3205$	
Extinction coefficient	n/a	
Largest diff. peak and hole	2.200 and -0.750 Å ⁻³	

Diffraction: Rigaku FRE+ equipped with VHF Varimax confocal mirrors and an AFC12 goniometer and HG Saturn 724+ detector. **Cell determination and data collection:** CrysAlisPro (Rigaku, V1.171.39.9g, 2015) **Data reduction, cell refinement and absorption correction:** CrysAlisPro (Rigaku, V1.171.39.9g, 2015). **Structure solution:** ShelXT (Sheldrick, 2015). **Structure refinement:** ShelXL (Sheldrick, 2015). **Special details:** Large Q-peak suggests Cl is disordered over two sites but modelling leads to unrealistic bond lengths

Citations

CrysAlisPro Software System, Rigaku Oxford Diffraction, Yarnton, Oxford, UK (2016).
CrystalClear, Rigaku Corporation, The Woodlands, Texas, U.S.A., (2008-2014).
O.V. Dolomanov and L.J. Bourhis and R.J. Gildea and J.A.K. Howard and H. Puschmann, Olex2: A complete structure solution, refinement and analysis program, *J. Appl. Cryst.*, (2009), **42**, 339-341.
Sheldrick, G.M., Crystal structure refinement with ShelXL, *Acta Cryst.*, (2015), **C27**, 3-8.
Sheldrick, G.M., ShelXT-Integrated space-group and crystal-structure determination, *Acta Cryst.*, (2015), **A71**, 3-8.

2 Crystallographic data for naphthalimide (10)

Table 2. Crystal data and structure refinement details for **naphthalimide (10)**.

Identification code	2016ncs0907xaCAP	
Empirical formula	C ₂₁ H ₂₂ N ₂ O ₅	
Formula weight	382.40	
Temperature	100(2) K	
Wavelength	0.71075 Å	
Crystal system	Monoclinic	
Space group	P2 ₁ /n	
Unit cell dimensions	$a = 25.7629(5)$ Å	$\alpha = 90.0^\circ$
	$b = 4.83852(9)$ Å	$\beta = 99.154(2)^\circ$
	$c = 29.4982(6)$ Å	$\gamma = 90.0^\circ$
Volume	3630.24(13) Å ³	
Z	8	
Density (calculated)	1.399 Mg / m ³	
Absorption coefficient	0.101 mm ⁻¹	
F(000)	488	
Crystal	Plate; yellow	
Crystal size	0.20 × 0.02 × 0.01 mm ³	
θ range for data collection	2.393 – 27.485°	
Index ranges	–33 ≤ h ≤ 30, –6 ≤ k ≤ 6, –37 ≤ l ≤ 38	
Reflections collected	46525	
Independent reflections	8338 [$R_{int} = 0.0480$]	
Completeness to $\theta = 27.5^\circ$	99.9 %	
Absorption correction	Semi-empirical from equivalents	
Max. and min. transmission	1.000 and 0.857	
Refinement method	Full-matrix least-squares on F^2	
Data / restraints / parameters	6864 / 0 / 507	
Goodness-of-fit on F^2	1.090	
Final R indices [$F^2 > 2\sigma(F^2)$]	$R1 = 0.0590$, $wR2 = 0.1273$	
R indices (all data)	$R1 = 0.0759$, $wR2 = 0.1362$	
Extinction coefficient	n/a	
Largest diff. peak and hole	0.648 and –0.345 Å ⁻³	

Diffractometer: Rigaku FRE+ equipped with VHF Varimax confocal mirrors and an AFC12 goniometer and HG Saturn 724+ detector. **Cell determination and data collection:** CrysAlisPro (Rigaku, V1.171.39.9g, 2015) **Data reduction, cell refinement and absorption correction:** CrysAlisPro (Rigaku, V1.171.39.9g, 2015). **Structure solution:** ShelXT (Sheldrick, 2015). **Structure refinement:** ShelXL (Sheldrick, 2015).

Citations

CrysAlisPro Software System, Rigaku Oxford Diffraction, Yarnton, Oxford, UK (2016).
CrystalClear, Rigaku Corporation, The Woodlands, Texas, U.S.A., (2008-2014).
O.V. Dolomanov and L.J. Bourhis and R.J. Gildea and J.A.K. Howard and H. Puschmann, Olex2: A complete structure solution, refinement and analysis program, *J. Appl. Cryst.*, (2009), **42**, 339-341.
Sheldrick, G.M., Crystal structure refinement with ShelXL, *Acta Cryst.*, (2015), **C27**, 3-8.
Sheldrick, G.M., ShelXT-Integrated space-group and crystal-structure determination, *Acta Cryst.*, (2015), **A71**, 3-8.

3 Crystallographic data for complex ZnL¹

Table 3. Crystal data and structure refinement details for ZnL¹.

Identification code	2014ncs0434 (ZnL1)	
Empirical formula	C ₂₈ H ₄₈ N ₁₂ O ₈ S ₄ Zn ₂	
Formula weight	939.76	
Temperature	100(2) K	
Wavelength	0.71075 Å	
Crystal system	Triclinic	
Space group	P-1	
Unit cell dimensions	<i>a</i> = 9.944(8) Å	α = 110.88(2)°
	<i>b</i> = 10.072(9) Å	β = 92.672(14)°
	<i>c</i> = 10.2874(10) Å	γ = 90.046(12)°
Volume	961.5(12) Å ³	
Z	1	
Density (calculated)	1.623 Mg / m ³	
Absorption coefficient	1.528 mm ⁻¹	
<i>F</i> (000)	488	
Crystal	Column; orange	
Crystal size	0.200 × 0.040 × 0.020 mm ³	
θ range for data collection	2.165 – 27.534°	
Index ranges	-12 ≤ <i>h</i> ≤ 12, -13 ≤ <i>k</i> ≤ 12, -12 ≤ <i>l</i> ≤ 13	
Reflections collected	12230	
Independent reflections	4325 [<i>R</i> _{int} = 0.1355]	
Completeness to θ = 25.242°	98.8 %	
Absorption correction	Semi-empirical from equivalents	
Max. and min. transmission	1.000 and 0.131	
Refinement method	Full-matrix least-squares on <i>F</i> ²	
Data / restraints / parameters	4325 / 0 / 248	
Goodness-of-fit on <i>F</i> ²	0.921	
Final R indices [<i>F</i> ² > 2σ(<i>F</i> ²)]	<i>R</i> 1 = 0.0839, <i>wR</i> 2 = 0.1911	
R indices (all data)	<i>R</i> 1 = 0.0987, <i>wR</i> 2 = 0.1974	
Extinction coefficient	n/a	
Largest diff. peak and hole	1.941 and -0.759 e Å ⁻³	

Diffraction: Rigaku AFC12 goniometer equipped with an enhanced sensitivity (HG) Saturn724+ detector mounted at the window of an FR-E+ SuperBright molybdenum rotating anode generator with HF Varimax optics (100m focus). **Cell determination and data collection:** CrystalClear-SM Expert 2.0 r11 (Rigaku, 2011). **Data reduction, cell refinement and absorption correction:** CrystalClear-SM Expert 2.1 r29 (Rigaku, 2011). **Structure solution:** SUPERFLIP (Palatinus, L. & Chapuis, G. (2007). *J. Appl. Cryst.* 40, 786-790). **Structure refinement:** SHELXL-2013 (Sheldrick, G.M. (2008). *Acta Cryst. A* 64, 112-122). **Special details:** The crystal used gave split (twinned) diffraction pattern. However, integrating one component was enough to solve structure.

Table 4. Selected Bond lengths [Å] and angles [°] for **ZnL¹**.

Zn1–N4	2.115(5)
Zn1–N3	2.119(4)
Zn1–S2	2.3384(15)
Zn1–S1	2.4197(18)
Zn1–S1ⁱ	2.504(2)
S2–C10	1.748(6)
S1–C5	1.794(5)
N2–C5	1.306(7)
N2–N3	1.378(6)
N3–C6	1.302(7)
N5–C10	1.325(7)
N5–N4	1.371(6)
N4–C8	1.289(7)
C9–C8	1.498(7)
C8–C6	1.506(7)
C7–C6	1.491(7)
N4–Zn1–N3	74.95(17)
N4–Zn1–S2	81.39(13)
N3–Zn1–S2	144.80(14)
N4–Zn1–S1	152.91(12)
N3–Zn1–S1	80.26(13)
S2–Zn1–S1	114.73(6)
N4–Zn1–S1ⁱ	98.15(15)
N3–Zn1–S1ⁱ	100.29(13)
S2–Zn1–S1ⁱ	108.65(5)
S1–Zn1–S1ⁱ	96.84(8)
Zn1–S1–Zn1ⁱ	83.15(7)
C5–N2–N3	113.6(4)
C10–N5–N4	112.3(4)
N5–C10–S2	127.4(4)
N2–C5–S1	126.7(4)

Symmetry transformations used to generate equivalent atoms:

(i) $-x, -y, -z+1$

4 Crystallographic data for complex CdL¹

Table 5. Crystal data and structure refinement details for CdL¹.

Identification code	2014ncs0633 (CdL1)	
Empirical formula	C ₂₉ H ₄₅ Cd ₂ Cl ₃ N ₁₂ O ₈ S ₄	
Formula weight	1149.16	
Temperature	100(2) K	
Wavelength	0.71075 Å	
Crystal system	Monoclinic	
Space group	C2/c	
Unit cell dimensions	$a = 26.9437(19)$ Å	$\alpha = 90^\circ$
	$b = 11.8945(9)$ Å	$\beta = 111.132(8)^\circ$
	$c = 15.0987(11)$ Å	$\gamma = 90^\circ$
Volume	4513.5(6) Å ³	
Z	4	
Density (calculated)	1.691 Mg / m ³	
Absorption coefficient	1.363 mm ⁻¹	
$F(000)$	2312	
Crystal	Needle; pale yellow	
Crystal size	0.250 × 0.020 × 0.010 mm ³	
θ range for data collection	3.205 – 27.483°	
Index ranges	–34 ≤ h ≤ 34, –15 ≤ k ≤ 15, –19 ≤ l ≤ 19	
Reflections collected	29354	
Independent reflections	5179 [$R_{int} = 0.1006$]	
Completeness to $\theta = 25.242^\circ$	99.8 %	
Absorption correction	Semi-empirical from equivalents	
Max. and min. transmission	1.000 and 0.567	
Refinement method	Full-matrix least-squares on F^2	
Data / restraints / parameters	5179 / 490 / 304	
Goodness-of-fit on F^2	1.003	
Final R indices [$F^2 > 2\sigma(F^2)$]	$R1 = 0.0497$, $wR2 = 0.1038$	
R indices (all data)	$R1 = 0.0867$, $wR2 = 0.1186$	
Extinction coefficient	n/a	
Largest diff. peak and hole	0.826 and –0.778 e Å ⁻³	

Diffractionmeter: Rigaku AFC12 goniometer equipped with an enhanced sensitivity (HG) Saturn724+ detector mounted at the window of an FR-E+ SuperBright molybdenum rotating anode generator with HF Varimax optics (100m focus). **Cell determination and data collection:** CrystalClear-SM Expert 2.0 r11 (Rigaku, 2011). **Data reduction, cell refinement and absorption correction:** CrystalClear-SM Expert 2.1 r29 (Rigaku, 2011). **Structure solution:** SUPERFLIP (Palatinus, L. & Chapuis, G. (2007). J. Appl. Cryst. 40, 786-790). **Structure refinement:** SHELXL-2013 (Sheldrick, G.M. (2008). Acta Cryst. A64, 112-122). **Special details:** In the crystal structure one CHCl₃ is disordered 50/50 ratio over centre of inversion. Additionally, in the main residue one C9-C10 being part of aliphatic chain was modelled as disordered over two sites with 54/46 ratio. DFIX as well as SIMU, DELU and RIGU restraints have been used to maintain sensible molecular geometry and atomic displacement parameters.

Table 6. Selected Bond lengths [Å] and angles [°] for CdL¹.

Cd1–N1	2.326(4)
Cd1–N4	2.327(3)
Cd1–S1	2.5029(12)
Cd1–S2	2.5239(12)
Cd1–S2 ⁱ	2.8706(12)
Cd1–S1 ⁱⁱ	2.9574(12)
S2–Cd1 ⁱ	2.8706(12)
N2–C5	1.322(6)
N2–N1	1.367(5)
N4–C3	1.280(6)
N4–N5	1.372(4)
N1–C2	1.289(6)
N5–C9	1.315(6)
C12–C11	1.501(6)
C2–C3	1.490(6)
S1–Cd1 ⁱⁱ	2.9574(12)
N1–Cd1–N4	69.59(12)
N1–Cd1–S1	76.08(9)
N4–Cd1–S1	143.77(9)
N1–Cd1–S2	145.30(9)
N4–Cd1–S2	76.14(9)
S1–Cd1–S2	138.58(4)
N1–Cd1–S2 ⁱ	89.71(9)
N4–Cd1–S2 ⁱ	100.34(9)
S1–Cd1–S2 ⁱ	90.57(4)
S2–Cd1–S2 ⁱ	91.17(3)
N1–Cd1–S1 ⁱⁱ	81.27(9)
N4–Cd1–S1 ⁱⁱ	74.36(9)
S1–Cd1–S1 ⁱⁱ	89.56(3)
S2–Cd1–S1 ⁱⁱ	94.90(4)
S2 ⁱ –Cd1–S1 ⁱⁱ	170.68(4)
C9–S2–Cd1	96.26(15)
C9–S2–Cd1 ⁱ	96.40(15)
Cd1–S2–Cd1 ⁱ	86.29(3)
C5–N2–N1	112.9(4)
C9–N5–N4	114.1(3)
N1–C2–C3	116.3(4)
N4–C3–C2	117.0(4)

Symmetry transformations used to generate equivalent atoms:

(i) $-x+1, y, -z+3/2$ (ii) $-x+1, -y+1, -z+1$
